Université catholique de Louvain

Secteur des sciences et technologies

Institut de recherche en mathématique et physique

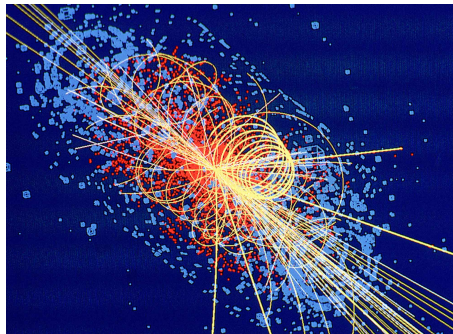Centre for Cosmology, Particle Physics and Phenomenology

UCL
Université
catholique
de Louvain

Loop-induced production of scalar particles in the Two-Higgs-Doublet Model at the LHC

Doctoral dissertation presented by

Benoît Hespel

in fulfilment of the requirements for the degree of Doctor in Sciences

Jury de thèse

Prof. Vincent Lemaître (president)	UCL, Belgium
Prof. Fabio Maltoni (promoter)	UCL, Belgium
Prof. Jean-Marc Gérard (promoter)	UCL, Belgium
Prof. Christophe Delaere	UCL, Belgium
Dr. Andrea Giammanco	UCL, Belgium
Prof. Emanuele Re	LAPTH, Annecy, France

September 4, 2017

Remerciements

Lors de la rédaction de cette thèse, de ce bref survol théorique de la physique des particules, je me suis rendu compte que rien de ceci n'aurait été possible sans l'aide et le soutien de nombreuses personnes. C'est pourquoi je tenais à commencer par vous rendre hommage.

Tout d'abord je voudrais remercier mes promoteurs, Prof. Fabio Maltoni et Prof. Jean-Marc Gérard. Merci beaucoup à vous deux pour ces quatre années passées à vos côtés en tant que doctorant. Merci pour votre enthousiasme, votre impressionante connaissance ainsi que vos précieux conseils. Merci pour toutes les réponses que vous m'avez données, pour les nouvelles idées à explorer que vous m'avez proposées. Je voulais aussi vous remercier tout particulièrement Jean-Marc car sans vous je n'aurais probablement jamais fait de thèse de doctorat. En effet, avant ma défense de mémoire, j'étais bien décidé à quitter l'université une fois mon diplôme de master obtenu. Cependant vous avez trouvé les mots qu'il fallait pour me faire hésiter. Après plusieurs jours de réflexion à peser le pour et le contre, j'ai finalement décidé de me lancer dans cette belle aventure scientifique. C'est alors que ton soutien, Fabio, a été déterminant. Tu m'as aidé à rédiger un projet de thèse en quelques semaines seulement, tu m'as aussi encouragé et coaché pour que je parvienne à me défendre correctement face au jury du FRIA afin de finalement décrocher la bourse et ainsi être assuré de pouvoir mener à bien ma thèse. Pour toutes ces raisons, merci à vous deux !

Merci aussi aux autres membres de mon jury d'avoir accepté d'en faire partie, merci pour les discussions très intéressantes lors de la défense privée qui m'ont permis d'en apprendre encore plus et pour vos commentaires constructifs et pertinents sur le texte qui m'ont aidé à l'améliorer.

Ensuite je voudrais me tourner vers toutes les personnes avec qui j'ai collaboré lors de mes recherches. Tout d'abord je voulais remercier Eleni avec qui j'ai travaillé tout

Évidemment, je ne pouvais terminer sans remercier mes amis. Merci à toi, Antony, pour tous les midis que nous avons passés à discuter physique et à rigoler, pour tes conseils en python et nos franches rigolades. Merci également à toi, Ioanis, pour nos discussions de chromodynamique qunatique ainsi que les bons moments passés en écoles doctorales. Merci à vous, Brieuc, Sébastien et Martin, pour votre collaboration pendant les MasterClasses ainsi que pour avoir si bien organisé les voyages au Cern avec les étudiants chaque année, moments inoubliables également. Enfin merci à toi Valentin, mon ami de longue date, pour nos discussions physico-mathématiques et tes encouragements réguliers.

Pour terminer, je voulais remercier mes parents, Chantal Bonnart et Ruddy Hespel, sans qui je ne serai pas là où je suis. Merci de m'avoir inculqué la notion de travail, de m'avoir motivé à me dépasser et de m'avoir montré la voie à suivre. Merci de m'avoir demandé comment se passait ma thèse même si vous ne compreniez pas tout lorsque je vous en parlais. Merci d'avoir demandé à voir mes articles dès qu'ils étaient terminés même si l'anglais n'est pas une langue facile pour vous. Bref merci d'avoir été fier de moi toutes ces années et de m'avoir soutenu. Merci également à mes grands-parents qui ont également toujours été intéressé par ce que je faisais lors de mon doctorat. Enfin merci à toi ma chérie pour ton soutien quotidien, pour tous les bons moments que nous passons et pour l'amour que tu me donnes.

Introduction

"Learn from yesterday, live for today, hope for tomorrow. The important thing is not to stop questioning"

Albert Einstein (1879 - 1955)

The Standard Model (SM) is the particle physics theory that describes (for now) best the reality at the smallest scales which are currently probed by experiments. It was formulated by S. Glashow, A. Salam and S. Weinberg in the 60's as a gauge theory based on the $SU(2) \times U(1)$ group unifying electromagnetism and weak interactions. It predicted that gauge bosons should be massless. However weak interaction is a very short distance interaction. The easiest explanation was that the force carriers should be massive. Their mass was in fact fixed by P.W. Higgs, R. Brout, F. Englert, G. Guralnik, C. Hagen and T. Kibble's theory, in which they added a new scalar doublet field interacting with bosons in a gauge invariant way. Due to its non-vanishing vacuum expectation value, once the theory is expanded around this minimum, mass-terms for the weak gauge bosons appear as well as a new scalar particle, the famous Higgs boson. This is now known as the BEH mechanism. Experimental data confirmed eventually that weak gauge bosons (W and Z bosons) were indeed quite heavy, explaining at the same time the weakness of this interaction.

In the meantime M. Gell-Mann, H. Fritzsch, D. Gross, F. Wilczek and H. D. Politzer put the foundation of the Quantum Chromodynamics (QCD) which is the theory describing strong interactions. Their formulation, based on the $SU(3)$ group, was driven by surprising results in nucleons experiments. From then hadrons like protons and neutrons started to be seen as bunches of new partons called quarks and gluons.

The SM has then remained barely the same for almost forty years, experimentalists measuring parameters and processes still more precisely, until the Higgs boson was

discovered at the Large Hadron Collider (LHC) on 4th July 2012. This was the last missing confirmation of the validity of the SM. At present, five years later, data confirmed that this new particle has indeed the right characteristics to be considered as the Higgs boson that was postulated fifty years ago.

All these major achivements in particle physics wouldn't have been possible without the rigorous work of thousands of physicists around the world either involved in making precise theoretical predictions or building, running and operating impressive accelerators. Given the LHC is colliding protons at very high energy, processes including strong interactions represent a huge background for all kind of searches because QCD rates are usually much bigger than those of other electroweak processes. Moreover since in particle physics any observable is computed in perturbation theory, and since the strong coupling constant $\alpha_s \simeq 0.1$ is not so small, QCD can induce sizable corrections to these observables. This explains why a lot of efforts have been spent last years in improving computations that include QCD corrections, at least at the first order, and in providing automated simulation tools to get theoretical predictions much easily.

Despite its beauty, the SM is known to be incomplete. Many different extensions have been suggested over the years to solve important issues raised by experimental observations or theoretical considerations. There are for example too many apparently free parameters which calls for an elucidation; the large hierarchies between some of them look unnatural; Dark Matter nature remains unknown; there is no fully satisfactory explanation for the matter anti-matter asymmetry of the universe; etc. All SM extensions not only have to be self-consistent from a theoretical point of view but they also have to be compatible with available experimental data and new predictions should make them testable experimentally.

All these Beyond-SM (BSM) theories are in general characterized by a set of new physical states interacting weakly and possibly strongly with the known SM particles. If their couplings are sufficiently large and their masses are in the kinematical reach of the LHC, these particles are expected to be produced and to decay in the detectors (or to escape them), giving visible signatures (or missing transverse energy). Extracting these new physics imprints from the huge amount of data is a real challenge given the numerous QCD radiations, both from theoretical and experimental points of view.

The link between pure theory and experiment is however not straightforward to establish since the technicality of both approaches requires a high level of specialization. This is where phenomenology enters the game. This branch of particle physics is concerned with filling possible gaps between these two sub-fields by developing interesting theoretical models and comparing predictions to experimental data in order to put limits on the model parameters. Phenomenologists provide experimentalists with

the theoretical input, the strategies and tools needed to analyse the rough information obtained from their impressive detectors.

Physics strategies can generally be classified into two distinctive categories. Top-down approaches focus on a particular theory (model) and try to use the maximal amount of available theoretical, indirect and direct constraints in order to define specific benchmark points. The possible signatures of the theory for these particular benchmark points are then investigated in great detail. The hope is of course that New Physics would be discovered around one of these benchmark scenarios. This is mainly the approach we will adopt in this thesis. The other possibility is to consider several signatures ("inspired" by realistic theories) from a model independent point of view and to scan the whole free parameter space to identify winning search strategies. Looking at particularly sensitive physical quantities, for example the top anti-top quark pair invariant mass distribution, in order to find deviations from the SM prediction is usually referred to as a "bottom-up" approach.

The electroweak symmetry breaking mechanism predicts the strength of all Higgs boson couplings to be uniquely determined by the masses of the elementary particles. This also includes the triple and quartic Higgs boson self–couplings, which in the SM are linked to the Higgs mass and its vacuum expectation value (VEV), and are therefore fully fixed after the Higgs mass measurement. Current measurements of the Higgs couplings to fermions and vector bosons [1] agree within 10-20% with the SM predictions, while no direct information is available on the Higgs boson self–interactions. In view of this experimental picture, possible non–minimal Higgs sectors are constrained, but certainly not ruled out. While some new physics models are no longer compatible with the present collider data, there are still many extended Higgs sectors which can accommodate a 125 GeV Higgs boson with coupling strengths similar to the SM. As detailed later in this thesis one possible candidate for such a theory is the Two–Higgs–Doublet Model (2HDM) [2].

If effectively realized in Nature, the 2HDM could lead to genuine indications of new physics at colliders. For instance, the direct production of additional heavy scalars offers excellent prospects to identify these novel particles through a variety of decay modes and final–state signatures [3–7] . Not less important are the indirect signatures from such extended Higgs sectors, which could arise via modified Higgs couplings to the fermions and gauge bosons, as well as through modified Higgs self–interactions.

The production of Higgs boson pairs at hadron colliders provides a direct handle on the trilinear Higgs self–coupling. Its direct experimental measurement plays a paramount role in the reconstruction of the Higgs potential and represents a key step towards unraveling the fundamental structure of electroweak symmetry breaking. While the profile of the 125 GeV resonance discovered at the LHC largely agrees with a SM Higgs profile, there is still experimental room, and also strong theoretical motivation,

for a non–minimal Higgs sector. Accurate predictions for Higgs production cross sections and distributions, including reliable estimates on the theoretical uncertainties, are thus necessary to identify and characterize eventual deviations from the SM. The 2HDM constitutes therefore an exemplary framework in which to describe the possible signatures of an extended Higgs sector.

In this thesis I will present the state-of-the-art predictions for the most dominant production mode (gluon fusion) for several processes involving new Higgses from the 2HDM. We will use the 2HDM as a generic SM extension of the scalar sector and study it from the perspective of precision test and for its signatures at the LHC.

In chapter 1 I will give a detailed introduction to the two main physics models I will use for the results. First I will present the mathematical framework of the SM, its particle content as well as its interactions, with a particular focus on the Higgs sector. After reviewing the current status of the experimental constraints on Higgs properties and couplings I will switch to the 2HDM. I will briefly review the new Higgs potential before looking at the consequences on the couplings. Finally I will conclude this first chapter by reviewing the numerical tools that have been used to get the results of the following chapters. I will introduce the main method we adopt to overcome the limitation of automatic Monte Carlo events generators and discuss most of the constraints that need to be taken into account when designing new physics benchmarks in the context of a 2HDM.

In chapter 2 I will present the first loop-induced process of interest: $gg \to ZH$ production. I will start first by reviewing the calculation in the SM and then extend the tools and analyses to the 2HDM. In chapter 3 we will turn to the study of Higgs pair production at the LHC at high precision level. Finally in chapter 4 we will dig more into the $t\bar{t}$ final state coming from a single Higgs boson production. Special accent will be put on the interference between signal and background. We will start first by reviewing some important feature in the SM then we will look at some simplified models that can be linked to the DM context and some 2HDM benchmarks.

This thesis is based on the following publications:

- [8] Higgs pair production via gluon fusion in the Two-Higgs-Doublet Model

- [9] Higgs and Z boson associated production via gluon fusion in the SM and the 2HDM

- [10] A comprehensive approach to dark matter studies: exploration of simplified top-philic models

- [11] Signal background interference effects in heavy scalar production and decay to a top-anti-top pair

and on the results in the following sections of the CERN Yellow Reports 4 [12]: Handbook of LHC Higgs Cross Sections: 4. Deciphering the Nature of the Higgs Sector.

- Chapter I.5: VBF and VH

- Chapter I.7: Higgs pair production

- Chapter I.8: Off-shell Higgs Production and Higgs Interference

During my PhD I also had the opportunity to present my research work at several places:

- Talk on Higgs pair production at PhD day Panda school "Physics and astrophysics" (22/05/14)

- Talk on Higgs pair production at Cargese international summer school: multi-TeV probes of the Standard Model and Beyond (21/07/14)

- Poster at MCnet summer school Spa (02/07/15)

- Talk on ZH production at the annual ERC miniworkshop at Cern (2/06/15)

- Talk on ZH production at the 28th Rencontres de Blois: Particle physics and cosmology (31/05/16)

- Talk on interference effect in top-antitop production at the annual ERC miniworkshop at Cern (05/07/16)

Finally I was also allowed to teach general physics to veterinary students 2h/week and I enjoyed this a lot.

Contents

xiii

Phenomenological framework

"It doesn't matter how beautiful your theory is, it doesn't matter how smart you are. If it doesn't agree with experiment, it's wrong."

Richard P. Feynman (1918 - 1988)

In this first chapter we present a brief summary of the main models we will use to make predictions in this thesis. We start by introducing the main elements of the Standard Model (SM), more details can be found in [13]. After reviewing the SM matter content, the gauge structure of its fundamental interactions is discussed. Based on these required ingredients, we then review the major role played by the spontaneous breaking of the electroweak symmetry and the Brout-Englert-Higgs (BEH) mechanism, and how the latter explains the mass of the particles in the SM.

Then we will have a brief overview of the Higgs production mechanisms as well as its decays. We will introduce some Effective Field Theory (EFT) notation and shortcuts and then we will explore the current experimental constraints on the Higgs boson. In the last section we will devote our attention to an extension of the scalar sector of the SM which is called the Two-Higgs-Doublet Model (2HDM). In particular we will study the new Higgs potential, the resulting couplings to the new spin-0 particles and their decay rates in order to set the path for the analyses presented in the following chapters.

1.1   The Standard Model

The SM is one of the most successful theories of physics up-to-date, surviving decades
of research in high-energy physics. It describes three of the four fundamental inter-
actions observed in Nature and is the result of two theories formulated during the
second half of the 20th century, namely, the electroweak theory of Glashow, Wein-
berg and Salam based on the gauge symmetry group $SU(2)_L \times U(1)_Y$ which unifies
electromagnetism and weak interactions, together with Quantum Chromo-Dynamics
(QCD), the theory of strong interactions associated to the $SU(3)_c$ group. From then
all these three interactions stopped to be seen as of completely different nature but
rather as three different representations of the same object, in the same way as light-
ing up a cylinder from different sides can result in viewing either a rectangle, a circle
or a parallelogram shadow.

Technically the SM is a quantum, gauge, relativistic and renormalisable theory based
on $SU(3)_c \times SU(2)_L \times U(1)_Y$ which contains and describes all the elementary par-
ticles we have observed until now along with their interactions. Both are described in
the context of a quantum field theory (QFT) based on several underlying symmetries.
The first one is a space-time symmetry under translations, rotations and boosts which
constitute the class of simultaneous transformations of both space and time. The sec-
ond main symmetry principle is called *gauge invariance* and will be explained when
we will introduce interactions between matter particles.

Particle Content

At the particle level, the SM includes two kinds of fields: matter and gauge fields.
All elementary particles can be classed in two groups according to their quantum
numbers. The matter particles, called *fermions*, carry a half-integer spin, whereas the
mediators of the fundamental interactions, the *bosons*, have an integer spin. For every
fermion, there exists an antiparticle partner with identical mass, but differing from its
counterpart by opposite signs of its quantum numbers.

The twelve fermions are divided themselves in two types of Dirac chiral matter fields.
There are six *quarks* which have electric, weak and color charges, and six *leptons*
which only carry electric and weak charges. The left-handed components of the fields
transform as doublets under the weak isospin group $SU(2)_L$, while the right-handed
components transform as singlets. The upper and lower partners of each doublet have
a weak isospin projection T_3 equal to 1/2 and -1/2 respectively, whereas the third axis
projection of the weak isospin vanishes for singlets.

Quarks and leptons are grouped together to form three generations with identical properties except for their mass, which increases from the first to the last generation. Leptons generations consist in one electrically charged particle with the fundamental electric charge $Q = -e$ and one neutral massless particle called neutrino. As they do not carry colour, they are only affected by the electromagnetic and weak forces. The electron (e) and the electron-neutrino (ν_e) compose the first generation, while the muon (μ) and the tau (τ) are similarly arranged with the corresponding neutrinos (ν_μ and ν_τ) to form the second and third generations. Note that since right-handed neutrinos completely decouple in the SM (zero isospin, no electric charge nor hypercharge), they will not be considered in what follows.

$$ L_L^i = \left(\begin{array}{c} \nu_e \\ e^- \end{array} \right)_L , \left(\begin{array}{c} \nu_\mu \\ \mu^- \end{array} \right)_L , \left(\begin{array}{c} \nu_\tau \\ \tau^- \end{array} \right)_L \quad ; \quad e_R^i = (e^-)_R,\ (\mu^-)_R,\ (\tau^-)_R $$

Similarly each of the three families of quarks consists of two types of quarks, carrying an electric charge $Q_{up} = 2e/3$ and $Q_{down} = -e/3$, respectively. Up and down quarks (u, d) form the lightest generation, the second family contains the charm and strange quarks (c, s) while the heaviest generation is formed by the top and bottom quarks (t, b). As observed, all these six quarks have an additional quantum number with respect to leptons: colour. As a consequence, quarks are the only known matter particles sensitive to the strong interaction, and transform as triplets under $SU(3)_c$. Because of this additional property, quarks are submitted to what is called *color confinement*, meaning that quarks cannot be observed in nature as free particles. They always have to combine with other quarks, in a process called *hadronization*, in order to form 'white' colored bound states. Up to now two distinct possible combinations have been observed: *mesons* which are composed of a quark and a antiquark and *baryons* which are made of three quarks. These two categories form the *hadrons*.

$$ Q_L^i = \left(\begin{array}{c} u \\ d \end{array} \right)_L , \left(\begin{array}{c} c \\ s \end{array} \right)_L , \left(\begin{array}{c} t \\ b \end{array} \right)_L $$

$$ u_R^i = (u)_R,\ (c)_R,\ (t)_R \quad ; \quad d_R^i = (d)_R,\ (s)_R,\ (b)_R $$

In addition to matter fields, the SM contains gauge fields which are responsible for the interactions between all the fermions. We can distinguish eight gluons G_μ^a associated to the eight $SU(3)_c$ group generators, one neutral boson B_μ associated to the $U(1)_Y$ group generator along with three weak bosons W_μ^i associated to the three $SU(2)_L$ group generators. These last four electroweak gauge bosons will then give birth to the photon (γ) and the $W^\pm$ and Z^0 bosons after spontaneous symmetry breaking (see Sec. 1.1.2). This mechanism also explains the existence of the lately discovered Higgs boson.

The particle content of the SM, its associated fields and their quantum numbers are summarised in Tab. 1.1. Note that the hypercharge Y which corresponds to the

Fields	N_c	T_3	Y	Q
u_{Li}^I	3	+1/2	1/3	2/3
d_{Li}^I	3	-1/2	1/3	-1/3
u_{Ri}^I	3	0	4/3	2/3
d_{Ri}^I	3	0	-2/3	-1/3
ν_{Li}^I	1	+1/2	-1	0
l_{Li}^I	1	-1/2	-1	-1
l_{Ri}^I	1	0	-2	-1
g	3	0	0	0
γ	1	0	0	0
W^+	1	+1/2	+1	+1
Z^0	1	0	0	0
W^-	1	-1/2	-1	-1
H	1	-1/2	+1	0

Table 1.1: SM particle content and their quantum numbers.

conserved charged associated to the $U(1)_Y$ group verifies the Gell-Mann-Nishijima relation which was originally introduced in the context of the strong interaction:

$$Q = T_3 + \frac{Y}{2} \tag{1.1}$$

1.1.1   Lagrangian and symmetries

We will now build the SM lagrangian step by step. First of all it's important to respect global Lorentz transformations, so that physics that will be derived from it won't depend on the choice of a reference frame. A second necessary ingredient is renormalisability in order to allow theoretical predictions on observables to be made thanks to perturbative computations. A necessary (but not sufficient) condition for renormalisability is gauge invariance. Last but not least the SM lagrangian must respect unitarity so that probability amplitudes are finite and can be renormalised.

Gauge invariance

Gauge invariance is a key notion in quantum field theory as this principle is at the basis of all fundamental interactions described by the SM. As a reminder, let's recap

on gauge transformation. Let's consider symmetry group $SU(N)$, with generators T^a, $a = 1, \ldots, N^2 - 1$. A local gauge transformation for this group is given by the unitary matrix $U(x)$:

$$\Psi(x) \longrightarrow \Psi'(x) = U(x)\Psi(x) \tag{1.2}$$

with $U(x) = \exp^{ig\alpha_a(x)T^a} = 1 + ig\alpha_a(x)T^a + \mathcal{O}(g^2\alpha^2)$, where $\alpha_a(x)$ is a phase factor and g the coupling constant associated to the interaction described by the group. The Lie algebra of the generators is given by

$$[T^a, T^b] = if^{abc}T_c \tag{1.3}$$

where the f^{abc} are called *structure constants* of the group. For an abelian group as $U(1)$, there is only one generator, so that the commutator hereabove vanishes, resulting in an associated boson with no charge. However in Yang-Mills theories (weak and strong interactions), structure constants are not trivial and bosons can interact among themselves, leading to more complex computations and less predictability for these interactions.

As we will see, all interactions in the SM are derived from a lagrangian density. Imposing gauge invariance on this lagrangian leads to gauge transformation laws for fermions and bosons. This can be achieved by introducing a covariant derivative D_μ. Since we want to have $D_\mu\psi(x) \longrightarrow U(x)D_\mu\psi(x)$, we need $D_\mu \longrightarrow U(x)D_\mu U^\dagger(x)$ so that,

$$\partial_\mu \longrightarrow D_\mu = \partial_\mu - igA_\mu^a(x)T^a \tag{1.4}$$

where $A_\mu^a(x)$ is a generic gauge boson transforming like:

$$
\begin{aligned}
A_\mu^a(x) \quad \longrightarrow \quad & U(x)A_\mu^a(x)U^{-1}(x) + \frac{1}{g}U(x)\partial_\mu U^{-1}(x) \\
= \quad & A_\mu^a(x) + \frac{1}{g}\partial_\mu\alpha^a(x) + f^{abc}A_\mu^b(x)\alpha^c
\end{aligned}
\tag{1.5}
$$

It is common to define a *field strength tensor* associated to the gauge fields as

$$
\begin{aligned}
F_{\mu\nu} &= F_{\mu\nu}^a T^a \\
F_{\mu\nu}^a &= \partial_\mu A_\nu^a - \partial_\nu A_\mu^a + gf^{abc}A_\mu^b A_\nu^c \\
[D_\mu, D_\nu] &= -igF_{\mu\nu}
\end{aligned}
\tag{1.6}
$$

Actually the SM lagrangian can be divided into two contributions: the free lagrangian $\mathcal{L}_0$, which we will also refer to as the kinetic part, as it accounts for free particles

propagation, and the interaction lagrangian $\mathcal{L}_I$, which is responsible for all possible kinds of interactions between particles (diffusion, decay, ...).

As a result general solutions are described as perturbations associated to the free solutions. This expansion is called *Dyson series* and is at the very basis of the powerful graphical method in perturbation theory in particle physics. This method relies on *Feynman diagrams* which represent any process at a given order in this expansion. The first order is called *Leading Order* (LO) and corresponds in general to tree-level diagrams. The second term in the expansion in called *Next-to-Leading Order* (NLO) and includes extra boson emissions as well a virtual corrections which form what is called *loops*. NLO is the standard level of precision nowadays. However some processes are now known at NNLO or even up to N^{3}LO, reducing the theoretical uncertainties by a large factor.

The free part can always be solved exactly by the principle of least action:

$$\partial_\mu \left(\frac{\partial \mathcal{L}}{\partial(\partial_\mu \phi)} \right) - \frac{\partial \mathcal{L}}{\partial \phi} = 0 \tag{1.7}$$

which leads to the two main equations for the free fields dynamics:

- *The Dirac equation* for fermionic fields : $(i\partial\!\!\!/ - m_f)\psi_f = 0$

- *The Klein-Gordon equation* for bosonic fields : $(\partial^\mu \partial_\mu + M^2)\psi_b = 0$

Let's now have a look at each of the three main groups of the SM separately.

SU(3)   The eight generators (T^a) of this group are defined by the Gell-Mann matrices (λ^a) via $T^a = \frac{1}{2}\lambda^a$ and the eight associated gauge fields correspond to the eight gluons (G_μ^a). Gell-Mann matrices are three by three hemitian matrices verifying the following identites:

$$
\begin{aligned}
tr[\lambda^a] &= 0 \\
[\lambda^a, \lambda^b] &= 2if^{abc}\lambda^c \\
tr[\lambda^a, \lambda^b] &= 2\delta^{ab} \\
\text{with} \quad if^{abc} &= 2Tr\left(\left[\frac{\lambda^a}{2}, \frac{\lambda^b}{2} \right], \frac{\lambda^c}{2} \right)
\end{aligned}
\tag{1.8}
$$

Explicitly, they read:

$$\lambda_1 = \begin{pmatrix} 0 & 1 & 0 \\ 1 & 0 & 0 \\ 0 & 0 & 0 \end{pmatrix}, \ \lambda_2 = \begin{pmatrix} 0 & -i & 0 \\ i & 0 & 0 \\ 0 & 0 & 0 \end{pmatrix}, \ \lambda_3 = \begin{pmatrix} 1 & 0 & 0 \\ 0 & -1 & 0 \\ 0 & 0 & 0 \end{pmatrix},$$

$$\lambda_4 = \begin{pmatrix} 0 & 0 & 1 \\ 0 & 0 & 0 \\ 1 & 0 & 0 \end{pmatrix} \lambda_5 = \begin{pmatrix} 0 & 0 & -i \\ 0 & 0 & 0 \\ i & 0 & 0 \end{pmatrix}, \ \lambda_6 = \begin{pmatrix} 0 & 0 & 0 \\ 0 & 0 & 1 \\ 0 & 1 & 0 \end{pmatrix},$$

$$\lambda_7 = \begin{pmatrix} 0 & 0 & 0 \\ 0 & 0 & -i \\ 0 & i & 0 \end{pmatrix}, \ \lambda_8 = \frac{1}{\sqrt{3}} \begin{pmatrix} 1 & 0 & 0 \\ 0 & 1 & 0 \\ 0 & 0 & -2 \end{pmatrix} \tag{1.9}$$

The tensor associated to the strong interaction is written $G_{\mu\nu} = G^a_{\mu\nu} T^a$, with $G^a_{\mu\nu} = \partial_\mu G^a_\nu - \partial_\nu G^a_\mu + g_s f^{abc} G^b_\mu G^c_\nu$

SU(2) The three generators of this group (T^i) are defined with the Pauli matrices (σ^i) and are related to the three weak gauge fields (W^i_μ). The Pauli matrices are two by two hermitian matrices verifying:

$$\begin{aligned} tr[\sigma^i] &= 0 \\ [\sigma^i, \sigma^j] &= 2i\varepsilon^{ijk}\sigma^k \end{aligned} \tag{1.10}$$

Explicitly, they are given by:

$$\sigma_1 = \begin{pmatrix} 0 & 1 \\ 1 & 0 \end{pmatrix}, \ \sigma_2 = \begin{pmatrix} 0 & -i \\ i & 0 \end{pmatrix}, \ \sigma_3 = \begin{pmatrix} 1 & 0 \\ 0 & -1 \end{pmatrix} \tag{1.11}$$

where ε^{ijk} is the fully antisymmetric Levi-Civita tensor.

The tensor associated to the weak bosons is written $W_{\mu\nu} = W^i_{\mu\nu} \tau^i$, with $W^i_{\mu\nu} = \partial_\mu W^i_\nu - \partial_\nu W^i_\mu + g\varepsilon^{ijk} W^j_\mu W^k_\nu$.

U(1) The only generator is the hypercharge Y and its associated electromagnetic boson is called B_μ. The tensor associated to the electromagnetic boson is written $B_{\mu\nu} = \partial_\mu B_\nu - \partial_\nu B_\mu$.

Now, all the pieces can be put together to form the kinetic part of the lagrangian for the gauge bosons:

$$\mathcal{L}_0 \supset \mathcal{L}^{bosons}_{kin} = -\frac{1}{4} B_{\mu\nu} B^{\mu\nu} - \frac{1}{2} Tr(W_{\mu\nu} W^{\mu\nu}) - \frac{1}{2} Tr(G_{\mu\nu} G^{\mu\nu}) \tag{1.12}$$

The last missing part to have the full free lagrangian of the SM is to include the kinetic part for the fermions. In the SM, fermions are discribed by Dirac spinors ψ with

four components. While bosons fields are associated to a Lie algebra with particular commutation relations as seen in 1.3, fermion spinors form a space on which acts a Clifford algebra. The matrix representation of this algebra is generated by the four by four *Dirac matrices* (or gamma matrices) which follow anticommutation rules:

$$\{\gamma^\mu, \gamma^\nu\} = 2\eta^{\mu\nu}I_4 \quad , \quad \mu, \nu \in [0,3] \tag{1.13}$$

$\eta^{\mu\nu}$ is the Minkowski metric with signature $(+ - --)$ and I_4 is the 4x4 identity matrix. In the standard representation they are given by:

$$\gamma^0 = \begin{pmatrix} I_2 & 0 \\ 0 & -I_2 \end{pmatrix}, \quad \gamma^i = \begin{pmatrix} 0 & \sigma^i \\ -\sigma^i & 0 \end{pmatrix} \quad i \in 1,2,3 \tag{1.14}$$

The kinetic part of the fermion lagrangian is then written:

$$\mathcal{L}_{kin}^{fermions} = \sum_j i\bar{\psi}_j \partial_\mu \gamma^\mu \psi_j = \sum_j i\bar{\psi}_j \slashed{\partial} \psi_j \tag{1.15}$$

where we introduce the Feynman slash notation ($\slashed{\partial} = \partial_\mu \gamma^\mu$) and where the index j runs for all possible fermions. Sometimes it's more interesting to express this lagrangian in term of the chiral fermion states. This can be achieved by using the γ^5 matrix defined by:

$$\gamma^5 = i\gamma^0\gamma^1\gamma^2\gamma^3 = \begin{pmatrix} 0 & I_2 \\ I_2 & 0 \end{pmatrix} \tag{1.16}$$

This matrix can then be used to project the spinor ψ onto its left and right components via:

$$\begin{aligned} \psi &= \psi_L + \psi_R \\ \psi_L &= P_L\psi = \frac{1}{2}(1 - \gamma^5)\psi \\ \psi_R &= P_R\psi = \frac{1}{2}(1 + \gamma^5)\psi \end{aligned} \tag{1.17}$$

where P_L and P_R are projectors :

$$P_L^2 = P_L, \quad P_R^2 = P_R, \quad P_L P_R = P_R P_L = 0, \quad \bar{P}_L = P_R \tag{1.18}$$

This leads to the chiral decomposition:

$$\begin{aligned} \bar{\Psi}\gamma^\mu\Psi &= \bar{\Psi}_L\gamma^\mu\Psi_L + \bar{\Psi}_R\gamma^\mu\Psi_R \\ \bar{\Psi}\Psi &= \bar{\Psi}_L\Psi_R + \bar{\Psi}_R\Psi_L \end{aligned} \tag{1.19}$$

The lagrangian 1.15 can then be written in term of the chiral states shown in Tab. 1.1:

$$\mathcal{L}_{kin}^{fermions} = \sum_{j=1}^{3} \left(i\bar{Q}_L^j \slashed{\partial} Q_L^j + i\bar{u}_R^j \slashed{\partial} u_R^j + i\bar{d}_R^j \slashed{\partial} d_R^j + i\bar{L}_L^j \slashed{\partial} L_L^j + i\bar{e}_R^j \slashed{\partial} e_R^j \right) \quad (1.20)$$

Fundamental interactions

Now that the free lagrangian is complete, let's introduce some interactions between these free particles. Among the four fundamental interactions that are currently known only three of them can be described by the SM in a unified mathematical framework (quantum gravity still needs to be implemented):

Electromagnetism is responsible for the infinite range force between any electrically charged particles and also describes light propagation. It rules many of the interactions of our daily life, from the chemical bounds to communications.

Weak interaction is responsible for nuclear phenomena such as beta decay. It's range is limited since the carriers of the interaction (the Z and $W^{\pm}$ bosons) are massive. Although this interaction seems to be more exotic than the other two, it's present in our everyday life as it allows our sun to shine.

Strong interaction is responsible for the cohesion of the nucleus (and of all the hadrons) and also explains the interaction between quarks and gluons. This is the strongest force at short distances but, due to confinement, its range is limited.

The SM describes these interactions at the quantum level. At small scales gravity is so weak compared to the other three forces that it can be safely neglected, something that we systematically do when computing cross-sections and decays of particles in high-energy experiments. The main problem with gravity as one of the gauge theories in the SM comes from the fact that the quantum description of General Relativity is not renormalisable.

The key to get interactions between bosons and fermions is gauge invariance. The principle of minimal coupling allows us to simply replace any simple partial derivative ∂_μ appearing in the kinetic lagrangian with the covariant derivative D_μ to get the proper interactions among the SM particles. In the same way as for Eq. 1.4 we get the following transformation by taking into account all three interactions:

$$\partial_\mu \longrightarrow D_\mu = \partial_\mu - ig_s G_\mu^a L^a - ig_w W_\mu^i \tau^i - \frac{Y}{2} ig_w' B_\mu \quad (1.21)$$

where g_s is the strong coupling while g_w, g'_w are the electroweak couplings. Substituting this in the free lagrangian leads to:

$$\mathcal{L}_{kin} + \mathcal{L}_{int} = \sum_i \left(i\bar{\Psi}_i \slashed{D} \Psi_i \right) - \frac{1}{4} B_{\mu\nu} B^{\mu\nu} - \frac{1}{4} W^i_{\mu\nu} W^{\mu\nu i} - \frac{1}{4} G^a_{\mu\nu} G^{\mu\nu a} \quad (1.22)$$

All the basic ingredients are now in the SM lagrangian. A few problems persist though. Gauge invariance imposes all particles appearing in the lagrangian to be massless. We know however by experimental results that this is clearly not the case (with W and Z bosons being roughly eighty times heavier than a proton). The solution comes from the spontaneous symmetry breaking (SSB) of the electroweak interaction. This last step is known as the Brout-Englert-Higgs (BEH) mechanism.

1.1.2 Brout-Englert-Higgs mechanism

Up to now, all particles (fermions and bosons) we introduced have to be massless in order to verify local gauge invariance. However, in the SM, we observed that some electroweak gauge bosons are massive (their mass is in fact related to the small range of the weak interaction and hence to the relatively long lifetime of particles decaying via weak interaction). This requires at least the presence of three scalars to be absorbed as the longitudinal degrees of freedom of these vector fields in addition to the extra scalar needed to trigger this mechanism.

The minimal solution is to group these four fields into one $SU(2)_L$ complex doublet, called *Higgs doublet*, with weak hypercharge $Y = +1$

$$\phi \equiv \begin{pmatrix} \phi^+ \\ \phi^0 \end{pmatrix} \equiv \frac{1}{\sqrt{2}} \begin{pmatrix} \phi^1 + i\phi^2 \\ \phi^3 + i\phi^4 \end{pmatrix} \quad (1.23)$$

The most general gauge invariant and renormalizable scalar lagrangian can be written as the difference between a kinetic part (where we already apply the principle of minimal coupling to get interaction between this Higgs doublet and the other electroweak gauge bosons) and the Higgs potential:

$$\mathcal{L}_S = \mathcal{L}^S_{kin} - V(\phi) = (D^\mu \phi)^\dagger D_\mu \phi - \frac{1}{2} \mu^2 \phi^\dagger \phi - \frac{1}{4} \lambda (\phi^\dagger \phi)^2 \quad . \quad (1.24)$$

where $\lambda > 0$ to ensure the scalar potential to be bounded from below. The minimum of this potential corresponds to the vacuum expectation of the scalar field and is obtained by solving:

$$\frac{\partial V}{\partial \phi} = \mu^2 \phi + \lambda \phi^3 = 0 \quad (1.25)$$
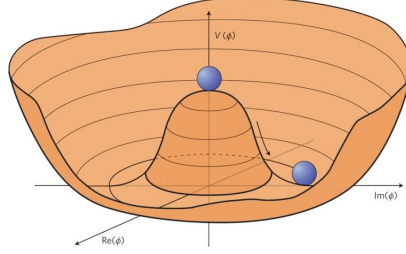
Figure 1.1: Higgs potential and spontaneous symmetry breaking.

The sign of μ^2 is essential because it triggers the spontaneous symmetry breaking.

- If $\mu^2 > 0$, the minimum is given by $\langle\phi\rangle_0 = 0$ and there is no breaking, the symmetry is said to be explicitly realized and the corresponding fields remain massless.

- If $\mu^2 < 0$ the potential becomes a mexican hat shape as depicted in Fig. 1.1 with a non-zero vacuum state.

In this last case $V(\phi)$ is still invariant under $SU(2)_L$ transformations (the minimal energy state is degenerated under rotation in the plane (ϕ^+, ϕ^0)) but choosing a particular direction is now equivalent to choosing a particular gauge. That's why the minimum of the potential in $\mathcal{L}_S$ can always be arranged using a $SU(2)_L \times U(1)_Y$ transformation to become

$$\langle\phi\rangle_0 = \frac{1}{\sqrt{2}} \begin{pmatrix} 0 \\ v \end{pmatrix} \quad . \tag{1.26}$$

where $v \simeq 246$ GeV is the *vacuum expectation value* (VEV) and is derived from:

$$(\phi\phi^\dagger)_{min} = \frac{-\mu^2}{\lambda} \equiv v^2 \tag{1.27}$$

It corresponds to the energy scale associated to the electroweak symmetry breaking $SU(2)_L \times U(1)_Y \to U(1)_{em}$. To get the physical meaning of the lagrangian we can develop the field ϕ around its minimum, so that:

$$\phi(x) = \frac{e^{\frac{i}{v}\chi^i(x)\frac{\sigma^i}{2}}}{\sqrt{2}} \begin{pmatrix} 0 \\ v + H(x) \end{pmatrix} \tag{1.28}$$

and the scalar potential becomes:

$$V(H) = \frac{1}{4}\lambda v^4 + \lambda v^2 H^2 + \lambda v H^3 + \frac{1}{4}\lambda H^4 \tag{1.29}$$

with $\langle H(x) \rangle = 0$, $H(x)$ being associated to the Higgs boson and $\chi^i(x)$ to the Goldstone bosons[1]. By applying a new $SU(2)_L$ gauge transformation with parameter $-\chi^i(x)/v$ we get:

$$\phi(x) = \frac{1}{\sqrt{2}} \begin{pmatrix} 0 \\ v + h(x) \end{pmatrix} \quad ; \quad \phi^c = i\sigma_2 \phi^* = \frac{1}{\sqrt{2}} \begin{pmatrix} v + h(x) \\ 0 \end{pmatrix} \quad (1.30)$$

This particular choice is known as the *unitary gauge*. In this case the Goldstone bosons get combined with the weak gauge bosons so that they acquire a mass. We can now define the physical states (mass eigenstates) for the electroweak gauge bosons by combining the interaction states W^i_μ and B_μ:

$$\begin{aligned} W^\pm_\mu &\equiv \frac{1}{\sqrt{2}}(W^1_\mu \mp iW^2_\mu) \\ A_\mu &\equiv \cos\theta_W B_\mu + \sin\theta_W W^3_\mu \\ Z_\mu &\equiv -\sin\theta_W B_\mu + \cos\theta_W W^3_\mu \end{aligned} \quad (1.31)$$

The masses of the physical bosons are then given by:

$$m_\gamma = 0 \quad , \quad m_W = \frac{g_w v}{2} \quad , \quad m_Z = \frac{m_W}{\cos\theta_W} = \frac{\sqrt{g_w^2 + g_w'^2}\, v}{2} \quad (1.32)$$

where the Weinberg angle (θ_W) is defined by

$$\cos\theta_W = \frac{g_w}{\sqrt{g_w^2 + g_w'^2}} \quad ; \quad \sin\theta_W = \frac{g_w'}{\sqrt{g_w^2 + g_w'^2}} \quad (1.33)$$

It's then possible to relate the VEV to the Fermi constant $G_F = 1.16637.10^{-5}\text{GeV}^{-2}$ via:

$$\frac{G_F}{\sqrt{2}} = \frac{g_w^2}{8m_W^2} = \frac{g_w^2}{8(\frac{1}{4}v^2 g_w^2)} = \frac{1}{2v^2} \Rightarrow v = \frac{1}{\sqrt{G_F \sqrt{2}}} \quad (1.34)$$

The values of the $W^\pm$ and Z bosons masses predicted by the theory are in excellent agreement with their experimental values, $m_W = 80.385 \pm 0.015$ GeV and $m_Z = 91.1876 \pm 0.021$ GeV [14]. It's important to stress that the photon A^μ stays massless after this process because the $U(1)_{em}$ remains unbroken. Another important consequence is that its coupling constant is related to the g_w, g_w' electroweak couplings as a result of the SSB:

$$e = g_w \sin\theta_W = g_w' \cos\theta_W \quad (1.35)$$

---

[1] They are massless spin 0 particles which appear each time a continuous symmetry is broken spontaneously as a vertue of the Goldstone theorem

In summary we saw that the fundamental principle behind the BEH mechanism is the transfer of three degrees of freedom originally associated to a complex scalar field to the three gauge vector fields W_μ^i which then become massive. In this process an additional massive scalar fields H, the so-called Higgs boson, had been introduced in the theory. Its mass, $m_H = \sqrt{2\lambda v^2}$ can be infered from Eq. 1.29 but was not known numerically given that μ and λ are not predicted by the theory. The three interactions are now well separated and the particle content is realized. The massless photon A^μ is responsible for electromagnetism interaction as it couples to electrically charged particles proportionaly to their charge. The charged weak bosons $W^\pm$ couples to both quarks and leptons and, as will be discussed in Sec. 1.1.2, are responsible for flavour changes. The neutral Z^0 boson on the other hand is responsible for neutral current in the SM, along with the photon. Finally the eight gluons G_a^μ couple to quarks and are responsible for strong interactions.

Moreover on 4th July 2012, the ATLAS and CMS collaborations of the Large Hadron Collider jointly announced that they had observed a new boson in the mass region of 125 GeV [15]. On 14th March 2013, CERN officially confirmed the existence of the Higgs particle. On 8th October 2013, the Nobel prize in physics was awarded both to F. Englert and P. Higgs for "the theoretical discovery of a mechanism that contributes to our understanding of the origin of mass of subatomic particles", and which has recently been confirmed through the discovery of the predicted fundamental particle. As of 2017, it is now acknowledged that the properties of this scalar particle are consistent with those predicted by the SM and the BEH mechanism. With the impressive amount of data collected since the start of the LHC, the ATLAS and CMS collaborations put a final end to a 50 years effort for proving the existence of the ultimate building block of the standard electroweak theory.

Origin of fermion masses and Yukawa couplings

Although the spontaneous breaking of the electroweak symmetry allows the W, Z and H bosons to acquire a mass through the BEH mechanism, the experimental observations of massive quarks and leptons still have to be explained in the SM.

By definition, chiral fields belong to inequivalent representations of $SU(2)_L \times U(1)_Y$, and cannot be massive in the SM because explicit Dirac mass terms are not gauge invariant since they mix fermions with opposite chirality:

$$m_i \bar\psi^i \psi_i = m_i \bar\psi_L^i \psi_{Ri} + m_i \bar\psi_R^i \psi_{Li} \tag{1.36}$$

The solution comes once again from the BEH mechanism we just introduced. In fact it not only gives mass to the electroweak gauge bosons but it also explains all fermion

masses and fermions-Higgs interactions via the so-called Yukawa couplings:

$$
\begin{aligned}
\mathcal{L}_{Yukawa} &= -\sum_{i,j} \bar{\psi}_L^i Y_{ij} \phi \psi_R^j \\
&= -\sum_{i,j=1}^{3} \left(\bar{Q}_L^i Y_{ij}^u \phi^c u_R^j + \bar{Q}_L^i Y_{ij}^d \phi d_R^j + \bar{L}_L^i Y_{ij}^e \phi e_R^j \right)
\end{aligned}
\tag{1.37}
$$

with $\phi^c = i\sigma_2\phi$. In the last equation we wrote explicitly mass terms for up(down)-type quarks and lepton separately. Y_{ij} are 3x3 complex matrices that mix the flavor eigenstates i and j and define their Yukawa couplings. After spontaneous symmetry breaking we get:

$$
\begin{aligned}
\mathcal{L}_Y &= -\sum_{i,j=1}^{3} \left(\bar{Q}_L^i Y_{ij}^u \frac{(v+H)}{\sqrt{2}} u_R^j + \bar{Q}_L^i Y_{ij}^d \frac{(v+H)}{\sqrt{2}} d_R^j \right. \\
&\quad + \left. \bar{L}_L^i Y_{ij}^e \frac{(v+H)}{\sqrt{2}} e_R^j \right)
\end{aligned}
\tag{1.38}
$$

A famous algebra theorem states that any complex matrices Y can be diagonalized by unitary left and right matrices $V_{L/R}$ such that $Y_{diag} = V_L^\dagger Y V_R$. The same unitary matrices can then be used to rotate the flavour eigenstates into the mass eigenstate basis as

$$
f_{L/R}^I = V_{L/R}^f f_{L/R}^{phys}
\tag{1.39}
$$

so that we finally get:

$$
\begin{aligned}
\mathcal{L}_Y &= -\sum_{i,j=1}^{3} \left(\bar{u}_L^i (V_L^{u\dagger} Y_{ij}^u V_R^u) \frac{(v+H)}{\sqrt{2}} u_R^j + \bar{u}_L^i (V_L^{d\dagger} Y_{ij}^d V_R^d) \frac{(v+H)}{\sqrt{2}} d_R^j \right. \\
&\quad + \left. \bar{e}_L^i (V_L^{e\dagger} Y_{ij}^e V_R^e) \frac{(v+H)}{\sqrt{2}} e_R^j \right) \\
&= -\sum_{i=1}^{3} \left(\bar{u}_L^i Y_{ii}^u \frac{(v+H)}{\sqrt{2}} u_R^i + \bar{d}_L^i Y_{ii}^d \frac{(v+H)}{\sqrt{2}} d_R^i + \bar{e}_L^i Y_{ii}^e \frac{(v+H)}{\sqrt{2}} e_R^i \right) \\
&= -\sum_{i=1}^{3} \left(y_u^i \bar{u}^i u^i \frac{(v+H)}{\sqrt{2}} + y_d^i \bar{d}^i d^i \frac{(v+H)}{\sqrt{2}} + y_e^i \bar{e}^i e^i \frac{(v+H)}{\sqrt{2}} \right) \\
&= -\sum_{fermions} m_f \bar{f} (1 + \frac{H}{v}) f
\end{aligned}
\tag{1.40}
$$

with $m_f = \frac{v y_f}{\sqrt{2}}$. This leads to new Feynman rules for the Yukawa couplings: $g_{hff} = \frac{-i m_f}{v}$. The fact that this coupling is proportional to the mass is a general feature imposed by the breaking mechanism and is very important for Higgs boson phenomenology.

Complete SM lagrangian

In this section we gather all the lagrangian pieces we build before. In its minimal form, the final SM lagrangian reads:

$$
\begin{aligned}
\mathcal{L}_{SM} &= \frac{-1}{4} F_{\mu\nu} F^{\mu\nu} \\
&+ i\bar{\psi} \slashed{D} \psi + (h.c.) \\
&+ \bar{\psi}^i y_{ij} \psi^j \phi + (h.c.) \\
&+ |D_\mu \phi|^2 - V(\phi)
\end{aligned}
\tag{1.41}
$$

By expanding the field strength tensors in the first line we get the kinetic terms for the gauge bosons as well as their self-interactions. Substituting the expression for the covariant derivative in the second line gives the kinetic term for the fermions and their interactions with the gauge bosons. The third line contains the fermion mass terms and their interaction with the Higgs boson. Finally the last line includes Higgs self interaction and kinetic terms along with its interactions with massive gauge bosons.

Another way to express the interactions of fermions with gauge bosons is via currents J^μ associated to each interaction: $eA_\mu J^\mu_{em}$, $g_w(W^+_\mu J^\mu_{W^+} + W^-_\mu J^\mu_{W^-} + Z_\mu J^\mu_Z)$ and $g_s A^a_\mu J^{a,\mu}_s$. These currents are conserved ($\partial_\mu J^\mu = 0$) as a result of Noether theorem[2] and are given explicitly by:

---

[2]Noether's theorem states that to every infinitesimal transformation which let the action invariant corresponds a conserved quantity.

$$
\begin{aligned}
J_{em}^{\mu} &= -\bar{e}^i\gamma^\mu e_i + \frac{2}{3}\bar{u}^i\gamma^\mu u_i - \frac{1}{3}\bar{d}^i\gamma^\mu d_i \\
J_{W^+}^{\mu} &= \frac{1}{\sqrt{2}}(\bar{\nu}_L^i\gamma^\mu e_{Li} + \bar{u}_L^i\gamma^\mu V_{CKM}d_{Li}) \\
J_{W^-}^{\mu} &= \frac{1}{\sqrt{2}}(\bar{e}_L^i\gamma^\mu \nu_{Li} + \bar{d}_L^i\gamma^\mu V_{CKM}^{\dagger}u_{Li}) \\
J_Z^{\mu} &= \frac{1}{\cos\theta_W}\left[\frac{1}{2}\bar{\nu}_L^i\gamma^\mu \nu_{Li} + \left(-\frac{1}{2} + \sin^2\theta_W\right)\bar{e}_L^i\gamma^\mu e_{Li} + \sin^2\theta_W \bar{e}_R^i\gamma^\mu e_{Ri} \right. \\
&\quad + \left(\frac{1}{2} - \frac{2}{3}\sin^2\theta_W\right)\bar{u}_L^i\gamma^\mu u_{Li} - \frac{2}{3}\sin^2\theta_W \bar{u}_R^i\gamma^\mu u_{Ri} \\
&\quad + \left.\left(-\frac{1}{2} + \frac{1}{3}\sin^2\theta_W\right)\bar{d}_L^i\gamma^\mu d_{Li} + \frac{1}{3}\sin^2\theta_W \bar{d}_R^i\gamma^\mu d_{Ri}\right] \\
J_s^{a,\mu} &= \bar{u}_i^{\ i}\gamma^\mu T_3^a u_i + \bar{d}_i^{\ i}\gamma^\mu T_3^a d_i
\end{aligned}
\tag{1.42}
$$

While electromagnetic and strong interactions don't change the flavor of the fermions, this is no longer true for the weak interaction. It allows transitions inside and between generations of fermions. It comes from the fact that the quark interacting states are different from the flavor states (see Eq. 1.39). Explicitly we have

$$
\begin{aligned}
u_R &= V_R^u u_R' \quad ; \quad u_L = V_L^u u_L' \\
d_R &= V_R^d d_R' \quad ; \quad d_L = V_L^d d_L'
\end{aligned}
\tag{1.43}
$$

By convention, the flavour and mass eigenstate are chosen to be the same for up-type quarks, that is $V_L^u = V_R^u$. Inserting this into the $qq'W^\pm$ interactions terms we get:

$$
\mathcal{L}_W = \frac{g}{\sqrt{2}}u_{Li}'\gamma^\mu V_{CKM}^{ij}d_{Rj}'W_\mu^+ + (h.c.)
\tag{1.44}
$$

where we introduced the Cabibbo-Kobayashi-Maskawa (CKM) mixing matrix:

$$
V_{CKM} = (V_L^u)^{\dagger}V_L^d
\tag{1.45}
$$

The elements of this matrix encode the transition probabilities between the different quark flavours through weak interaction and are measured experimentally:

$$
V_{CKM} = \begin{pmatrix} V_{ud} & V_{us} & V_{ub} \\ V_{cd} & V_{cs} & V_{cb} \\ V_{td} & V_{ts} & V_{tb} \end{pmatrix} \simeq \begin{pmatrix} 0,974 & 0,225 & 0,003 \\ 0,225 & 0,973 & 0,041 \\ 0,008 & 0,040 & 0,999 \end{pmatrix}
\tag{1.46}
$$

In its standard parametrization, the CKM matrix is given in terms of three mixing angles (Euler angles) and one complex phase which allows direct CP violation in the

SM. The presence of such a phase is linked to the number of fermion generations, as with only two generations it could be reabsorbed in the fields definition.

Note that this change of basis doesn't affect the currents with the Z boson or the photon. This implies that neutral current couplings do not allow for flavour-changing processes, as they can only couple a fermion to its corresponding antifermion. This is summarised by the so-called Glashow-Iliopoulos-Maiani (GIM) mechanism, which states that there are no flavour-changing neutral currents (FCNC) among chiral quarks at tree-level in the SM.

There is in principle no natural explanation for the hierarchy observed in the CKM matrix elements. Although the SM fermion masses are generated from the same mechanism, the original Yukawa matrices from which they originate are arbitrarily free. This issue is known as the fermionic mass hierarchy and could be the indication for new physics beyond the electroweak scale as discussed in Sec. 1.1.5. For instance, deviations from these values could be a hint of the existence of new fermions.

1.1.3   Higgs boson phenomenology

The Higgs boson is at the heart of this thesis. In this section we will describe its properties and its couplings to the other SM particles in more detail. The SM Higgs boson is a 125 GeV (the heaviest boson) spin-0 scalar eletrically neutral and colorless particle. It only couples to massive particles such as W, Z bosons and massive fermions, via Yukawa terms.

By developping the covariant derivative and expanding ϕ in the Higgs lagrangian of Eq. 1.24 after SSB we get the Higgs interactions with weak gauge bosons:

$$
\begin{aligned}
\mathcal{L}_H &= \frac{1}{2}\partial^\mu H \partial_\mu H - \frac{1}{2}W_{\mu\nu}W^{\mu\nu} - \frac{1}{4}F_{\mu\nu}F^{\mu\nu} - \frac{1}{4}Z_{\mu\nu}Z^{\mu\nu} \\
&+ \frac{g_w^2 v^2}{8}\left[(W_\mu^+)^2 + (W_\mu^-)^2\right] + \frac{(g_w^2 + g_w'^2)v^2}{8}(Z_\mu)^2 \\
&+ \frac{g_w^2 v}{2}HW_\mu^+ W^{\mu-} + \frac{g_w^2}{4}H^2 W_\mu^+ W^{\mu-} \\
&+ \frac{(g_w^2 + g_w'^2)v}{4}HZ_\mu Z^\mu + \frac{(g_w^2 + g_w'^2)}{8}H^2 Z_\mu Z^\mu \\
&+ \mu^2 H^2 - \lambda v H^3 - \frac{1}{4}\lambda H^4 + \dots
\end{aligned}
\tag{1.47}
$$
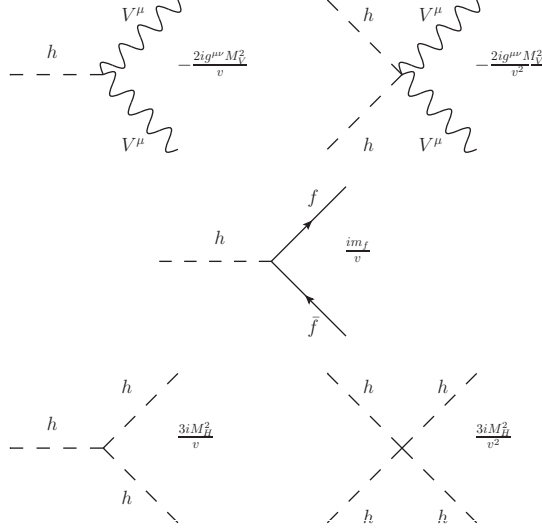
Figure 1.2: Higgs boson Feynman rules in the SM.

From this expression we can then derive the corresponding Feynman rules and couplings:

$$
\begin{aligned}
g_{HWW} &= \tfrac{i}{2}v g_w^2 &&= ig_w m_W &&= \tfrac{2im_W^2}{v} \\
g_{HZZ} &= \tfrac{i}{2}v(g_w^2 + g_w'^2) &&= \tfrac{iv g_w^2}{2\cos^2\theta_W} &&= \tfrac{2im_Z^2}{v} \\
g_{HHWW} &= \tfrac{i}{2}g_w^2 &&= \tfrac{1}{v}g_{HWW} &&= \tfrac{2im_W^2}{v^2} \\
g_{HHZZ} &= \tfrac{i}{2}(g_w^2 + g_w'^2) &&= \tfrac{1}{v}g_{HZZ} &&= \tfrac{2im_Z^2}{v^2} \\
g_{HHH} &= \tfrac{-3im_H^2}{v} \\
g_{HHHH} &= \tfrac{-3im_H^2}{v^2}
\end{aligned}
\tag{1.48}
$$

with $m_H^2 = -2\mu^2 = 2\lambda v^2$. We already wrote the couplings to fermions in Eq. 1.40 so that we can summarize its couplings like this:

$$
g_{Hf\bar{f}} = \frac{-im_f}{v} \quad ; \quad g_{HVV} = \frac{2im_V^2}{v} \quad ; \quad g_{HHVV} = \frac{2im_V^2}{v^2} = \frac{g_{HVV}}{v} \tag{1.49}
$$

The fact that the Higgs bosons couples proportionnaly to the mass (or mass squared) explains why it will interact mostly with heavy particles (top quark, weak bosons) and why it was so hard to discover: it rarely decays to electrons or muons which are the most easily trackable particles.
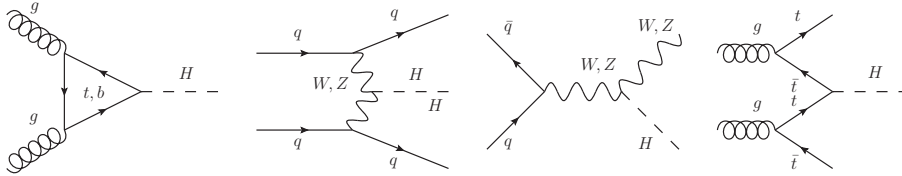
Figure 1.3: Main Higgs production modes at the LHC.

Note that the SM Higgs boson is the minimal solution to the problem of fermion and boson masses. Other complex solutions involving extra doublets exist, one famous example will be discussed in Sec. 1.2 and will be further investigated in the main part of this thesis.

Production modes and decay channels

The Higgs boson was already searched for at LEP and Tevatron before being discovered five years ago at the LHC. Up to now, all tests and property analyses made on Higgs data tend to confirm it is well the predicted Higgs boson of the SM.

As we saw in the last section the Higgs boson couples to particles with a strength proportional to the particle mass. It's then evident that the four main production processes at the LHC involve each either a Higgs boson coupling to the $W^\pm/Z$ bosons or to the top quark, as can be seen on the corresponding Feynamn diagrams depicted in Fig. 1.3. Sorted by decreasing total rate, we have:

- gluon fusion, via top/bottom quark loop

- vector boson fusion (VBF)

- WH/ZH associated production

- $t\bar{t}H$ associated production

An exhaustive study of these four production modes can be found in the Handbook of LHC Higgs cross sections 4 [12]. In this thesis we will only focus on the gluon fusion process for two main reasons. First it's the dominant production mode. The parton distribution functions are depicted in Fig. 1.4. We can see that at small Bjorken-x the gluon PDF is dominant, as at high energy, a lot of gluons exist inside a proton, leading to a higher probability of colliding gluons when two protons interact. The second main reason is that it is a loop-induced process. This requires much more
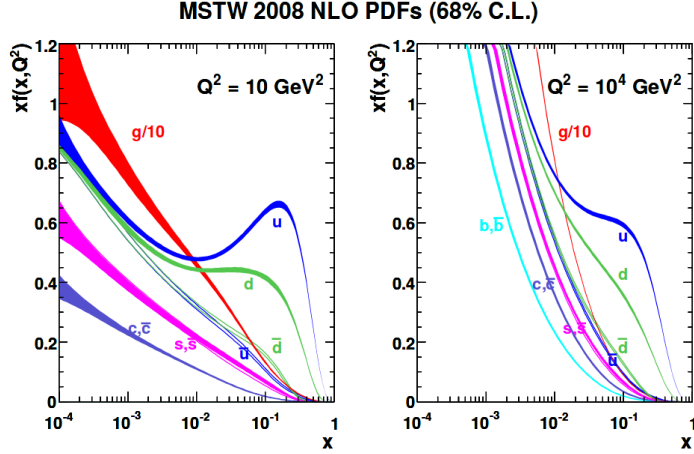
Figure 1.4: MSTW 2008 NLO PDF's at different Q^2 energy [16]

effort to be computed as the simplest diagram already contains a loop. NLO involves thus two-loop topologies which are very difficult to compute.

The state-of-art predictions for the total rates at the LHC at $\sqrt{s} = 13$ TeV are shown in Fig. 1.5. The total cross section for gluon fusion is known up to next-to-next-to-next-to-leading-order (N^3LO in QCD [17] in the infinite top mass limit, including soft gluon resummation up to NNLL). VBF has been computed up to NNLO in QCD [18] as well as VH [19]. Finally $t\bar{t}H$ is known up to NLO QCD [20].

In the last years, two main goals emerge from the theory point of view in particle physics: computing as accurately and precisely as possible total rates by developing new computation techniques and developing numerical automated tools for fully differential prediction of observables. In Sec. 1.3 we will describe one of these tools, MADGRAPH5_AMC@NLO , and give more technical details about the computation techniques we will use throughout this thesis to overcome the lack of automated numerical tools in the past[3].

Even though we will focus on the production and not on what happens next to the Higgs boson, for completeness we simply review the possible decay modes of the Higgs boson. As shown on Fig. 1.6 for $m_H = 125$ GeV the main decay channels are $b\bar{b}(\sim 60\%), W^+W^-(\sim 20\%), gg(\sim 10\%)$ and $\tau^+\tau^-(\sim 6\%)$ as they are the most

---

[3]This is no longer the case since MG5_aMC_v_2_3_x (released in July 2015) which allows loop-induced event generation at LO.
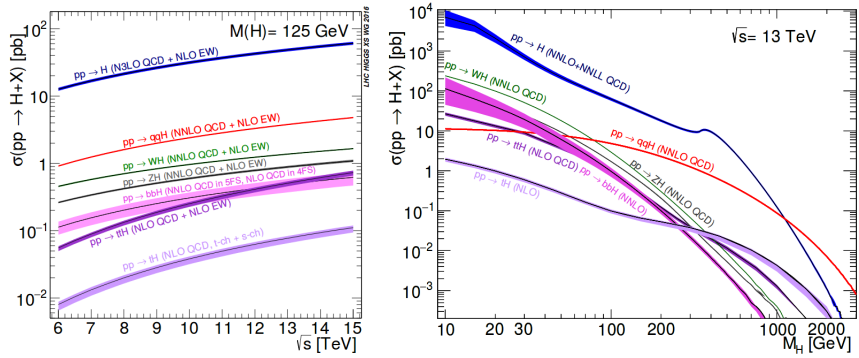
Figure 1.5: Left Higgs production cross sections as a function of the centre-of-mass energy. Right: Higgs production cross sections as a function of the Higgs mass at 13 TeV. These plots are taken from [12]
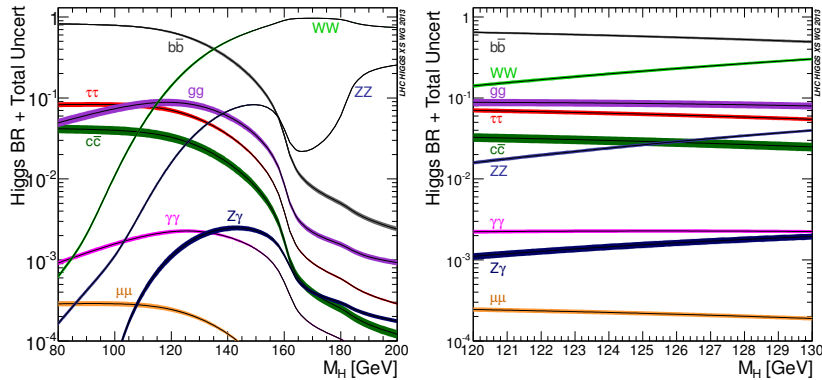
Figure 1.6: SM Higgs boson decay branching ratios. Right: zoom on the $m_H = 125$ GeV.

massive particles with $m < m_H/2$. Note however that the Higgs discovery was made in two other decay channels: four leptons coming from ZZ^* and two photons final states. Even if the branching ratios of these channels are relatively small ($< 1\%$), they lead to cleaner signatures in the detectors and hence were more easily analysed.

Effective field theory and Higgs operators

As we saw, the Higgs boson doesn't directly couple to gluons and photons as they are massless. As a result the Higgs can only couple to these bosons indirectly via a triangle loop of massive particles. Coupling to gluons occurs via quark loops (top

and bottom mainly) while coupling to photons also includes a W boson loop (which dominates over the fermion loop).

In some exotic toy models we would like to have new spin-0 particles that directly couple to the gluons and/or photons This can be achieved in the CP conserving case through the following dimension-5 operators:

$$L_g = \frac{\alpha_s c_g^S}{12\pi v} G_{\mu\nu} G^{\mu\nu} H^0 - \frac{\alpha_s c_g^P}{8\pi v} G_{\mu\nu} \tilde{G}^{\mu\nu} A^0 \tag{1.50}$$

$$L_\gamma = -\frac{2\alpha_{em} c_\gamma^S}{9\pi v} F_{\mu\nu} F^{\mu\nu} H^0 - \frac{\alpha_{em} c_\gamma^P}{3\pi v} F_{\mu\nu} \tilde{F}^{\mu\nu} A^0 \tag{1.51}$$

This form of interaction is what one obtains in the case of additional heavy states in the loop which can be integrated out, with c_g^P and c_g^S corresponding to the rescaling factor of the heavy quark Yukawa couplings with respect to that of the top in the SM. In fact, the operators in Eq. 1.50 match the infinite top mass limit used for the SM Higgs when $c_g^S = 1$ and $c_g^P = 0$; this approach is called Higgs Effective Field Theory (HEFT) and allows to have a LO tree level diagram instead of a loop-induced one. As will be explained in details in Sec. 1.3.2 we will use these kind of HEFT models to generate events for several processes involving Higgs bosons and build a reweighting technique to improve the precision on the theoretical predictions

1.1.4   Experimental constraints

The Large Hadron Collider

The Large Hadron Collider (LHC) is a 27 km long circular accelerator (synchrotron) built 100 m under the ground and installed near Geneva. It uses the former LEP tunnel, but accelerates and collides protons instead of electrons/positrons.

The LHC is currently running at 13 TeV of centre of mass energy. To reach such high energies, a few steps are required to accelerate the protons. As shown on Fig. 1.7 the protons go through different smaller linear injectors and circular pre-accelerators called in order LINAC2, BOOSTER, PS (Proton Synchrotron) and SPS (Super Proton Synchrotron) before they reach the LHC ring. The protons comes first from hydrogen ionization. They are then grouped into bunches and first accelerated by the LINAC2 accelerator up to 50 MeV. In the BOOSTER they acquire a kinetic energy of 1.4 GeV. They enter then in the PS where they are accelerated up to 25 GeV. The time separation between two proton bunch is 25 ns. Finally after passing through the SPS, where they increase their energy up to 450 GeV, they enter into the LHC for their final

CERN's Accelerator Complex
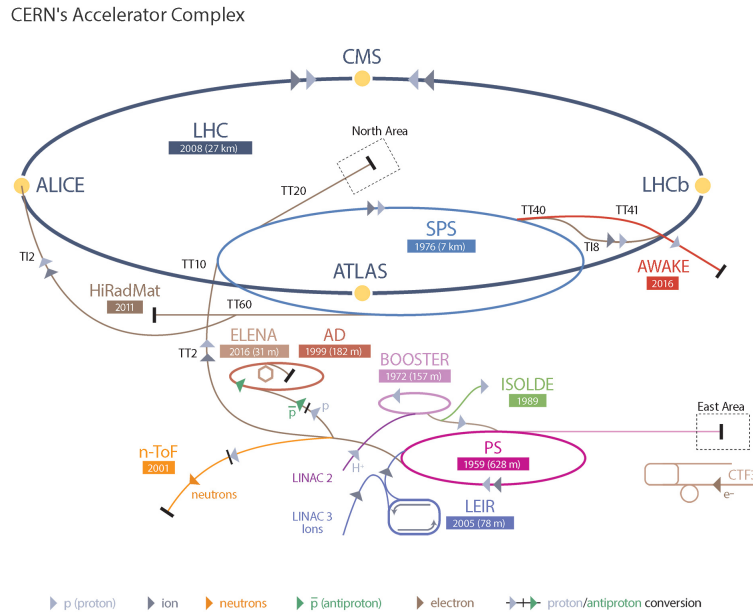
Figure 1.7: LHC acceleration's chain and detectors.

acceleration with radio frequency cavities. Run-I (2011-2013) of the LHC consisted of protons of 3.5 TeV and 4 TeV. Then, after its first upgrade, the LHC reached his current energy of 6.5 TeV by proton in Run-II (2015-2018). Finally it should reach its maximal energy in Run-III (2021), when protons will then have 7 TeV of energy. The magnetic field needed to curve their path is about 8.33 T, and is created in the 1282 dipoles that form the LHC accelerator. Note that such intense magnetic fields can only be achieved using superconductive technology ($\simeq 2$ K).

The two beams of protons circulate in opposite directions in separated pipes and only cross at four particular points of the LHC where impressive detectors are installed (CMS, ATLAS, ALICE, LHCb). Each of the 2800 bunches contains on average 10^{11} protons in a volume of a cylinder of more or less 8 cm long and 6 μm radius at the interaction points.

Among the four main experiments CMS and ATLAS are called "multi-purpose" detectors by opposition to the other two, ALICE and LHCb which are oriented towards more specific processes involving heavy ions collisions to study QCD plasma physics (ALICE) and CP violation in B physics (LHCb). That's why in this thesis we will only focus on the constraints brought by CMS and ATLAS. Their main motivation is

to observe new particles (like they did for the Higgs) and to measure their properties with the best level of accuracy.

The probability to observe a particular process at the LHC is related to the production cross section (σ) of this process. The number of expected events in the detectors of the LHC is then (from a pure theoretical point of view):

$$N = \mathcal{L}\sigma \tag{1.52}$$

where $\mathcal{L}$ is called *luminosity* and represents the density of protons at the interaction point in a given time interval. This instantaneous luminosity is defined by:

$$\mathcal{L} = \nu k \frac{N_1 N_2}{\pi \sigma^2} \tag{1.53}$$

with ν the frequency of crossing, $N_{1,2}$ the number of protons per bunch, k a factor of beam occupancy level and σ the estimated root mean squared of the bunch distribution in the transverse plane. As the LHC is running the luminosity sums up so that we speak in terms of *integrated luminosity* to refer to the total amount of data accumulated at a given moment. The SI units of luminosity and cross sections are respectively $m^{-2}s^{-1}$ and m^2. In particle physics however we use much smaller units: 1 barn = $10^{-28}m^2$, but even in these units cross sections are often expressed in pb or fb.

The choice of using protons as colliding particles is related to the desire of having high luminosity. Tevatron used $p\bar{p}$ collisions because at ~ 2 TeV the production is dominated by quark antiquarks interactions, while at the LHC at 13 TeV this is no longer the case as gg interactions become dominant, as we saw in Fig. 1.5.

The cross section of a process with two hadrons as initial state, each having a momentum P_i, is given by:

$$\sigma(P_1, P_2) = \sum_{a,b} \int_0^1 \int_0^1 \hat{\sigma_{a,b}}(p_1, p_2, \frac{Q^2}{\mu_F^2}) f_a(x_1, \mu_F^2) f_b(x_2, \mu_F^2) dx_1 dx_2 \tag{1.54}$$

where the sum goes over all the possible partons (g, u, d, s, c, b and their antiparticles), $x_{1,2}$ are the fraction of the momentum carried by the partons ($p_i = x_i P_i$), $\hat{\sigma}$ corresponds to the partonic cross section, Q^2 is the typical scale of the process (usually close the the masses involved), μ_F is called factorisation scale and the f_i are the parton density functions (PDF) shown in Fig. 1.4.

The factorisation scale is an arbitrary parameter defining the separation between the hard and soft perturbative regimes at NLO and highers orders. Soft parton emissions from the initial states lead to logarithmic divergencies that can then be reabsorbed into the PDF if μ_F is close to the scale of the hard scattering. This means we can then focus on the interesting part of the process, the partons interaction, without having to

bother with how these partons were obtained. This idea of process factorisation will be further explored in Sec. 1.3.1.

Another important scale in any process is the *renormalisation scale* μ_R which corresponds to the energy scale at which coupling constants are evaluated. In QED for example, vacuum polarisation effects screen the bare electron charge. There is an infinite number of "screening" diagrams. Summing them all up, we obtain at large energy Q^2:

$$\alpha(Q^2) = \alpha_0 \left[1 + \frac{\alpha_0}{3\pi} \log \frac{Q^2}{M^2} + \left(\frac{\alpha_0}{3\pi} \log \frac{Q^2}{M^2} \right)^2 + ... \right] = \frac{\alpha_0}{1 - \frac{\alpha_0}{3\pi} \log \frac{Q^2}{M^2}} \quad (1.55)$$

where M is a cut-off on the loop momentum to prevent infinite contribution. This dependence on the cut-off can be eliminated by introducing the renormalisation scale μ_R:

$$\alpha(Q^2) = \frac{\alpha(\mu_R^2)}{1 - \frac{\alpha(\mu_R^2)}{3\pi} \log \frac{Q^2}{\mu_R^2}} \quad (1.56)$$

In QCD a similar mechanism occurs except that, contrary to photons, gluons self-interact. There are then additional vacuum polarisation diagrams with gluon loops which "anti-screen" the colour charge. The corresponding evolution equation is given by:

$$\alpha_s(Q^2) = \frac{\alpha_s(\mu_R^2)}{1 - b_0 \alpha_s(\mu_R^2) \log \frac{Q^2}{\mu_R^2}} \quad ; \quad b_0 = -\frac{n_f}{6\pi} + \frac{33}{12\pi} \quad (1.57)$$

where n_f corresponds to the number of quarks with $m_q < Q$. The Dyson expansion can then be expressed as: $R = \sum_n c_n \alpha_s^n$ which, after renormalisation, becomes $R(\log(Q^2/\mu_R^2), \alpha_s(\mu_R^2))$ and satisfies the renormalisation group equation (RGE):

$$\frac{dR}{d \log \mu_R^2} = \left(\frac{\partial}{\partial \log \mu_R^2} + \frac{\partial \alpha_s}{\partial \log \mu_R^2} \frac{\partial}{\partial \alpha_s} \right) R = 0 \quad (1.58)$$

It follows that $R(\log(Q^2/\mu_R^2), \alpha_s(\mu_R^2)) = R(1, \alpha_s(Q^2))$, meaning that it is completely determined by the running of α_s which is described by the β-function at one loop:

$$\beta(\alpha_s) \equiv \frac{\partial \alpha_s}{\partial \log \mu_R^2} = -b_0 \alpha_s^2 \quad (1.59)$$

CMS and ATLAS detectors

Most of the particles of interest are experimentally detectable only through their decay products: leptons, jets (quarks,gluons), photons, neutrinos (via missing energy). The

two general purpose detectors were thus optimized to detect them and measure their properties in order to discover new heavy particles.

Quarks and gluons, due to hadronization, are never observed directly, but form jets instead. A big issue comes from the residual partons coming from the protons that don't interact during the collision. These partons create forward jets which can have a very large total momentum even if their transverse momentum is small. The jets need then to be removed from the analysis by imposing cuts as the are not likely to originate from the hard process of interest. Electrons and muons on the other hand lead to cleaner signature because they can be directly observed through their electromagnetic interaction. A good detector needs to track the particles, stop them in calorimeter to measure their energy, have a high magnetic field to measure their transverse momentum and distinguish positively and negatively charged particles and finally have some techniques to identify separated jets in order to infer the presence of quarks/gluons.

Visual representations of the CMS and ATLAS are displayed in Fig. 1.8. A complete description can be found in [21, 22] while here we only summarize the main points. The central feature of the CMS is a superconducting solenoid of 6m internal diameter, providing a magnetic field of 3.8 T. Within the solenoid volume are located in concentric layers a silicon pixel and strip tracker, a lead tungstate crystal electromagnetic calorimeter (ECAL), and a brass and scintillator hadron calorimeter (HCAL), each composed of one barrel and two endcap sections. The apparatus is completed by ionisation muon chambers which surround the solenoid and are embedded in the steel flux-return yoke. Three technologies are used for these chambers: drift tubes, cathode strip chambers, and resistive plate chambers. The ATLAS detector also consists of inner tracking devices (silicon pixel detector, silicon microstrip tracker and transition radiation tracker) surrounded by a superconducting solenoid providing 2T magnetic fields, a liquid argon ECAl, a steel scintillator-like HCAL and muon spectrometer.

Constraints on the Higgs boson

As we saw the Higgs mass was not predicted by the SM, it is a function of the μ^2, λ parameters. Only experiments could help us to get its value. In Fig. 1.9 we show ATLAS and CMS combined results for the Higgs mass in the two main channels we already discussed. The resulting Higgs mass are taken from [23] for CMS, [24] for ATLAS and [25] for the combined measurement:

$$m_H = \begin{cases} 125.03^{+0.26}_{-0.27} \text{ (stat.)}^{+0.13}_{-0.15} \text{ (syst.) GeV} & \text{CMS} \\ 125.36 \pm 0.37 \text{ (stat.)} \pm 0.18 \text{ (syst.) GeV} & \text{ATLAS} \\ 125.09 \pm 0.21 \text{ (stat.)} \pm 0.11 \text{ (syst.) GeV} & \text{combined} \end{cases} \quad (1.60)$$
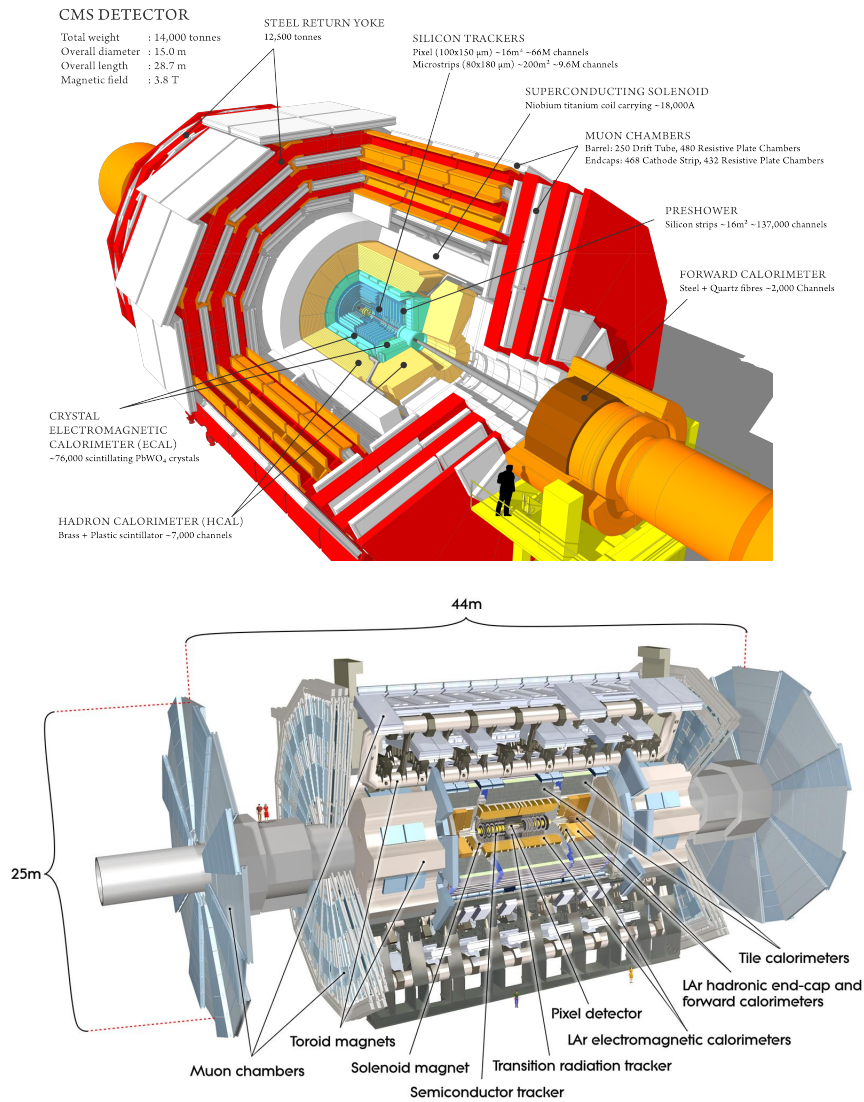
Figure 1.8: CMS and ATLAS detectors

In order to check if the observed scalar boson is well the Higgs boson predicted by the BEH mechanism it's of vital importance to measure precisely its couplings to fermions and gauge bosons. This is done in the so called κ framework which presents ratios over the SM couplings. The precision achieved by the two experimental collaborations has become higher over the years. Two years ago, CMS and ATLAS collaboration
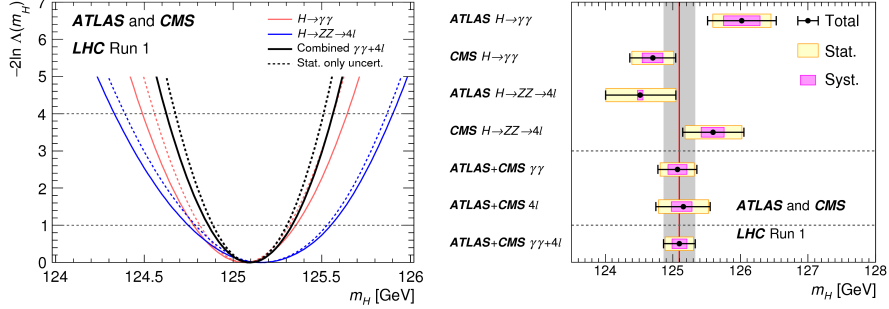
Figure 1.9: Left: Log-likelihood ratio as a function of the Higgs boson mass m_H for the ATLAS and CMS combination of the $H \to \gamma\gamma$ (red), $H \to ZZ \to 4l$ (blue), and combined (black) channels. The dashed curves show the results accounting for statistical uncertainties only, with all nuisance parameters associated with systematic uncertainties fixed to their best-fit values. The 1 and 2 standard deviation limits are indicated by the intersections of the horizontal lines at 1 and 4, respectively, with the log-likelihood scan curves. Right: Summary of Higgs boson mass measurements from the individual analyses of ATLAS and CMS from the combined Higgs boson mass measured from each experiment and from the combined analysis. The systematic (narrower, magenta-shaded bands), statistical (wider, yellow-shaded bands), and total (black error bars) uncertainties are indicated. The (red) vertical line and corresponding (gray) shaded column indicate the central value and the total uncertainty of the combined measurement, respectively.

released their combined measurements of the Higgs boson production and decay rates and their constraints on its coupling using data at $\sqrt{s} = 7$ and 8 TeV [1]. We will now review a few of these results.

The global signal strength is the most precisely measured Higgs boson coupling-related observable. However, since it combines all production and decay measurements by assuming that all their ratios are the same in the SM, it is very model-dependent. A less model-dependent approach consists in relaxing these assumptions separately for production cross sections and decay branching ratios. The five main production rates are shown in Fig. 1.10 as well as the five main decay rates.

We can see that both CMS and ATLAS agree within 1σ for all processes. All combined results are very close to the SM predictions except in the $t\bar{t}H$ mode where there is a small tension (excess of $\simeq 2.3\sigma$). The conclusions hold also for the decay channels where all combined measurements are in agreement within 1σ with the SM expectations. SM is thus incredibly well established.
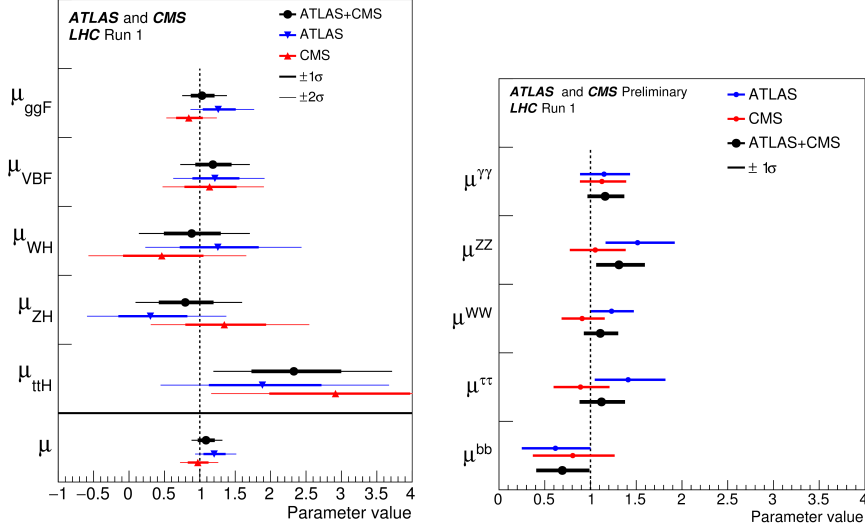
Figure 1.10: Left: Best-fit results for the production signal strengths for the combination of ATLAS and CMS. For completeness results for each experiment separately are also shown. The error bars indicate the 1σ (thick lines) and 2σ (thin lines) intervals. The measurements of the global signal strength μ are also shown. Right: Best-fit results for the decay signal strengths for the combination of ATLAS and CMS. For completeness results for each experiment separately are also shown. The error bars indicate the 1σ intervals.

To directly measure the individual coupling modifiers, an assumption about the Higgs boson is necessary. Two scenarios were considered in [1]: the first one leaves $BR_{BSM} \geq 0$ free and assumes $|\kappa_V| \leq 1$ while the second assumes $BR_{BSM} = 0$. The constraints assumed in the first scenario are compatible with a wide range of BSM physics, which may occur in the loop contributions from new particles or shifted couplings. This is probed at the LHC via the effective coupling modifiers to gluons and photons κ_g, κ_γ which are a very convenient way to express Higgs production via gluon fusion and decay into two photons, for example:

$$\frac{\sigma(gg \to H)Br(H \to \gamma\gamma)}{\sigma_{SM}(gg \to H)Br_{SM}(H \to \gamma\gamma)} = \kappa_g^2 \cdot \frac{\kappa_\gamma^2}{0,75\kappa_g^2 + 0,25\kappa_\gamma^2} \tag{1.61}$$

where the factors 0.75 and 0.25 come from branching ratios (which in turn is due to color charge).
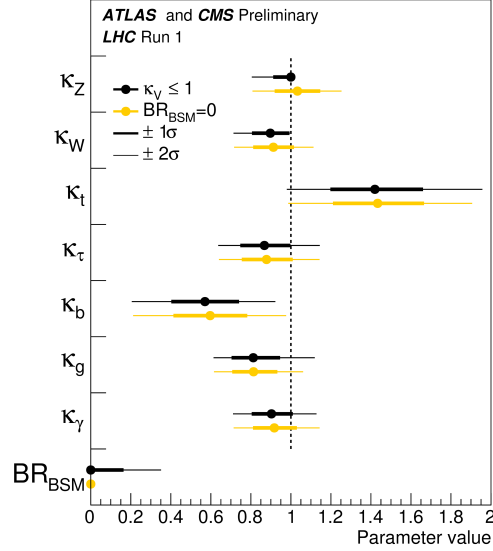
Figure 1.11: Fit results for the two parameterisations allowing BSM loop couplings, with $\kappa_V \leq 1$, where κ_V stands for κ_Z or κ_W, or without additional BSM contributions to the Higgs boson width, i.e. $BR_{BSM} = 0$. The measured results for the combination of ATLAS and CMS are reported together with their uncertainties. The error bars indicate the 1σ (thick lines) and 2σ (thin lines) intervals. The uncertainties are not indicated when the parameters are constrained and hit a boundary, namely $\kappa_V = 1$ or $BR_{BSM} = 0$.

Furthermore, potential deviations of the tree-level couplings to SM particles are also parametrized with their respecting coupling modifiers. There are then seven independent coupling modifiers which are show in Fig. 1.11.

We can see that some of the kappa's are 2σ away from the SM expectation. This is the case for the top and bottom quark couplings which also have the biggest uncertainties. Since in the rest of this thesis we will mainly work with gluon fusion the κ_g quantity is also important. The current limits in the first scenario are shown in Eq. 1.62, along with those on κ_γ.

$$
\begin{aligned}
\frac{\kappa_g^{obs}}{\kappa_g^{SM}} &= 0.69^{+0.21}_{-0.13} \quad \text{(CMS)} \quad ; \quad 0.94^{+0,23}_{-0,16} \quad \text{(ATLAS)} \\
\frac{\kappa_\gamma^{obs}}{\kappa_\gamma^{SM}} &= 0.89^{+0.17}_{-0.13} \quad \text{(CMS)} \quad ; \quad 0.87^{+0.15}_{-0.14} \quad \text{(ATLAS)}
\end{aligned}
\tag{1.62}
$$
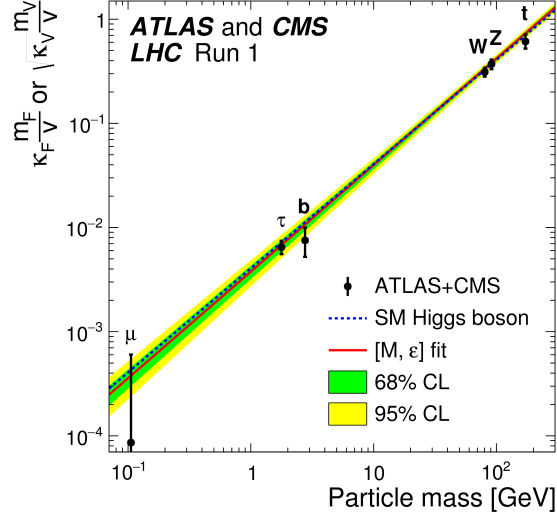
Figure 1.12: Best fit values as a function of particle mass for the combination of AT-LAS and CMS data in the case of the parameterisation described in the text, with parameters defined as $\kappa_f m_f / v$ for the fermions, and as $\sqrt{\kappa_V} m_V / v$ for the weak vector bosons. The dashed (blue) line indicates the predicted dependence on the particle mass in the case of the SM Higgs boson. The solid (red) line indicates the best fit result with the corresponding 68% and 95% CL bands.

One final interesting feature is shown in Fig. 1.12 where we see that all measured Higgs couplings are indeed compatible with equation 1.49.

1.1.5   SM limitations

Hierarchy problem

Even though the SM is currently an exceptionally accurate theory both in the electroweak and QCD sectors, there are a few theoretical problems. As we saw in the BEH mechanism, both weak gauge bosons masses and fermions masses originate from the Higgs boson. No theoretical argument can however explain the apparent mass hiereachy between the fermion generations:

$$m_e \ll m_\mu \ll m_\tau \quad ; \quad m_u \ll m_c \ll m_t \quad ; \quad m_d \ll m_s \ll m_b \qquad (1.63)$$

nor the large mass splitting within the third generation: $m_\tau \simeq m_b \ll m_t$. In the SM the only natural mass scale appears to be the one given by the top quark, as

it is the only SM particle with a Yukawa coupling of order 1 ($y_t = \frac{m_t\sqrt{2}}{v} \simeq 1$).
In that sense, the other particle masses seem 'unnatural'. This is what is called the
naturalness problem. We would have expected that all fermion masses would have
been proportional in the same way to the VEV of the Higgs fields. So despite the
elegance of the BEH mechanism and the discovery of the Higgs boson, the origin of
masses and mixings remains unexplained.

The Higgs mass m_H^2 corresponds by definition to the pole of the free propagator of the
H boson in momentum space: $\frac{i}{k^2-m_H^2}$. Since it is not protected by any symmetry, m_H^2
receives quadratically divergent corrections at the quantum level from highers orders
in the perturbative expansion of the Higgs two-point function. The mass corrections
at the one-loop level include three main contributions: top quark, Higgs boson and
electroweak gauge bosons. If we adopt the cut-off regularization scheme and evaluate
the corrections at large momentum, in the unitary gauge, we have:

$$\delta m_H^2 = m_H^2 - m_H^{(0)} = \frac{3}{8\pi^2 v^2}(4m_t^2 - m_H^2 - 2m_W^2 - 4m_Z^2)\Lambda^2 + \mathcal{O}(\ln(\Lambda^2)) \quad (1.64)$$

where Λ is the cut-off scale. It's important to notice that the largest contribution comes
from the top quark. Radiative corrections for the Higgs mass are then much larger, by
many orders of magnitude, than its final mass itself. In order to add up to 125 GeV,
fine-tuning is required i.e. to let the bare Higgs mass perfectly balance the radiative
corrections. This problem is called the *hierarchy problem* and is one motivation of
many theorists to introduce new scenarios beyond the SM.

All this is in fact linked to the huge gap between the weak scale ($\simeq 10^2$ GeV) and the
Planck scale ($\simeq 10^{19}$ GeV) where we expect quantum effects of gravity to become
strong. Even if this is not a problem of the SM in itself it suggests that there is room
for new physics in these seventeen orders of magnitude. These new particles could
then contribute to the mass of the Higgs boson.

On the other hand this argument can be turned around to predict the scale Λ at which
new physics should appear to cancel the unwanted divergencies in the radiative cor-
rections to the Higgs mass. A common feature to the numerous proposals that have
been made is to associate the radiative m_H stability to new symmetries. Supersym-
metry for example relates bosons and fermions, so that every SM field have a new
super-partner whose spin differs by a half-integer, but share the same mass and qua-
tum numbers. These new particles also bring new corrections to the Higgs mass, and
solve the instability due to the fact that all fermionic particles enters with a negative
sign in Eq. 1.64 while all bosonic super-partners come with a positive sign, leading to
an exact cancellation and vice-versa. The remaining terms in Eq. 1.64 diverge at most
logarithmically, solving the quadratic divergence.

Apart from SUSY a lot of other models try to solve this problem by adding extra fermion generations, new gauge bosons or new scalar particles. In this thesis we will focus on an extended scalar sector as described by the 2HDM.

1.2 The Two-Higgs-Doublet-Model

1.2.1 Motivation

The 2HDM [2] extends the minimal scalar sector of the SM by introducing a second $SU(2)_L$ doublet Φ_2 with weak hypercharge $Y = +1$.

$$
\phi_1 = \left(\begin{array}{c} \phi_1^+ \\ \phi_1^0 \end{array} \right) \quad , \quad \phi_2 = \left(\begin{array}{c} \phi_2^+ \\ \phi_2^0 \end{array} \right) \tag{1.65}
$$

This gives rise to an enlarged particle content with five physical Higgs bosons, *i.e.* in the case of CP conservation, a light CP-even one, h^0, a heavier CP-even one, H^0, a CP-odd one, A^0, and two charged Higgs bosons $H^\pm$.

The 2HDM provides a simple UV–complete perturbative extension of the SM, which can be viewed as the low–energy Higgs sector of more fundamental theories such as the MSSM [26, 27], GUTs [28, 29], composite Higgs models [30, 31], and little Higgs models [32, 33].

A popular motivation for the 2HDM is supersymmetry. In supersymmetric theories the scalars belong to chiral multiplets and their complex conjugates belong to multiplets of the opposite chirality. Since multiplets of different chiralities cannot couple together in the lagrangian, a single Higgs doublet is unable to give mass simultaneously to the charge +2/3 and charge -1/3 quarks. Besides, since scalars are in chiral multiplets together with chiral spin 1/2 fields, the cancellation of anomalies also requires an additional doublet to be added. This is called the Minimal Supersymmetric Standard Model (MSSM).

Aside from its very rich and distinctive phenomenology, the 2HDM also sets the ground for novel approaches to diverse unsettled conundrums, from e.g. the origin of neutrino masses [34] to Naturalness [35], Electroweak Baryogenesis [36, 37] and Dark Matter [38, 39]. In summary the 2HDM should be seen as a tool, not as a final answer in itself.

1.2.2   Higgs potential

This new theoretical framework is described by modifying the Higgs lagrangian of the SM in this way:

$$\mathcal{L}_\phi = \sum_{i=1}^{2} (D_\mu \phi_i)^\dagger (D^\mu \phi_i) - V(\phi_1, \phi_2) \tag{1.66}$$

Expanding the covariant derivatives as seen before gives interaction with the SM gauge bosons. The most generic form of the 2HDM potential reads:

$$
\begin{aligned}
V(\phi_1, \phi_2) &= m_{11}^2 \phi_1^\dagger \phi_1 + m_{22}^2 \phi_2^\dagger \phi_2 - \left(m_{12}^2 \phi_1^\dagger \phi_2 + h.c. \right) \\
&+ \frac{1}{2}\lambda_1 \left(\phi_1^\dagger \phi_1 \right)^2 + \frac{1}{2}\lambda_2 \left(\phi_2^\dagger \phi_2 \right)^2 + \lambda_3 \left(\phi_1^\dagger \phi_1 \right) \left(\phi_2^\dagger \phi_2 \right) \\
&+ \lambda_4 \left(\phi_1^\dagger \phi_2 \right) \left(\phi_2^\dagger \phi_1 \right) + \left[\frac{1}{2}\lambda_5 \left(\phi_1^\dagger \phi_2 \right)^2 \right. \\
&+ \left. \lambda_6 \left(\phi_1^\dagger \phi_1 \right) \left(\phi_1^\dagger \phi_2 \right) + \lambda_7 \left(\phi_2^\dagger \phi_2 \right) \left(\phi_1^\dagger \phi_2 \right) + h.c. \right]
\end{aligned} \tag{1.67}
$$

There are fourteen independent free parameters: m_{11}^2, m_{22}^2 and $\lambda_{1,2,3,4}$ are real while m_{12}^2 and $\lambda_{5,6,7}$ are complex. However most phenomenological studies of 2HDM make several simplifying assumptions. For example in this thesis we will impose CP conservation; this leads to $\lambda_6 = \lambda_7 = 0$ while λ_5 and m_{12}^2 become real, and allows to distinguish between scalars and pseudoscalars. Assuming natural flavor conservation [40], the absence of tree–level FCNC interactions is protected by a global, flavor–blind, Z_2 discrete symmetry $\phi_i \rightarrow (-1)^i \phi_i$. The latter is approximate up to the soft–breaking mass term $\mathcal{L}_{\text{soft}} \supset m_{12}^2\, \phi_1^\dagger\, \phi_2 + h.c.$ Note that we keep the m_{12}^2 term as it gives more room to accomodate large enhancements in the trilinear couplings and yet comply with vacuum stability and unitarity constraints. It's also a matter of generality: there is no need to enforce a symmetry, if nothing tells that it should be fulfilled. Finally it's the minimal way to accomodate larger mass spectrum which would otherwise be much more constrained.

After electroweak symmetry breaking, the neutral components of the Higgs doublets acquire real VEVs, $\phi_i^0 = v_i/\sqrt{2}$. The eight independent parameters in the lagrangian basis are then:

$$m_{11}^2, m_{22}^2, m_{12}^2, \lambda_1, \lambda_2, \lambda_3, \lambda_4, \lambda_5 \tag{1.68}$$

Three out of the eight remaining degrees of freedom are reabsorbed to give mass to the $W^\pm$ and Z gauge bosons in a similar way to the BEH mechanism, the other five lead to the five physical spin-0 Higgs fields.

Requiring $v^2 \equiv v_1^2 + v_2^2 = G_F^{-1}/\sqrt{2}$ so that the 2HDM Higgs mechanism does implement the EWSB of the SM, removes one parameter. The ratio of the two VEV's is then given as $\tan\beta \equiv v_2/v_1$. Overall, we are left with seven parameters which form the physical basis:

$$\tan\beta \, , \sin(\beta - \alpha) \, , m_{h^0} \, , m_{H^0} \, , m_{A^0} \, , m_{H^\pm} \, , m_{12}^2. \tag{1.69}$$

The convention $0 \le \beta - \alpha < \pi$ (with $0 < \beta < \pi/2$) guarantees that the Higgs couplings to the weak gauge bosons have the same sign in the 2HDM and in the SM. This criterion fixes the possible sign ambiguities in the generic parametrization of the model [41].

The mass of the new heavy bosons are expressed as:

$$
\begin{aligned}
m_{H^\pm}^2 &= \frac{m_{12}^2}{\cos\beta\sin\beta} - (\lambda_4 + \lambda_5)\frac{v^2}{2} \\
m_A^2 &= \frac{m_{12}^2}{\cos\beta\sin\beta} - \lambda_5\frac{v^2}{2} = m_{H^\pm}^2 + (\lambda_4 - \lambda_5)\frac{v^2}{2} \\
m_H^2 &= \frac{m_{12}^2}{\cos\beta\sin\beta}
\end{aligned}
\tag{1.70}
$$

To avoid large deviations on the ρ parameter defined by:

$$\rho = \frac{m_W^2}{m_Z^2 \cos^2\theta_W} \tag{1.71}$$

custodial symmetry is imposed and leads to two cases [42, 43]: usual or inverted hierarchy (also called *twisted 2HDM*)

- $\lambda_4 = \lambda_5 \implies m_{H^\pm} = m_A$; $m_{12}^2 = (m_A^2 + \lambda_5 v^2)\cos\beta\sin\beta$

- $\lambda_4 = -\lambda_5 \implies m_{H^\pm} = m_H$; $m_{12}^2 = m_H^2 \cos\beta\sin\beta$

Custodial symmetry leads thus to a degeneracy in mass between the charged Higgs and either the scalar H^0 or the pseudoscalar A^0 and the soft breaking mass m_{12} is linked to the mass of one of these new particles. Note that in the MSSM no custodial symmetry is imposed but it arises from further constraints (decoupling of the $H^0, A^0, H^\pm$) and leads to the only possible relation $m_{H^\pm}^2 = m_A^2 + m_W^2$; $m_{12}^2 = m_A^2 \cos\beta\sin\beta$ with $\lambda_4 = -g^2/2, \lambda_5 = 0$.

The angle β corresponds to the rotation angle which diagonalizes the mass-squared matrices of the charged scalars and of the pseudoscalar. A mixing angle α is also introduced to diagonalize the $\mathcal{CP}$–even squared mass matrix.

$$
\begin{aligned}
h^0 &= H_1 \sin\alpha - H_2 \cos\alpha \\
H^0 &= -H_1 \cos\alpha - H_2 \sin\alpha
\end{aligned}
\tag{1.72}
$$
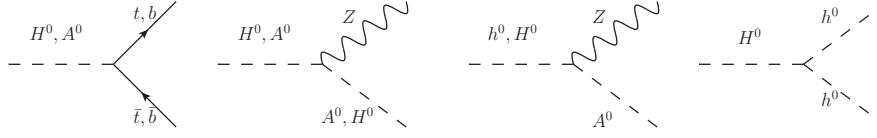
Figure 1.13: New feynman rules of interest for the process studied in this thesis.

Recalling from the definition of $\tan\beta$ we can write $v_1 = v\cos\beta, v_2 = v\sin\beta$ so that the SM Higgs boson can be written as

$$H^{SM} = H_1 \cos\beta + H_2 \sin\beta \tag{1.73}$$

Using Eq. 1.72, we end up with Eq. 1.74 which encourages us to identify the light state h^0 with the Higgs particle observed at the LHC, given that $\sin(\beta - \alpha) \simeq 1$ as will be discussed in Sec. 1.3.4, and to fix its mass to $m_{h^0} = 125$ GeV.

$$H^{SM} = h^0 \sin(\beta - \alpha) - H^0 \cos(\beta - \alpha) \tag{1.74}$$

The different possible choices of fermion field transformations under Z_2 lead to different Yukawa coupling patterns. We will hereafter focus on two canonical setups: i) *type–I*, in which all fermions couple to only one Higgs doublets (ϕ_2); and ii) *type–II*, where up–type (down–type) fermions couple exclusively to ϕ_2 (ϕ_1).

1.2.3   2HDM couplings

The existence of new particles with respect to the SM leads to new possible diagrams and Feynman rules. A condensed set of Feynman diagrams that will be studied in more detail in this thesis are shown on Fig. 1.13. In this section we will study separately the couplings to fermions and gauge bosons.

Yukawa couplings

The dependance of the relevant Yukawa couplings on the 2HDM parameters is shown in Tab. 1.2, for type-I and type-II setups, as rescalings of their SM counterparts.

Yukawa couplings appear in nearly all Higgs production processes. Studying these couplings experimentally is more efficient in processes where only Yukawa couplings appears. This is for example the case in $gg \to \phi \to t\bar{t}$ production (see Chap. 4 for

Coupling	Type-I	Type-II
$\hat{g}_{h^0 t\bar{t}}$	$\cos\alpha/\sin\beta$	$\cos\alpha/\sin\beta$
$\hat{g}_{h^0 b\bar{b}}$	$\cos\alpha/\sin\beta$	$-\sin\alpha/\cos\beta$
$\hat{g}_{H^0 t\bar{t}}$	$\sin\alpha/\sin\beta$	$\sin\alpha/\sin\beta$
$\hat{g}_{H^0 b\bar{b}}$	$\sin\alpha/\sin\beta$	$\cos\alpha/\cos\beta$
$\hat{g}_{A^0 t\bar{t}}$	$\cot\beta$	$\cot\beta$
$\hat{g}_{A^0 b\bar{b}}$	$-\cot\beta$	$\tan\beta$

Table 1.2: Dependence of the Yukawa couplings for up and down-type quarks on the 2HDM parameters for type-I and type-II setups. All couplings are normalized to their SM counterpart, as denoted by $\hat{g}_{hq\bar{q}} \equiv g^{\text{2HDM}}_{hq\bar{q}}/g^{\text{SM}}_{Hq\bar{q}}$.
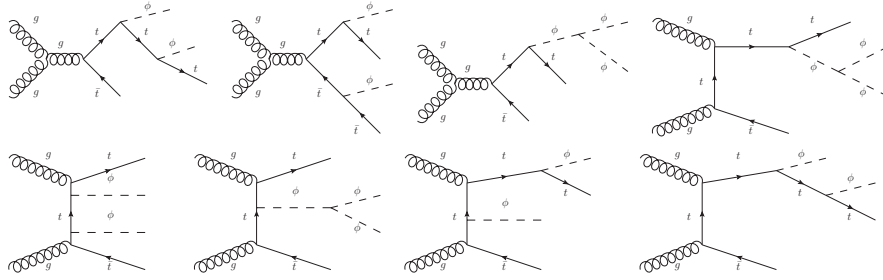
Figure 1.14: $t\bar{t}\phi\phi$ associated production diagrams with $\phi = h^0, H^0, A^0$.

more details). Another example is $gg \to t\bar{t}\phi\phi$ whose diagrams are shown in Fig. 1.14 and which has been studied in [44]. However this process also features diagram with Higgs self interactions. This diagram will be much suppressed though and won't contribute a lot to total rates except in case of a resonance decaying to two light Higgs bosons.

In order to have a better idea of the possible values of the bottom and top Yukawa couplings to the 2HDM Higgs bosons we draw scatter plots in Fig. 1.15 by varying the two angles randomly and independently in the range $0 < \tan\beta < 10$ and $|\sin(\beta - \alpha)| \le 1$ for a type-II 2HDM.

As a general feature, Yukawa couplings to h^0 and H^0 vary in the opposite direction as can be inferred from the formulae. When $\tan\beta > 1$ bottom Yukawas can have a wide variety of values as they are proportional to $1/\cos\beta$ which increases when $\tan\beta$ increases. Top Yukawa values on the other hand tends to stay relatively small because
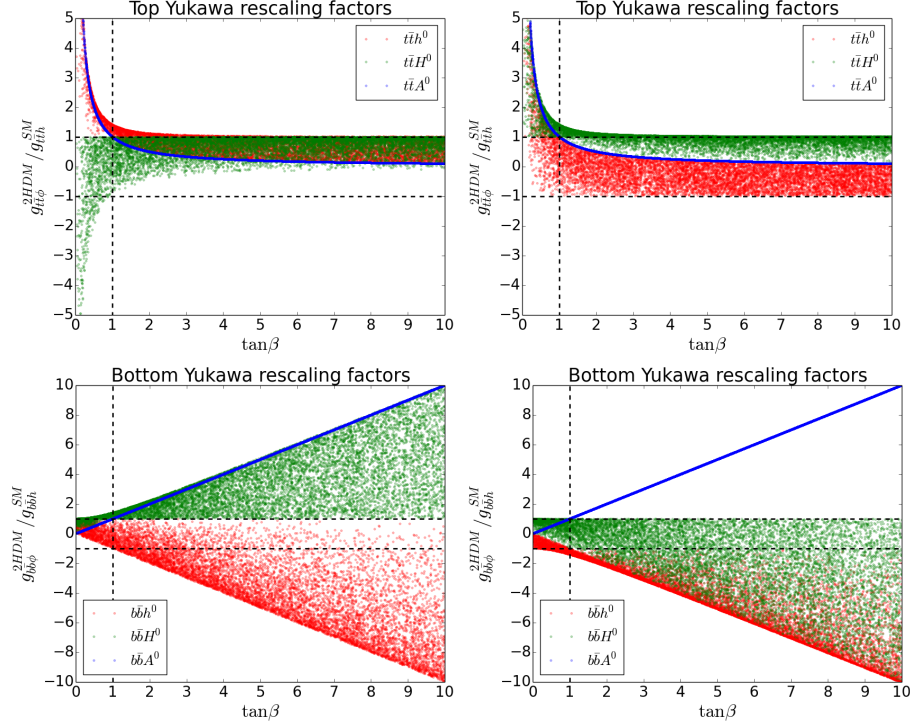
Figure 1.15: Yukawa values normalized to their SM value as a function of $\tan\beta$ and $\sin(\beta - \alpha)$. Left plots are for $0 < \sin(\beta - \alpha) < 1$ while the right plots correspond to $-1 < \sin(\beta - \alpha) < 0$. Dashed lines define region where Yukawa couplings are smaller than the SM value.

they vary as $1/\sin\beta$. Note also that $\hat{g}_{h^0 q\bar{q}}$ and $\hat{g}_{H^0 q\bar{q}}$ can have a wide range of values because they depend on both angles while $\hat{g}_{A^0 q\bar{q}}$ only depends on the β angle.

An important point to make here is that $|\hat{g}_{\phi t\bar{t}}|$ is maximum when $\tan\beta$ is small ($\tan\beta < 1$) leading to enhanced top Yukawa couplings compared to their SM values. This range is interesting in order to show deviations from the SM predictions in a wide variety of processes where the top couples to the Higgs boson (ZH, HH, $t\bar{t}$, thj, etc.). However such a region is mostly inaccessible as it is already excluded by theoretical and experimental constraints as will be discussed in Sec. 1.3.4

	h^0	H^0	A^0
$h^0 Z$	0	0	$\cos(\beta - \alpha)$
$H^0 Z$	0	0	$-\sin(\beta - \alpha)$
$A^0 Z$	$\cos(\beta - \alpha)$	$-\sin(\beta - \alpha)$	0
VV	$\sin(\beta - \alpha)$	$\cos(\beta - \alpha)$	0
$H^\pm W^\mp$	$\cos(\beta - \alpha)$	$\sin(\beta - \alpha)$	1

Table 1.3: Higgs coulings to the SM gauge bosons ($V = Z, W^\pm$) as rescaling of the SM value. These couplings are identical for type-I and type-II 2HDM.
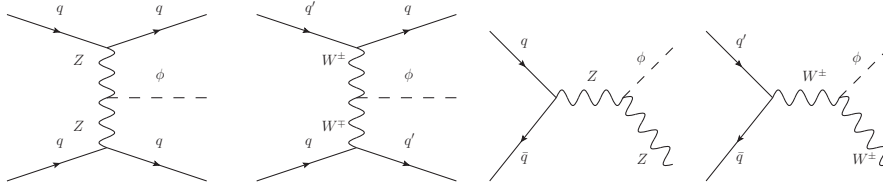
Figure 1.16: Vector boson fusion and Drell-Yan $V\phi$ production diagrams with $\phi = h^0, H^0$.

Gauge boson couplings

While it was not straightforward to see the effect of mixing angles on Yukawa couplings, the Higgs gauge bosons couplings are much simpler to visualize. This time all couplings only depend on the difference between the two angles α and β. They are summarized in Tab. 1.3.

Such couplings arise in vector boson fusion Higgs production mode (see diagrams in Fig. 1.16) where their values can be directly derived from the total rate as only this new coupling appears in the diagrams. Another important channel for studying the ϕVV couplings is the associated production of a Higgs with a Z or $W^\pm$ boson: $q\bar{q} \to V\phi$. This Drell-Yan process is well known up to NLO. However at NNLO a new contribution comes from $gg \to Z\phi$ (loop-induced diagram) which will be studied in Chap. 2 in detail.

Note that up to now we were able to isolate each coupling independently by looking at particular production modes. However if one is interested in the relative sign (phase) between the Yukawa couplings and gauge boson couplings for example this is not possible. To do so we need a production process involving all these couplings at the

Figure 1.17: Generic Feynman diagrams describing $pp \rightarrow th^0/H^0 j$ production in the 2HDM at leading order.

same time. This is the case for example in the $H \rightarrow \gamma\gamma$ decay mode due to the negative interference at LO between the W boson loop and the heavy quark loop [45, 46].

Another very interesting process for studying this relative phase is single top + Higgs + jets production process $pp \rightarrow t\phi j$. For the sake of brevity in this thesis we only mention qualitative results, while partial quantitative results were obtained at NLO. For a detailed analysis in the SM, see [47].

The diagrams of interest are shown in Fig. 1.17. When working in the 5-flavour scheme, bottom quarks are considered massless and are thus incorporated in the PDF. The special feature of this process is that it involves $\phi b\bar{b}, \phi t\bar{t}, \phi W^+W^-$ and $H^\pm bt$ couplings. Moreover, each coupling appears at most once in each diagram, which allows us to access the relative phase between these couplings. Note that since we are interested in Higgs phenomenology, we discarded diagrams with an s-channel W boson. It's important to keep in mind that diagram 1 and 4 (involving Yukawa couplings) will interfer destructively with diagram 3 (involving coupling to gauge bosons).

In general third and fourth diagrams will dominate while the first diagram will be quite small and the second one will be very suppressed by the Wh^0H^- coupling which is proportional to $\cos(\beta - \alpha)$. That's why we don't expect much deviation from the SM in this channel.

Diagrams for $tH^0 j$ production are the same as in Fig. 1.17. In this case however couplings are very different. First diagram is now enhanced with respect to the fourth diagram while the third diagram nearly vanishes because of the $\cos(\beta - \alpha)$ factor. The diagram involving the charged Higgs will also be small.

We conclude this discussion with the last possible process where the top quark is produced along with a pseudoscalar particle. Because A^0 cannot couple to the gauge bosons, there is one diagram missing with respect to the other processes (Fig. 1.18).
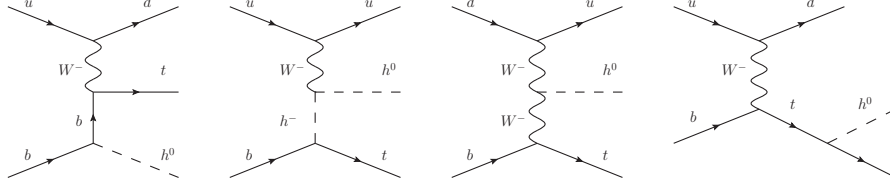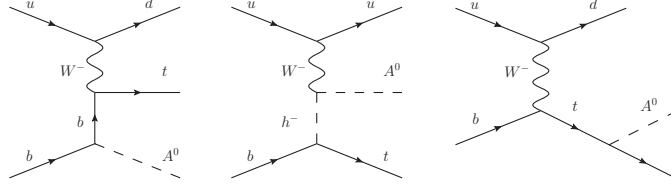
Figure 1.18: Generic Feynman diagrams describing $pp \rightarrow tA^0j$ production in the 2HDM at leading order.

Here again we expect the first diagram to be enhanced by the Yukawa coupling while the last one will be suppressed. The second diagram on the other hand will this time be enhanced as the WA^0H^- couplings is independent of the mixing angles and tbH^- varies as $\cot\beta$.

When computing these diagrams for several benchmarks we found that th^0j gives rates similar to the SM expectation, small enhancements being due to soft Yukawa shifts. tH^0j however has smaller rates because the H^0WW couplings is much suppressed and top Yukawas are reduced. Finally tA^0j is also very small. Given the existing constraints on the 2HDM model (both from theory and experiments) it seems that single top production in association with a Higgs and one jet is for now out of reach at the LHC given the very small rates.

1.2.4 Gluon fusion production and decay rates

Now that we reviewed all the couplings between all the particles in the 2HDM let's compute the total rates for Higgs production via gluon fusion both for a scalar Higgs or a pseudoscalar hypothetical particle:

$$
\begin{aligned}
\sigma_{gg \rightarrow H^0} &= \frac{\alpha_s^2 G_F}{128\sqrt{2}\pi} M_H^2 |\sum_q \hat{g}_{H^0 q\bar{q}} F_S(\tau_q)|^2 \delta(\hat{s} - M_H^2) \\
\sigma_{gg \rightarrow A^0} &= \frac{\alpha_s^2 G_F}{128\sqrt{2}\pi} M_A^2 |\sum_q \hat{g}_{A^0 q\bar{q}} F_P(\tau_q)|^2 \delta(\hat{s} - M_A^2)
\end{aligned}
\tag{1.75}
$$

where $\tau_q = \dfrac{4m_q^2}{M_H^2}$. The $F(\tau_q) = F_\triangle(\tau_q)$ functions are called form factors (FF). They encode the information of the triangle loop and are given for a scalar (F_S) and

	Mass	$|F_S|$	$|F_P|$
Bottom	4.5 GeV	0.066	0.070
Top	173 GeV	0.688	1.046

Table 1.4: Values of the Higgs FF for the two heaviest quarks ($m_{h^0} = 125$ GeV).

pseudoscalar (F_P) particle by:

$$
\begin{aligned}
F_S(\tau) &= \tau\left[1 + (1-\tau)f(\tau)\right] \\
F_P(\tau) &= \tau f(\tau) \\
f(\tau) &= \arctan^2\left(\frac{1}{\sqrt{\tau-1}}\right)
\end{aligned}
\tag{1.76}
$$

For heavy quarks[4] ($\tau_f \gg 1$) we get by expanding the arctan function:

$$
F_S(\tau) = \frac{2}{3} + \frac{7}{45\tau} + O(\frac{1}{\tau^2})
\tag{1.77}
$$

$$
F_P(\tau) = 1 + \frac{1}{3\tau} + O(\frac{1}{\tau^2})
\tag{1.78}
$$

which leads to $F_S(+\infty) = 2/3$ and $F_P(+\infty) = 1$. This results was one evidence to rule out the existence of a fourth generation of quarks. Indeed adding an extra very massive quark would add a term $2/3$ in the total rate sum for Higgs production leading to predictions far beyond the observed production rates.

For light quarks ($\tau_q \ll 1$), i.e. basically all quarks except the top quark, we get:

$$
F_S(\tau) = \tau\left(1 + \frac{\pi^2}{4}\right) + O(\tau\ln(\tau)) \to 0
\tag{1.79}
$$

which leads to $F_S(0) = F_P(0) \simeq 0$, meaning that the light quarks impact (u, d, c, s) in the triangle loop is very limited both for scalar and pseudoscalar particles. This is the reason why in this thesis will only consider the top (and bottom quarks when relevant) in our calculations. Values of their form factors are computed in Tab. 1.4 for $m_{h^0} = 125$ GeV.

To conclude the analysis of the FF, we plot in Fig. 1.19 real and imaginary parts of the FF as a function of the mass of the particle in the loop. We clearly see both limits we computed before as well as the imaginary part which vanishes as soons as $m_q > \frac{m_H}{2}$.

---

[4]Note in the SM this is only the case for the top quark
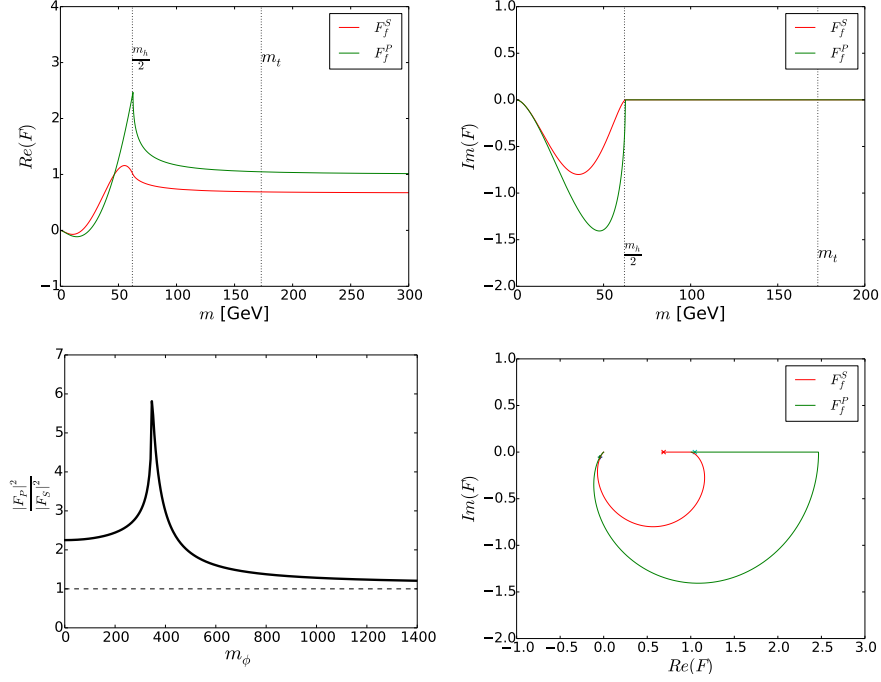
Figure 1.19: Graphical representation of the scalar and pseudoscalar FF. On the top we show FF as a function of the mass of the circulating quark (left: real part, right: imaginary part). The lower left plot shows the ratio of modulus squared of pseudoscalar FF over scalar FF as a function of the Higgs mass. The lower right plot shows these functions in the complex plane. '+' marks correspond to the bottom quark and 'x' to the top quark.

This behaviour will be important when we will study interference in $t\bar{t}$ production in Chap. 4. We also see that F_P is alway bigger than the corresponding F_S, this effect being maximal when $m_\phi = 2m_t$.

1.3   Numerical tools

In this section we present the numerical framework we used to get the results of the following chapters and explain some important notion in particle physics computations. All the numerical results have been obtained using MADGRAPH5_AMC@NLO [48]. It is a Monte Carlo simulation based program which allows users to automatically gen-

erate the code to generate events at LO and NLO accuracy in QCD for many processes in the SM or some more exotic models the user implements.

1.3.1   Monte Carlo simulations

The first approach to model a collision is via the matrix element technique where the Feynman amplitudes associated to a process are computed exactly, taking into account the possible interference between diagrams, spin correlations, etc. The integration over the phase space gives an estimation of the cross section and allows to generate events. Many other generators can be used for this purpose: Sherpa [49], CalcHep/CompHEP [50], Alpgen [51], Whizard [52]. MADGRAPH5_AMC@NLO , besides being very flexible, allows to get fully differential results for NLO processes in an automated way. Recently it has been updated to allow event generation for loop-induced process like Higgs production through gluon fusion [53], and another module has been added for automated reweighting [54]

Basically, calculating the cross section of a process requires to compute a phase space integral. Monte Carlo (MC) generators as MADGRAPH5_AMC@NLO use MC integrations as it is one of the most efficient numerical integration technique to estimate multi-dimensional integrals. With this method, the error decreases like $1/\sqrt{N}$ no matter the number of dimensions. The most basic principle to solve the integral I of a real function $f(z)$ defined in a hypervolume $[0,1]^d$ is to generate a sample of N random points $z_1, z_2, ..., z_N$ according to a uniform distribution and to approximate it by:

$$I = \int f(z)dz \simeq \mu = \frac{1}{N} \sum_{n=1}^{N} f(z_n) \tag{1.80}$$

The error on the estimator (σ_I) is related to the variance of the function which in turn can be estimated by S^2:

$$\sigma_I = \frac{\sigma(f)}{\sqrt{N}} \approx \frac{S}{\sqrt{N}} \quad ; \quad S^2 = \frac{1}{N-1} \sum_{n=1}^{N} [f(z_n) - \mu]^2 \tag{1.81}$$

In order to improve the efficiency of MC integration, instead of using random points following a uniform distribution, we can use a different probability density which depends on the function to be integrated. Of course determining the optimal phase-space mapping for a given integrand is in general difficult because it depends on the shape of the integrand which can be hidden in complicated expressions.

In MADGRAPH5_AMC@NLO the particle content and interactions can be adapted to any particle physics model. To build such a model, another public tool called FEYN-RULES [55] is available. As an addon to Mathematica [56], it allows the user to define

its own fields, couplings, and lagrangians. Then FEYNRULES computes all the relevant couplings, vertices and Lorentz structures and output the model in a UFO format that can then be directly used in MADGRAPH5_AMC@NLO . Recently progress has been made to create NLO models with all required counter terms.

The approach of matrix element technique is appropriate only in certain regions of the phase space where the hard part of the process takes place. However the calculation of cross sections with emission of massless partons (soft radiations) will only be correct if they are sufficiently separated in the phase space, as fixed order calculations suffer from collinear and infrared divergencies.

In the soft and collinear limit of gluons emission for example, the cross section σ_n associated to a process with n partons, is modified by the splitting of one parton as

$$d\sigma_n = d\sigma_{n-1} \frac{\alpha_s}{2\pi} \frac{dt}{t} P(z) dz \tag{1.82}$$

where t is the virtuality of the incoming splitted parton, z is the ratio between the energy of this parton and the energy of one of the outgoing partons and $P(z)$ is the *Altarelli-Parisi splitting function* which depends on the nature of the involved partons.

In the soft/collinear limit, the problem is thus facotrizable in two pieces: the born cross section, which can be evaluated only once, and the terms containing the divergencies which can be considered separately:

$$\sigma \sim \sigma_0 \frac{\alpha_s^N}{N!} \left[\ln \left(\frac{Q^2}{t_0} \right) \right]^N \tag{1.83}$$

with Q the starting scale of the emission and t_0 the threshold under which no splitting is allowed and which is typically linked to the hadronization scale. σ_0 corresponds to the partonic cross section and can be calculated with the matrix element method while the logarithmically divergent terms are best given by parton shower simulations as implemented in Pythia8 [57] or Herwig++ [58] for example. For both initial and final state radiation, the algorithm creates a tree structure of branching controlled by the *DGLAP evolution equation* which determines the μ evolution of the parton density functions $f_q(x, \mu^2)$:

$$\frac{\partial f_q(x, \mu^2)}{\partial \log \mu^2} = \frac{\alpha_s}{2\pi} \int_x^1 \frac{dy}{y} f_q(y, \mu^2) P \left(\frac{x}{y} \right) \tag{1.84}$$

The key principle is that for initial state emissions the virtuality increases with successive parton emissions while in the final shower it decreases towards the hadronization scale. In other words, branchings and splittings happen as long as the virtuality is bigger than the hadronization scale in the final state radiation or lower than the hard scattering scale for the initial state radiation. The shower structure is therefore related

to the probability of having an emission above a certain threshold. This probability is called *Sudakov form factor* and is given by:

$$\Delta(t_a, t_b) = \exp\left[-\int_{t_b}^{t_a} \frac{dt'}{t'} \int_{\epsilon}^{1-\epsilon} dz \frac{\alpha_s(t)}{2\pi} P(z)\right] \tag{1.85}$$

The shower algorithms also use MC methods as they control the branching by assigning to $\Delta(t_a, t_b)$ a random number from a uniform distribution in the interval [0,1]. The value of the momentum fraction hold by each parton is also calculated in the same way according to a probability proportional to $P(z)$.

In the following chapters we will use PYTHIA8 for parton shower and hadronisation. The matching to the PYTHIA8 parton shower (virtually ordered and p_T–ordered) is also automated within MADGRAPH5_AMC@NLO , see Sec. 1.3.3. This is also the case for the scale and PDF uncertainties which are generated at no extra computational cost, following the reweighting prescription of [59]. In our analyses we varied independently both scales in the range $\mu_0/2 < \mu_R, \mu_F < 2\mu_0$ and PDF uncertainties at the 68% C.L. were extracted by following the prescription given by the MSTW collaboration [16].

1.3.2   Reweighting techniques

As we saw in section 1.1.3, Higgs boson phenomenology often includes loops even at LO. Few years ago, generating events for this kind of diagrams was not possible in MADGRAPH5_AMC@NLO . However it was already possible to obtain the one-loop amplitudes $|\mathcal{M}|^2$ with MADLOOP [60] for such processes by computing one–loop matrix elements using the OPP integrand–reduction method [61] (as implemented in CUTTOOLS [62]). To overcome the past limitations concerning event generation for loop-induced processes we used another technique based on additional manual reweighting.

This reweighting method has been employed for a series of processes within the MADGRAPH5_AMC@NLO framework [8, 63, 64] both at LO and NLO accuracy and it has recently been automated (at LO) and made public as part of the official code release [54]. Finally, note that our reweighting strategy also helped to validate the loop-induced event generation inside MADGRAPH5_AMC@NLO .

LO reweighting

In practice this procedure involves generating events through the implementation of a tree-level effective field theory UFO model [65, 66]. After events generation, events
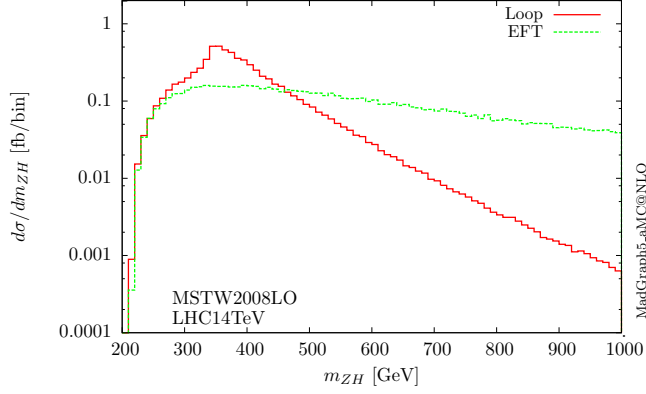
Figure 1.20: Comparison of the invariant mass of the ZH system for $gg \rightarrow ZH$ production in the SM using FT and EFT models.

weights obtained from the tree-level EFT amplitudes are modified by the ratio of the full one-loop amplitude (computed by MADLOOP) over the EFT ones, *i.e.*, $r = |\mathcal{M}^2_{Loop}|/|\mathcal{M}^2_{EFT}|$, where $|\mathcal{M}^2_{Loop}|$ represents the numerical amplitude as obtained from MADLOOP.

In our cases, manual reweighting proved to be efficient in terms of computational speed, as the loop amplitudes have to be calculated for significantly fewer phase-space points than what is needed to integrate them directly. Moreover the EFT leads to distributions that are in general harder in the tails, and therefore the EFT events populate regions that are later suppressed by the exact loop matrix elements, resulting to no significant degradation of the statistical uncertainty.

NLO reweighting

One important aspect is the treatment of the NLO corrections to the gluon fusion channels. Given that this production mechanism is loop–induced at LO, two ingredients would be needed for an exact NLO calculation: i) the one–loop $2 \rightarrow 3$ real–emission amplitudes; ii) the two–loop $2 \rightarrow 2$ virtual correction amplitudes. While the former can be calculated by means of standard techniques, the latter were beyond the reach of the state–of–the–art calculations.

On the other hand, in Fig. 1.20, we show an example of the well–known fact that HEFT provides only a rough estimate of total rates [67], while it poorly reproduces the kinematical distributions [68]. The usual approach in higher–order studies is to extract the QCD corrections from the HEFT, and then employ the exact one–loop LO

amplitudes to reweight the HEFT virtual- and real–emission matrix elements. This conventional strategy, as implemented in HPAIR [69, 70], will be referred to as the "*born–improved*" approach in Chap. 3. One important point in this procedure is that the reweighting of the $2 \to 3$ real–emission part is based on its factorization into the $2 \to 2$ LO matrix element, which is then reweighted by the full LO amplitude, times a global factor, whatever the extra jet being soft or hard.

As an alternative, we developed a "*loop-improved*" approach which was first presented in [71]. In the "loop-improved" calculation we include the exact one–loop results not only for the $2 \to 2$ LO amplitudes, but also for the NLO $2 \to 3$ real-emission matrix elements. Therefore, the only approximation we make at the amplitude level concerns the finite part of the NLO virtual corrections which, in the absence of the exact two–loop calculation, was first taken from the one–loop HEFT results, and then reweighted with the exact one–loop LO matrix elements.

Including the exact one–loop $2 \to 3$ matrix elements provides a more accurate description of the tails of the distributions. In this phase space region, where hard parton emissions take place, the factorization of the $2 \to 3$ real–emission amplitudes into the $2 \to 2$ LO amplitudes, as implicit in the "born–improved" approach, cannot accurately describe the hard parton kinematics.

Despite the upgraded treatment of hard real emission, our "loop–improved" method still relies on the one–loop HEFT virtual corrections in place of the exact two–loop results. The impact of these exact two–loop results have been only recently quantified due to recent progress in two-loop NLO QCD computation for Higgs pair production in [72] and will be discussed in Chap. 3.

From the technical point of view, in the MADGRAPH5_AMC@NLO setup, NLO computations are carried out using two independent modules: i) MADFKS [73], which takes care of the Born and the real–emission amplitudes, subtracts the infrared singularities according to the FKS prescription [74], and generates the parton shower subtraction terms required by the MC@NLO method [75]; ii) MADLOOP and the OPENLOOPS method [76].

1.3.3   Matching-merging

Matrix Element combined with Parton shower (ME+PS) schemes allow the consistent combination of matrix elements with different jet multiplicities via their matching to a parton shower. This merging-matching approach makes use of the fact that while tree level fixed-order amplitudes describe reliably the region of hard and well separated jets, the parton shower provides a better description of the soft and collinear regions. Combining the two requires of course a consistent treatment to avoid double-counting

which would affect the value of the cross sections as well as the distributions. The principle of jet matching is to divide the phase space into two independent regions charaterized by the hardness of QCD emissions. This is achieved by various merging algorithms. Methods that are widely used for tree level merging are CKKW [77, 78], CKKW-L [79] (and their later improvements [80]), and MLM [81]. More recently new methods have been developed in MADGRAPH5_AMC@NLO to perform merging at NLO, see for example FxFx [82] and UNLOPS [83], yet not directly applicable to $2 \to 2$ loop-induced processes at the Born level yet, mainly due the absence of analytic results for the two-loop $2 \to 2$ matrix elements.

The implementation of MLM merging in MADGRAPH5_AMC@NLO /PYTHIA 8 comes in two variants: the traditional k_T-MLM and the shower-k_T schemes. They both give comparable results as discussed in detail in [84]. In this thesis we employ the shower-k_T scheme and we only mention here its main features. While this scheme has been used for phenomenological studies with PYTHIA 6 in the past, see for example [85], we employ the most recent implementation of the scheme in MADGRAPH5_AMC@NLO combined with PYTHIA 8.

In the shower-k_T scheme, matrix element events are generated with a minimum separation $p_{T_{\min}}$, between parton and the initial state (iB), and Q_{cut} between final-state partons (ij), defined by the measure:

$$d_{iB}^2 = p_{T_i}^2 > p_{T_{\min}}^2, \quad d_{ij}^2 = \min(p_{T_i}^2, p_{T_j}^2)\Delta R_{ij}^2 > Q_{\text{cut}}^2, \tag{1.86}$$

where $\Delta R_{ij}^2 = 2[\cosh(\eta_i - \eta_j) - \cos(\phi_i - \phi_j)]$ and p_{T_i}, η_i and ϕ_i are the transverse momentum, pseudorapidity and azimuthal angle of particle i. Short distance (parton level) events are then passed to PYTHIA 8 which evolves them down using the p_T-ordered shower. In practice, for each event PYTHIA 8 records the scale of the hardest shower emission: Q_{hardest}^{PS}. This scale is then used to accept or reject the event as follows: for the low multiplicity events, the event is rejected if $Q_{\text{hardest}}^{PS} > Q_{\text{cut}}^{ME}$, while for the highest multiplicity the event is rejected if $Q_{\text{hardest}}^{PS} > Q_{\text{softest}}^{ME}$, with Q_{softest}^{ME} being the scale of the softest matrix-element parton in the event. The value of Q_{cut}^{ME} is selected on a process-by-process basis to ensure that there is a smooth transition between the ME and PS regimes. In practice, this is assessed by examining the differential jet rate distributions which show if the transition is indeed smooth. Matching and merging up to one jet will be used in Chap. 2 in order to improve current predictions.

SM Parameters	Values
$\alpha_{em}(M_Z)$	$\frac{1}{127.934}$
$\alpha_s(M_Z)$	0.118
G_F	$1.16637e^{-5}$ GeV^{-2}
m_Z	91.188 GeV
m_W	80.385 GeV
m_H	125 GeV
m_b	4.5 GeV
m_t	173 GeV
Γ_Z	2.49 GeV
Γ_W	2.08 GeV
Γ_H	4.04 MeV
Γ_t	1.49 GeV

Table 1.5: Values of the SM parameters used in our simulations. These values are in agreement with the Particle Data Group [14]

1.3.4   Benchmarks design

Model implementation

As for the 2HDM implementation, we use the 2HDM@NLO model obtained with the NLOCT package [86]. The model is based on the FEYNRULES and UFO frameworks. It includes all relevant UV counterterms and R2 vertices needed for the MAD-LOOP calculation, and allows to compute tree–level and one–loop processes within a completely general 2HDM setup.

The 2HDM benchmarks are imported into MADGRAPH5_AMC@NLO using a parameter card, constructed with the help of the public calculator 2HDMC [87].The values of the SM parameters that are used as input in our 2HDM card generator are summarized in Tab. 1.5. PDF, factorization and renormalisation scales, CM energy of the collision and other cuts will be specified separately for each studied process.

Theoretical and experimental constraints on 2HDM parameters

Multiple conditions place constraints on the parameter space of the model. On one hand, there are theoretical constraints like unitarity [88–90], perturbativity [91] and vacuum stability [92–94] that guarantee the correct high–energy behavior of the the-
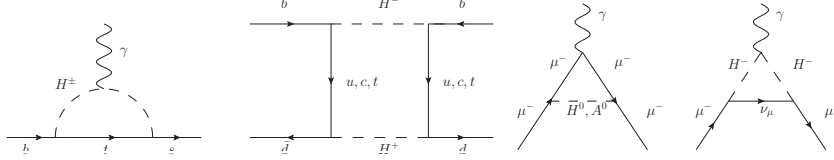
Figure 1.21: Example of diagrams modified by the new scalar charged particles.

ory. One important consequence is that the Higgs self–interactions cannot be arbitrarily large. On the other hand, agreement with electroweak precision tests compresses the allowed mass splitting between the heavy scalar fields [95–97], and therefore prevents any exceedingly large deviation from the (approximate) custodial $SU(2)$ invariance [98]. Fixing the Higgs mass to $m_H = 125$ GeV, a global fit to electroweak precision observables in terms of the oblique parameters S, T, U [99] yields $S = 0.03 \pm 0.01$, $T = 0.05 \pm 0.12$, and $U = 0.03 \pm 0.10$ [14, 100, 101].

Aside from these conditions connected to the structure of the model, the allowed parameter space shrinks even further as we enforce compatibility with the average LHC Higgs signal strength [23, 46] and the direct collider mass bounds on the heavy neutral [102–106] and charged Higgs bosons [107, 108].

Finally, low–energy heavy flavor physics [109–111] and the muon $(g-2)_\mu$ data [112, 113] place additional indirect constraints on the $(m_{H^\pm}) - \tan\beta$ plane. Indeed many flavor changing decays are now modified by the presence of the additional charged Higgs bosons $H^\pm$ while in the SM, only the $W^\pm$ was present. The charged Higgs bosons could then induce deviations in $b \to s\gamma$ process, $B_0 - \bar{B}_0$ mixing as can be seen for example in Fig. 1.21

In order to take into account all these theoretical and experimental constraints when designing our benchmarks for the processes we review in this thesis we used several public tools along with additional routines of our own:

2HDMC [87] is a C++ code that performs calculations in a general CP-conserving 2HDM. It features conversion between different parametrization of the 2HDM potential, checks its positivity and perturbativity as well as S-matrix unitarity, computes decay widths and contains methods for calculating the 2HDM contributions to the oblique parameters (S,T,U,V,W,X) and to the anomalous magnetic moment of the muon $(g-2)_\mu$. The last important achievement of this program is to provide an interface to the other tools we describe hereafter.

HiggsBounds [114–116] allows us to test models with arbitrary Higgs sector against the published exclusion bounds from Higgs searches at the LEP, Tevatron and

LHC experiments[5]. To achieve this, it takes the Higgs masses, BR, cross sections and total decay widths as input (provided by 2HDMC in the form of a SLHA file) and calculates the predicted signal rates for search channels considered in experimental data. These rates are then compared to the expected and observed cross section limits for the Higgs searches to determine whether this benchmark point is excluded or not at 95% confidence level. The list of all the analyses included in the tool can be found in the mentioned reference.

HiggsSignals [117,118] is a fortran code that tests the compatibility of extended Higgs sector predictions against Higgs rates and masses as measured at the LHC or Tevatron based on the same input as HiggsBounds. It features two statistical tests, one which determines the compatibility of the model with experimentally observed Higgs signals, and a second which tests for general compatibility with the observed Higgs data at the predicted mass(es) of the Higgs boson(s) in the theory. Since the two tests are complementary, it also provides a method to perform both simultaneously and to use the combined results for models with multiple Higgs bosons.

SuperIso [119,120] is a program to evaluate flavor physics observables in the SM, 2HDM and MSSM like the isospin asymmetry of $B \to K^*\gamma$, branching ratio of $B \to X_s\gamma$, $B_s \to \mu^+\mu^-$, $B \to \tau\nu_\tau$, $B \to D\tau\nu_\tau$, $K \to \mu\nu_\mu$, $D_s \to \tau\nu_\tau$ and $D_s \to \mu\nu_\mu$. As the two previous tools it requires SLHA file as input.

In addition, we also considered the findings in [121], where values of $\tan\beta < 1$ (resulting in enhanced top Yukawa couplings) are ruled out for a type–I 2HDM by $BR(B \to X_s\gamma)$ and ΔM_{B_d} experimental constraints but are allowed for a type–II 2HDM as long as $m_{H^\pm} > 600$ GeV.

Despite the large amount of constraints, 2HDM scenarios that satisfy these limits and yet have a significantly different phenomenology than the SM exist and have been studied extensively in the literature [91, 122–126]. These scenarios arise in two cases: the *alignment limit*, *i.e.*, in the limit of $\cos(\beta - \alpha) \ll 1$ or in the *decoupling limit*, which ensures that the masses of the additional Higgs bosons lie well above the light-Higgs one. Note that decoupling implies alignment while the opposite is not true. Indeed in the decoupling limit the 2HDM can be mapped onto an effective theory, whose expansion parameter $\cos(\beta - \alpha) \sim v^2/M_{\text{heavy}}^2 \ll 1$ determines the hierarchy between the light $m_{h^0} = \mathcal{O}(v)$ and the heavy scalar masses $m_{H^0} \simeq m_{A^0} \simeq m_{H^\pm} \simeq \mathcal{O}(M_{\text{heavy}})$ [127, 128].

Interestingly, the decoupling limit is not the only 2HDM realisation which is consistent with all parameter space constraints. Scenarios with light additional Higgs bosons are also allowed in the "alignment limit" [129, 130].

---

[5]It includes the latest LHC results presented in 2013, many of which are based on the full 8 TeV dataset
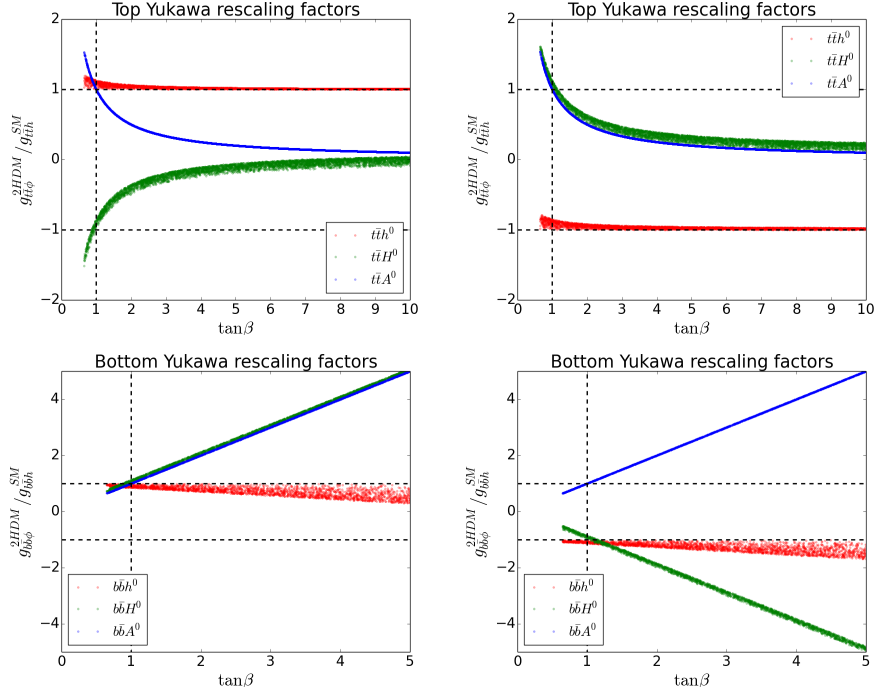
Figure 1.22: Yukawa values normalized to the SM value as a function of the $\tan\beta$ and $\sin(\beta - \alpha)$ with constraints of Eq. 1.87. Left plots are for $0 < \sin(\beta - \alpha) < 1$ while the right plots correspond to $-1 < \sin(\beta - \alpha) < 0$.

We conclude this chapter by illustrating the impact of experimental constraints on the Yukawa couplings. Roughly speaking, global and basic requirements are

$$|\sin(\beta - \alpha)| \simeq 1 \quad , \quad 0.7 \leq \tan\beta \leq 20 \tag{1.87}$$

When we apply these restrictions to the previous plots of Fig. 1.15, the allowed regions get much smaller as we see in Fig. 1.22. We also show heatmaps in Fig. 1.23 to get a better understanding on how α impacts the values of the Yukawa couplings. The results in these plots will reflect in all the benchmarks we will introduce during our study of the 2HDM processes in the next chapters.
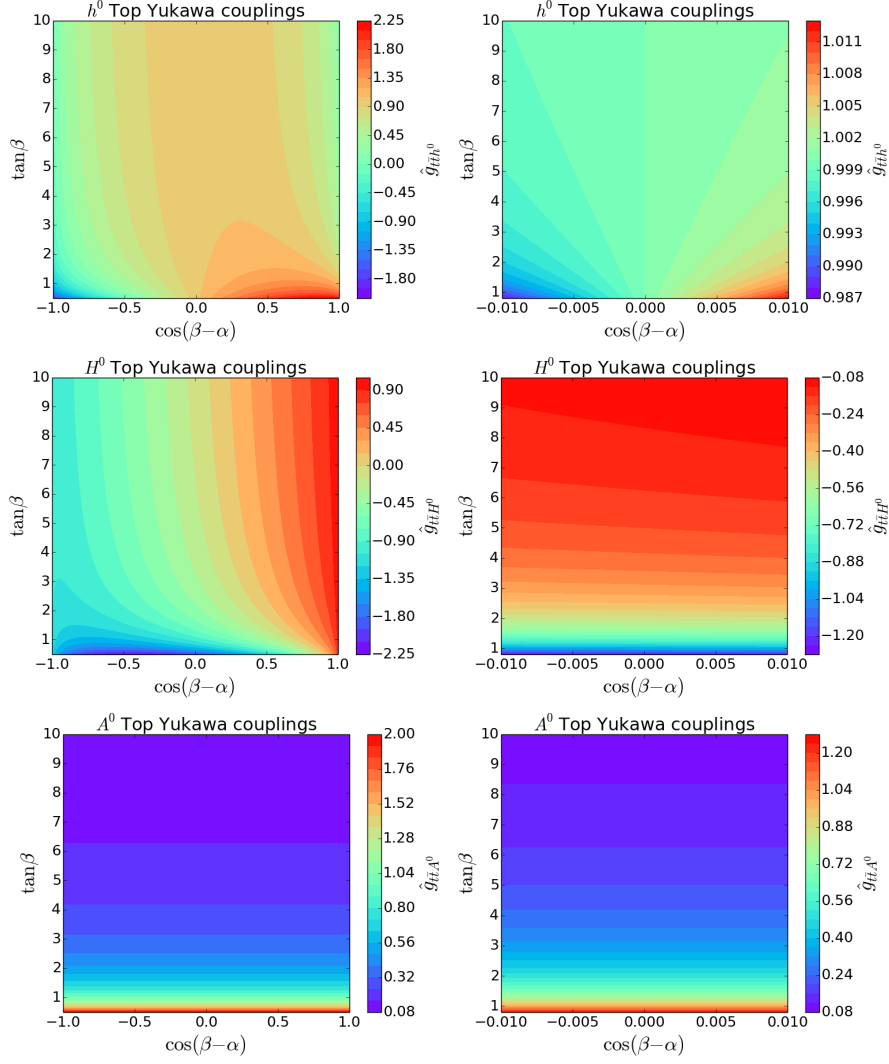
Figure 1.23: 2HDM Yukawa rescaling factors as a function of the two mixing angles. Left: No constraints. Right: Zoom on the allowed region.

It's also interesting to analyze the relative size of the Higgs production cross sections via gluon fusion. The three ratios are given by:

$$
\begin{aligned}
\frac{\sigma_{gg\to H^0}}{\sigma_{gg\to h^0}} &= \frac{\hat{g}^2_{H^0 t\bar{t}}}{\hat{g}^2_{h^0 t\bar{t}}} = \tan^2\alpha \\
\frac{\sigma_{gg\to A^0}}{\sigma_{gg\to h^0}} &= \frac{\hat{g}^2_{A^0 t\bar{t}}}{\hat{g}^2_{h^0 t\bar{t}}}\frac{|F^t_P|^2}{|F^t_S|^2} = \frac{\cos^2\beta}{\sin^2\alpha}\frac{|F^t_P|^2}{|F^t_S|^2} \\
\frac{\sigma_{gg\to A^0}}{\sigma_{gg\to H^0}} &= \frac{\hat{g}^2_{A^0 t\bar{t}}}{\hat{g}^2_{H^0 t\bar{t}}}\frac{|F^t_P|^2}{|F^t_S|^2} = \frac{\cos^2\beta}{\cos^2\alpha}\frac{|F^t_P|^2}{|F^t_S|^2}
\end{aligned}
\tag{1.88}
$$

In Fig. 1.24 they are shown as a function of $\cos(\beta - \alpha)$ and $\tan\beta$. We can see that these ratios are small in a wide part of the parameter space, with small regions where differences are significant. Once constraints are taken into account, the three final states have nearly the same total rates, indicating no huge cross section should be expected in the 2HDM for single Higgs production.
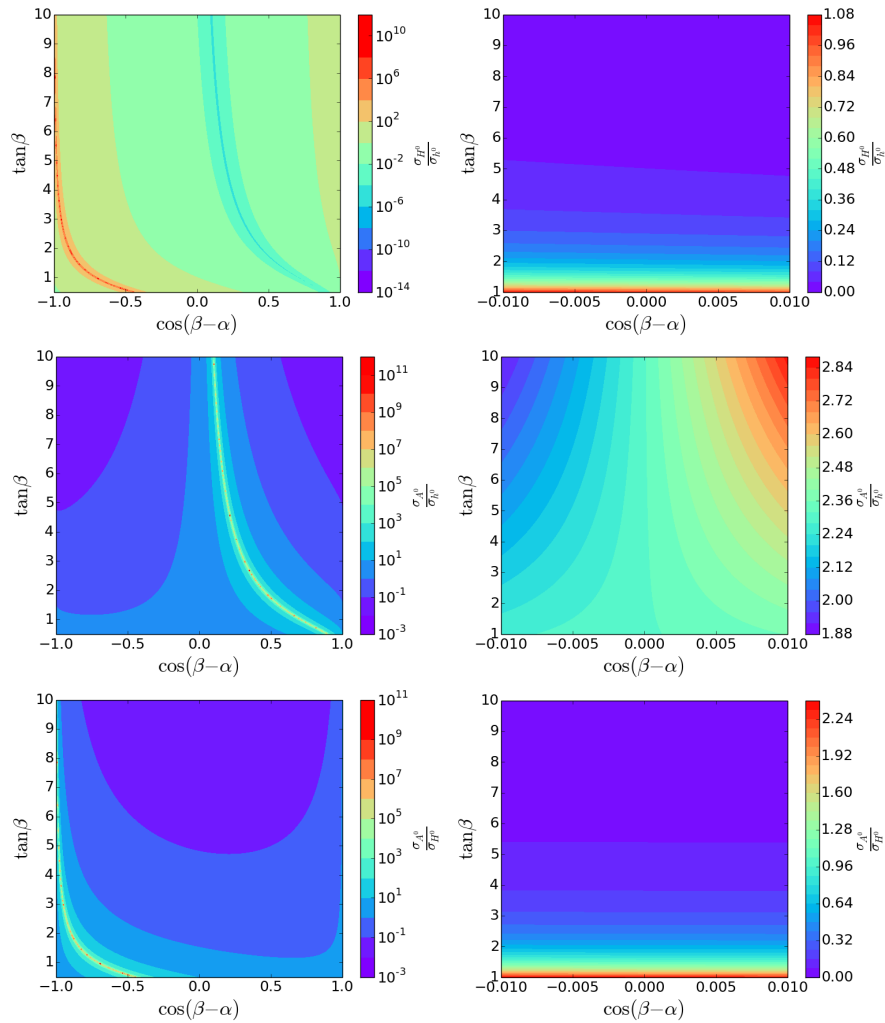
Figure 1.24: Ratios of 2HDM Higgs production cross sections via gluon fusion as a function of the two mixing angles for the same spin-0 mass. Left: No constraints. Right: Zoom on the allowed region.

Chapter 2

Higgs and Z boson associated production via gluon fusion

"All of physics is either impossible or trivial. It is impossible until you understand it, and then it becomes trivial"

Ernest Rutherford (1871 - 1937)

2.1   Introduction

Among processes probed at the LHC to study Higgs couplings is the associated production of a Higgs boson together with a vector boson V, either a $W^{\pm}$ or a Z, also known as Higgs-strahlung, *i.e.*, at the leading order in QCD, the Drell-Yan production of an off-shell vector boson $q\bar{q} \to V^*$ with its subsequent decay $V^* \to VH$. While suppressed in the SM with respect to the leading gluon-gluon and vector boson fusion channels, VH production is of phenomenological interest mostly because the presence of the vector boson (and possibly of leptons coming from its decay) in the final state can help to access the large yet challenging $H \to b\bar{b}$ decay mode. For instance, Higgs-strahlung has been the dominant Higgs search mode at the Tevatron [131]. At the LHC, the ATLAS [132] and the CMS [133] collaborations have investigated VH production, with the Higgs boson decaying to a $b-$quark pair, both reporting small excesses above the background only hypothesis. Searches for Higgs

57

decaying to W^+W^- [134, 135] and to invisible states [136, 137] have also been performed by both ATLAS and CMS.

On the theory side, predictions for ZH production are known at NNLO in QCD and at NLO electroweak in EW theory. The NNLO QCD cross section includes the Drell-Yan type terms of $\mathcal{O}(g^4\alpha_s^2)$ first computed in [138, 139]. In addition to Higgs-strahlung, it has been noted that contributions from quark–anti-quark initiated diagrams where the Higgs is emitted from a top quark loop arise at the same order. These diagrams interfere with the LO and NLO Drell-Yan amplitudes and have been computed in [140], where they were found to contribute to the inclusive NNLO cross section at the percent level. Implementations of the NNLO QCD calculations are publicly available in VH@NNLO [141] and HVNNLO. Fully differential NLO QCD and EW results can be obtained with the program HAWK [142, 143], while event generation accurate at NLO in QCD (inclusively and for higher jet-multiplicitites), can be nowadays obtained (automatically or semiautomatically) in several frameworks, *i.e.*, MADGRAPH5_AMC@NLO / POWHEG [144] + PYTHIA 8 /HERWIG++ and SHERPA.

At NNLO, a purely virtual gluon fusion contribution emerges, through the $gg \to ZH$ amplitude squared, which at the LHC can be enhanced by the large gluon-gluon luminosity at small Bjorken x. Its contribution to the total cross section has been known for a long time [145, 146] and it has been included in the implementations of the NNLO calculations [19, 141]. The gluon fusion component is separately gauge invariant, IR and UV finite and accounts for about 10% of the total NNLO cross section at 14 TeV. Being essentially a leading-order contribution, $gg \to ZH$ introduces a rather strong scale dependence to the NNLO result, which in turn is known quite precisely. In order to reduce the associated theoretical uncertainty, recently, NLO corrections for the gluon fusion contribution have been estimated by computing them in the infinite top-quark mass limit [147]. The NLO corrections to this process, $\mathcal{O}(\alpha_s^3)$, while formally part of the N^{3}LO ZH cross section, are expected to be large, similarly to other gluon fusion processes such as Higgs single or pair production. The computation of the approximate NLO corrections in the infinite top mass limit has confirmed this expectation. The NLO computation in the infinite top mass limit reduces the scale uncertainty by a factor of two, yet the size of the finite top-quark mass effects remains unknown: the exact NLO result requires two-loop multi-scale amplitudes whose analytic form is beyond the current advances in the multi-loop technology. In an effort to further reduce the theoretical uncertainties in this process, a soft gluon resummation for the gluon-gluon contribution has been performed in [148] promoting the previous results to NLO+NLL accuracy. We should note here that in contrast with single Higgs production, where the infinite top-quark mass limit provides a good description of the process, and allows the computation of higher order corrections, here, similarly to (yet with even less control than) Higgs pair production, the much higher scales involved

make the effective field-theory approach unreliable, especially so at the differential level.

In addition to the SM production mechanism and characteristics, interesting features can be expected from Higgs production in association with a Z boson in BSM scenarios. The 2HDM is an attractive framework in which Higgs-strahlung can lead to interesting features. First the range of channels is richer: in addition to the production of the light (125 GeV) Higgs boson in association with a Z boson (Zh^0), Z associated production of the heavy scalar (ZH^0) and pseudoscalar boson (ZA^0) are also possible [5]. Experimental searches are already underway to look for signals of these processes, especially in the case where cross-sections can be enhanced by the resonant production of an intermediate scalar (H^0 or A^0) with subsequent decays into Z and a lighter scalar. In particular, CMS has searched for signals of the decay of the pseudoscalar A^0 into a Zh^0 pair [149, 150] and that of the heavy scalar H^0 into a ZA^0 pair [151] and the results have been used to set constraints on the 2HDM parameter space.

So far considerable effort has been devoted to provide accurate total rates in this channel for both the SM and the 2HDM, but accuracy and precision in the differential distributions is also of vital importance. This need becomes more important for experimental analyses which make use of exclusive observables, in order to tame the typically very large QCD backgrounds. Moving in that direction, it has been noted in the literature [5, 152] that the gluon induced component can play an important role. The gluon fusion Higgs p_T distribution peaks at higher values than the corresponding Drell-Yan one, and therefore its relative contribution becomes more important in boosted Higgs searches, which are preferred experimentally to reduce the backgrounds. The prospects of such searches have improved recently due to progress in jet substructure techniques, after the seminal suggestion in [153].

The aim of this chapter is to contribute to the understanding of gluon induced ZH production and to improve the predictions for the differential distributions. We consider the $2 \to 2$ and $2 \to 3$ matrix elements entering the gluon fusion contribution to Z Higgs-strahlung. We first review the main features of the $2 \to 2$ ones and then examine the importance of the $2 \to 3$ contributions. Given the lack of an exact and fully differential NLO computation for this process, we provide a better description of the kinematics for this component by combining the $2 \to 2$ and $2 \to 3$ matrix elements in a merged sample, matched to a Parton Shower (PS). This provides a fully exclusive control at the hadron level. A similar approach has been followed for other loop induced processes, such as single Higgs production [154] and Higgs pair production [155, 156]. In general, this method provides a better description of the kinematics, yet as the formal accuracy for total rates remains at LO, it is often combined with a normalisation obtained from higher-order computations, when available.
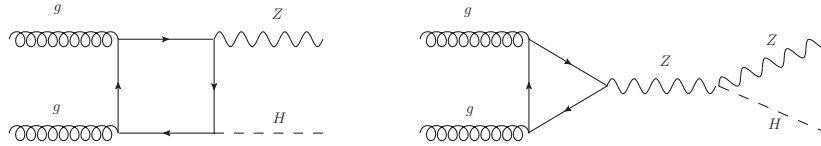
Figure 2.1: Representative Feynman diagrams for ZH production in gluon fusion in the SM.

In this chapter we study gluon induced Higgs-strahlung at the LHC, presenting the first merged-matched results for $gg \rightarrow Z\phi$, with ϕ being a generic scalar, by employing the 0 and 1-jet matrix elements for the SM and the 2HDM. It is organised as follows. In Sec. 2.2, we discuss the process within the SM, first by reviewing the important features coming from the $gg \rightarrow ZH$ matrix elements. We also consider the behaviour of the $2 \rightarrow 3$ matrix elements, which we then combine with the $2 \rightarrow 2$ ones. We describe our methodology, and present results both at the parton level and after merging and matching to a parton shower. In Sec. 2.3, we explore the results of various 2HDM scenarios using the same calculation setup. We draw our conclusions in the final section.

2.2   Gluon induced ZH production in the SM

Representative Feynman diagrams contributing to the $gg \rightarrow ZH$ process in the SM are shown in Fig. 2.1. Massive fermions, t and $b-$quarks, run in the box, while all flavours run in the triangle. The contribution of the two light generations to the triangle vanishes as required by the anomaly cancellation. In practice, it is only the axial vector part of the heavy-quark-Z coupling that contributes to the amplitude. The amplitude for this process was first computed in [145, 146].

In what follows, we will first review the main features of the $2 \rightarrow 2$ process for gluon induced ZH production before discussing the implications of the $2 \rightarrow 3$ one. A sample of the relevant diagrams contributing to ZHj is shown in Fig. 2.2. In addition to the gg initial state amplitudes, the qg and $q\bar{q}$ channels also open up, when an additional jet is allowed. The $gg \rightarrow ZHg$ amplitudes were used in [157] to calculate the gg part of the ZHj cross-section at the LHC for various jet transverse momentum cuts. In what follows, we will consider these along with the qg and $q\bar{q}$ diagrams to discuss the behaviour of the $2 \rightarrow 3$ amplitudes and subsequently to obtain a merged sample of 0 and 1-jet multiplicitities.
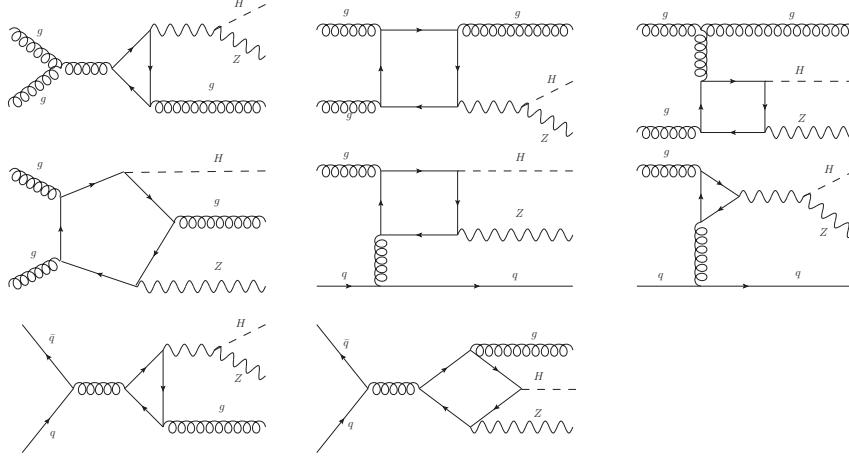
Figure 2.2: Representative Feynman diagrams for gluon induced ZHj production in the SM.

This procedure involves generating events through the implementation of a tree-level effective field theory (EFT), in this case obtained by taking the limit of infinite top-quark mass with all other quarks being massless.

2.2.1   Parton-level results

Before proceeding to the technical setup and presenting results of the merging-matching, we consider the salient aspects as observed at the parton level. The one-loop amplitudes squared for ZH and ZHj can be obtained with the help of MADLOOP. The findings of this study will reveal some previously unnoticed features of $gg \to ZH$ and will act as a motivation to employ a merging-matching procedure in the following section.

We note here that finite width effects in the propagators of the loops can be taken consistently into account within MADGRAPH5_AMC@NLO via the implementation of the complex mass scheme [158, 159]. The effect of a non-zero top width is shown in Fig. 2.3, where the matrix element squared for $gg \to ZH$, for 90^0 scattering, is shown as a function of the invariant mass of the ZH system. The correction is more important at the $t\bar{t}$ threshold, where it reaches 20%. Finally, when integrated over all centre-of-mass energies and scattering angles, we find the top-quark width to modify the $gg \to ZH$ cross-section by $\sim$2% at 14TeV, an effect similar to that observed for
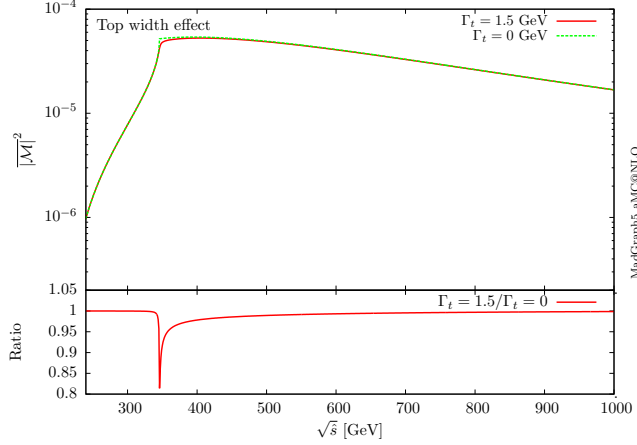
Figure 2.3: Top width effect on the matrix element squared for $gg \rightarrow ZH$. Results for Γ_t=0 and 1.5 GeV are shown along with their ratio.

single and double Higgs production in [160] and [63], respectively. For the rest of the results presented in this work the width of the top quark is set to zero.

An interesting aspect of the $gg \rightarrow ZH$ matrix element is its angular dependence. While in Fig. 2.3 we have fixed the scattering angle to 90^0, in Fig. 2.4, we show the dependence of the amplitude squared on the centre-of-mass scattering angle, for various values of $\hat{s}$. The matrix element starts with no angular dependence at low energies, but varies significantly with the angle at high energies. This angular dependence of the matrix element implies that at high energies, very forward or backward scattering is favoured over 90^0 scattering. This behaviour originates from the interplay between the triangle and the box diagrams, and their respective angular behaviour. As we will also discuss later, box and triangle interfere destructively, with the triangle contribution dominating at low energies. The cancellation becomes nearly exact at high energies, mostly leaving a remainder from the box contribution that is strongly dependent on the scattering angle.

We now proceed to discuss results for the LHC. As loop-induced event generation was not yet implemented in MADGRAPH5_AMC@NLO in 2014, our procedure involved generating events through the implementation of a tree-level effective field theory (EFT), in this case obtained by taking the limit of infinite top-quark mass with all other quarks being massless. Then a reweighting was applied as discussed in Sec. 1.3.2 in order to take into account the finite top mass in the loop. Parton distribution functions (PDFs) are evaluated using the MSTW2008LO set [16] and the central renormalisation and factorisation scales are set to the invariant mass of the ZH sys-
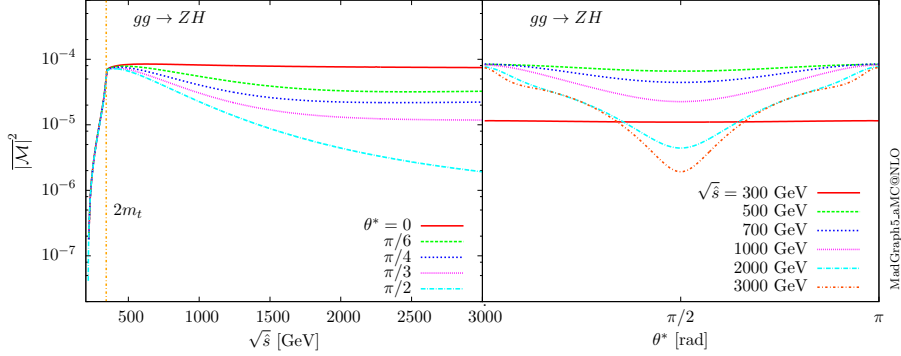
Figure 2.4: Matrix element squared for $gg \rightarrow ZH$ as a function of the centre-of-mass energy for different values of scattering angles (left) and as a function of the centre-of-mass scattering angle for various values of $\sqrt{\hat{s}}$ (right).

tem: $\mu^0 = \mu_R^0 = \mu_F^0 = m_{ZH}$. In our results, scale variations are obtained by varying the scales in the range of $\mu^0/2 < \mu_{R,F} < 2\mu^0$.

Tab. 2.1 summarises results for the $gg \rightarrow ZH$ cross section and the "loop-induced" ZHj contribution, originating from the square of the amplitudes shown in Fig. 2.2. For reference we also include the total $pp \rightarrow ZH$ cross section at NNLO obtained with VH@NNLO. The NNLO cross section includes the $gg \rightarrow ZH$ result of the first row, for which excellent agreement has been found between our computation and the result of VH@NNLO. We note that the results shown in the second row of Tab. 2.1 for ZHj are obtained using the loop amplitudes shown in Fig. 2.2. These qg and $q\bar{q}$ amplitudes can interfere with the Drell-Yan type real emission amplitudes. This interference contribution to the cross section has been computed in [140] and found to be at the per-mille level. In our computation we use these amplitudes squared, *i.e.*, at $\mathcal{O}(\alpha_s^3)$. It is clear that at this order, other qg loop-induced contributions can enter squared, for example, the set of diagrams where the Z couples to a light quark and the H to a top-quark loop. We have not included these diagrams here, as we consider them of a different origin, but we have checked that their amplitude squared contribution to the cross section is small, below the femtobarn level, and therefore at least one order of magnitude smaller than those in Fig. 2.2. The interference of this type of diagrams with the Drell-Yan amplitude was computed in [140] and also found to be small.

Given that the ZHj amplitude is divergent in the limit of a collinear or soft jet, we apply a cut on the p_T of the jet to obtain finite results. We have set this cut to 30 GeV in Tab. 2.1. The $2 \rightarrow 3$ contribution comes mainly from the gg initiated diagrams, with qg giving about 20% of the ZHj cross section. The ZHj contribution is not as suppressed as expected from the extra power of α_s, leading to results comparable in

Contribution [fb]	$\sqrt{s} = 8$ TeV	$\sqrt{s} = 13$ TeV	$\sqrt{s} = 14$ TeV
$gg \to ZH$	$17.4\,^{+34\%}_{-24\%}$	$58.5\,^{+30\%}_{-21\%}$	$70.7\,^{+29\%}_{-21\%}$
$pp \to ZHj$ ($p_T^j > 30$ GeV)	$12.4\,^{+52\%}_{-32\%}$	$49.0\,^{+44\%}_{-32\%}$	$58.4\,^{+47\%}_{-31\%}$
$pp \to ZH$ (NNLO)	$387\,^{+2.2\%}_{-1.6\%}$	$795\,^{+3.2\%}_{-2.0\%}$	$886\,^{+3.2\%}_{-2.3\%}$

Table 2.1: Cross sections (in fb) for ZH associated production at the LHC at $\sqrt{s} = 8, 13$ and 14 TeV. The uncertainties (in percent) refer to scale variations. No cuts are applied to final state particles apart from the jet p_T cut in the second row ($p_T^j > 30$ GeV) and no Higgs or Z branching ratios are included. The ZHj contribution shown here is obtained from the loop diagrams shown in Fig. 2.2, while the NNLO results are obtained with VH@NNLO.

size to the $gg \to ZH$ cross section. Of course these results are extremely sensitive to the chosen cut for the transverse momentum of the additional parton, as the cross section diverges in the IR limit. Such a problem would not arise in the case of a NLO computation matched to a parton shower, for example with the MC@NLO method, in which all divergences are regularised and cancelled for inclusive observables.

The results in Tab. 2.1 also demonstrate the problem of large scale uncertainties for the LO gg cross section, that contribute significantly to the total NNLO scale uncertainty. The problem persists also for the loop-induced ZHj contribution. A significant reduction of these intrinsic QCD uncertainties can only be achieved by a complete NLO computation, as discussed in [147].

In addition to the total cross-section results presented in Tab. 2.1, interesting observations can be made by studying the differential distributions for the gluon fusion process. We start by presenting distributions for the invariant mass of the ZH system and the transverse momentum of the Higgs in Fig. 2.5 for the LHC at 14 TeV. These distributions have been shown elsewhere in the literature, for example in [152]. In addition to the gluon fusion results, we also include the NLO Drell-Yan like distributions obtained automatically with MADGRAPH5_AMC@NLO . We note here that differential NNLO results for the Drell-Yan like contribution can be provided by the code HVNNLO. As is evident from [19], the NNLO computation leads to an overall 20% decrease of the Drell-Yan component but not to any significant shape difference compared to the corresponding NLO one.

The first observation regards the clear presence of the $2m_t$ threshold, at which the gluon fusion amplitude acquires an absorptive part, related to the on-shell $gg \to t\bar{t}$,
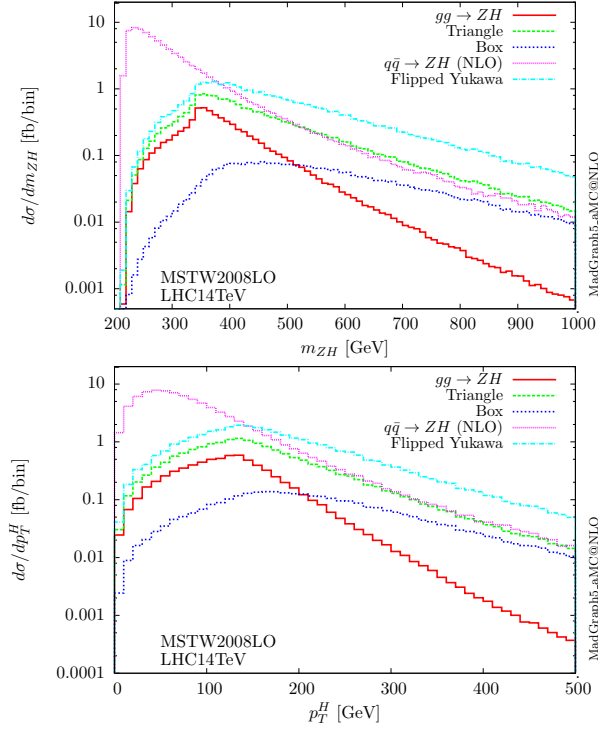
Figure 2.5: Invariant ZH mass and p_T^H distributions for ZH production at $\sqrt{s} = 14$ TeV. The gluon fusion contribution is decomposed into the triangle and box contribution. For completeness we also plot the Drell-Yan type contributions at NLO obtained with MADGRAPH5_AMC@NLO .

$t\bar{t} \to ZH$ scattering, leading to a characteristic rise in the invariant mass distribution. It is evident from Fig. 2.5 that the gluon fusion component leads to distributions of fundamentally different shape from the Drell-Yan ones and therefore it should be considered in all relevant studies, in particular in the boosted region of $p_T^H > 100$ GeV, where its relative importance increases.

In the plots, we decompose the gluon fusion result into the triangle and box components. The two interfere destructively over the whole range of centre-of-mass energies, with the cancellation between the two being nearly exact at high energies. Such a cancellation is due to unitarity: while each of the two diagrams grows with energy the cancellation leads to a well-behaved amplitude at high energies. We stress here that this behaviour of the amplitude is not present in the infinite top mass limit. In this limit, the amplitude for the box diagram vanishes and therefore only the triangle contributes to the amplitude, giving a rather bad approximation of the one-loop amplitude
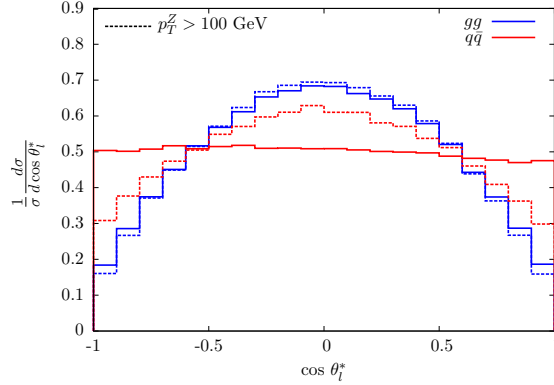
Figure 2.6: Normalised distributions of the lepton angle $\theta_{l^-}^*$ for gluon fusion and Drell-Yan like ZH production at $\sqrt{s} = 14$ TeV. Results for an imposed cut of 100 GeV on the p_T of the Z are shown in dashed lines.

at high energies. In addition, we note that this is a process highly sensitive to the relative phase between the HZZ and $Ht\bar{t}$ couplings. To demonstrate this, in Fig. 2.5 we show the result obtained by changing the relative sign between the top Yukawa and the HZZ coupling. In pair with other processes where such unitarity cancellations take place, such as $H \rightarrow \gamma\gamma$ or $pp \rightarrow tHj$ [161–163], flipping the sign results in an increase in the gluon fusion induced contribution by a factor of five, and much harder distributions as the interference between triangle and box becomes constructive, see Fig. 2.5. We conclude that, given the difference in the shape as well as the size of the cross section above $2m_t$, the ZH invariant mass or transverse momentum of the Higgs or the Z could also be used to bound the relative phase between the Higgs couplings to fermions and to vector bosons.

The difference in the p_T shape between the Drell-Yan and gluon fusion production persists also in the distribution of the lepton p_T coming from the Z decay. Besides, another interesting aspect of the gluon fusion process is that it leads to different angular distributions for the resulting leptons compared to the Drell-Yan component [164]. This is evident from studying Fig. 2.6 wich shows the normalised distributions of the angle $\theta_{l^-}^*$, defined as the angle in the Z rest frame between the lepton and Z flight direction in the lab frame. In the plot, we use the NLO Drell-Yan result, and plot the distributions with and without a cut of 100 GeV on the p_T of the Z. The shape of the distribution without any cut, is significantly different, with the tree-level ZH giving a flat distribution while the gluon-fusion one peaks at 90^0. The shape becomes similar for $p_T^Z > 100$ GeV, while a 200 GeV cut (not shown here) completely eliminates the difference. This behaviour is related to the polarisation of the Z which differs

Process	f_0 (%)	f_L (%)	f_R (%)
$gg \to ZH$	82.2	8.9	8.9
$gg \to ZH, p_T^Z > 100$ GeV	86.3	6.9	6.8
$q\bar{q} \to ZH$	35.6	32.4	32.0
$q\bar{q} \to ZH, p_T^Z > 100$ GeV	62.6	18.8	18.6

Table 2.2: Polarisation fractions for the gluon fusion and NLO Drell-Yan production mode of ZH at 14 TeV with and without a cut on the Z p_T.

between the two production modes. This can be quantified by examining the relevant polarisation fractions in Tab. 2.2, as they are defined in [165].

$$
\begin{aligned}
f_0 &= 2 - 5 \langle \cos \theta^* \rangle^2 \\
f_L &= \frac{-1}{2} - \frac{c_L^2 - c_R^2}{c_L^2 + c_R^2} \langle \cos \theta^* \rangle + \frac{5}{2} \langle \cos \theta^* \rangle^2 \\
f_R &= \frac{-1}{2} + \frac{c_L^2 - c_R^2}{c_L^2 + c_R^2} \langle \cos \theta^* \rangle + \frac{5}{2} \langle \cos \theta^* \rangle^2
\end{aligned}
\tag{2.1}
$$

where $c_R = \sin^2 \theta_w = 0.23$ and $c_L = T_3^e - Q_e \sin^2 \theta_w = -0.27$ are the left and right couplings of Z boson to fermions (see Eq. 1.42). The fact that the Z in $gg \to ZH$ is predominantly longitudinal leads to the central peak, while the small difference between f_L and f_R leads to a very mild asymmetry for $q\bar{q}$. Setting a 100 GeV cut on p_T^Z changes these values in agreement with the equivalence theorem[1], *i.e.*, by increasing the longitudinal polarisation fraction. For completeness, we also mention here that the main background for this process, $Z + b$-jets leads to predominantly left-handed Z bosons [165, 167] and therefore to different angular distributions, that could be potentially used as an additional discriminating handle to distinguish signal and background.

Further to the $gg \to ZH$ results that we have discussed above, interesting conclusions can be drawn by studying the loop-induced ZHj distributions. We have seen in Tab. 2.1 that these contributions are not negligible and their relative importance increases with the centre of mass energy. A complete NLO computation for $gg \to ZH$ would be fully inclusive in these contributions but as such a computation is not available yet, we aim to draw some conclusions by studying them independently. For such a study a minimum cut has to be set on the transverse momentum of the additional jet to avoid

---

[1]The equivalence theorem states that, at an energy $E \gg m_V$, the LO amplitude with longitudinally polarized vector bosons on mass-shell is given by the amplitude in which these vector bosons are replaced by the corresponding Higgs ghosts [166]

Figure 2.7: Invariant ZH mass and p_T^H distributions for loop-induced ZH and ZHj production at $\sqrt{s} = 14$ TeV. The results for the ZHj distributions are shown for various jet p_T cuts: 30, 50 and 100 GeV and again concern only the loop diagrams of Fig. 2.2

the divergent soft and collinear limit. We compare the distributions of the invariant mass of ZH and the p_T^H to those from $2 \to 2$ amplitudes by varying the p_T cut set on the additional jet in Fig. 2.7.

The ZH invariant mass distribution shows that for all values of the jet p_T cut the bulk of the cross-section remains close to the $2m_t$ threshold. The characteristic threshold behaviour due to the absorptive part of the amplitude remains visible for all cuts. At high invariant masses, we find that the amplitudes with an extra parton fall more slowly and overtake the $2 \to 2$ process.

In contrast to the invariant mass distribution where no extreme modification of the shape takes place, the p_T^H distribution is very much affected. First, we note that the threshold corresponding to $m_{ZH} \sim 2m_t$ is now not visible in the p_T distributions for ZHj. The second and more striking observation is that above 300 GeV the $2 \to 3$
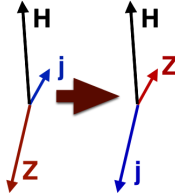
Figure 2.8: New preferred jet configuration

process leads to a much harder p_T spectrum compared to the $2 \rightarrow 2$ one. Moreover, for p_T^H values above 400 GeV all three distributions for ZHj coincide. The fact that in this region the result is insensitive to the jet p_T cut implies that hard jet emissions are dominating. This occurs because by allowing the emission of a parton new kinematic configurations open up. In this high p_T region, the kinematic configuration in which a soft jet is emitted and the Z and H basically recoil against each other is not the most favourable one. Instead, the configuration in which a hard jet recoils against the H, with the Z remaining rather soft becomes the preferred one (see Fig. 2.8). We have explicitly confirmed this behaviour by setting a high cut on the p_T of the Higgs, and studying the corresponding jet and Z transverse momentum distributions. A clear preference for the configurations where the jet is hard and the Z is rather soft is found when sufficiently far from the IR divergence. The behaviour of the $2 \rightarrow 3$ amplitudes at high p_T can be traced back to the presence of $t-$channel gluon diagram such as the $gg \rightarrow ZHg$ one shown in the top right of Fig. 2.2, which becomes dominant in this region. The same behaviour is displayed by the $qg \rightarrow ZHq$ contributions, when these are considered separately, as they include diagrams of the same type as shown in the second row of Fig. 2.2.

In conclusion, we have found that, especially for the transverse momentum distribution of the Higgs, the emission of an additional jet can dramatically modify the shape, due to new allowed kinematic configurations. This effect might prove important in studies involving highly boosted Higgs as discussed for example in [152]. The $2 \rightarrow 3$ matrix elements are important and therefore need to be taken into account for accurate simulations. To combine the two in a consistent way and therefore provide a more realistic picture of the differential distributions, we will resort to merging and matching to a parton shower. In the following section we will discuss how this method allows us to provide more accurate predictions for the distributions.

2.2.2   Merged sample results up to 1 jet

Given the lack of a complete NLO computation and the relevance of the $2 \rightarrow 3$ matrix elements, the best available procedure to accurately predict the distribution shapes is to employ the Matrix-Element–Parton Shower (ME+PS) procedure. In our study we employ the MLM shower k_T scheme as implemented in MADGRAPH5_AMC@NLO . Merged samples are then passed to PYTHIA 8 [168] for PS.

Using the setup described previously in Sec. 1.3.3 for the merging and matching, we present in this section our merged results for various observables. In our simulations we keep the H and Z stable. For the merging performed here, the shower-k_T scheme is used with $Q_{\text{cut}} = p_{T_{\min}} = 30$ GeV. We have checked that this choice leads to smooth differential jet rate distributions, and therefore a smooth transition between the ME and PS regimes.

We start by presenting the results for the invariant mass of the ZH system and the p_T of the Higgs in Fig. 2.9, while p_T^{ZH} and p_T^j distributions are shown in Fig. 2.10. A comparison is made between the $gg \rightarrow ZH$ sample showered with PYTHIA 8 and the merged 0 and 1-jet matched sample, presented in combination with the uncertainties associated with scale choices for both the factorisation/renormalisation scale of the hard process and the shower starting scale. We set the central value for the renormalisation and factorisation scales to m_{ZH}, as for the parton-level results. The shower starting scale in PYTHIA 8 can be set to either the kinematical limit ($p_T = \frac{\sqrt{\hat{s}}}{2}$), corresponding to what we refer to as *"power"–shower* or the factorisation scale of each event (m_{ZH} in our case), *i.e.*, *"wimpy"–shower*. PYTHIA 8 allows us, for the *"wimpy"-shower* case, to modify the shower starting scale in the range of $0.5\mu_F < Q_{PS} < 2\mu_F$. This gives us the possibility to systematically study the dependence of the results on the choice of the shower scale for both the merged and $gg \rightarrow ZH$-only samples, as shown by the blue bands in the plots. To study the systematic uncertainties due to renormalisation and factorisation scale variations, we vary the scales between $0.5\mu_0 < \mu_{R,F} < 2\mu_0$, with $\mu_0 = m_{ZH}$. This variation is shown by the yellow bands in the plots (with the central prediction being the *"power"-shower* result). In the results shown for m_{ZH} and p_T^H in Fig. 2.9, we also include the parton-level results for comparison purposes.

First, we notice that not all distributions are sensitive to the procedure of merging-matching. In particular, the invariant mass of the ZH system shows no shape variation. In this process, we only have initial state radiation and therefore significant changes in the shape are not expected for an observable like m_{ZH}. Other observables, on the other hand, are highly sensitive to the choice of shower parameters. The distributions for the transverse momentum of the Higgs, p_T^H, but more importantly the
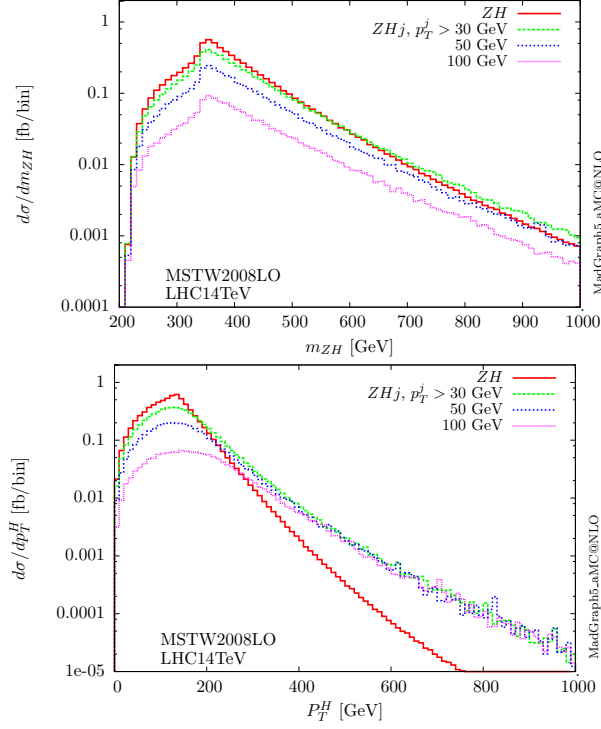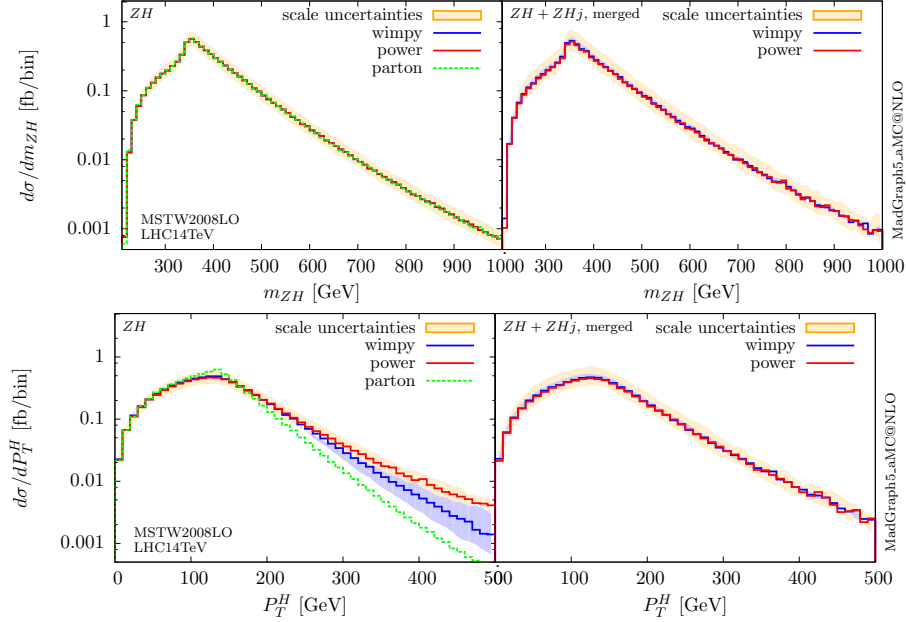
Figure 2.9: Invariant ZH mass and p_T^H distributions for gluon induced ZH production at $\sqrt{s} = 14$ TeV. The left column shows the results obtained for the $gg \to ZH$ case, with different starting scale for the shower: *"wimp"* and *"power" shower*. The blue band shows the variation of the shower scale for *"wimpy" shower* in the range $0.5\mu_F < Q_{PS} < 2\mu_F$, while the yellow bands show the uncertainty associated with a factor of two variation of the renormalisation and factorisation scales with respect to their central value. The right column shows the same results for the merged sample. The green curves in the left column correspond to the parton level results before passing them through PYTHIA 8.

transverse momentum of the ZH system, p_T^{ZH}, and that of the hardest jet, p_T^j, which are trivially zero at parton-level, depend strongly on the shower parameters. We first notice that the shower produces a p_T^H distribution harder than the parton-level one for all shower scale choices. This is related to the harder behaviour of the $2 \to 3$ distributions discussed earlier.

Another interesting observation to be made is related to the shape changes associated with the shower scale choice. The "power" shower leads to consistently harder distributions, while the "wimpy" shower gives softer distributions. The different shower predictions start to diverge in a region correlated with the invariant mass of the ZH system, as this is the factorisation scale which is taken to be the starting scale of the "wimpy" shower. The shower scale uncertainty bands become wider at larger p_T val-
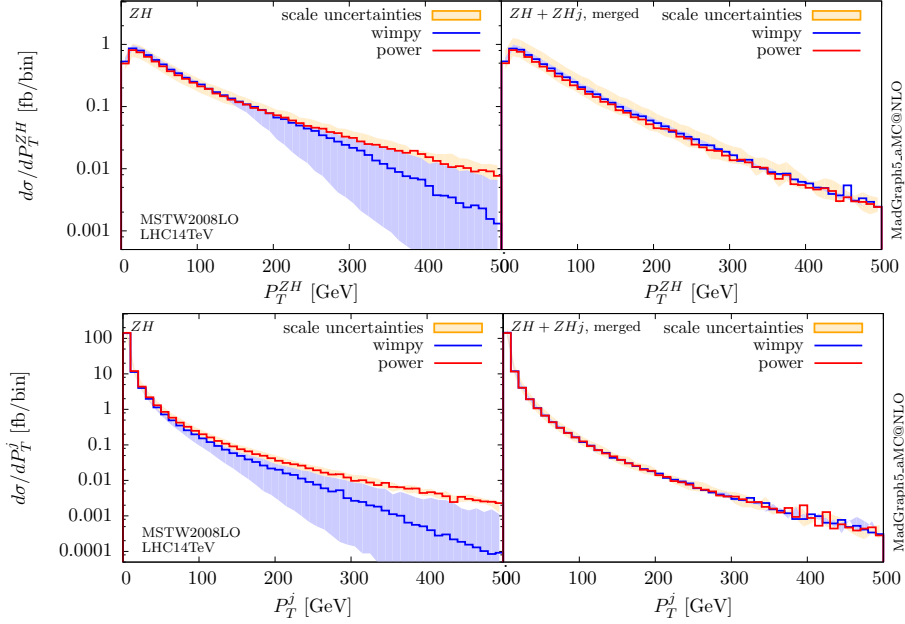
Figure 2.10: Transverse momentum of the ZH system and hardest jet p_T distributions for ZH production at $\sqrt{s} = 14$ TeV. The setup is the same as in Fig. 2.9.

ues. This is more evident in the second set of observables, p_T^{ZH} and p_T^j, for which the non-merged predictions can vary by more than one order of magnitude between different shower scale options. At high transverse momentum, the shower uncertainty becomes more important than the intrinsic QCD one associated to the factorisation and renormalisation scale choice for the hard process. We note here that despite the fact that the factorisation and renormalisation scale uncertainty is large, as evident from the yellow bands, it seems to mainly affect the normalisation of the curves.

The advantage of the ME+PS procedure is then made obvious by noticing that the shower scale uncertainty is almost completely eliminated in the merged predictions. For all observables, the shower scale uncertainty bands remain well within the corresponding renormalisation and factorisation scale uncertainty ones, even at high transverse momentum. ME+PS predictions are therefore more accurate/precise and predictive than the parton shower alone as they include the exact $2 \to 3$ matrix elements. These play an important role in the phase space regions populated by highly boosted objects which is often the case for LHC searches.
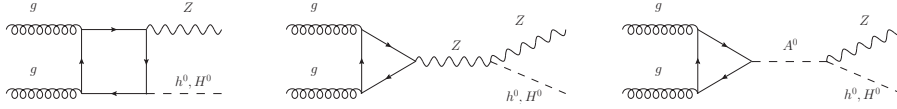
Figure 2.11: Representative Feynman diagrams for ZH^0/Zh^0 production in gluon fusion in the 2HDM.
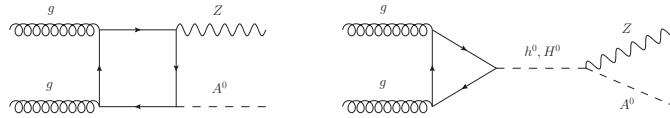
Figure 2.12: Representative Feynman diagrams for ZA^0 production in gluon fusion in the 2HDM.

2.3 Zφ production in the 2HDM

In the previous section we discussed gluon induced ZH production in the SM, employing the ME+PS merging method to improve the accuracy of the predictions for the differential distributions at the LHC. In this section, we will follow a similar approach for a BSM scenario.

Some examples of viable 2HDM scenarios will be considered in this section to explore possible 2HDM signatures in Higgs production in association with a Z boson. Interesting features can arise in this process, not only because of possible deviations of the light Higgs couplings from their SM values, but most importantly because of the presence of the heavier states, H^0 and A^0, which can lead to resonant production of $Z\phi$ final states. Three neutral combinations of final states are possible: Zh^0, ZH^0 and ZA^0. These 2HDM processes have already been discussed in [5]. Similarly to ZH production in the SM, the production of the Zh^0 and ZH^0 final states can occur through Drell-Yan type diagrams, and in gluon-gluon fusion. The Drell-Yan like cross sections can be obtained straightforwardly by the appropriate rescaling of the SM cross-sections by the ratio of the $g_{\phi ZZ}$ coupling over its SM counterpart, but the situation for the gluon fusion case is more involved. This can be inferred by considering the corresponding Feynman diagrams for the gluon fusion processes, shown in Fig. 2.11 and 2.12. The possibility of resonant production depends on the masses of A^0 and H^0, while interesting interference patterns can arise due to relative sign of the $A^0\phi Z$ couplings.

	Type	$\tan\beta$	$\cos(\beta-\alpha)$	m_{H^0}	m_{A^0}	$m_{H^\pm}$	m_{12}^2
B1	II	1.75	0.07	300	441	442	38300
B2	I	1.20	0.14	200	500	500	-60000
B3	II	1.70	0.02	350	250	350	12000

Table 2.3: Parameter choices for the different 2HDM benchmarks used in our study. All masses are given in GeV. The lightest Higgs mass is fixed in all cases to $m_{h^0} = 125$ GeV.

We stress here that several studies have been presented in the literature in particular for the A^0Z process, mostly in the context of the MSSM [169–171]. In the case of the MSSM, there are more constraints on the values of the Higgs couplings, while the 2HDM allows more freedom that can lead to more striking signals. A particularly interesting cosmologically motivated 2HDM scenario leading to a $A^0 \to ZH^0$ signature at the LHC is presented in [172], that finds very good prospects for discovery or exclusion even for the low-luminosity LHC. We also mention that various 2HDM scenarios allow significantly enhanced bottom Yukawas, and the $Z\phi$ states can be produced mainly through $b\bar{b}$ annihilation. This has been extensively discussed in the literature [170, 173, 174], and in relation with the subtleties of the treatment of the bottom quarks [175]. In this section, we will be focussing on the gluon fusion channel, presenting results for a series of 2HDM benchmarks.

2.3.1 2HDM benchmarks

The calculation setup, regarding the reweighting and the ME+PS merging procedure, follows closely that described in the previous section for the SM.

Three benchmarks will be employed to present the 2HDM results, with the corresponding parameters shown in Tab. 2.3. Here we briefly mention the main features of each benchmark. These benchmarks were chosen because they exhibit each a different mass hierarchy and have different top Yukawa couplings due to the various values of the $\tan\beta$. The values fo the relevant couplings for $gg \to Z\phi$ production are listed in Tab. 2.4 according to Tab. 1.2 and 1.3.

- **Benchmark B1**: It is a type-II 2HDM scenario with moderately heavy Higgs masses taken from benchmark H1 in Ref. [176]. Small $\tan\beta$ and $\cos(\beta - \alpha)$ values ensure that the couplings of the light Higgs boson remain SM-like with a slightly enhanced bottom Yukawa ($\mathcal{O}(10)\%$). This is also the reason why this

	$\hat{g}_{h^0 t\bar{t}}$	$\hat{g}_{h^0 b\bar{b}}$	$\hat{g}_{H^0 t\bar{t}}$	$\hat{g}_{H^0 b\bar{b}}$	$\hat{g}_{A^0 t\bar{t}}$	$\hat{g}_{A^0 b\bar{b}}$
B1	0.96	1.12	-0.64	1.68	0.57	1.75
B2	1.11	1.11	-0.68	-0.68	0.83	-0.83
B3	0.99	1.03	-0.61	1.68	0.59	1.70

	$\hat{g}_{A^0 Z h^0}$	$\hat{g}_{A^0 Z H^0}$	$\hat{g}_{ZZH^0}$	$\hat{g}_{ZZh^0}$
B1	-0.07	-0.99	-0.07	0.99
B2	0.14	-0.99	0.14	0.99
B3	-0.02	-1.00	-0.02	1.00

Table 2.4: Normalised heavy–quark Yukawa couplings and Higgs Z couplings for the different 2HDM benchmarks defined in Tab. 2.3. Yukawa couplings are normalised to their SM counterparts as discussed in Sec. 1.2.3.

benchmark evades CMS [151] and ATLAS limits [177]. This scenario allows a resonant production of both the light and Heavy Higgs with a Z boson through the decay of the pseudoscalar A^0. The sign of the Zh^0A^0 coupling determines the interference of the A^0-mediated production with the SM-like diagrams.

- **Benchmark B2**: Type-I 2HDM scenario with a relatively light heavy Higgs H^0 and a significantly heavier pseudoscalar A^0. Both light-Higgs top and bottom Yukawas are enhanced by $\sim 10\%$. The large and negative value of m_{12}^2 protects the stability of the vacuum as can be seen from the formulae in the appendix of [178] where the interplay between m_{12} and the lambda self couplings parameters is shown. This scenario also allows the resonant production of both the light and Heavy Higgs with a Z boson through the decay of the pseudoscalar A^0.

- **Benchmark B3**: Another type-II 2HDM scenario with a reversed mass hierarchy between the heavy scalar H^0 and the pseudoscalar A^0. The small $\tan\beta$ value allows us not to over-suppress the $\hat{g}_{A^0 t\bar{t}}$ coupling, while the $\hat{g}_{A^0 b\bar{b}}$ is enhanced. Thanks to the inverted mass hierarchy $m_{h^0} < m_{A^0} < m_{H^0}$ the resonant production of A^0 with a Z boson due to the heavy neutral Higgs decay becomes kinematically allowed.

	$gg \to Zh^0$	$gg \to ZH^0$	$gg \to ZA^0$
B1	$113\ ^{+30\%}_{-21\%}$	$686\ ^{+30\%}_{-22\%}$	$0.622\ ^{+32\%}_{-23\%}$
B2	$85.8\ ^{+30\%}_{-21\%}$	$1544\ ^{+30\%}_{-22\%}$	$0.869\ ^{+34\%}_{-23\%}$
B3	$167\ ^{+31\%}_{-19\%}$	$0.89\ ^{+33\%}_{-21\%}$	$1325\ ^{+28\%}_{-21\%}$
SM	$70.7^{+29\%}_{-21\%}$		

Table 2.5: Cross sections (in fb) for gluon induced Z Higgs associated production at the LHC at $\sqrt{s} = 14$ TeV for three 2HDM benchmarks. The uncertainties (in percent) refer to scale variations. No cuts are applied to final state particles and no Higgs or Z branching ratios are included.

2.3.2   2HDM results

In this section we present our results for the three 2HDM benchmarks introduced in the previous paragraph. We start by considering the total cross section for each process, which is shown in Tab. 2.5. The rest of the calculation details, such as the scale and PDF choices follow closely those of the SM calculation. We note here that where possible, we compared our results with the VH@NNLO version described in [5] and found very good agreement between the two implementations.

Before moving to the discussion of some differential results, we first comment on the results in Tab. 2.5. First we notice that the cross-section for the Zh^0 process can be significantly enhanced. To be more precise, benchmark B3 leads to a cross section nearly twice the SM prediction, benchmark B1 to a 60% enhancement, while B2 is gives a smaller $\sim$20% increase. The main source of the increase in the cross-section is the presence of the resonant decay $A^0 \to Zh^0$, which is kinematically allowed in all three scenarios. The relative change in the Zh^0 cross section is strongly correlated with the mass of the pseudoscalar and the value of the A^0Zh^0 coupling. We remind ourselves that this coupling is proportional to $\cos(\beta - \alpha)$, *i.e.*, it tends to zero in the alignment limit. For all scenarios considered here, its value remains small as seen in Tab. 2.4. Consequently, it is not possible for this process to receive extremely large contributions from the resonance. This is in contrast with what can be seen in light Higgs pair production (see Chap. 3) where the resonant decay of the heavy Higgs can lead to an enhancement of up to a factor of 60 for the $gg \to h^0h^0$ cross section [8].

The most interesting feature of Tab. 2.5, is the potential size of the cross section for the ZH^0 process. We find that this can exceed 1 pb when the pseudoscalar A^0 is sufficiently heavy to allow the resonant decay into the heavy Higgs and a Z. This

has been noticed and discussed recently in [172], as a signature for a cosmologically motivated 2HDM scenario. It is remarkable that even if the production threshold lies significantly higher, this process can lead to larger cross sections compared to the Zh^0. This is possible as the relevant coupling, $\hat{g}_{ZH^0A^0}$, as shown in Tab. 2.4, is not suppressed by the "SM-like" light Higgs constraints. Despite the fact that the prospects for discovery depend strongly on the resulting decay products of the heavy Higgs, it is worth noting that even in the scenarios where H^0 decays predominantly into $b\bar{b}$, the current experimental searches for ZH set a cut on the invariant mass of the $b\bar{b}$ pair close to the light Higgs mass and would therefore miss this signal. Finally, we note that the ZA^0 production cross section remains very small in the scenarios where the A^0 is heavier than H^0, but can reach the picobarn level in a scenario such as benchmark B3, as a result of the inverted mass hierarchy.

Further interesting information on these processes can be extracted from the differential distributions. For brevity we present only those for the invariant mass of the system and the transverse momentum of the Higgs, but our setup is fully differential and any distribution can be plotted. We show these in Fig. 2.13, for the cases in which the cross section is not negligible. The results shown here are obtained with merged samples of 0 and 1-jet matched to PYTHIA 8 for parton shower, in the same setup as that described in Sec. 2.2 for the SM.

For the Zh^0 final state we also show the SM prediction for comparison. Resonance peaks arise in all scenarios for Zh^0, each time located at the mass of the pseudoscalar A^0. The sharpness of the peak varies with the mass of A^0, as heavier A^0 have larger widths going from 0.01 GeV for B3, to 7 GeV for B1 and 35 GeV in B2. We also notice various interesting interference patterns, clearly visible for benchmarks B1 and B2. The A^0-mediated diagram interferes with the SM-like amplitude, with the interference switching sign at $\sqrt{s} = m_{A^0}$. Comparing scenarios B1 and B2, we see that the Zh^0A^0 couplings have opposite signs and therefore in one case the dip appears right before the resonance peak, and in the other right after. More subtle features are also visible in the plots away from the resonance peaks. These features can always be traced back to the 2HDM parameters and the value of the relevant couplings as shown in Tab. 2.4. One such example is the fact that the B2 m_{Zh^0} curve lies a bit lower than the SM one in the region below 350 GeV, which can be linked to the enhanced top Yukawa leading to a bigger box contribution. The box is in turn interfering destructively with the triangle leading to a smaller total amplitude for the $gg \rightarrow Zh^0$ process.

For the ZH^0 process, only the two benchmarks that give measurable cross sections are shown. The plots shown for this process are dominated by the resonant decay of A^0. This is more obvious in the B1 curve as the resonant peak is closer to the threshold.
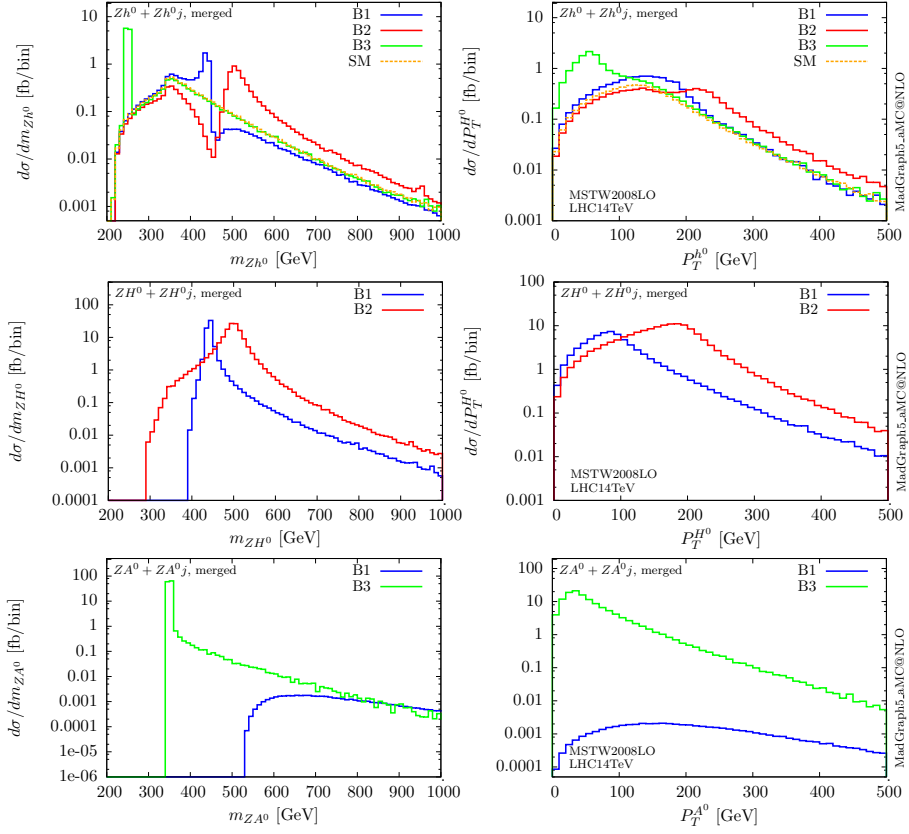
Figure 2.13: Differential distributions for gluon induced Zh^0, ZH^0 and ZA^0 production at $\sqrt{s} = 14$ TeV for the three 2HDM benchmarks and comparison with the SM. Left: Invariant mass of the $Z\phi$ system. Right: Transverse momentum of the Higgs.

Scenario B2 receives some non-negligible off-peak contributions from the Z triangle and box diagrams, which in this case interfere constructively, as the H^0 top Yukawa sign is flipped. For B1 both the top Yukawa and ZZH^0 couplings signs are flipped, therefore the interference between triangle and box is destructive, and the result in the tails away from the resonant peaks, is suppressed compared to B2.

The situation is less complicated for ZA^0 for which in B3 a resonance very close to the $m_Z + m_{A^0}$ threshold dominates the plots, while the cross sections for B1 and B2 are extremely suppressed as no resonant decay is kinematically allowed. Moreover the production of a rather heavy ZA^0 pair probes the gluon luminosity at large partonic x values and is therefore suppressed.

2.4 Conclusions

An important process to be more precisely measured at the LHC is the associated production of a Higgs with a Z boson. In addition to the Drell-Yan type contributions, this process acquires a gluon fusion component at NNLO, which proves to be of particular importance in the boosted regime. In this chapter, we have reviewed the main features of the $gg \rightarrow ZH$ process, both at the matrix-element and cross-section level. We have examined the behaviour and the relative importance of the $2 \rightarrow 2$ and $2 \rightarrow 3$ matrix elements for the gluon induced component. We have found that in the high p_T regions the $2 \rightarrow 3$ matrix elements behave in a different way from the $2 \rightarrow 2$ ones and therefore have to be taken into account to provide accurate predictions for the differential distributions. To achieve this, we have combined the two in a consistent way, by merging different jet multiplicity samples and matching them to a parton shower.

Our results have been obtained within the MADGRAPH5_AMC@NLO framework with the help of PYTHIA 8 for the parton shower. The ME+PS approach provides a more accurate description of the process compared to the parton shower alone. In particular, it significantly reduces the uncertainty associated with the shower scale choice. For observables such as the transverse momentum of radiated jets in the hard region, the prediction of the parton shower alone can be misleading as here the results are extremely sensitive to the shower parameters. We find that in the merged predictions this sensitivity is almost completely eliminated, with the shower uncertainty remaining well within the intrinsic QCD uncertainty due to the renormalisation and factorisation scale variations.

The reduction of the uncertainties associated with the SM prediction and especially the accurate description of differential distributions is crucial for searches for beyond the SM scenarios. One scenario that the LHC aims to explore is the 2HDM. In this chapter, we have also provided predictions for the gluon fusion component of the $Z\phi$ associated production in the 2HDM. Following the same setup as in the SM, we have presented our predictions for three representative 2HDM benchmarks. We have considered all three neutral Higgs bosons, presenting results for the cross sections and the differential distributions.

In the production of the light Higgs in association with a Z, large enhancements can be achieved compared to the SM prediction if the resonant decay of the pseudoscalar A^0 is kinematically allowed. Moreover, interference patterns arise between the additional diagrams and the SM-like ones, leading to interesting features in the differential distributions. The resonant production of a $H^0 Z$ pair also becomes important as the $H^0 Z A^0$ coupling is not suppressed, leading to large cross sections for $gg \rightarrow ZH^0$ if the pseudoscalar A^0 is heavier then H^0. Finally in scenarios where the pseudoscalar

A^0 is lighter than the heavy Higgs, $gg \to H^0 \to ZA^0$ production is allowed and leads to large cross sections in still-to-be-excluded scenarios.

Chapter 3

Higgs pair production via gluon fusion in the 2HDM

"Whether you can observe a thing or not depends on the theory which you use. It is the theory which decides what can be observed."

Albert Einstein (1879 - 1955)

3.1 Introduction

At present, the experimental reconstruction of the Higgs potential is a major step towards the fundamental understanding of the EW symmetry breaking mechanism. This task can be fully accomplished through the direct measurement of the Higgs boson three–point and four–point interactions [179, 180] or via an alternative method relying on the precision effects of electroweak loops featuring an anomalous trilinear coupling that would imprint on single Higgs production at the LHC [181]. In this chapter we focus on multiple Higgs boson production processes which are instrumental in this endeavour, not only because they directly depend on the Higgs self–couplings, but also because they are sensitive to possible new heavier states and/or to higher–dimensional operators [67, 68, 182–184]. Extracting the Higgs self–couplings from collider data is known to be an arduous task [185, 186]. While the triple Higgs rates lie beyond the reach of the LHC capabilities [187, 188], the prospects of measuring Higgs pair pro-

duction are better, but still challenging. There are multiple production channels which lead to Higgs boson pairs at hadron colliders, including vector boson fusion; associated production with gauge bosons and heavy quarks; and gluon fusion. The latter is dominant in the SM and gives an approximate next–to–leading order (NLO) cross section of approximately 35 fb at the 14 TeV LHC [71]. Recent studies [68,155,189–192] have investigated the potential of digging out the di–Higgs signal over its backgrounds in various Higgs decay channels, among them $\gamma\gamma b\bar{b}$, $W^+W^-b\bar{b}$, $b\bar{b}\tau^+\tau^-$ and $b\bar{b}b\bar{b}$, assisted e.g. by jet substructure techniques. The current picture is that, aside from potential new physics effects, the extraction of the coupling g_{hhh} will require copious integrated luminosity. Optimistic estimates point towards values of 3000 fb^{-1} at 14 TeV in order to reach an accuracy of $\sim 40\%$ [193]. The reason is not only the rather modest total rate, but also the limited sensitivity to the trilinear coupling g_{hhh} and the large theoretical uncertainties. With this research program ahead, accurate predictions for the total and differential di–Higgs rates are in order – for the SM and beyond, while more sophisticated experimental analyses are required to explore the precise reach of the LHC.

In this chapter we investigate the phenomenological possibilities of Higgs pair production via gluon fusion in and beyond the SM. Many BSM physics models with SM-compatible single Higgs boson signal strengths can exhibit a di-Higgs phenomenology vastly different from the SM expectation. We resort to the 2HDM as an illustrative new physics framework, and present results for all seven combinations of 2HDM Higgs pair final states. We compute the total and differential Higgs pair rates at NLO accuracy in QCD, matched to the PYTHIA8 parton shower (PS) with the MC@NLO method. The dedicated reweighting strategy described in Sec. 1.3.2 is employed to improve the NLO calculation beyond the infinite top–mass limit, by also employing the exact real–emission matrix elements. The results presented here improve upon, and further extend, the earlier studies in the literature. To the best of our knowledge, this work provided for the first time NLO+PS event samples for these processes, which can be readily used for realistic simulations, including those at the detector level once the Higgs bosons are allowed to decay. Accurate predictions for the differential rates are also important, as they can be used to identify the distinctive properties of the signal kinematics and compare them to the backgrounds. This is e.g. instrumental in the context of jet substructure techniques [68, 184], which are known to improve upon the more traditional search strategies based on inclusive observables.

The remainder of this chapter is organized as follows. Sec. 3.2.1 defines a series of 2HDM benchmark scenarios, which are constructed to cover all representative phenomenological features of the model. In Sec. 3.2.2 we move on to describe the theoretical structure of Higgs pair production at leading and next–to–leading order. In the second part of the chapter we present a comprehensive numerical analysis of all Higgs

	Type I	Type II
$\hat{g}_{h^0 t\bar{t}}$	$1 + \xi/\tan\beta - \xi^2/2$	$1 + \xi/\tan\beta - \xi^2/2$
$\hat{g}_{h^0 b\bar{b}}$	$1 + \xi/\tan\beta - \xi^2/2$	$1 - \xi\,\tan\beta - \xi^2/2$
$\hat{g}_{H^0 t\bar{t}}$	$-1/\tan\beta + \xi + \xi^2/(2\tan\beta)$	$-1/\tan\beta + \xi + \xi^2/(2\tan\beta)$
$\hat{g}_{H^0 b\bar{b}}$	$-1/\tan\beta + \xi + \xi^2/(2\tan\beta)$	$\tan\beta + \xi - \xi^2/2\,\tan\beta$

Table 3.1: Heavy–quark Yukawa couplings to the light (heavy) $\mathcal{CP}$–even Higgs bosons for type I and type II 2HDM. Their decoupling behavior is given in terms of the expansion parameter $\xi \equiv \cos(\beta - \alpha)$ up to $\mathcal{O}(\xi^3)$.

pair production channels within the 2HDM. Total rates are documented and discussed in Sec. 3.3.2, while in Sec. 3.3.3 we focus on the light di–Higgs differential distributions. We then look at up-to-date predictions for Higgs pair and triple production in the SM in Sec. 3.4 and finally, we summarize and conclude in Sec. 3.5.

3.2 Phenomenological framework

3.2.1 2HDM Benchmarks

The decoupling condition $\xi \ll 1$ correlates the two mixing angles through the rough approximations

$$\sin^2\alpha \sim \frac{1}{1 + \tan^2\beta} \qquad \text{or} \qquad \xi \sim \frac{2\tan\beta}{1 + \tan^2\beta} \; . \tag{3.1}$$

The right formula is obtained from the first one by performing Taylor expansions and dropping higher order terms. The behavior of the relevant Higgs interactions in the decoupling limit is explicitly shown in Tab. 3.1 and Eq. 3.2. Notice that even for $\xi \ll 1$ some of the couplings may be substantially shifted. This behavior appears for instance in the $\tan\beta \gg 1$ ($\tan\beta \ll 1$) regimes (delayed decoupling) [194] ($\cos(\beta - \alpha)\tan\beta \sim \mathcal{O}(1)$). As for the Yukawa couplings, these shifts may be more (in type–I) or less (in type–II) correlated within each fermion generation and can lead to enhanced, suppressed, or even sign–flipped couplings [195].

$$\lambda_{h^0 h^0 h^0} = 3m_{h^0}^2 + \xi^2 \left[\frac{9m_{h^0}^2}{2} - \frac{12m_{12}^2}{\sin 2\beta} \right]$$

$$\lambda_{h^0 h^0 H^0} = -\xi \left(2m_{h^0}^2 + m_{H^0}^2 - \frac{8m_{12}^2}{\sin 2\beta} \right) - \frac{2\xi^2}{\tan 2\beta} \left(2m_{h^0}^2 + m_{H^0}^2 - \frac{6m_{12}^2}{\sin 2\beta} \right)$$

$$\lambda_{H^0 H^0 h^0} = m_{h^0}^2 + 2m_{H^0}^2 - \frac{4\,m_{12}^2}{\sin 2\beta} + \frac{2\xi}{\tan 2\beta} \left(m_{h^0}^2 + 2m_{H^0}^2 - \frac{6m_{12}^2}{\sin 2\beta} \right)$$

$$+ \; \xi^2 \left(\frac{14m_{12}^2}{\sin 2\beta} - \frac{5}{2} (m_{h^0}^2 + 2m_{H^0}^2) \right)$$

$$\lambda_{H^0 H^0 H^0} = \frac{-6}{\tan 2\beta} \left[m_{H^0}^2 - \frac{2m_{12}^2}{\sin 2\beta} \right] + \xi \left(9m_{H^0}^2 - \frac{12\,m_{12}^2}{\sin 2\beta} \right)$$

$$+ \; \frac{3\xi^2}{\tan 2\beta} \left(3m_{H^0}^2 - \frac{6m_{12}^2}{\sin 2\beta} \right) \tag{3.2}$$

The decoupling behaviour of the triple Higgs self–interactions involving the neutral $\mathcal{CP}$–even Higgs fields in the 2HDM are given in Eq. 3.2 in terms of the expansion parameter ξ up to $\mathcal{O}(\xi^3)$. They are normalized as $\lambda_{\phi\phi\phi} \equiv i\,v\,g_{\phi\phi\phi}$, with the SM Higgs self–coupling being $g_{HHH}^{\mathrm{SM}} = -3im_H^2/v$. The triple Higgs self–coupling $g_{h^0 h^0 h^0}$ may be enhanced by up to 100% above the SM in type–I models – while for type–II, LHC data favours $g_{h^0 h^0 h^0} \lesssim g_{HHH}^{\mathrm{SM}}$ with allowed suppressions up to $\mathcal{O}(50)\%$ [196]. Let us also note that in the exact alignment limit, see Eq. 3.3, the light Higgs trilinear coupling becomes $g_{h^0 h^0 h^0} \to g_{HHH}^{\mathrm{SM}}$ and $g_{H^0 h^0 h^0} \to 0$ while the others couplings can be substantially shifted. The potentially large Higgs self–coupling deviations constitute a genuine trait of the 2HDM, with no counterpart in e.g. the Higgs sector of the MSSM. In the latter case, SUSY relates all Higgs self–couplings to the gauge couplings, implying that their size becomes restricted.

$$\lambda_{h^0 h^0 h^0} = 3m_{h^0}^2$$

$$\lambda_{h^0 h^0 H^0} = 0$$

$$\lambda_{h^0 XX} = m_{h^0}^2 + 2m_X^2 - \frac{2m_{12}^2}{\cos\beta \sin\beta}, \quad \text{for } X = H^0, A^0, H^\pm$$

$$\lambda_{H^0 H^0 H^0} = 3(\tan\beta - \cot\beta) \left(m_{H^0}^2 - \frac{m_{12}^2}{\cos\beta \sin\beta} \right)$$

$$\lambda_{H^0 XX} = (\tan\beta - \cot\beta) \left(m_{H^0}^2 - \frac{m_{12}^2}{\cos\beta \sin\beta} \right), \quad \text{for } X = A^0, H^\pm \tag{3.3}$$

	Type	$\tan\beta$	α/π	m_{H^0}	m_{A^0}	$m_{H^\pm}$	m_{12}^2
B1	II	1.75	-0.1872	300	441	442	38300
B2	I	1.20	-0.1760	200	500	500	-60000
B4	II	1.50	-0.2162	700	701	670	180000
B5	II	2.22	-0.1397	200	350	350	12000
B6	I	20.00	0.0000	200	500	500	2000
B7	II	10.00	-0.0382	500	500	500	24746
B8	II	10.00	0.0323	500	500	500	24746

Table 3.2: Parameter choices for the different 2HDM benchmarks used in our study. All masses are given in GeV. The lightest Higgs mass is fixed in all cases to $m_{h^0} = 125$ GeV.

	$\hat{g}_{h^0 tt}$	$\hat{g}_{h^0 bb}$	$\hat{g}_{H^0 tt}$	$\hat{g}_{H^0 bb}$	$\hat{g}_{A^0 tt}$	$\hat{g}_{A^0 bb}$	$\hat{g}_{h^0 h^0 h^0}$	$\hat{g}_{H^0 h^0 h^0}$
B1	0.958	1.118	-0.639	1.677	0.571	1.75	0.956	-0.317
B2	1.108	1.108	-0.684	-0.684	0.833	-0.833	1.324	-1.542
B4	0.935	1.132	-0.755	1.403	0.667	1.50	0.592	-2.058
B5	0.993	1.035	-0.466	2.204	0.450	2.22	0.999	-0.019
B6	1.001	1.001	0	0	0.05	-0.05	0.995	0.042
B7	0.998	1.203	-0.120	9.978	0.1	10	0.986	-0.346
B8	0.999	-1.018	0.102	9.998	0.1	10	0.991	-0.951

Table 3.3: Normalized heavy–quark Yukawa and trilinear Higgs self–couplings for the different 2HDM benchmarks defined in Tab. 3.2. All couplings are normalized to their SM counterparts.

These rich phenomenological possibilities are captured by the set of 2HDM benchmark scenarios which we introduce in Tab. 3.2. Two of them were already used in our ZH investigation while the other five are new. They have been designed to exhibit different trilinear couplings, small changes of the top Yukawa couplings and various mass scales. We employ them further down in Sec. 3.3 to examine the distinctive 2HDM signatures on the Higgs pair production observables. Note the impact of the m_{12}^2 parameters on the trilinear couplings, as can be seen in Eq. 3.2.

In Tab. 3.3 we quote the numerical values for all the Yukawa couplings and for the Higgs self–couplings which are relevant to the light Higgs pair production for all seven 2HDM benchmarks defined in Tab. 3.2. Their expression can be found in Tab. 1.2 and Eq. 3.2. Note that in Tab. 3.1 we expressed these couplings in term of ξ as it is

more easy to infer what happens in the alignment limit, on which all our benchmarks relies. The key physics properties of the different 2HDM scenarios are summarized as follows:

- **B1: Moderate mass hierarchy -** It corresponds to a type II 2HDM with moderate (viz. $300 - 500$ GeV) heavy Higgs masses. The small values of $\tan\beta$ and $\cos(\beta - \alpha)$ lead to an $\mathcal{O}(5)\%$ suppression in the triple Higgs self coupling As we will show in Sec. 3.3, the major new physics effects in this case originate from the resonant heavy Higgs–mediated contribution $gg \to H^0 \to h^0 h^0$. These effects are particularly enhanced here due to the dominant heavy Higgs cascade decay $H^0 \to h^0 h^0$, whose branching fraction is $\mathrm{BR}_{h^0 h^0} \simeq 0.6$.

- **B2: Enhanced triple Higgs self–coupling –** we assume i) type–I Yukawa couplings, for which the LHC Higgs signal strength imposes weaker constraints; ii) a small $\tan\beta$ value; iii) a value of ξ for which the Higgs coupling to the gauge bosons $g_{hVV} \sim \sin(\beta - \alpha) \sim 1 - \xi^2/2$ is reduced by $\sim \mathcal{O}(1)\%$; iv) a soft–breaking mass term close to the unitarity limit. Such parameter setup leads to an $\mathcal{O}(30)\%$ enhancement for the light Higgs triple self–coupling, and of $\mathcal{O}(10)\%$ for the heavy quark Yukawas. The relatively low mass $m_{H^0} < 2m_{h^0}$ prevents the resonant heavy Higgs production and allows to better access the genuine model–specific imprints on the di–Higgs production observables.

- **B4: Large mass hierarchy -** taken from benchmark a.1 in Ref. [176]. At variance with the B1 scenario above, all of the additional Higgs bosons have in this case masses of $\mathcal{O}(700)$ GeV, so that they effectively decouple. The very large Z_2 soft–breaking term m_{12}^2 is responsible for the $\mathcal{O}(40)\%$ suppression of the trilinear Higgs self–coupling $\hat{g}_{h^0 h^0 h^0}$, while at the same time it enlarges $\hat{g}_{H^0 h^0 h^0}$.

- **B5: Non–resonant SM limit -** in which the relatively light $\mathcal{CP}$–even Higgs companion $m_{H^0} = 200\,\mathrm{GeV} < 2\,m_{h^0}$ precludes the resonant production $gg \to H^0 \to h^0 h^0$. The parameter choice is inspired by the benchmarks of class [c] from Ref. [176]. They are characterized by a rather light Higgs spectrum, along with moderate values for $\tan\beta$ and m_{12}^2. The Yukawa interactions are once again fixed according to a type–II setup. The resulting coupling patterns in this case are SM–like for the lightest Higgs field, with mild deviations not larger than 1%. For the heavy neutral field H^0 we find a suppressed (resp. enhanced) Yukawa coupling to the top (resp. bottom) with opposite signs, and a strongly reduced trilinear coupling $g_{H^0 h^0 h^0}$.

- **B6: Fermiophobic heavy Higgs –** a situation which can only be accomplished in type–I models for $\sin\alpha = 0$. On the one hand, compatibility with the LHC

Higgs signal strength enforces $\xi \ll 1$, meaning that these scenarios are only viable at large $\tan\beta$, according to Eq. (3.1). The value of m_{12}^2 is tailored to fulfill the vacuum stability and unitarity bounds, which become very tight at large $\tan\beta$. Notice that for $\xi \ll 1$ the (relatively low–mass) heavy Higgs H^0 hardly couples to the gauge bosons and the light Higgs h^0, while by construction it cannot couple to any fermion either. Consequently, in this case there is no heavy Higgs contribution to the light di–Higgs production $gg \to H^0 \to h^0 h^0$.

- **B7 and B8: Enhanced and sign–flipped bottom Yukawa –** both instances are possible in type–II models at large $\tan\beta$, where the bottom Yukawa coupling $g_{h^0bb} = (1 - \xi \tan\beta) \, g_{Hbb}^{\mathrm{SM}}$ may yield either $g_{h^0bb} \simeq -g_{Hbb}^{\mathrm{SM}}$ or $g_{h^0bb} > g_{Hbb}^{\mathrm{SM}}$, in correspondence to the two branches $\sin\alpha > 0$ and $\sin\alpha < 0$ along the decoupling condition of Eq. (3.1). The possibility of a strongly modified bottom Yukawa, with all of the remaining couplings being SM–like, is a trademark property of the 2HDM [195], and relies on the *delayed decoupling* behavior mentioned earlier [194]. A similar mechanism occurs for top Yukawa coupling to H^0 when $\tan\beta < 1$, although this situation is in practice disfavored by the flavor constraints.

3.2.2   Higgs pair production in the 2HDM

The pair production of Higgs bosons at hadron colliders can proceed via weak gauge boson fusion [197, 198], double Higgs–strahlung off the W and Z bosons [199], and gluon fusion [69, 200]. Because of the large gluon luminosity in the high–energy proton beams, the gluon gluon fusion channel dominates. Predictions for the SM are known at NLO [70] and NNLO [201] in QCD, both in the infinite top–mass effective theory. Further studies have reported on the subleading $\mathcal{O}(1/m_t^2)$ terms [202], threshold resummation [203], as well as on gluon fusion results merged to one jet [156]. More recently, predictions for all Higgs pair production channels at NLO and matched to parton showers have been presented in Ref. [71]. These studies conclude that higher–order effects are large, especially for the dominant gluon fusion channel, and that including them significantly reduces the theoretical uncertainties.

In this study we focus on the Higgs pair production in the 2HDM, and consider the seven possible final–state double Higgs combinations. These may be sorted out into the following three categories:

1. Neutral Higgs boson pairs: $h^0 h^0, h^0 H^0, H^0 H^0, A^0 A^0$.
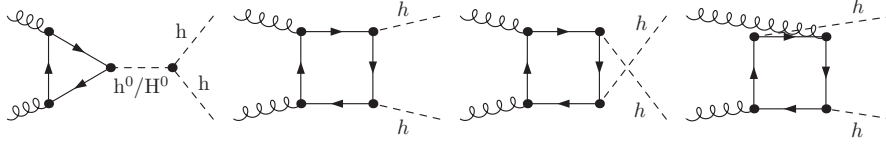
Figure 3.1: Generic Feynman diagrams describing the production of neutral Higgs boson pairs ($h = h^0, H^0, A^0$) in the 2HDM through gluon fusion at leading order. The Feynman diagrams have been generated using FEYNARTS.STY [204].
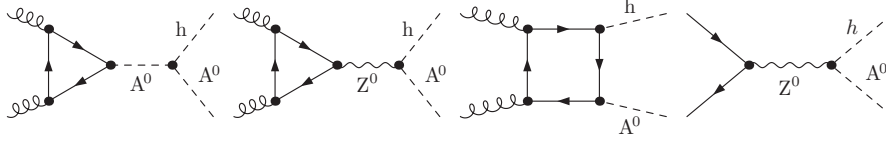
Figure 3.2: Generic Feynman diagrams describing the production of mixed $\mathcal{CP}$–even / $\mathcal{CP}$–odd neutral Higgs boson pairs [$h^0 A^0, H^0 A^0$] in the 2HDM at leading order. We separately show the two possible partonic initial–states i) gluon fusion (left, center); ii) $q\bar{q}$ annihilation (right–most).

   2. Mixed $\mathcal{CP}$–even/$\mathcal{CP}$–odd neutral Higgs boson pairs: $h^0 A^0, H^0 A^0$.

   3. Charged Higgs boson pairs: $H^+ H^-$.

There are two LO mechanisms contributing to the gluon fusion di–Higgs channels $pp(gg) \to hh$ (with $h = h^0, H^0, A^0$), whose generic Feynman diagrams we display in Fig. 3.1. These correspond to:

   1. Triangle topologies, which give rise to $\mathcal{O}(G_F \, \alpha_s \, \hat{g}_q)$ contributions through the s–channel exchange of a neutral Higgs boson. The Higgs boson couples to the gluons via the usual heavy–quark loops.

   2. Box topologies, which contribute at $\mathcal{O}(G_F \, \alpha_s \, \hat{g}_q^2)$ through the virtual heavy quark exchange.

While the triangle topologies have a linear dependence in the Yulawa and Higgs self–coupling, the boxes are quadratic in the former. In the SM, and similarly to what happened to ZH, the two topologies interfere destructively. This effect is particularly strong near the threshold as seen in Fig. 3.3 or Ref. [205] and explains in part why the total rates are quite modest. One additional destructive interference arises between the
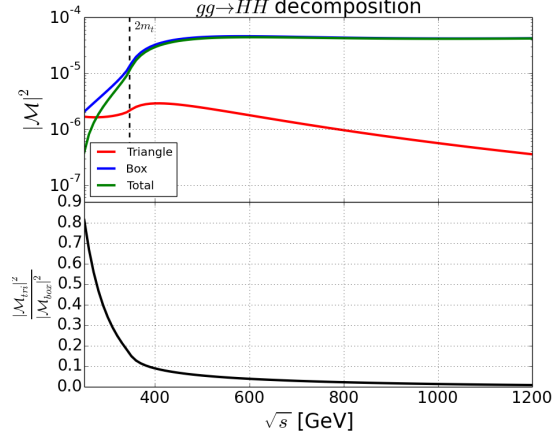
Figure 3.3: Top: amplitude squared for the triangle and box contribution in HH production. Bottom: ratio of triangle contribution over the box one.

top and bottom–mediated loops, although the bottom quark effects are very small in the SM.

For category 2), we have additional tree–level contributions for which a quark-antiquark pair annihilates into a virtual Z–boson (cf. the right–most diagram in Fig. 3.2). For the charged Higgs boson pairs of category 3), also the photon exchange from the $q\bar{q}$– annihilation contributes. The relative size of these $q\bar{q}$–initiated subchannels is quantified in Sec. 3.3.2.

To gain further insight into the structure of the (loop–induced) gluon fusion mechanism, let us focus on the neutral $\mathcal{CP}$–even Higgs pairs of category 1). The partonic cross–section at leading order may be written as

$$\frac{d\hat{\sigma}(gg \rightarrow h_i h_j)}{d\hat{t}} = c_{ij} \frac{G_F^2 \alpha_s^2}{2^8 (2\pi)^3} \left\{ \left| \sum_{\substack{q=t,b \\ h=h^0, H^0}} \left(\frac{g_{hqq} v}{m_q} \times \frac{g_{h\, h_i\, h_j}\, v}{s - m_h^2 + i\, m_h\, \Gamma_h} \right) F_\triangle(\hat{s}) \right. \right.$$

$$\left. \left. + \frac{g_{h_i\, qq}\, g_{h_j\, qq}\, v^2}{m_q^2} F_\square(\hat{s}, \hat{t}, \hat{u}) \right|^2 + \left| \sum_{q=t,b} \frac{g_{h_i\, qq}\, g_{h_j\, qq}\, v^2}{m_q^2} G_\square(\hat{s}, \hat{t}, \hat{u}) \right|^2 \right\} \quad (3.4)$$

The functions $F_\triangle$ was already introduced in Eq. 1.76, while $F_\square$ and $G_\square$ denote the one–loop gauge–invariant form factors from the box contribution, and depend on the

Mandelstam kinematical invariants and the quark and Higgs masses. Their expression can be found in the appendix of [69]. The variable $\hat{t}$ corresponds to the momentum transfer squared from one of the incoming initial–state gluons to one of the Higgs bosons in the final state. The sum over the neutral $\mathcal{CP}$–even Higgs fields $h = h^0, H^0$ accounts for the respective Higgs–mediated triangle topologies. Notice that the s–channel exchange of the $\mathcal{CP}$–odd Higgs A^0 is forbidden by $\mathcal{CP}$–conservation. The model–dependent Yukawa couplings are related to their SM counterparts through the coupling shifts quoted in Tab. 3.1.

Finally, the symmetry factor $c_{ij} = 1/2\,(1)$ for $i = j\,(i \neq j)$ properly accounts for the cases with identical (different) final–state particles. The overall normalization of Eq. 3.4 is consistent with the notation of Ref. [69]. The corresponding hadronic cross section is obtained by convoluting Eq. 3.4 with the gluon luminosities.

The two box form factors $F_\square, G_\square$ correspond to the two possible S–wave and D–wave contributions. These are linked to equal (resp. opposite) gluon helicities, which respectively add to a total angular momentum $J_z = 0$ (resp. $J_z = 2$) along the collision axis. Instead, the triangle diagrams only contribute for $J_z = 0$ and hence give rise to a single form factor $F_\triangle$. The large (resp. low) mass limits of the loop form factors read [69]:

$$F_\triangle^t = \frac{2}{3} + \mathcal{O}(\hat{s}/m_t^2); \qquad F_\triangle^b = -\frac{m_b^2}{\hat{s}} \left[\log\left(\frac{m_b^2}{\hat{s}}\right) + i\pi \right]^2 + \mathcal{O}(m_b^2/\hat{s})$$

$$F_\square^t = -\frac{2}{3} + \mathcal{O}(\hat{s}/m_t^2); \qquad F_\square^b = \mathcal{O}(m_b^2/\hat{s})$$

$$G_\square^t = \mathcal{O}(\hat{s}/m_t^2); \qquad\qquad G_\square^b = \mathcal{O}(m_b^2/\hat{s}) \tag{3.5}$$

The opposite signs for these form factors reflect the negative interference patterns between i) boxes and triangles; ii) top and bottom–mediated loops.

The Higgs pair total rates and distribution shapes are determined by the size and relative signs of these different loop–induced contributions, and the way they interplay according to Eq. 3.4. The results are thereby sensitive to the underlying 2HDM dynamics. For instance, sign–flipped couplings may revert the partial cancellation between the triangle and the box loops. The possible variations in the Yukawa and the Higgs self–couplings may either enhance or suppress these interference patterns. If kinematically allowed, the on–shell production of a heavy neutral $\mathcal{CP}$–even Higgs through the heavy top triangle, followed by the cascade decay $H^0 \to h^0 h^0$, will overwhelm the SM expectations. All these cases will be examined in Sec. 3.3 with the help of the different 2HDM benchmark scenarios defined in Tab. 3.2.
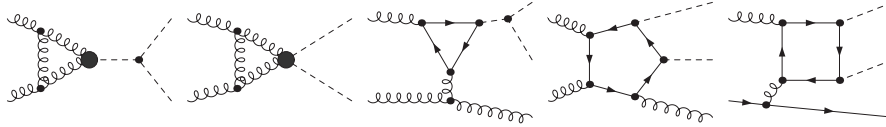
Figure 3.4: Sample Feynman diagrams describing the production of neutral Higgs pairs (h^0, H^0) via gluon fusion at next–to–leading order in the 2HDM. The shaded blobs denote the effective Higgs couplings to the gluons in the HEFT approach.

3.2.3 Next–to–leading order corrections

The NLO QCD corrections arise at $\mathcal{O}(\alpha_s^3)$ and are obviously linked to the color charges of the initial partons. They originate from i) virtual gluon exchange; and ii) light parton radiation. The NLO virtual corrections to $gg \to hh$ are intrinsically a two–loop effect, and, as already stated, have only been computed recently. As an alternative, Higgs pair production studies at NLO and NNLO [70, 201] resorted to the HEFT framework.

A selection of the Feynman diagrams describing the relevant NLO QCD effects are illustrated in Fig. 3.4. The NLO virtual corrections in the HEFT picture are obtained from one–loop topologies, as shown by the first two Feynman diagrams of Fig. 3.4. The shaded blobs denote the effective three–point and four–point Higgs couplings to the gluons. In our calculation, these HEFT virtual corrections are combined with the exact $2 \to 3$ real–emission amplitudes (cf. the right–most diagrams in Fig. 3.4) as an alternative to the more traditional approach, which only uses the exact LO result to improve upon the infinite top–mass limit. Further details are provided in Sec. 1.3.2. Aside from the leading–order gg–initiated partonic subchannel, notice that for the NLO real–emission contributions also the mixed qg fusion channels open up.

3.3 2HDM results

3.3.1 Numerical setup

As already mentioned, the HEFT description from Eq. (1.51) relies on the infinite top–mass approximation and thereby has a limited validity. In this section, we compare the Higgs pair total rate predictions obtained within the *"born–improved"* (in which only the exact one–loop $2 \to 2$ LO matrix elements are used for reweighting) and the *"loop–improved"* methods (with both the exact $2 \to 2$ LO matrix elements and

the exact one–loop $2 \rightarrow 3$ real–emission matrix elements used to reweight the HEFT results), while for the differential rates we concentrate on the "loop-improved" results.

The validity of the approximation is nonetheless limited, not only because the top quark mass is not parametrically large as compared to the other relevant scales of the process, but also because of the enhanced bottom–quark contributions which are possible in the 2HDM. Given that the low–energy theorems do not hold for bottom–mediated loops, we expect the HEFT virtual results for certain 2HDM configurations to be less reliable than in the SM case. Let us also note that, for the gg–induced production of the mixed $\mathcal{CP}$– even/$\mathcal{CP}$– odd pairs, the NLO virtual corrections must again be approximated by the one–loop HEFT results. As for the s–channel Z–mediated contributions in the latter cases, we use the same factorized form as for the A^0–mediated ones, which is exact in the $m_t \rightarrow \infty, m_b \rightarrow 0$ limit as discussed in Ref. [70]. Concerning the NLO real–emission corrections, in all these channels we include the full set of non–zero Feynman diagrams contributing to $gg \rightarrow gh^0 A^0/H^0 A^0$, among them the box diagrams of the form $gg \rightarrow gZ^* \rightarrow gh^0 A^0/H^0 A^0$. The latter were not included in the analysis of Ref. [70], as they cannot be factorized into the LO amplitude and a universal correction factor. These contributions are infrared and collinear–finite and are expected to be small, but we nevertheless calculate them for completeness. Similar approximations are made for the charged Higgs pair case.

From the technical point of view, for the 2HDM Higgs pair processes which are tree–level at LO, such as the $q\bar{q} \rightarrow h^0 A^0$ subchannels, the NLO results may be obtained automatically within MADGRAPH5_AMC@NLO . At variance, for the loop–induced gluon fusion channel events are generated at NLO using the HEFT results and then reweighted using the exact $2 \rightarrow 2$ and $2 \rightarrow 3$ one–loop amplitudes, by means of a separate reweighting routine. All one–loop matrix elements are computed by MAD-LOOP. The final results are in all cases fully differential, so that they can be used to obtain any distribution at will, after matching with the parton shower.

The lightest neutral $\mathcal{CP}$–even mass–eigenstate of the 2HDM is identified with the SM Higgs boson, with a mass $m_{h^0} = 125$ GeV. The LHC center–of-mass energy is fixed to $\sqrt{s} = 14$ TeV. All particle widths are set to zero in the loop propagators, while the s–channel Higgs boson widths are computed with 2HDMC and included in the MADGRAPH5_AMC@NLO parameter cards. Finite width effects in the heavy quark loop propagators are not taken into account.

Parton distribution functions (PDFs) are evaluated using the MSTW2008 sets with four active flavors at LO and NLO consistently [16]. Therefore, the $b\bar{b}$–initiated channels are not included in our calculation. For all results that follow in this study, we set common factorisation and renormalisation scales, fixing their central value to half the invariant mass of the Higgs pair $\mu_R^0 = \mu_F^0 = m_{h_i h_j}/2$, where ij account for all

possible final–state combinations. This scale choice has been proved to yield perturbatively stable results for the Higgs boson pair production at NLO [71], and to behave very similarly with respect to alternative scale settings used in the literature (cf. e.g. Ref. [70, 206]). The strong coupling constant is evaluated at the renormalization scale $\alpha_s(\mu_R^0)$ along with the PDFs. For conciseness, only observables linked to the final–state Higgs pair are shown in the following. This implies that the Higgs bosons are kept stable at the parton shower stage.

The dedicated codes for the calculation of the gluon fusion channels can be downloaded from [207]. This website contains in addition a selection of standalone codes for different Higgs pair production processes in the SM and beyond.

3.3.2 Total rates

We report on the 2HDM predictions for the Higgs pair total cross sections at the LHC. Our results are documented in Tab. 3.4–3.10. Characteristic model–dependent features are highlighted by the different benchmarks defined in Sec. 3.2.1. For the sake of brevity, we select a representative subset of them (B1, B4, B5) to compute the total rates for all seven combinations of 2HDM Higgs pair final states. The corresponding results are shown in Tab. 3.4–3.9. For the remaining parameter choices (B2, B6 – B8), we concentrate on the light di–Higgs production $h^0 h^0$ (cf. Tab. 3.10). In addition to the total rate predictions for the (leading) gluon fusion mechanism, Tab. 3.5, 3.7 and 3.9 include the contribution from the additional $q\bar{q}$–initiated channels. The latter only feature for the mixed neutral Higgs pairs ($h^0 A^0$, $H^0 A^0$) and the charged Higgs pairs $H^+ H^-$, and occur already at tree–level through the s–channel Z^0 boson exchange – as well as through photon exchange in the charged Higgs case. We show in all cases the total rate predictions at LO and NLO accuracy in QCD. For the gluon fusion channels, we explicitly distinguish between the two reweighting schemes in use, as described in Sec. 1.3.2. The total rate central values are shown along with the scale and PDF uncertainties. The size of the NLO corrections is quantified in terms of the K–factor, provided in the right–most column of the tables. The latter is defined consistently through $K \equiv \sigma^{\mathrm{NLO}}/\sigma^{\mathrm{LO}}$, where the NLO cross section for the gg–initiated channels stands for the "loop–improved" result. For the $q\bar{q}$–initiated channels, the NLO prediction corresponds to the exact result.

Before we discuss the characteristic model–dependent features, some general comments are in order. First of all, we find large NLO corrections, with typical K–factors in the range of $1.5 - 1.7$ for the gg–initiated channels. These sizable QCD effects are primarily due to the NLO real emission. This is a well–known fact for processes with

Benchmark B1

$gg \rightarrow$	LO	NLO–loop improved	NLO–Born improved	K
$h^0 h^0$	$1480^{+29.8+1.5\%}_{-21.6-2.1\%}$	$2400^{+18+1.6\%}_{-14.4-1.9\%}$	$2500^{+19.2+1.6\%}_{-15.0-1.9\%}$	1.62
$h^0 H^0$	$10.5^{+33.5+2.3\%}_{-23.5-2.5\%}$	$16.1^{+15.2+2.3\%}_{-13.7-2.8\%}$	$17.9^{+18.5+2.3\%}_{-15.3-2.8\%}$	1.54
$H^0 H^0$	$0.55^{+35.3+2.8\%}_{-24.4-2.9\%}$	$0.86^{+14.7+2.8\%}_{-13.8-3.6\%}$	$0.94^{+17.6+2.8\%}_{-15.3-3.5\%}$	1.56
$h^0 A^0$	$5.22^{+34.4+2.5\%}_{-23.9-2.7\%}$	$8.68^{+17.1+2.5\%}_{-14.8-3.1\%}$	$8.90^{+17.9+2.5\%}_{-15.2-3.1\%}$	1.66
$H^0 A^0$	$0.46^{+36.4+3.1\%}_{-24.9-3.2\%}$	$0.73^{+15.2+3.3\%}_{-14.3-4.1\%}$	$0.80^{+17.8+3.2\%}_{-15.5-4.0\%}$	1.60
$A^0 A^0$	$0.22^{+37.3+3.4\%}_{-25.4-3.5\%}$	$0.35^{+14.8+3.7\%}_{-14.2-4.6\%}$	$0.38^{+17.4+3.7\%}_{-15.5-4.6\%}$	1.59
$H^+ H^-$	$0.32^{+37.3+3.4\%}_{-25.4-3.5\%}$	$0.53^{+16.1+3.7\%}_{-14.9-4.6\%}$	$0.56^{+17.7+3.7\%}_{-15.7-4.6\%}$	1.65

Table 3.4: Total Higgs pair cross sections via gluon fusion $pp(gg) \rightarrow h_i h_j$ (in fb) for all seven final–state combinations within the 2HDM. The rates are computed at LO and NLO, including the QCD corrections within either the "loop–improved" or "born–improved" approach. The associated K–factors are displayed in the right–most column. The total rate central values are folded with the theory uncertainty estimates from scale variations (first quote) and PDFs (second quote). The LHC center–of mass energy is $\sqrt{s} = 14$ TeV. The 2HDM parameters are fixed to benchmark B1 in Tab. 3.2.

Benchmark B1

$q\bar{q} \rightarrow$	LO	NLO	K
$h^0 A^0$	$0.018^{+3.7+1.7\%}_{-3.6-1.7\%}$	$0.023^{+2.1+2.3\%}_{-1.8-1.8\%}$	1.29
$H^0 A^0$	$1.53^{+5.2+1.9\%}_{-4.8-1.9\%}$	$1.95^{+2.2+2.4\%}_{-2.0-1.9\%}$	1.27
$H^+ H^-$	$0.81^{+6.1+2.1\%}_{-5.6-2.1\%}$	$1.02^{+2.3+2.6\%}_{-2.2-1.9\%}$	1.25

Table 3.5: Total Higgs pair cross sections via quark–antiquark annihilation $pp(q\bar{q}) \rightarrow h_i h_j$ (in fb) for the mixed $\mathcal{CP}$–even/$\mathcal{CP}$–odd and charged Higgs pair combinations within the 2HDM, in the same setup as Tab. 3.4. The 2HDM parameters are fixed to benchmark B1 in Tab. 3.2.

color–singlet final states, where there is plenty of phase space to accommodate the radiation of initial–state light partons [68, 208–210]. Notice that these K–factors do not change significantly as we compare the different gg–initiated di–Higgs final–states. Likewise, they do not depend on the chosen benchmark and they are quantitatively similar to the SM prediction. We note here for completeness that the corresponding predictions for the SM give a LO cross section of 23.0 fb, a NLO "loop-improved" result of 34.9 fb and a NLO "Born-improved" one of 38.9 fb [71] and therefore a K–factor of 1.52. These traits can be again explained by the structure of the QCD

corrections (cf. Sec. 3.2.3), which is common to all Higgs pair channels and unlinked to the underlying 2HDM dynamics. Actually, all genuine 2HDM imprints (viz. the modified couplings and the heavy resonances) modify the LO and NLO predictions in exactly the same way, leaving the K–factor values unaltered.

The reduction of the theoretical uncertantities is manifest in the smaller scale variations when we compare the total rates at LO and NLO accuracy. For gluon fusion, we find typical scale uncertainties spanning $\Delta\sigma/\sigma \equiv [\sigma(\mu^0/2) - \sigma(2\mu^0)]/\sigma \sim 30 - 40\%$ at LO, while they shrink down to $\Delta\sigma/\sigma \sim 15 - 20\%$ at NLO. The PDF uncertainties lie at the per–cent level and increase with heavier Higgs masses. This behavior can be attributed to the uncertainty in the gluon parton density, which increases with the Bjorken variable x in the kinematically relevant regions for these processes. On the other hand, the $q\bar{q}$–initiated subprocesses exhibit an overall milder scale uncertainty, in line with the fact that they do not depend on α_s at LO. The corresponding K–factors are also smaller in these cases (cf. Tab. 3.5, 3.7 and 3.9) and remain in the range $K \sim 1.2 - 1.3$, as expected for Drell–Yan–like processes. Notice also that, unlike the scale uncertainties, the PDF uncertainties slightly grow from the LO to the NLO predictions. This is explained by the additional initial–state partons which become active at NLO. The differences between the "loop–improved" and "born–improved" results are typically smaller than 10% and therefore lie within the theoretical uncertainties. Another aspect to mention is the relative size of the (tree–level) $q\bar{q}$–initiated channels versus the (loop–induced) gg–fusion mechanism. This varies significantly with the different Higgs pair combinations. For instance, while gluon fusion prevails for $h^0 A^0$, in the case of $H^0 A^0$ we find that the bulk contribution is $q\bar{q}$ induced. This difference can be traced back to the coupling $g_{h^0 A^0 Z^0}$ (resp. $g_{H^0 A^0 Z^0}$), which is proportional to $\cos(\beta - \alpha)$ (resp. $\sin(\beta - \alpha)$) and therefore vanishes (resp. maximizes) in the decoupling limit $\cos(\beta - \alpha) \to 0$.

While the K–factors barely depend on the specific 2HDM scenario, the total rates critically rely on the chosen benchmark. In the light Higgs pair case, these can vary from $\sigma^{\mathrm{NLO}} \sim 30$ fb up to $\sigma^{\mathrm{NLO}} \sim 2$ pb. The latter pb–level rates are roughly two orders of magnitude above the SM expectations, and are linked to the resonant heavy Higgs contribution $gg \to H^0 \to h^0 h^0$. This trait is common to all scenarios in which the cascade decay $H^0 \to h^0 h^0$ is kinematically accessible ($m_{H^0} > 2m_{h^0}$) and reflects the fact that the resonant production effectively involves one power of G_F less compared to the continuum pair production. Such enhancements are tamed if the position of the resonance is shifted away from the di–Higgs threshold $2m_{h^0}$ and vanish consistently in the SM limit of $\cos(\beta - \alpha) \to 0$ and $m_{H^0} \gg m_{h^0}$. The fact that the resonant contribution to $\sigma(h^0 h^0)$ decreases with increasing m_{H^0} values is explained by i) the larger phase space required to produce the intermediate heavy state H^0; and

Benchmark B4

$gg \rightarrow$	LO	NLO–loop improved	NLO–Born improved	K
$h^0 h^0$	$85.1^{+33.5+2.3\%}_{-23.5-2.5\%}$	$135^{+15.9+2.3\%}_{-14.0-2.8\%}$	$147^{+18.4+2.3\%}_{-15.3-2.8\%}$	1.59
$h^0 H^0$	$0.85^{+36.9+3.3\%}_{-25.2-3.4\%}$	$1.42^{+14.5+3.4\%}_{-14.0-4.3\%}$	$1.51^{+16.5+3.5\%}_{-15.0-4.3\%}$	1.67
$H^0 H^0$	$0.008^{+40.5+5.1\%}_{-26.9-5.0\%}$	$0.013^{+15.8+5.9\%}_{-15.3-6.9\%}$	$0.013^{+17.4+5.9\%}_{-16.1-6.7\%}$	1.65
$h^0 A^0$	$0.61^{+36.7+3.2\%}_{-25.1-3.3\%}$	$0.99^{+16.9+3.3\%}_{-15.1-4.1\%}$	$1.02^{+17.9+3.3\%}_{-15.6-4.1\%}$	1.62
$H^0 A^0$	$0.005^{+40.2+4.8\%}_{-26.8-4.8\%}$	$0.008^{+13.9+5.8\%}_{-14.4-6.5\%}$	$0.009^{+17.5+5.6\%}_{-15.7-6.5\%}$	1.53
$A^0 A^0$	$0.016^{+40.2+4.9\%}_{-26.8-4.9\%}$	$0.025^{+13.4+5.7\%}_{-14.1-6.7\%}$	$0.027^{+16.8+5.6\%}_{-15.7-6.5\%}$	1.54
$H^+ H^-$	$0.024^{+40.0+4.7\%}_{-26.7-4.8\%}$	$0.039^{+15.2+5.6\%}_{-15.0-6.5\%}$	$0.042^{+17.6+5.5\%}_{-16.1-6.3\%}$	1.62

Table 3.6: Total Higgs pair cross sections via gluon fusion $pp(gg) \rightarrow h_i\, h_j$ (in fb) for all seven final–state combinations within the 2HDM, in the same setup as Tab. 3.4. The 2HDM parameters are fixed to benchmark B4 in Tab. 3.2.

Benchmark B4

$q\bar{q} \rightarrow$	LO	NLO	K
$h^0 A^0$	$5.6{\cdot}10^{-3}\,^{+6.2+2.1\%}_{-5.6-2.0\%}$	$7.1{\cdot}10^{-3}\,^{+2.2+2.6\%}_{-2.2-1.9\%}$	1.3
$H^0 A^0$	$0.083^{+9.1+3.0\%}_{-7.9-2.6\%}$	$0.10^{+2.7+3.4\%}_{-2.9-2.2\%}$	1.21
$H^+ H^-$	$0.12^{+8.6+2.9\%}_{-7.5-2.7\%}$	$0.14^{+2.6+3.3\%}_{-2.8-2.2\%}$	1.22

Table 3.7: Total Higgs pair cross sections via quark–antiquark annihilation $pp(q\bar{q}) \rightarrow h_i\, h_j$ (in fb) for the mixed $\mathcal{CP}$–even/$\mathcal{CP}$–odd and charged Higgs pair combinations within the 2HDM, in the same setup as Tab. 3.4. The 2HDM parameters are fixed to benchmark B4 in Tab. 3.2.

ii) the correspondingly lower gluon luminosity, which is probed at larger x–values, the more massive the heavy field becomes. It is also remarkable that these resonant situations are almost insensitive to the actual value of the triple Higgs self–couplings. This is due to the fact that i) the dependence of the resonant production $gg \rightarrow H^0$ on the coupling $g_{H^0 h^0 h^0}$ is cancelled by the dominant decay mode $H^0 \rightarrow h^0 h^0$ and ii) the light Higgs–mediated diagrams $gg \rightarrow h^{0*} \rightarrow h^0 h^0$ are subdominant with respect to the resonant part, in such a way that the dependence on the coupling $g_{h^0 h^0 h^0}$ is overshadowed.

A number of model–specific fingerprints can be unraveled by comparing the total rate predictions for the different 2HDM benchmarks. These can be ultimately traced back to the characteristic coupling patterns and the extra Higgs boson masses in each scenario, given in Tab. 3.2 and 3.3. For the resonant scenarios, B1 and B4 , the on–shell

Benchmark B5

$gg \rightarrow$	LO	NLO–loop improved	NLO–Born improved	K
$h^0 h^0$	$22.1^{+32.4+2.0\%}_{-22.9-2.3\%}$	$33.9^{+15.2+2.0\%}_{-13.5-2.4\%}$	$37.5^{+18.3+2.0\%}_{-15.1-2.4\%}$	1.53
$h^0 H^0$	$11.1^{+32.5+2.1\%}_{-23.0-2.4\%}$	$17.1^{+15.1+2.1\%}_{-13.4-2.5\%}$	$19.0^{+18.5+2.0\%}_{-15.1-2.5\%}$	1.53
$H^0 H^0$	$0.70^{+33.2+2.2\%}_{-23.3-2.5\%}$	$1.08^{+14.3+2.2\%}_{-13.1-2.7\%}$	$1.22^{+17.7+2.2\%}_{-14.9-2.7\%}$	1.54
$h^0 A^0$	$6.53^{+33.5+2.3\%}_{-23.5-2.5\%}$	$11.1^{+18.1+2.2\%}_{-15.2-2.7\%}$	$12.8^{+18.3+2.2\%}_{-15.3-2.7\%}$	1.70
$H^0 A^0$	$2.51^{+34.6+2.6\%}_{-24.0-2.7\%}$	$4.08^{+16.1+2.6\%}_{-14.4-3.2\%}$	$4.39^{+18.3+2.6\%}_{-15.5-3.2\%}$	1.62
$A^0 A^0$	$0.49^{+36.0+3.0\%}_{-24.7-3.1\%}$	$0.79^{+15.7+3.1\%}_{-14.4-3.9\%}$	$0.84^{+17.7+3.1\%}_{-15.4-3.9\%}$	1.62
$H^+ H^-$	$0.84^{+35.9+3.0\%}_{-24.7-3.1\%}$	$1.40^{+15.7+3.1\%}_{-14.4-3.9\%}$	$1.50^{+17.8+3.0\%}_{-15.4-3.8\%}$	1.67

Table 3.8: Total Higgs pair cross sections via gluon fusion $pp(gg) \rightarrow h_i \, h_j$ (in fb) for all seven final–state combinations within the 2HDM, in the same setup as Tab. 3.4. The 2HDM parameters are fixed to benchmark B5 in Tab. 3.2.

production of the heavy Higgs field H^0 is responsible for the total rate enhancement in $\sigma(h^0 h^0)$, by a factor 70 (resp. 4) above the SM. The difference of one order of magnitude between the two scenarios is linked to the fact that, while in B1 the heavy Higgs mass is relatively low and lies right above the di–Higgs threshold $m_{H^0} \simeq 2m_{h^0}$, in scenario B4 the H^0 field is substantially heavier. The total $h^0 h^0$ rates in the first case thus benefit from the larger on–shell single H^0 rates; as well as from the overly dominant decay mode $H^0 \rightarrow h^0 h^0$. For scenarios B7 and B8 in Tab. 3.10 we find milder ($\sim 30\%$) resonant enhancements of the $h^0 h^0$ cross section as compared to B1, even though the H^0 mass is also quite low in these cases. This is because the H^0 contribution through $gg \rightarrow H^0 \rightarrow h^0 h^0$ is suppressed by the reduced heavy Higgs top Yukawa $g_t^{H^0}$. Finally, for the non–resonant scenarios (viz. B5, B2 and B6) our predictions for $\sigma(h^0 h^0)$ fall down to values close, or even slightly below the SM. This is explained naturally by the SM–like coupling pattern of B5 and B6 (cf. Tab. 3.3). For B2, the reduced rate is a consequence of the stronger destructive interference between i) the triangle–mediated contributions $gg \rightarrow h^{0*} \rightarrow h^0 h^0$ and $gg \rightarrow H^{0*} \rightarrow h^0 h^0$, which are enhanced by the larger trilinear couplings; and ii) the box–mediated diagrams. Barring possible on–shell resonances, we conclude that significant deviations from the SM Higgs pair predictions are not possible rate–wise. This is in agreement with the findings reported in Ref. [176]. Similarly, we see that the distinctive model–specific features have very little impact on the total rates and on the size of the QCD corrections.

Benchmark B5

$q\bar{q} \rightarrow$	LO	NLO	K
$h^0 A^0$	$1.96{\cdot}10^{-3}\,{}^{+2.6+1.5\%}_{-2.7-1.6\%}$	$2.55{\cdot}10^{-3}\,{}^{+1.9+2.2\%}_{-1.6-1.7\%}$	1.30
$H^0 A^0$	$5.02\,{}^{+3.4+1.6\%}_{-3.4-1.7\%}$	$6.50\,{}^{+2.1+2.2\%}_{-1.8-1.7\%}$	1.29
$H^+ H^-$	$2.17\,{}^{+4.7+1.8\%}_{-4.4-1.9\%}$	$2.76\,{}^{+2.1+2.4\%}_{-1.9-1.8\%}$	1.27

Table 3.9: Total Higgs pair cross sections via quark–antiquark annihilation $pp(q\bar{q}) \rightarrow h_i h_j$ (in fb) for the mixed $\mathcal{CP}$–even/$\mathcal{CP}$–odd and charged Higgs pair combinations within the 2HDM, in the same setup as Tab. 3.4. The 2HDM parameters are fixed to benchmark B5 in Tab. 3.2.

Benchmarks B2, B6 – B8

	LO	NLO–loop improved	NLO–Born improved	K
B2	$18.0^{+32.0+1.9\%}_{-22.7-2.3\%}$	$28.7^{+16.6+2.0\%}_{-14.1-2.4\%}$	$30.5^{+18.4+1.9\%}_{-15.0-2.3\%}$	1.59
B6	$23.4^{+32.3+2.0\%}_{-22.9-2.3\%}$	$35.3^{+15.1+2.0\%}_{-13.4-2.4\%}$	$39.4^{18.4+2.0\%}_{-15.1-2.4\%}$	1.50
B7	$30.3^{+32.4+2.0\%}_{-22.9-2.3\%}$	$45.5^{+14.5+2.0\%}_{-13.1-2.5\%}$	$51.8^{+18.4+2.0\%}_{-15.1-2.4\%}$	1.50
B8	$29.1^{+32.6+2.1\%}_{-23.0-2.4\%}$	$44.9^{+15.4+2.1\%}_{-13.6-2.5\%}$	$49.5^{+18.3+2.0\%}_{-15.1-2.5\%}$	1.54

Table 3.10: Total light Higgs pair cross sections via gluon fusion $pp(gg) \rightarrow h^0 h^0$ (in fb) within the 2HDM, in the same setup as Tab. 3.4. The 2HDM parameters are fixed to benchmarks B2, B6 – B8 in Tab. 3.2.

Before closing this discussion, let us devote one last word to the heavier di–Higgs combinations, shown in Tab. 3.4, 3.6 and 3.8 for the B1, B4 and B5 scenarios respectively. The reported total rates span a wide range from $\sigma \sim \mathcal{O}(10^{-2})$ fb to $\sigma \sim \mathcal{O}(10)$ fb and lie in all cases below the light di–Higgs pair predictions. The reason is twofold: i) the relative phase space suppression and ii) the lower initial–parton luminosities involved in the production of these heavier states. The cases in which different rates are obtained for different Higgs pair combinations of similar masses (e.g. for $h^0 H^0$ and $H^0 H^0$ in benchmark B5) can be understood by considering the size of the Higgs couplings in the given scenario.

3.3.3 Differential distributions

As we have seen so far, the most apparent 2HDM imprints rate–wise are of resonant nature. These appear when the on–shell subprocess $gg \rightarrow H^0 \rightarrow h^0 h^0$ is kinematically available and adds to the continuum production. This possibility crucially depends on the heavy Higgs spectrum and is almost insensitive to the distinctive cou-

pling patterns of the 2HDM. The mere observation of an enhancement in the total rate would thus not be undisputed evidence of an underlying 2HDM structure.

Instead, a richer landscape opens up as we move on to the kinematical distributions. These are particularly helpful to track down the model–specific effects which are otherwise smeared once we integrate over the whole phase space. For the remainder of this section we shall focus on the light neutral $\mathcal{CP}$–even Higgs pair channel $h^0 h^0$ and study representative di–Higgs distributions for the LHC at 14 TeV. Our results are displayed in Fig. 3.5–3.10, in which we show the light Higgs pair rates as a function of the di–Higgs invariant mass $m_{h^0 h^0}$ (left panels) and the hardest Higgs transverse momentum $p_T^{h^0}$ (right panels). We concentrate on these two for the sake of conciseness, even though any alternative distribution can be obtained at will, as our setup is once again fully differential. All histograms are shown at both LO+PS and NLO+PS accuracy, where the NLO results follow from the "loop–improved" approach. The SM prediction (also at NLO+PS) is overlayed for comparison. In the lower subpanels we display the bin–by–bin ratio of the 2HDM NLO+PS results over the SM values.

We begin by pointing out a number of features common to all 2HDM scenarios. Let us first recall that, unlike the SM, there are two types of triangle topologies that contribute in the 2HDM; one of them is linked to the s–channel exchange of the light Higgs boson h^0, while the other one proceeds through the heavy Higgs exchange H^0. The first subprocess $gg \to h^{0*} \to h^0 h^0$ follows the shape of the virtual Higgs boson propagator and would peak around $\hat{s} \simeq m_{h^0}^2$. At larger invariant masses, the light Higgs propagator is probed off–shell, which means that for these kinematical configurations, the light Higgs triangles become subleading. The virtual heavy Higgs counterpart $gg \to H^{0*} \to h^0 h^0$ becomes relevant at larger invariant mass values $m_{h^0 h^0} \sim m_{H^0}$ and may either add to, or partially cancel, the light Higgs triangle amplitudes in this region – depending on the relative signs of the different Yukawa and trilinear Higgs self–couplings. If $m_{H^0} > 2 m_{h^0}$, the heavy Higgs is produced on–shell and its resonant peak takes over. As suggested to above, these resonant situations overshadow all other possible new physics effects. In particular, neither the total nor the differential rates are sensitive to a possible enhancement or suppression of the trilinear Higgs self–couplings.

The interplay between the triangles and box topologies, which have different phase space dependence, generates a variety of model–specific signatures which are reflected in the histograms. For instance, a modified trilinear coupling $g_{h^0 h^0 h^0}$ will mostly reveal itself at low invariant masses. Instead, the boxes are unresponsive to variations in the triple Higgs self–interactions. Shifted Yukawa couplings will typically become more apparent in the larger $m_{h^0 h^0}$ and $p_T^{h^0}$ regions, through their influence on the box contributions. The latter topologies have a slower decrease with $m_{h^0 h^0}$ and $p_T^{h^0}$

compared to the triangles, and hence dominate in the hard Higgs tails. Independent changes in the top and bottom–quark Yukawas, which are possible for type–II models, can in addition modify the interference between the top and the bottom loops.

We can see from all histograms that, except the cases with low–mass H^0 resonances, the majority of the di–Higgs events concentrates on the invariant masses well above the Higgs pair threshold $\hat{s} \gtrsim 4m_{h^0}^2$. This is after all the reason for the breakdown of the infinite top–mass effective theory (HEFT), which is meant to hold for $\hat{s} \ll m_t^2$. The HEFT fails to correctly reproduce the exact distributions not only at large invariant masses but also for moderate values. The transverse momentum distributions are problematic for the same reason [211, 212].

We also notice that the QCD NLO effects, while quantitatively important rate–wise, have very little effect on the distribution shapes. Notice that both the LO and the NLO histograms in all figures vary in parallel, which implies a fairly constant K–factor. This is certainly not unexpected, in view of the structure of the NLO QCD corrections, as we have described in Sec. 3.2.3. Neither the exchange of virtual gluons between the incoming partons nor the light parton radiation off the initial–state colored legs can significantly influence the leading kinematical features appearing in the $m_{h^0h^0}$ and $p_T^{h^0}$ distributions, which rely fundamentally on ii) the relative sizes and signs of the heavy–quark Yukawa and the triple Higgs self–couplings; and iii) the potential enhancement due to a resonant (or close–to–resonant) intermediate heavy Higgs exchange – all these mechanisms being already present at the LO.

Let us now move on to the different model–specific features which can be appreciated in the plots. We begin in Fig. 3.5 by showing the results for benchmark B1. The on–shell heavy Higgs contribution $gg \to H^0 \to h^0h^0$ is evident in the resonant peaks for both the di–Higgs invariant mass ($m_{h^0h^0} \sim M_{H^0} = 300\text{GeV}$) and the hardest Higgs transverse momentum distributions ($p_T^{h^0} \sim \sqrt{(m_{H^0}/2)^2 - m_{h^0}^2}$), which of course overwhelm the SM expectations in the low $m_{h^0h^0}$ and $p_T^{h^0}$ regions. The dip in the signal right after the resonant peak is due to the interference between the boxes and the heavy Higgs–mediated triangles. The small deviations from the SM away from the resonant peak are caused by the modified trilinear and Yukawa couplings. As expected, at large invariant masses $m_{h^0h^0} \gtrsim 600$ GeV the cross section is dominated by the box diagrams. Thereby we explain the 2HDM/SM ratio through the rescaled top Yukawa $(g_{h^0t\bar{t}}/g_{Ht\bar{t}}^{\text{SM}})^4 \sim 0.85$.

A qualitatively similar situation is encountered for benchmark B4, as shown in Fig. 3.6. Again, the heavy Higgs resonant peak is manifest for $m_{h^0h^0} \simeq 700$ GeV and

Figure 3.5: Light Higgs pair differential rates as a function of a) the di–Higgs invariant mass $m_{h^0 h^0}$ (left panels); and b) the hardest Higgs transverse momentum $p_T^{h^0}$ (right panels). We separately show the results at LO+PS and NLO+PS accuracy in QCD, where the latter correspond to the "loop–improved" approach. The NLO+PS prediction for the SM is overlayed for comparison. In the lower subpannels we display the bin–by–bin ratio of the 2HDM prediction at NLO+PS over the corresponding SM result. The LHC center–of–mass energy is $\sqrt{s} = 14$ TeV. The 2HDM parameters are fixed to benchmark B1.

Figure 3.6: Light Higgs pair differential rates as a function of a) the di–Higgs invariant mass $m_{h^0 h^0}$ (left panels); and b) the hardest Higgs transverse momentum $p_T^{h^0}$ (right panels), in the same setup as for Fig. 3.5. The 2HDM parameters are fixed as in benchmark B4.
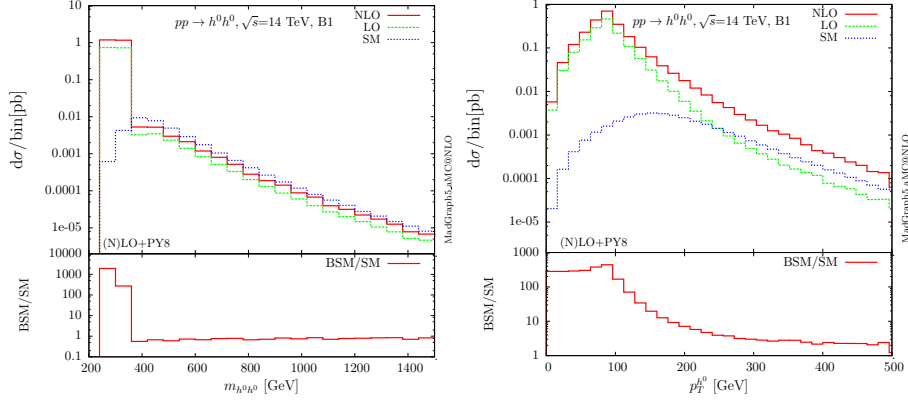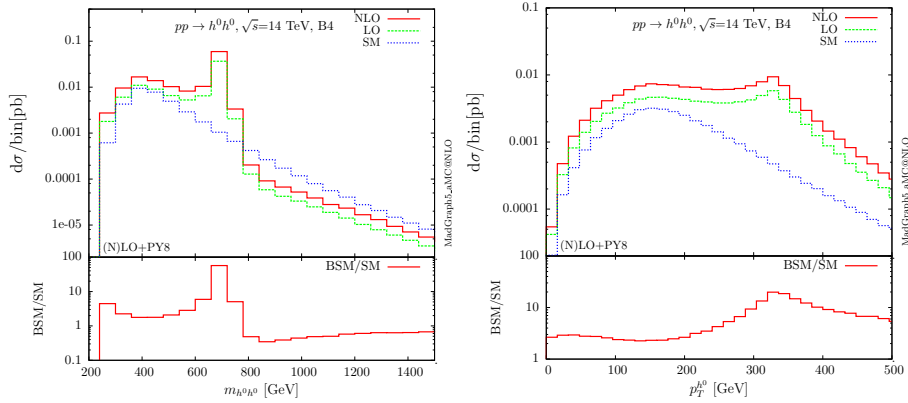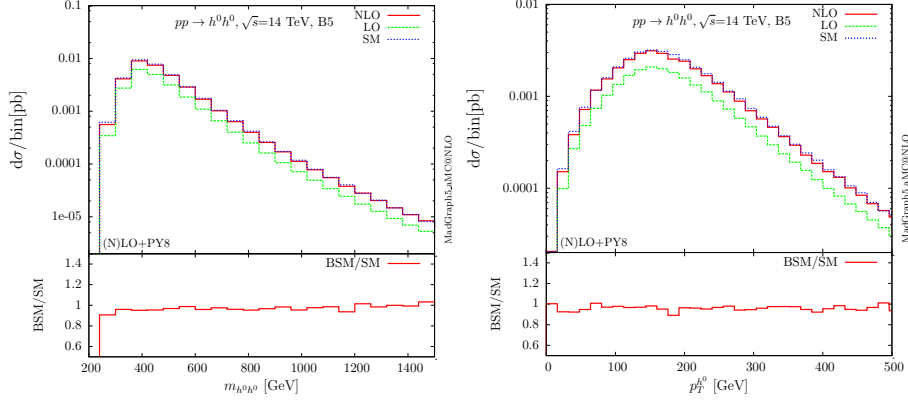
Figure 3.7: Light Higgs pair differential rates as a function of a) the di–Higgs invariant mass $m_{h^0 h^0}$ (left panels); and b) the hardest Higgs transverse momentum $p_T^{h^0}$ (right panels), in the same setup as for Fig. 3.5. The 2HDM parameters are fixed as in benchmark B5.

$p_T^{h^0} \simeq 330$ GeV. Given that the heavy Higgs mass is now larger, its on–shell single production via $gg \to H^0$ is suppressed by phase space and by the lower gluon luminosity. This accounts for the smaller rates with respect to the B1 scenario discussed above. Close to the light Higgs pair threshold $m_{h^0 h^0} \simeq 2m_{h^0}$, we find an enhanced differential rate with respect to the SM. The interplay between several effects is responsible for this behavior. On the one hand, the heavy Higgs–mediated triangles are small in these bins, while the light Higgs–mediated ones dominate. On the other hand, these leading triangle topologies are pulled down by the $\mathcal{O}(40)\%$ reduction of the trilinear Higgs self–coupling $g_{h^0 h^0 h^0}$. The net result is a reduced (destructive) interference with the box contributions. The sharp dip immediately after the resonant peak is once more due to the interference between the heavy Higgs triangles and the boxes – which again leads to a partial cancellation in this case, because the $g_{H^0 t \bar{t}}$ and $g_{H^0 h^0 h^0}$ couplings have the same (negative) sign. In the large $m_{h^0 h^0}$ tail, instead, the differential rates mostly depend on the box contributions, and hence lie roughly $\sim$ 20% below the SM yields.

In contrast to the previous cases, the differential distributions in scenario B5 (cf. Fig. 3.7) barely depart from the SM. The reason is twofold: i) the absence of the on–shell heavy Higgs contribution; ii) the SM–like pattern of all light Higgs couplings in the limit $\cos(\beta - \alpha) \to 0$. In this case, also the trilinear coupling $g_{H^0 h^0 h^0}$ is extremely suppressed, so that the heavy Higgs–mediated process $gg \to H^0 \to h^0 h^0$ barely contributes. The flat 2HDM/SM cross–section ratio is a further indication that no distinctive 2HDM imprints arise in any region of the phase space. The results for

Figure 3.8: Light Higgs pair differential rates as a function of a) the di–Higgs invariant mass $m_{h^0 h^0}$ (left panels); and b) the hardest Higgs transverse momentum $p_T^{h^0}$ (right panels), in the same setup as for Fig. 3.5. The 2HDM parameters are fixed as in benchmark B2.


Figure 3.9: Individual contributions to the light Higgs pair differential rates as a function of the di–Higgs invariant mass $m_{h^0 h^0}$. The results are shown separately for i) the light Higgs–mediated triangles (long–dashed, green), ii) the heavy Higgs–mediated triangles (short–dashed, blue); iii) the box topologies (dotted, magenta); and iv) the combined contribution. All histograms are computed to LO+PS accuracy. The 2HDM parameters are fixed as in benchmark B2.

benchmark B6, which we do not show explicitly, are also featureless. The SM–like profile in the latter case also results from the fermiophobic nature of the heavy Higgs boson, which cannot couple to the quarks and hence has no influence on the light di–Higgs production.

A variety of non–standard imprints can be appreciated in Fig. 3.8 for benchmark B2. These genuine 2HDM effects have in this case a non–resonant origin and can be better interpreted by analysing the individual components from the different topologies. The latter are shown separately in Fig. 3.9. One first observation is the increased rates right next to the di–Higgs threshold $m_{hh} \simeq 2m_{h^0}$. These are primarily caused by the additional heavy Higgs contribution, and are particularly strong in this case not only because of the low heavy Higgs mass $m_{H^0} = 200$ GeV, but also due to the unsuppressed trilinear coupling $g_{H^0 h^0 h^0}$ – in contrast to scenario B5 discussed above. In fact, it turns out that in this region (viz. the first bin of Fig. 3.9), the box and the heavy Higgs triangle amplitudes have comparable sizes but opposite signs. Given this effective cancellation, the net result comes from the (enhanced) light Higgs triangles only. The sharp dip in the $m_{h^0 h^0} \simeq 350$ GeV bin is related again to an accidental and nearly exact cancellation between the three contributions in the game. In this case, one can check that the two triangle–mediated contributions are largely cancelling the box–mediated ones. In the intermediate bins $m_{h^0 h^0} \simeq 400 - 700$ GeV, the di–Higgs rates lie below the SM expectations due to the additional interference between the boxes and the heavy Higgs–mediated triangles. This partial cancellation is quite strong in this case as both the top Yukawa $g_{h^0 t \bar{t}}$ and the trilinear coupling $g_{H^0 h^0 h^0}$ are enhanced. This effect is also manifest in the transverse momentum distributions in the region of 100 - 200 GeV (cf. right panels of Fig. 3.8). Finally, at large di–Higgs invariant masses and in the boosted Higgs tails (viz. $m_{h^0 h^0} \gtrsim 800$ GeV and $p_T \gtrsim 400$ GeV) the rates are dominated by the box contributions. Correspondingly, the $\mathcal{O}(10\%)$–enhanced Yukawa coupling accounts for the increased 2HDM rates in these tails, which exceed the SM results by up to $\mathcal{O}(50)\%$, as expected from the overall rescaling $(g_{h^0 tt}/g_{Htt}^{\rm SM})^4 \simeq 1.5$.

Last but not least, in Fig. 3.10 and 3.11 we study the impact of a strongly modified bottom–quark Yukawa, as realized by benchmarks B7 and B8. While the two scenarios share a number of similar features, their differences highlight some remarkable properties of the 2HDM. In both cases we observe the expected on–shell peak from the heavy Higgs cascade decay, although here it is softer as compared to the previous resonant scenarios. This milder effect is visible not only in the distributions but also rate–wise and can be explained by the strongly suppressed top–quark Yukawa coupling to the heavy Higgs $g_{H^0 t \bar{t}}$ (cf. Tab. 3.3). One further common trait to both benchmarks is the asymptotic behavior at large di–Higgs invariant masses and in the boosted Higgs tails, where we obtain results very close to the SM predictions. All that said, we can also appreciate some relevant differences. On the one hand, the $\mathcal{O}(20)\%$ enhanced bottom Yukawa in B7 reinforces the destructive interference between the top and bottom–mediated triangles. In addition, the amplitude of the individual triangle
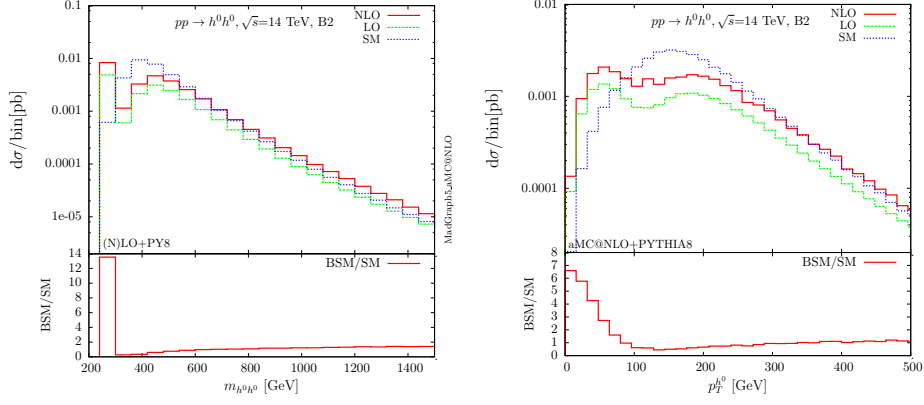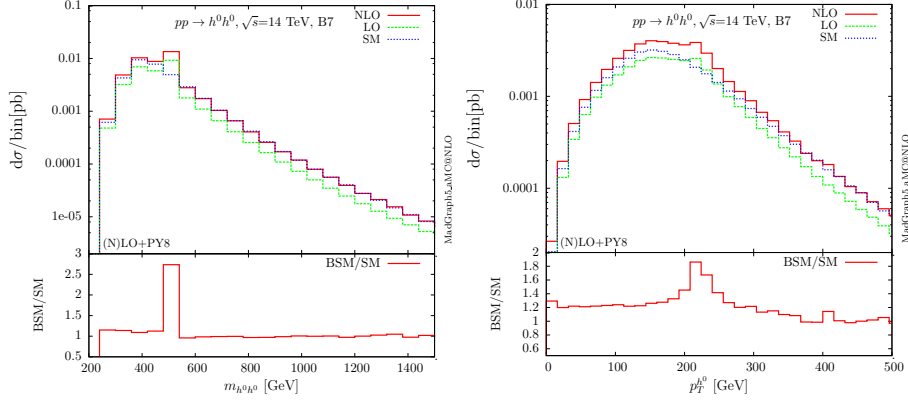
Figure 3.10: Light Higgs pair differential rates as a function of a) the di–Higgs invariant mass $m_{h^0h^0}$ (left panels); and b) the hardest Higgs transverse momentum $p_T^{h^0}$ (right panels), in the same setup as for Fig. 3.5. The 2HDM parameters are fixed as in benchmark B7.
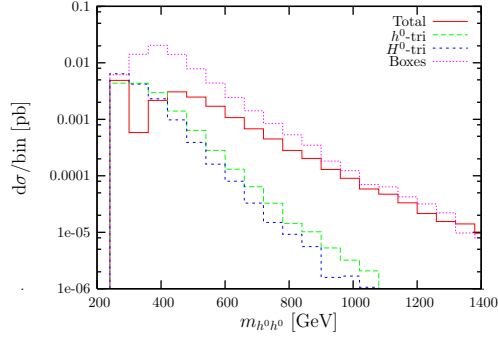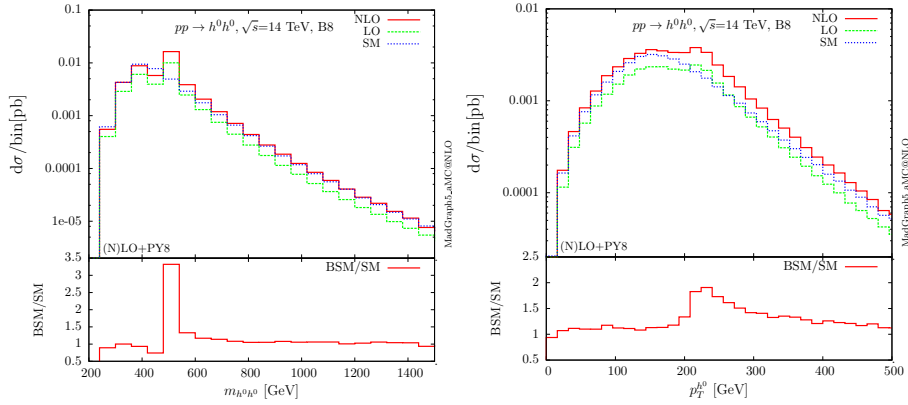

Figure 3.11: Light Higgs pair differential rates as a function of a) the di–Higgs invariant mass $m_{h^0h^0}$ (left panels); and b) the hardest Higgs transverse momentum $p_T^{h^0}$ (right panels), in the same setup as for Fig. 3.5. The 2HDM parameters are fixed as in benchmark B8.

diagrams is pulled down further by the (slightly suppressed) trilinear self–coupling $g_{h^0h^0h^0}$. Both effects cooperate to reduce the interference between the triangle and the box topologies in the lowest $m_{h^0h^0}$ and $p_T^{h^0}$ bins, in such a way that we obtain rates slightly above the SM expectations.

A similar mechanism operates in the B8 scenario, albeit in the opposite direction. In this case, the sign–flipped bottom–quark Yukawa causes the top and bottom–mediated triangles to interfere constructively. As a result, we are left with slightly enhanced triangle amplitudes, which thus reinforce the interference with the boxes. In agreement with this fact, the predicted number of events for $m_{h^0 h^0} \lesssim m_{H^0}$ falls slightly below the SM expectations. Unlike the previous resonant scenarios, in this case we find no dip right after the resonance peak. Instead, we obtain slightly enhanced rates for $m_{h^0 h^0} \gtrsim m_{H^0}$ because the fact that $(g_{H^0 h^0 h^0})(g_{H^0 tt}) < 0$ (cf. Tab. 3.3) leads to a constructive interference with the boxes. A dip does appear instead right below $m_{h^0 h^0} \lesssim m_{H^0}$ due to the additional negative sign from the heavy Higgs propagator $1/(s - m_{H^0}^2)$.

At this point, let us mention that we are aware of possible caveats in matching the NLO prediction to the parton shower in the case of enhanced bottom Yukawas. These have been discussed in the context of single Higgs production [6, 213] and are related to the heavy–quark mass dependence of the Higgs transverse momentum distributions, which is not known exactly beyond the LO. These issues mostly concern the low Higgs p_T region and become more relevant if the bottom–quark Yukawa increases. This is indeed the reason why we do not expect them to matter in our case, as in all of the scenarios that we have explored only the bottom–quark coupling to the heavy Higgs boson $g_{H^0 bb}$ is significantly enhanced. In view of this fact, and since the bottom–mediated effects to the gg–induced heavy Higgs production are very small, we do not find it necessary to adjust our setup to include a more dedicated treatment.

3.4   Higgs pair and triple production in the SM

We conclude this chapter by reviewing the latest results for multiple Higgs production in the SM (see Ref. [12] for a very detailed report on Higgs physics at the LHC in various channels)

Contrary to the 2HDM we studied previously, there is only one triangle contribution in SM Higgs pair production, with an off-shell Higgs as mediator. This implies that this contribution is very small, leading in turn to a very small cross section even at 14 TeV. Tab. 3.11 summaries the NLO in QCD cross sections for several centre of mass energies in the limit in which the top mass effects are retained in the real contributions and in the infinite top mass limit. The relative difference between the two predictions are around 10% and, as expected at lower energies, total rates doesn't differ much between both while at higher energies differences reach 15%. Recently, full top-mass dependance has been computed for NLO QCD Higgs pair production [72, 214]. Their study confirms, as expected, that loop-improved method is closer to the full NLO

	7 TeV	8 TeV	13 TeV	14 TeV	100 TeV
FT	$6.01^{+17.2\%}_{-15.6\%}$	$8.62^{+16.8\%}_{-15.2\%}$	$29.26^{+15.0\%}_{-13.4\%}$	$34.59^{+14.6\%}_{-13.1\%}$	$1237^{+14.3\%}_{-14.1\%}$
HEFT	$6.42^{+20.0\%}_{-16.8\%}$	$9.32^{+19.5\%}_{-16.4\%}$	$31.81^{+18.2\%}_{-15.0\%}$	$37.79^{+18.0\%}_{-14.8\%}$	$1464^{+16.1\%}_{-13.8\%}$
PDF	$\pm 4.0\%$	$\pm 3.7\%$	$\pm 2.7\%$	$\pm 2.6\%$	$\pm 2.1\%$
Δ	6.4%	7.5%	8.0%	8.5%	15.5%

Table 3.11: Signal cross section along with scale uncertainty (in fb) for $gg \rightarrow HH$ at NLO QCD with a central scale choice $\mu_0 = m_{HH}/2$ for $m_H = 125$ GeV at different centre-of-mass energies. The first row shows results in the loop-induced approximation (FT) while the second row represent the $m_t \rightarrow \infty$ limit, reweighted by the exact LO result, of Ref. [70, 206]. The PDF uncertainty based on the PDF4LHC15_nlo_mc set is shown on the third row for each energy. The last row shows the relative difference $\Delta = \frac{\sigma(EFT)-\sigma(FT)}{\sigma(EFT)}$ between both prediction models.

μ_0	7 TeV	8 TeV	13 TeV	14 TeV	100 TeV
$\frac{m_{HH}}{2}$	$6.01^{+17.2\%}_{-15.6\%}$	$8.62^{+16.8\%}_{-15.2\%}$	$29.26^{+15.0\%}_{-13.4\%}$	$34.59^{+14.6\%}_{-13.1\%}$	$1237^{+14.3\%}_{-14.1\%}$
m_{HH}	$5.08^{+18.5\%}_{-15.9\%}$	$7.41^{+17.9\%}_{-15.4\%}$	$25.33^{+15.4\%}_{-13.5\%}$	$30.15^{+15.1\%}_{-13.2\%}$	$1136^{+13.9\%}_{-13.1\%}$
PDF	$\pm 4.0\%$	$\pm 3.7\%$	$\pm 2.7\%$	$\pm 2.6\%$	$\pm 2.1\%$
Δ	15.5%	14.0%	13.4%	12.8%	8.2%

Table 3.12: Effect of the renormalisation and factorisation scale on the signal cross section (in fb) for $gg \rightarrow HH$ at NLO QCD for $m_H = 125$ Gev with $\mu_R = \mu_F = \mu_0$. The last row shows the relative difference $\Delta = \frac{\sigma(m_{HH}/2)-\sigma(m_{HH})}{\sigma(m_{HH}/2)}$ between both scale choice.

results than the born-improved one. In the tails of the Higgs transverse momentum distribution, they observe a 50% and 20% difference respectively for born-improved and loop-improved reweighting. They also show results for the total cross section where a reduction of 24% can be expected at 100 TeV compared to born improved total rates.

We already stressed the importance of the renormalisation and factorisation scales choice in Higgs production. In Tab. 3.12 we show the effect of going from m_{HH} to $m_{HH}/2$ on the total rates. As expected the scale dependence is reduced as the centre of mass energy increases.

We now present in Fig. 3.12 some distributions obtained using the loop-induced approximation for the NLO results to establish to which extent approximate NLO event
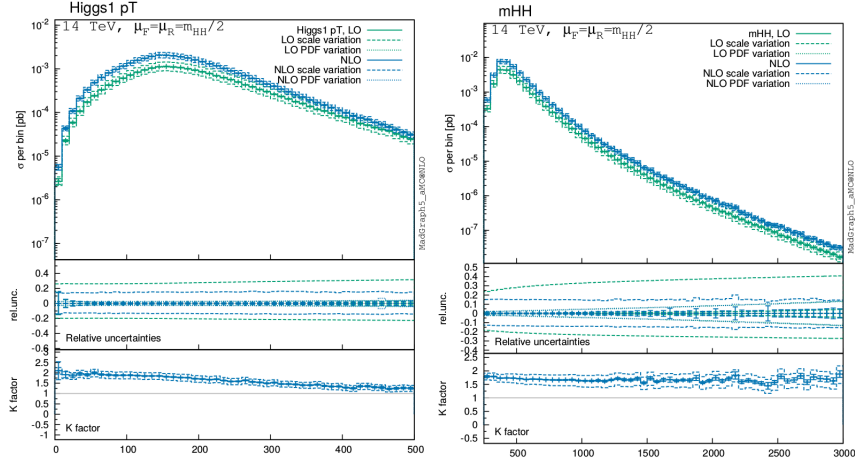
Figure 3.12: Transverse momentum distribution of the leading Higgs boson (left) and invariant di-Higgs boson mass differential distribution (right) in GeV for $pp \to HH$ at LO and NLO for $m_H = 125$ GeV and $\sqrt{s} = 14$ TeV. The scales are chosen to be $\mu_R = \mu_F = m_{HH}/2$. Scale and PDF uncertainties are added linearly in the distribution. The K-factor is defined as the ratio between NLO and LO cross sections.

generators can be used, and to which extent this calculation provides a guideline to relate fiducial cross sections to inclusively modeled quantities. Distributions were obtained for the five previous centre of mass energies but we only show results for 14 TeV here for brevety.

Due to the destructive interplay between the trilinear and box contributions, the top mass threshold significantly impacts the differential distributions for the gluon fusion process, and the invariant di-Higgs boson mass differential cross section in particular. On one hand, the momentum-dependent distributions of the di-Higgs system are exploited in phenomenological analyses (either implicitly or explicitly), as they exhibit a highly sensitive response to BSM-induced modifications of the SM coupling pattern. On the other hand, experimental characteristics of a particular set of selection cuts motivated from the desire to enhance signal over background strongly depend on the transverse Higgs momentum (and therefore on m_{HH}) selection threshold; boosted Higgs kinematics are a particularly drastic example of this.

Finally we also computed the triple Higgs production $gg \to HHH$ at NLO in QCD as shown in Tab. 3.13. The same conclusion about the scales effect can be drawn as for the HH production case.

μ_0	7 TeV	8 TeV	13 TeV	14 TeV	100 TeV
$\frac{m_{HHH}}{2}$	$12.03^{+17.8\%}_{-16.3\%}$	$17.99^{+16.5\%}_{-15.4\%}$	$73.43^{+14.7\%}_{-13.7\%}$	$86.84^{+14.0\%}_{-13.2\%}$	$4732^{+11.9\%}_{-11.6\%}$
m_{HHH}	$9.91^{+19.3\%}_{-16.6\%}$	$15.14^{+18.4\%}_{-16.0\%}$	$63.32^{+16.1\%}_{-14.1\%}$	$76.15^{+15.9\%}_{-14.0\%}$	$4306^{+14.0\%}_{-12.3\%}$
PDF	$\pm5.3\%$	$\pm4.8\%$	$\pm3.4\%$	$\pm3.2\%$	$\pm1.8\%$
Δ	17.6%	15.8%	13.8%	12.3%	9.0%

Table 3.13: Signal cross section (in ab) for $gg \rightarrow HHH$ at NLO QCD for $m_H = 125$ Gev with $\mu_R = \mu_F = \mu_0$. The last row shows the relative difference $\Delta = \frac{\sigma(m_{HHH}/2) - \sigma(m_{HHH})}{\sigma(m_{HHH}/2)}$ between both scale choice.

3.5 Conclusions

In this chapter we have examined the production of Higgs boson pairs via gluon fusion in the 2HDM. We have provided predictions for the 14 TeV LHC at NLO accuracy in QCD, matched to the PYTHIA8 parton shower. We have considered all seven possible final–state Higgs pair combinations in the model and explored representative up–to–date 2HDM benchmarks. The Higgs bosons in the final state have been kept stable in our simulated event samples. The NLO QCD corrections to the (loop–induced) gluon fusion channels have been handled via a reweighting procedure which includes the exact one–loop matrix elements. Dedicated codes for this computation are available in [207].

We have reported large QCD corrections, reflected in the sizable K–factors in the ballpark of $K \sim 1.5 - 1.7$ (for the gg–initiated channels) and $K \sim 1.2 - 1.3$ (for the $q\bar{q}$–initiated ones). These QCD effects are dominated by the initial–state light–parton radiation. They remain almost constant over the phase space and barely depend on the model parameters. Once they are taken into account, the theoretical uncertainties on the Higgs pair rate predictions are significantly reduced.

We have examined a variety of characteristic 2HDM features and evaluated their effect on the total Higgs pair rates and kinematical distributions. The underlying model structure influences the light di–Higgs production in different ways i) the virtual (real) heavy Higgs–mediated contribution $gg \rightarrow H^{0*}(H^0) \rightarrow h^0 h^0$, which may enhance the total rates by up to roughly 2 orders of magnitude above the SM expectations; ii) the diverse possible combinations of enhanced, suppressed and/or sign–flipped Higgs couplings, which lead to increased or reduced rates, particularly apparent in the differential distributions. Finally we presented the recent prediction for NLO results with top mass effect in the SM for several collider energies, giving insight on what could be achieved with a 100 TeV accelerator.

One further step would be to combine our current results with the corresponding Higgs branching ratios, and to evaluate the signal–over–background significances for the respective decay modes. Identifying the channels with the best prospects of being measured requires dedicated studies which should involve detector effects and selection cuts to optimize the signal extraction over the backgrounds. Complementary information can be obtained by including the additional double Higgs mechanisms besides the dominant gluon fusion mode, namely vector boson fusion; associated production with gauge bosons; and Higgs radiation off heavy quarks. The ultimate goal is to identify the most promising experimental opportunities for these extended Higgs sector searches at the LHC.

Chapter 4

Interference effects in heavy scalar production decaying to a top pair

"The measure of greatness in a scientific idea is the extent to which it stimulates thought and opens up new lines of research. "

Paul A. M. Dirac (1902 - 1984)

4.1   Introduction

The top quark might have a special role in electroweak symmetry breaking (EWSB), as it is the only fermion with a coupling to the Higgs of order one and therefore with a mass of the order of the Higgs field vacuum expectation value. This unique feature has been exploited in a wide range of BSM scenarios, from being a window into strongly interacting scenarios to triggering EWSB in supersymmetric theories. After the top discovery at the Tevatron more than 20 years ago, a plethora of searches have been performed to measure its properties and to look for hints of new physics both at the Tevatron and the LHC. Unlike all the other quarks, the top high mass makes its partial weak decay width to bW larger than the QCD hadronization scale meaning that it decays before being able to form mesons or baryons.

The main production channel at hadron colliders is in $t\bar{t}$ pairs via strong interactions, with the EW single production following with roughly a third of the cross-section. New physics effects in top pair production can generally be classified into two categories: resonant and non-resonant. Non-resonant effects are conveniently described within effective field theory, i.e. including the effect of dimension-6 operators [215–217]. Resonant effects arise in physics models which predict new particles that couple to the top, either via an s-channel or a t-channel, leading to top quark pairs possibly in association with other visible or invisible final states. The search for s-channel resonances above the $2m_t$ threshold but within the experimental reach, is particularly promising [218]. These can be spin-0, 1 or 2, colour octet or singlet depending on the model [219]. These resonances often arise only in top pair production if their couplings to light particles are suppressed.

Experimental searches for heavy scalar particles decaying into top quark pairs have been performed by both CMS [220] and ATLAS [221] in Run I of the LHC. These searches are interpreted in terms of upper bounds on production cross-section times branching ratio, assume a narrow width resonance, and generally ignore the interference of the signal with the SM background. Nevertheless, it has been shown that the interference should be taken into account, as the heavy state does not necessarily show up as a resonance bump in the top pair invariant mass distribution but most likely leads to a peak-dip structure [222, 223]. Similar effects have been discussed recently in [224] in the light of the excess reported at 750 GeV by ATLAS [225] and CMS [226].

In order to extract maximal information on the new physics in the presence of an excess or to constrain BSM scenarios in the absence of one, accurate predictions are not only needed for signal and background, but also for their interference. The QCD background is known at NNLO in QCD [227] and NLO in electroweak [228] (see also [229] for a detailed study at LHC 13 TeV). Recent work in the direction of promoting signal and interference predictions beyond LO has been presented in [230]. While all ingredients are available for the computation of the signal at NLO, this is often computed at LO or in some approximation such as the one in [230]. NLO K-factors computed for the scalar production cross-section, $\sigma(pp \to \Phi)$, are often applied to the signal, especially in studies assuming narrow width approximation. The bottleneck of a complete NLO computation is the virtual corrections to the interference between the signal and the QCD background, which involve two-loop multiscale integrals that are currently unknown.

In this chapter we investigate interference effects between the signal $gg \to \Phi \to t\bar{t}$ and background $gg \to t\bar{t}$, where Φ represents a spin-0 particle, taking higher order effects into account. Our method can be applied to any UV complete model involving heavy scalar particles. We demonstrate our results in a simplified model with an addi-

tional scalar or pseudoscalar particle and the 2HDM. The predictions for the signal and interference can then be compared with the experimental results to obtain constraints on models with new scalars. In particular the impact of higher order QCD effects and of taking into account the interference on the excluded parameter space regions can be explored. Our implementation is available within the MadGraph5_aMC@NLO framework.

This chapter is organised as follows. In Sec. 4.2 we discuss the simplified model and 2HDM benchmarks we will employ in our study. In Sec. 4.3 we explore the main features of top pair production in the presence of additional scalars. Higher order QCD effects including the effect of additional jet radiation and NLO corrections for the process are discussed in Sec. 4.4. In Sec. 4.5 we examine the impact of our improved predictions on the constraints that can be set on new physics models (including dark matter models) using top pair resonance searches. The implications of the reported diphoton excess at 750 GeV in the context of top pair production are studied in Sec. 4.6, before we conclude in Sec. 4.7.

4.2   Top pair production in the presence of heavy scalars

In the presence of additional scalar particles, the leading order, $\mathcal{O}(g_s^2)$, diagrams for the signal and the QCD background are shown in Fig. 4.1. Any possible CP-even (including the light 125 GeV Higgs), CP-odd or mixed CP scalars are denoted generically by Y in the Feynman diagrams.[1] A couple of observations are in place here. We first note that the signal/background interference is colour suppressed at leading order in QCD. The QCD amplitude (for instance the one on the right in figure 1) can interfere with the signal only when the top-quark pair is in a colour singlet (i.e. with probability $\simeq 1/N_c^2$, N_c being the number of colours). We also mention that the amplitude for the signal is proportional to the square of the coupling of the scalar to the top, which implies that unless another heavy coloured state runs in the loop, there is no sensitivity to the sign of the Yukawa coupling. In this chapter we will consider the process of Fig. 4.1 in a simplified model and the 2HDM. The parameters of our BSM models relevant for this process are briefly presented here.

---

[1] While bottom quarks couple to the SM Higgs and possibly to the heavy scalars, their contribution is very suppressed (for moderate bottom Yukawa couplings) in the region of interest which lies above the top–anti-top threshold. Therefore we will only consider top quark loops throughout this study.
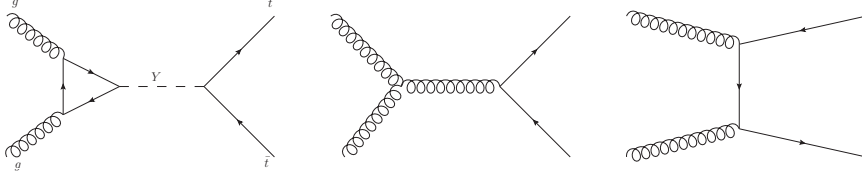
Figure 4.1: Leading order Feynman diagrams for $gg \to t\bar{t}$ production in the presence of spin-0 particles coupling to the top quark.

4.2.1 Simplified Model

A simplified model in which one or two additional scalars (one scalar and one pseudoscalar) are present is considered first. As in the 2HDM, heavier CP-even and CP-odd scalars are denoted by H^0 and A^0 respectively, coupling to the top in the following way:

$$\mathcal{L} \;=\; \bar{t}\frac{y^t}{\sqrt{2}}\hat{g}_t^S t\, H^0 + \bar{t}\frac{y^t}{\sqrt{2}}i\hat{g}_t^P\gamma^5 t\, A^0. \tag{4.1}$$

For convenience we normalise the scalar and pseudoscalar interactions with the top quark (t) by the SM top Yukawa coupling ($y^t = \frac{m_t}{v}$). We note here that a mixed state (Y) is also allowed in our model, coupling to the top in the following way:

$$\mathcal{L} \;=\; \bar{t}\frac{y^t}{\sqrt{2}}(\hat{g}_t^S + i\hat{g}_t^P\gamma^5)t\, Y, \tag{4.2}$$

with CP-violation present when both $\hat{g}_t^S$ and $\hat{g}_t^P$ are non-zero.

The above Lagrangian is not invariant under the SM gauge group. In ultraviolet completions where Y is one of the components of an $SU(2)_L$ doublet, as in the 2HDM, our simplified model corresponds to scenarios with a high degree of alignment. In this case, the couplings of the gauge bosons to the heavier CP-even scalar are suppressed, *e.g.* $\cos(\beta - \alpha) \sim 0$. Such setups are in particular common in minimal supersymmetric realisations. In contrast, if the mediator is a gauge singlet, it should mix with the Higgs sector, leading to a more complex phenomenology as in the so-called Higgs portal dark matter models (see *e.g.* the works of Ref. [231–236]). On the other hand, it has also recently been shown that the use of simplified models for LHC and future (feasible) collider studies does not break perturbative unitarity [237, 238].

In this simplified model, the parameters of interest for the production of the heavy scalars and decay into top pairs are: the Yukawa couplings $\hat{g}_t^S, \hat{g}_t^S$, the new particle

	Type	$\tan\beta$	α/π	m_{H^0}	m_{A^0}	$m_{H^\pm}$	m_{12}^2
B1	II	1.75	-0.1872	300	441	442	38300
B9	II	0.9	-0.267	500	550	620	10000
B10	II	0.7	-0.306	380	590	610	10000
B11	II	0.6	-0.328	500	710	720	10000

Table 4.1: Parameter choices for the different 2HDM benchmarks used in our study. All masses are given in GeV. The lightest Higgs mass is fixed in all cases to $m_{h^0} = 125$ GeV.

masses m_{H^0}, m_{A^0}, m_Y and their widths $\Gamma_{H^0}, \Gamma_{A^0}, \Gamma_Y$. A minimum value for the widths can be obtained by computing the partial top decay width and loop-induced (suppressed) decays to gluons and photons through top-quark loops. The parameters of the model can be matched to UV complete models such as the 2HDM. In particular the total width of the particle can be larger if it couples directly to other SM particles, or new states such as a Dark Matter (DM) candidate as explored in [10, 239, 240]. In what follows we will present results for the simplified model using the minimal width and a larger value allowing for other decay channels.

Finally we note that in our model implementation one can have spin-0 particles directly coupling to the gluons through the dimension-5 operators in the same way as presented in Eq. 1.51 for the Higgs boson. We will employ these operators in Sec. 4.6.

4.2.2 2HDM

Our set of representative 2HDM benchmark scenarios are introduced in Tab. 4.1. These are all type–II and have been constructed in agreement with all up–to–date parameter space constraints. Notice we used again benchmark B1 to allow comparison with the other processes we studied. The other three new benchmarks were designed to give highly enhanced top Yukawa couplings to heavy states and different mass scales.

In Tab. 4.2 we quote the numerical values for the top Yukawa couplings, scalar widths and top branching ratios for the benchmarks defined in Tab. 4.1. All couplings are again normalized to their SM counterparts, as denoted by $\hat{g}_{hxx} \equiv g_{hxx}^{\text{2HDM}} / g_{Hxx}^{\text{SM}}$, where H stands for the SM Higgs boson.

The properties of the different 2HDM scenarios can be summarised as follows:

	$\hat{g}_{h^0 tt}$	$\hat{g}_{H^0 tt}$	$\hat{g}_{A^0 tt}$	Γ_{H^0}	$BR_{H^0 \to t\bar{t}}$	Γ_{A^0}	$BR_{A^0 \to t\bar{t}}$
B1	0.96	-0.64	0.57	0.138	0.0	7.20	0.723
B9	1.00	-1.11	1.11	13.75	0.9997	29.97	0.999
B10	1.00	-1.43	1.43	3.39	0.9989	64.57	0.849
B11	1.00	-1.67	1.67	30.93	0.9998	105.23	0.896

Table 4.2: Normalised top quark Yukawa couplings, heavy scalar widths (in GeV) and top branching ratios for the different 2HDM benchmarks defined in Tab. 4.1. All couplings are normalised to their SM counterparts.

- **B1:** The $\tan\beta > 1$ is responsible for smaller top Yukawa couplings for the heavy scalars. The CP-even scalar has a rather narrow width (main decay channel is $h^0 h^0$) and lies below the resonant top–anti-top threshold while for the pseudoscalar the branching ratio to tops rises to more than 70%.

- **B9:** Both new resonances feature slightly enhanced top Yukawa couplings. In this scenario the new particles are all around 500 GeV and always decay into $t\bar{t}$. The widths of the heavy scalars remain below 10% of the mass.

- **B10:** The top Yukawa couplings are enhanced due to the smaller value of tan β. Compared to B9 the width of the scalar is suppressed due to its lower mass while the width of the pseudoscalar reaches $\sim$10% of its mass. The CP-even state decays almost exclusively to top quarks, while A^0 can also decay into a ZH pair.

- **B11:** Both resonances are rather broad due to the larger masses of the particlestheir and enhanced couplings to the top quark. Both H^0 and A^0 decay predominantly to top quarks.

4.3 Features of additional scalar contribution to top pair production

In this section we explore the main features of the top pair production process in the presence of new scalars. Conclusions can be drawn already at the amplitude squared level by varying the various model parameters. We investigate the interference patterns between the signal and the QCD background in the presence of

- one state, CP-even or CP-odd,

- one CP-mixed state

- two states, one CP-even and one CP-odd.

We note here that while both scalar and pseudoscalar amplitudes interfere with the QCD background, there is no interference between them if the two spin-0 states are one pure CP-even and one pure CP-odd. We also mention that bottom quarks in principle enter in this process as they have non-zero Yukawa couplings. However, as the effects we consider here concern the region above the top–anti-top threshold, any contribution of bottom quarks is expected to be very small for moderate values of the bottom Yukawa. In the 2HDM scenarios we consider a small value of $\tan\beta$, so that all bottom Yukawa couplings are small. Indeed in the 2HDM, when the top Yukawa coupling is increased, which is what our benchmarks aim to do, then the bottom Yukawa coupling is automatically reduced. In conclusion, we can safely ignore bottom-quark loops in what follows.

In the case of a CP-even or mixed state the signal interferes also with the SM-like Higgs (125 GeV) contribution. We find that this interference is suppressed compared to the interference with the QCD background yet we do include it in our results. We also compute the light Higgs contribution to the SM background, both the pure Higgs contribution and its interference with the QCD background. Both are extremely suppressed compared to the QCD background.

To demonstrate our results we select the invariant mass distribution of the top pair, an observable which can very clearly reveal the presence of a resonance.[2] As an example we show in Fig. 4.2 the amplitude squared for the signal, background and interference separately for a scalar, a pseudoscalar and mixed (equal scalar and pseudoscalar couplings) spin-0 state for various widths (90° centre-of-mass frame scattering angle). The Yukawa couplings ($g_t^{S,P}$) are all set to 1. The values of the widths chosen for the plots are i) the minimal width computed at LO assuming the scalar particle only couples to the top and ii) a larger width to allow for decays to other SM particles (e.g. vector bosons) or new states (such as a DM particle).

The plots show that the interference is important even for narrow resonances with widths as small as ∼2% of the mass, which is the case for the scalar 500 GeV resonance. The interference can be as large as the signal in size and leads to the characteristic peak-dip structure. The different width choices highlight the impact of the width of the additional particle on the relative importance of the interference. When the width of the heavy scalar becomes large ($\sim 10\%$ of the mass) the peak-dip structure becomes less pronounced and basically leads to a dip dominated by the interference.

---

[2]We note here that top decays can also be generated in our simulation framework. While observables involving top decay products are known to provide useful information on the nature of a top resonance [219], in this chapter for brevity we will only consider stable top quarks.
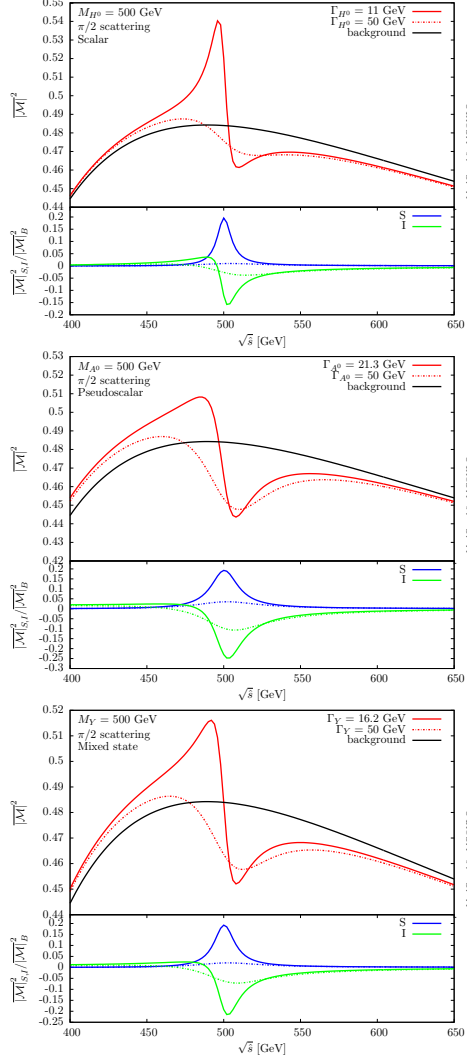
Figure 4.2: Amplitude squared for $gg(\to \Phi) \to t\bar{t}$ in the presence of a heavy scalar of 500 GeV as a function of the centre-of-mass energy for different widths. The centre-of-mass frame scattering angle is set to $90^{\rm o}$. Results are shown for a scalar state (top), a pseudoscalar one (middle) and a mixed one (bottom). The lower inset shows the ratio of the signal and interference over the QCD background.

Note also that the pseudoscalar resonance peak reaches larger values than the scalar
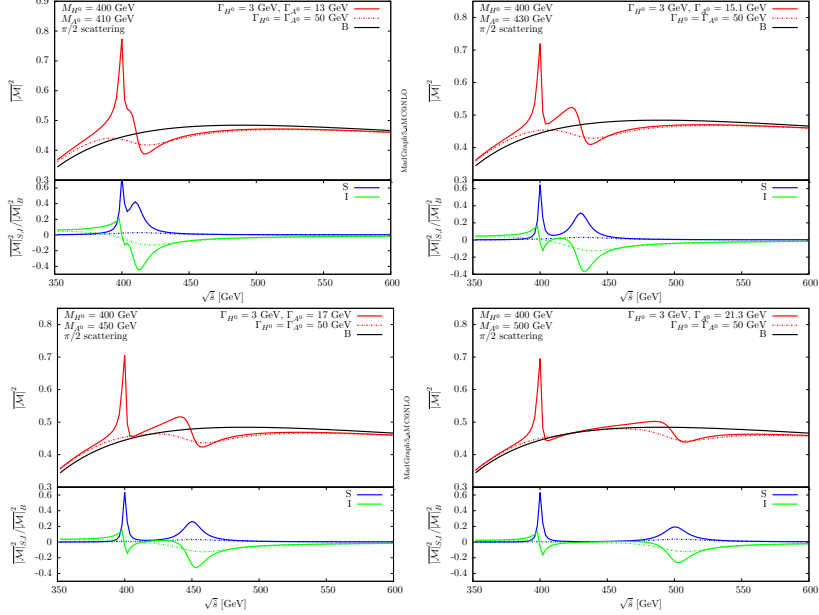
Figure 4.3: Amplitude squared for $gg(\to \Phi) \to t\bar{t}$ in the presence of a scalar and a pseudoscalar state as a function of the centre-of-mass energy for different mass splittings and widths. The centre-of-mass frame scattering angle is set to $90^{\rm o}$. Top left: small mass splitting ($\Delta m = 10$ GeV), top right: moderate mass splitting ($\Delta m = 30$ GeV), bottom left: large mass splitting ($\Delta m = 50$ GeV) and bottom right: larger mass splitting ($\Delta m = 100$ GeV). All couplings are equal to the SM top Yukawa. The lower inset shows the ratio of the signal and interference over the QCD background.

case for same mass and width, which is related to the structure of the top loop amplitudes for $gg \to H^0/A^0$, see Eq. 1.76.

In a scenario where both a heavy scalar, H^0, and a pseudoscalar, A^0, are present, more interesting features arise in the invariant mass distribution of the top pair as discussed also in [241]. We consider this scenario in Fig. 4.3, where the amplitude squared is studied in the presence of one scalar and one pseudoscalar particle. The patterns observed in the invariant mass distribution are determined by the mass splitting and widths of the two particles. In the narrow width case, for $\Delta m = 10$ GeV it is not possible to disentangle the two peaks. However, a larger mass splitting leads to two distinctive peak-dip structures. For the 50 GeV widths the effects are very mild compared to the background and dominated by the interference. In practice, the ex-
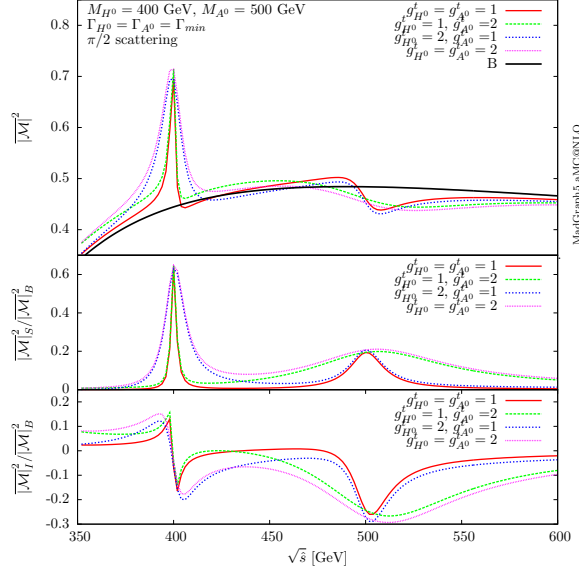
Figure 4.4: Amplitude squared for $gg(\to \Phi) \to t\bar{t}$ as a function of the centre-of-mass energy for the H^0 and A^0 resonances for different values of the Yukawa couplings. The widths are set to the minimum ones: for $\hat{g}_t = 1, \Gamma_{H^0} = 3$ GeV, $\Gamma_{A^0} = 21.3$ GeV and for $\hat{g}_t = 2, \Gamma_{H^0} = 12$ GeV, $\Gamma_{A^0} = 85.1$ GeV.

perimental top pair invariant mass resolution will determine the mass gap required for the two states to be distinguished even in the narrow width case.

To conclude our amplitude analysis of interference effects in top pair production, we modify the Yukawa couplings $\hat{g}_t^S$, $\hat{g}_t^S$ of the new particles. The results are shown in figure 4.4. Note that flipping the sign of the Yukawas has no effect on the interference pattern for this process as $\mathcal{M}_{signal} \propto (\hat{g}_t y_t)^2$. In this case, the width is computed at LO assuming only top decays for all values of the Yukawa couplings. The plot demonstrates the range of possible shapes one can expect in the case of two resonances with different signal strengths. The values of the Yukawa couplings change not only the normalisation but also the shape as the interference and signal have different functional dependences on the Yukawa coupling. We also note that the signal and interference cannot simply be rescaled when one changes the Yukawa couplings, as for consistency the width of the heavy state should be appropriately recomputed. In particular we notice that in this model the width rapidly increases with the Yukuwa couplings, quickly reaching values beyond the narrow width approximation.

	Scalar		Pseudoscalar	
Width	$\Gamma_{min} = 11.1$	$\Gamma = 50$	$\Gamma_{min} = 21.3$	$\Gamma = 50$
Signal	2.38	0.47	4.54	1.81
Interference	-1.27	-1.25	-2.19	-2.50

Table 4.3: Cross sections (in pb) for the LHC at 13 TeV for the signal and interference with the background for a new heavy scalar or pseudoscalar particle of $m_{H^0,A^0} = 500$ GeV for different width values (in GeV). Yukawas are equal to the SM values.

The same qualitative conclusions can be drawn by studying the results at the proton-proton cross-section level. Leading order results are presented for both the simplified model and the 2HDM scenarios presented above. Signal events and interferences are generated at LO with recent MADGRAPH5_AMC@NLO version, which allows event generation for loop-induced processes. All results are obtained for the LHC at $\sqrt{s} = 13$ TeV with MMHT2014LO PDFs [242]. The renormalisation and factorisation scales are set to $\mu_F = \mu_R = \mu_0 = m_{t\bar{t}}/2$. The cross sections obtained for the signal and interference at LO are shown in Tab. 4.3 for a scalar and pseudoscalar resonance of 500 GeV for two width choices. For comparison the LO QCD background (including the quark–anti-quark contribution) is $\sigma_{QCD} = 498.1^{+31.4\%}_{-22.4\%}$ pb and the interference between SM Higgs and QCD background is $\sigma_{H-QCD} = -0.90^{+32.4\%}_{-23.2\%}$ pb. In the following when we refer to background we will use $\sigma^{LO}_{background} = \sigma^{LO}_{QCD} + \sigma^{LO}_{H-QCD} = 497.2^{+31.4\%}_{-22.4\%}$ pb. Note that $\sigma_H = \sigma^{pp \to H \to t\bar{t}} = 22.15^{+33.3\%}_{-23.5\%}$ fb is also part of the SM background but since its contribution is very small it is here discarded.

Fig. 4.5 shows the $t\bar{t}$ invariant mass distribution for a scalar and pseudoscalar state separately and confirms our observations at the amplitude squared level. The effect of the scalar particle remains at the few percent level compared to the background and hardly visible especially due to a cancellation between the signal and interference contributions, as reported in Tab. 4.3. We note that the signal changes with the width following a $\propto 1/\Gamma$ behaviour at the total cross-section level, as expected in the narrow-width approximation. Effectively, increasing the total width without changing the partial top width decreases the branching ratio ($\Gamma_{t\bar{t}}/\Gamma$). The impact of changing the width on the interference is not straightforward to predict at the total cross-section level. The interference is decomposed into a part coming from the imaginary part of the one-loop amplitude which is always destructive and one coming from the real part which changes sign at the mass of the resonance, as also discussed in [224]. The total interference can be negative or positive depending on the relative size of these two
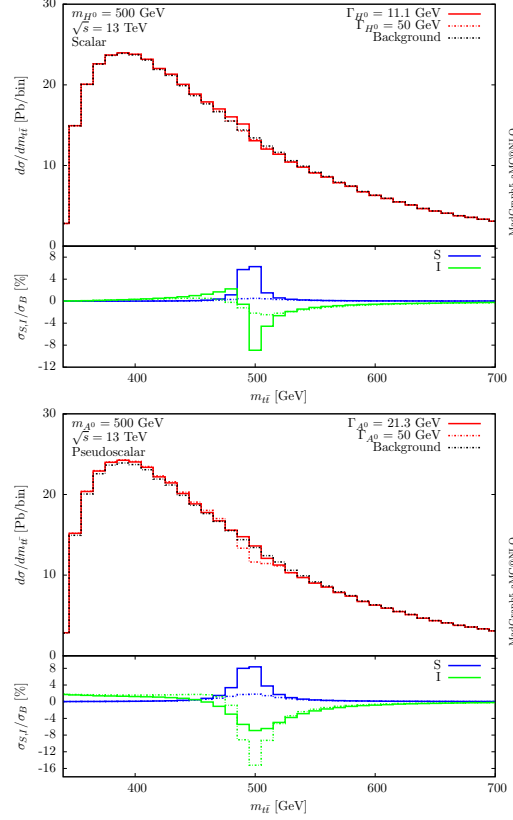
Figure 4.5: Top-pair invariant mass distribution for a single heavy resonance of $m = 500$ GeV with different widths at the LHC at 13 TeV. Top: scalar. Bottom: pseudoscalar. The contributions of the signal and interference are shown separately as a percentage of the QCD background in the lower panels.

components. In general though the relative importance of the interference compared to the signal is larger for larger widths as shown in Tab. 4.3.

In Fig. 4.6 we show the invariant mass distribution for a scenario in which both a scalar and pseudoscalar resonance are present. The corresponding LO cross sections for the signal and interference with the QCD continuum are reported in Tab. 4.4. In this case the mass splitting and widths of the two states are varied. The behaviour of the amplitude squared is replicated here. In the narrow width scenario, for a small mass splitting, we cannot distinguish between the two contributions. For $\Delta m = 50$ GeV two separate peaks appear. In general, we find that the interference is destructive and large compared to the signal, in particular when the widths are large, a case where
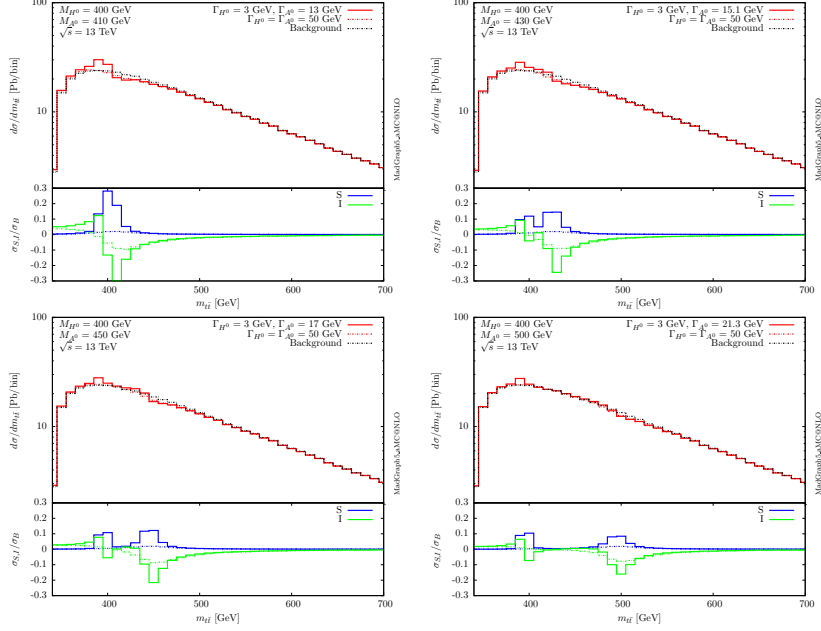
Figure 4.6: Top pair invariant mass distribution for the LHC at 13 TeV for the H^0 and A^0 resonances with different masses and widths. Top left: small mass splitting ($\Delta m = 10$ GeV), top right: moderate mass splitting ($\Delta m = 30$ GeV), bottom left: $\Delta m = 50$ GeV and bottom right: large mass splitting ($\Delta m = 100$ GeV). The ratio of the signal and interference over the QCD background is shown in the lower panels.

deviations from the background are generally suppressed. For all mass combinations, the interference is comparable in size with the signal even for the narrow width choices and its impact on the line-shape is important. The interference can lead to shapes very different from the resonance peaks that one expects from the signal alone.

We conclude this section by considering the 2HDM benchmarks presented in Sec. 4.1 to have a picture of possible deviations from the SM predictions in a UV-complete model. In this case the widths are computed using the 2HDM parameter input. The 2HDM parameters of interest i.e. the Yukawa couplings, the widths and top-quark branching ratios are given in Tab. 4.2. The corresponding cross sections are collected in Tab. 4.5, where we also show the corresponding scale uncertainties obtained by varying the renormalisation and factorisation scales up and down by a factor of two.

$m_{H^0} = 400$ GeV, $m_{A^0} = 410$ GeV	Γ_{min}	$\Gamma = 50$ GeV
Signal	17.56	3.09
Interference	-11.85	-10.69
$m_{H^0} = 400$ GeV, $m_{A^0} = 430$ GeV		
Signal	14.92	2.97
Interference	-9.60	-8.91
$m_{H^0} = 400$ GeV, $m_{A^0} = 450$ GeV		
Signal	12.92	2.77
Interference	-7.88	-7.46
$m_{H^0} = 400$ GeV, $m_{A^0} = 500$ GeV		
Signal	9.68	2.22
Interference	-5.23	-4.94

Table 4.4: Cross sections (in pb) for the LHC at 13 TeV for a new heavy scalar and pseudoscalar particle for different widths and masses. Yukawas are equal to the SM value.

	Total	Signal		Interference	
		Scalar	Pseudoscalar	Scalar	Pseudoscalar
B1	$497.1^{+31.7\%}_{-22.7\%}$	$0.01^{+32.7\%}_{-23.1\%}$	$2.13^{+32.2\%}_{-22.8\%}$	$-0.62^{+32.4\%}_{-23.0\%}$	$-1.78^{+33.7\%}_{-23.6\%}$
B9	$501.0^{+31.8\%}_{-22.7\%}$	$2.90^{+33.0\%}_{-23.3\%}$	$3.51^{+33.5\%}_{-23.5\%}$	$-1.55^{+34.9\%}_{-24.3\%}$	$-1.09^{+40.6\%}_{-27.1\%}$
B10	$504.0^{+32.3\%}_{-23.2\%}$	$10.86^{+31.3\%}_{-22.4\%}$	$3.35^{+33.8\%}_{-23.7\%}$	$-6.56^{+32.2\%}_{-22.9\%}$	$-1.15^{+42.4\%}_{-28.0\%}$
B11	$502.1^{+31.9\%}_{-22.8\%}$	$6.19^{+33.0\%}_{-23.3\%}$	$1.85^{+34.6\%}_{-24.1\%}$	$-3.53^{+34.7\%}_{-24.1\%}$	$0.30^{+67.6\%}_{-56.0\%}$

Table 4.5: Cross section at LO (in pb) for the LHC at 13 TeV for the 2HDM scenarios of Tab. 4.1 with scale uncertainties. The signal and interference is decomposed into contributions from the scalar and pseudoscalar resonances.

The interference is important and destructive for all scenarios, ranging in size from 40% to 100% of the signal at the total cross-section level. For completeness we also show the various contributions involving the light 125 GeV Higgs in Tab. 4.6. These are found to be small in all cases. The differences between the four scenarios in the contributions involving only the light Higgs are due to the differences in the light Higgs Yukuwa coupling. The invariant mass distribution of the top quark pair for the four scenarios is shown in Fig. 4.7. We can see that the dip due to the interference is very small and would therefore be very difficult to observe experimentally.

	$gg \to H \to t\bar{t}$	$H - H^0$ interference	H-QCD interference
B1	$0.019^{+33.2\%}_{-23.4\%}$	$0.03^{+32.7\%}_{-23.4\%}$	$-0.82^{+32.1\%}_{-23.1\%}$
B9	$0.022^{+33.3\%}_{-23.5\%}$	$0.01^{+34.2\%}_{-23.9\%}$	$-0.90^{+32.4\%}_{-23.2\%}$
B10	$0.022^{+33.3\%}_{-23.5\%}$	$0.25^{+32.3\%}_{-23.0\%}$	$-0.90^{+32.4\%}_{-23.2\%}$
B11	$0.022^{+33.3\%}_{-23.5\%}$	$0.03^{+34.3\%}_{-24.0\%}$	$-0.90^{+32.4\%}_{-23.2\%}$

Table 4.6: Cross sections at LO (in pb) for the LHC at 13 TeV for the 2HDM scenarios of Tab. 4.1 with scale uncertainties for the various contributions involving the light SM-like Higgs.

We find that benchmark B1 only shows deviations from the background around the mass of A^0, as H^0 lies below the top–anti-top threshold. The A^0 contribution is dominated by the interference leading to a dip in the invariant mass distribution. Scenario B9 shows a more involved structure due to the presence of two resonances with a 50 GeV mass splitting. All Yukawas are enhanced, nevertheless the large widths and the cancellation of the destructive interference with the signal lead to effects of a few percent compared to the background. Benchmark B10 is the only scenario that leads to a visible resonance peak at 380 GeV and a mild dip at around 590 GeV, corresponding to the narrow H^0 and broad A^0 resonances respectively. Finally B11 shows a small excess over the background at 500 GeV and a mild dip at around 700 GeV. Due to the large widths the effects on the invariant mass distribution are extremely mild and would therefore be difficult to detect.

4.4   Higher-order QCD effects

As we have seen in the previous subsection the interference between the signal and background can lead to interesting peak-dip structures, and needs to be taken into account to obtain a reliable prediction for the line-shape of a new resonance. It is well-known that the interference between the signal and the QCD background is colour-suppressed: i.e. the only background configuration which contributes to the interference is the one where the top–anti-top pair is in a colour singlet state. In this section we investigate whether this colour suppression could be lifted by allowing additional QCD radiation.
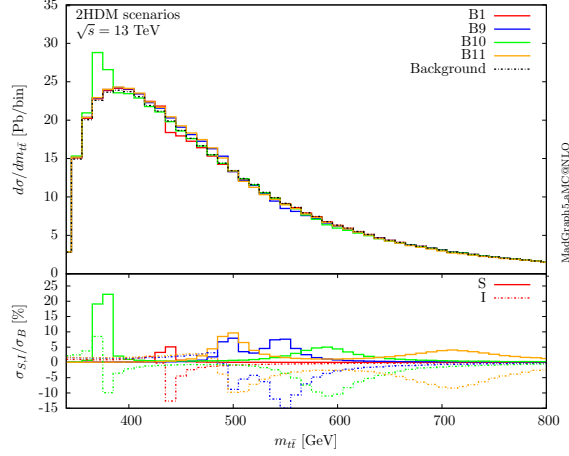
Figure 4.7: Invariant mass distribution for the $t\bar{t}$ pair for the different 2HDM benchmark points. The ratios of the signal and interference over the QCD background are shown in the lower panel.

4.4.1   Signal-background interference in $t\bar{t}$+jet

We consider for the first time signal and background interference effects for the $t\bar{t}$+jet process. Fig. 4.8 shows a comparison between the LO process $pp(\to Y) \to t\bar{t}$ and the one with an additional jet emission $pp(\to Y) \to t\bar{t}j$, for a scalar or pseudoscalar of $m_Y = 500$ GeV and $\Gamma_Y = \Gamma_{min}$. For the $pp(\to Y) \to t\bar{t}j$ process a cut has to be applied on the jet transverse momentum. The ratio of the signal and interference over the background is shown for various cuts on the jet p_T. We find that the extra jet does not give rise to a significant increase of the interference. For the scalar resonance the relative size of the interference is identical to that for the $2 \to 2$ process, while for the pseudoscalar a small increase is found. The line-shape of the resonance is not visibly modified by the QCD radiation. This persists even for very hard jets for which the cross-section is as expected suppressed. We associate this to the fact that the main contribution to the 1-jet process is related to initial state radiation, for which no change in the colour state of the top-quark pair is expected and therefore the colour suppression is not lifted.

We note here that a consistent way to include both 0 and 1 jet multiplicities would be to employ the ME+PS method. However given the results obtained for the 1-jet samples which show the very mild effect of the extra QCD radiation on the interference between signal and background and hence the line-shape of a heavy scalar, we refrain from performing a detailed analysis of a merged sample.
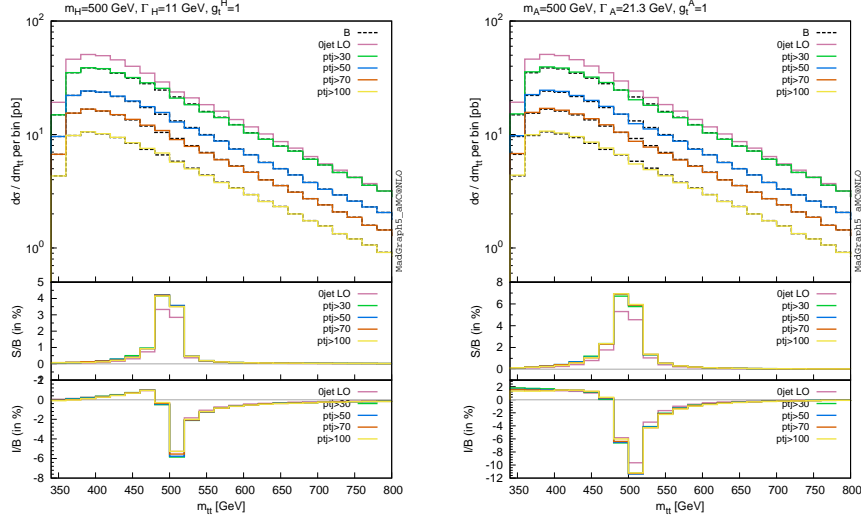
Figure 4.8: Top pair invariant mass distribution for the LHC at 13 TeV for $pp(\rightarrow Y) \rightarrow t\bar{t}(j)$ for a heavy scalar or pseudoscalar with $m_Y = 500$ GeV. Different p_T^j cuts are applied for the $t\bar{t}j$ process. The lower panels show the signal and interference ratios over the background.

4.4.2   NLO results

In order to improve the accuracy of the predictions for this process, we now examine the impact of NLO corrections. We start by reviewing the main ingredients needed for the computation of the signal, background and interference at NLO. The NLO QCD corrections for the signal require 1-loop real emission amplitudes and 2-loop virtual correction amplitudes. A sample of the required diagrams is shown in Fig. 4.9. These can be classified in three categories: initial state corrections, final state corrections and corrections connecting initial and final state, the so-called non-factorisable corrections. The initial state corrections are identical to the NLO corrections for single Higgs production and are well known [243, 244]. The final state corrections are also well known as part of the QCD corrections to the Higgs decay width to heavy quarks [245]. Results are not available for the class of two loop amplitudes shown in the centre of Fig. 4.9, as these require multiscale integrals at the edge of current multiloop technology. Exact results can be obtained for the signal at NLO, as this class of diagrams does not interfere with the Born amplitude as in the Born configuration the top quark pair is in a colour singlet. The non-factorisable corrections only play a
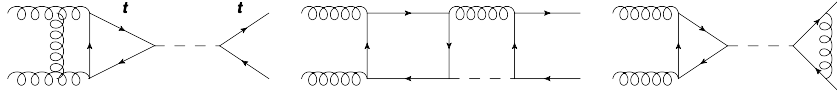
Figure 4.9: Two-loop virtual corrections diagrams for the heavy scalar signal.

role in the interference between the signal and the continuum background, which is therefore formally known only at leading order.

An approximation to the NLO results has been presented in [230], where two approximations are made. The first regards the interaction of the Higgs to the gluons, which is computed in the infinite top mass limit. The second is the computation of the NLO QCD corrections for the signal and interference in the soft gluon approximation. Here we follow a different approach. We compute the NLO corrections for the signal with the exact top mass dependence, while for the interference we employ a K-factor obtained from the geometric average of the signal and background K-factors. The K-factor approximation can be employed both at the total cross-section level and on a bin-by-bin basis for the differential distributions. A similar procedure is recommended for other loop-induced processes such as $gg(\to H) \to VV$ which also suffer from the lack of two-loop results. In the context of this study we have explicitly verified that the geometric average of the signal and background ratios of 1-jet over 0-jet cross section provides a good approximation for the corresponding ratio for the interference in the proximity of the resonance mass.

On the computational side, within MADGRAPH5_AMC@NLO , the background can be obtained automatically at NLO. For the signal the two loop virtual corrections for Higgs production are taken from those in SusHi [246] as implemented in aMC-SusHi [247]. These are combined with the 1-loop corrections in the final state which are computed with MADLOOP. The full 1-loop real and born amplitudes and 2-loop virtual corrections are inserted in the computation through a reweighting procedure.

We decompose the total cross section using the following additive prescription:

$$\sigma_{NLO} = \sigma_{NLO}^{back} + \sigma_{NLO}^{signal} + \sigma_{LO}^{inter} \sqrt{K_S K_B} \,, \tag{4.3}$$

where the signal and background are computed exactly at NLO in QCD. $\sqrt{K_S K_B}$ can involve either the total cross-section K-factors for the signal and the background or the bin-by-bin K-factors in the invariant mass spectrum as well as for any other observable of interest.

For brevity we present results at NLO only for our four 2HDM benchmarks. Results for the simplified model can be straightforwardly obtained with our setup. In Tab.

	Signal	K_S	Interference: $\sqrt{K_S K_B}\, \sigma_{LO}^{inter}$
B1	$3.31^{+16.8\%}_{-14.3\%}$	1.55	$-3.00^{+30.7\%}_{-22.4\%}$
B9	$9.02^{+13.7\%}_{-13.0\%}$	1.41	$-3.53^{+34.3\%}_{-24.1\%}$
B10	$25.37^{+20.0\%}_{-16.0\%}$	1.79	$-9.32^{+32.6\%}_{-24.1\%}$
B11	$11.51^{+14.3\%}_{-13.3\%}$	1.43	$-4.23^{+38.8\%}_{-30.1\%}$

Table 4.7: Cross sections and corresponding scale uncertainties at NLO (in pb) for the LHC at 13 TeV for the 2HDM scenarios. The corresponding K-factors and the interference with the QCD background obtained from the geometric average of the signal and background total cross-section K-factors ($K_B = 1.40$) are also given.

4.7 the signal at NLO with the scale uncertainties, the corresponding K-factors and the NLO approximation for the interference are given for the four scenarios. The interference is computed at LO with NLO PDFs and the result is subsequently adjusted by the K-factor. The total cross-section K-factors are used to obtain the interference K-factor used in Tab. 4.7. We note that the scale uncertainties for the interference are those obtained from a LO computation and therefore are much larger than those of the signal and background. For the interference, our results provide a more accurate prediction, however we do not improve the precision of this contribution and therefore keep the LO uncertainties. For completeness we mention the NLO QCD background cross section $\sigma_{QCD} = 698.6^{+13.2\%}_{-12.4\%}$ pb and the corresponding K-factor $K_B = 1.40$.

The top pair invariant mass distribution for the LHC at 13 TeV is shown in Fig. 4.10. The ratios of the signal and interference over the background are shown at LO and NLO, along with the signal and background K-factors with the corresponding scale uncertainties. We find large QCD corrections for the signal, with K-factors reaching two close to the resonance. The background K-factor is lower but rises with $m_{t\bar{t}}$. Due to the larger K-factor for the signal compared to the background we notice an increase of the signal and interference over background ratios. The significant reduction of the scale uncertainties at NLO is also evident in the results. We note here that for the distributions we have extracted the K-factor for the interference using the signal and background K-factors in each bin.
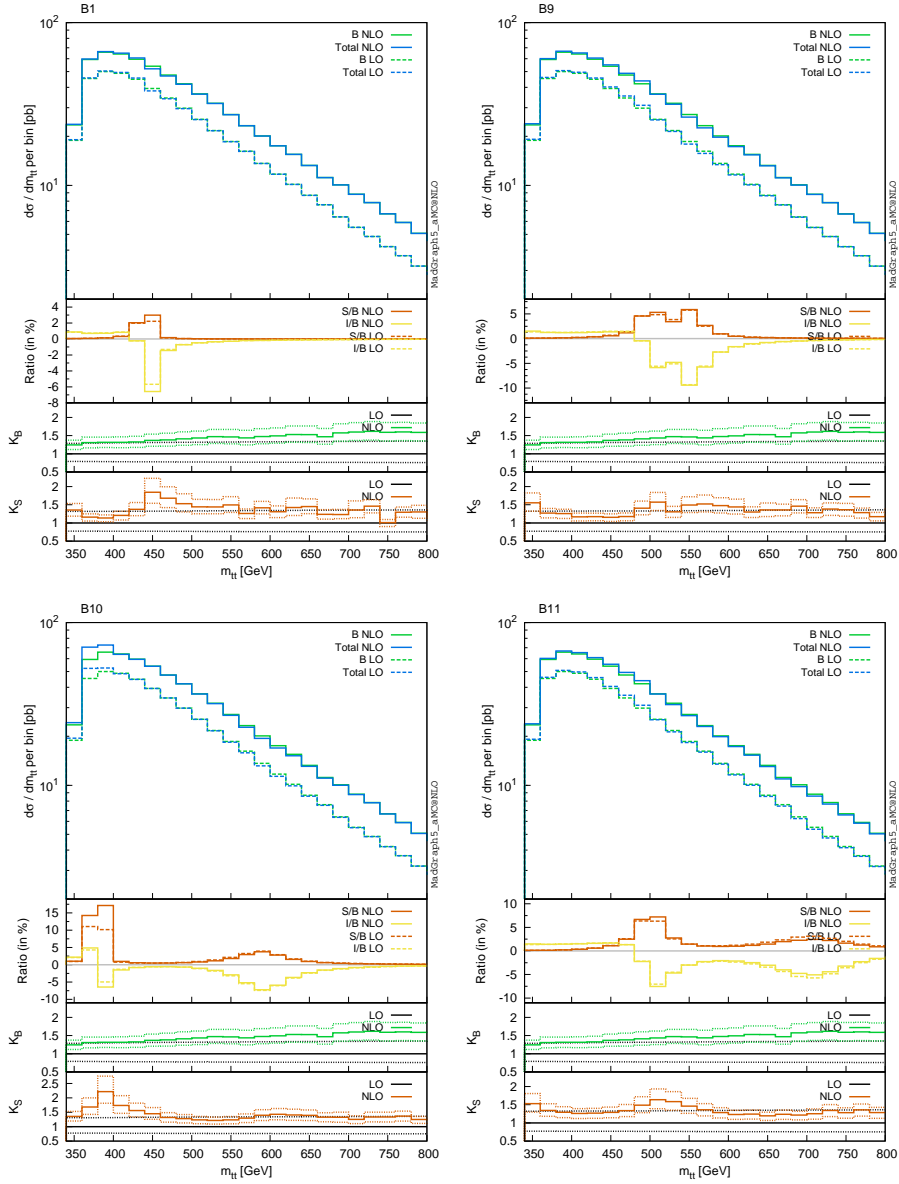
Figure 4.10: Top pair invariant mass distribution for the different 2HDM benchmark points at NLO for the LHC at 13 TeV. The signal and interference ratios over the background are shown in the second panel, while the third and fourth panels show the background and signal K-factors along with the corresponding scale uncertainty bands.

4.5   Comparison with experimental data

4.5.1   Constraints on a simplified Dark Matter model

Evidence for the existence of DM, although indirect, is quite convincing [248–250]. Measurements of the cosmic microwave background and baryonic acoustic oscillations predict a dominant dark matter component in the matter budget of the Universe (in the framework of standard cosmology). In addition, detection of gravitational anomalies, such as the flattening of galaxy rotation curves and the presence of gravitational lensing in the absence of visible matter (*e.g.* the bullet cluster [251]), strongly favours gravitational interactions of dark matter as plausible explanations.

The many hints for dark matter created a huge endeavour to detect it and measure its properties, leading to a number of experiments and searches which exploit very different ideas and approaches to dark matter detection. The experiments can be broadly grouped into three categories:

- A wide range of underground nuclear recoil experiments aimed at detecting galactic dark matter scattering off atomic nuclei;

- Searches for dark matter annihilation in the galaxy or nearby dense sources via measurements of, for instance, gamma-rays;

- Collider searches in channels with large missing transverse energy ($\not{E}_T$).

- Collider mediator searches without $\not{E}_T$.

However, despite an enormous experimental effort, the detection of the dark matter particles remains elusive. In fact, there is no clear indication that dark matter interacts with ordinary matter via forces other than gravity, and current experimental results are not able to put stringent bounds on the dark matter properties and couplings in a model-independent way.

As so little is known about the true nature of dark matter, it is a useful strategy to try and constrain viable dark matter scenarios in the most model-independent way (*i.e.* via simplified models [252]), confronting them with results from collider experiments, direct dark matter searches, astrophysical observations and cosmology.

The simplified top-philic dark matter model that we consider is constructed simply by supplementing the toy model we already used in this chapter with a Dirac-type fermionic dark matter candidate X. The interactions of the particles are described by

the Lagrangian :

$$\mathcal{L}_{t,X}^{Y} = -\Big(\hat{g}_t \frac{y_t}{\sqrt{2}} \bar{t}t + g_X \bar{X}X\Big)Y \,, \tag{4.4}$$

where the new physics interaction strength for the dark matter is denoted by g_X.

The model contains four free parameters (two couplings and two masses),

$$\{\hat{g}_t,\, g_X,\, m_X,\, m_Y\}\,, \tag{4.5}$$

while the width Γ_Y is fixed by the remaining model parameters.

In this section we will mainly focus on indirect collider searches in the $\gamma\gamma$, $t\bar{t}$ and four tops channels. We start by reviewing the constraints on them separately before putting them on top of cosmological and astronomical constraints[3].

Collider indirect searches

As discussed above, simplified top-philic dark matter scenarios can be probed at colliders through the production of the mediator either in association with a top-quark pair or through a top-quark loop. Depending on the mass and coupling hierarchy, the mediator decays either into a pair of dark matter particles, which results in signatures including missing transverse energy ($\not{E}_T$), or into SM final states. The size of the cross sections associated with these two classes of mediator production mechanisms, among other, is depicted in Fig. 4.11 where we present their dependence on the mediator mass m_Y. For the case where the mediator is singly produced, we use the Higgs cross section values that are reported in the Higgs Cross Section Working Group documentation [253] and evaluated at the next-to-next-to-leading order (NNLO) accuracy in QCD.

All cross sections shown in Fig. 4.11 are proportional to $\hat{g}_t^2$ and we therefore arbitrarily choose $\hat{g}_t = 1$ as a benchmark. In this case, sizeable cross sections of $10^1 - 10^3$ pb are expected for the production of light mediators with $m_Y \lesssim 100$ GeV at a centre-of-mass energy of 8 TeV, the dominant mechanism being the loop-induced $gg \to Y_0$ production mode. Requiring an extra hard jet in the final state reduces the cross section by a factor which depends on the missing energy (or the jet transverse momentum p_T) selection, and the production rates are not sensitive to the mediator mass as soon as the latter is smaller than the $\not{E}_T$ selection threshold. The cross sections for producing the mediator in association with a SM Higgs or Z boson are further suppressed and hence are not shown here. In contrast, the cross section related to the production of the

---

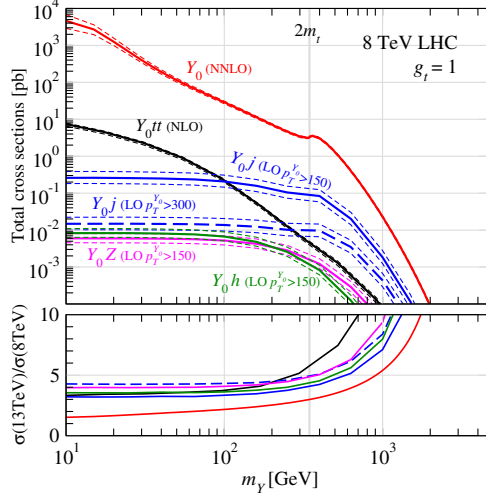[3]More detail about the cosmological part can be found in [10].

Figure 4.11: Total cross sections (with scale uncertainties) for various mediator production channels (with $\hat{g}_t = 1$) at a centre-of-mass energy of $\sqrt{s} = 8$ TeV as a function of the mediator mass. The NNLO cross section for single mediator production $\sigma(Y_0)$ is taken from the Higgs Cross Section Working Group report, the $Y_0 t\bar{t}$ one is computed at NLO accuracy and all other loop-induced processes are evaluated at LO accuracy. The monojet ($Y_0 j$), mono-Z ($Y_0 Z$) and mono-Higgs ($Y_0 h$) cross sections include a transverse momentum cut on the mediator as indicated in the figure. In the lower panel, we show the ratios of the cross sections evaluated at a centre-of-mass energy of $\sqrt{s} = 13$ TeV over those at 8 TeV.

mediator in association with a top-quark pair is significant for light mediators, but falls off quickly with the increase in the mediator mass due to phase-space suppression.

In this section we focus on searches relying on Y_0 resonant contributions to SM processes. In our scenario, dijet, diphoton, top-pair and four-top searches are expected to set constraints on the model parameter space. This is discussed in the next section.

Resonance constraints

Tab. 4.8 summarizes the 8 TeV LHC constraints on direct resonnance searches that we will use in this section.

We start by giving the partial width expressions for a scalar or pseudoscalar Y particle. We will mainly be interested in three kinds of decays: decays into fermions (mostly in $t\bar{t}$ pairs), gluons and photons (due to the large excitment there was around the 750 GeV

Final state	Imposed constraint	Reference	Comments
jj	$\sigma(m_Y = 500\,\mathrm{GeV}) < 10\,\mathrm{pb}$	CMS [254]	for $m_Y > 500\,\mathrm{GeV}$
$\gamma\gamma$	$\sigma(m_Y = 150\,\mathrm{GeV}) < 30\,\mathrm{fb}$	CMS [255]	for $m_Y > 150\,\mathrm{GeV}$
$t\bar{t}$	$\sigma(m_Y = 400\,\mathrm{GeV}) < 3\,\mathrm{pb}$	ATLAS [221]	for $m_Y > 400\,\mathrm{GeV}$
$t\bar{t}t\bar{t}$	$\sigma < 32\,\mathrm{fb}$	CMS [256]	Upper limit on σ^{SM}

Table 4.8: Summary of the 8 TeV LHC constraints used in this section.

excess in the diphoton channel). The last two decays include loops as the new spin-0 particle Y is not electrically charged nor coloured. These loops are again described at LO through the same two form factors given in Eq. 1.76. Note that in the following expression we include possible extra effective coupling to the gluons c_g and photons c_γ introduced in Eq. 1.50-1.51.

$$
\Gamma(Y_S \to t\bar{t}) = \hat{g}_{Yt\bar{t}}^2 \frac{3y_t^2 m_Y}{16\pi} \beta_t^3 \, \Theta(m_Y - 2m_t)\,,
$$

$$
\Gamma(Y_P \to t\bar{t}) = \hat{g}_{Yt\bar{t}}^2 \frac{3y_t^2 m_Y}{16\pi} \beta_t \, \Theta(m_Y - 2m_t)\,,
$$

$$
\Gamma(Y_S \to gg) = \frac{\alpha_s^2 m_Y^3}{72\pi^3 v^2} \left| \frac{3}{2}\hat{g}_{Yt\bar{t}}F_S(\tau_t) + c_g^S \right|^2,
$$

$$
\Gamma(Y_P \to gg) = \frac{\alpha_s^2 m_Y^3}{32\pi^3 v^2} \left| \hat{g}_{Yt\bar{t}}F_P(\tau_t) + c_g^P \right|^2,
$$

$$
\Gamma(Y_S \to \gamma\gamma) = \frac{\alpha_e^2 m_Y^3}{81\pi^3 v^2} \left| \frac{3}{2}\hat{g}_{Yt\bar{t}}F_S(\tau_t) + c_\gamma^S \right|^2,
$$

$$
\Gamma(Y_P \to \gamma\gamma) = \frac{\alpha_e^2 m_Y^3}{36\pi^3 v^2} \left| \hat{g}_{Yt\bar{t}}F_P(\tau_t) + c_\gamma^P \right|^2 \tag{4.6}
$$

with

$$
\beta_t = \sqrt{1 - \frac{4m_t^2}{m_Y^2}} \tag{4.7}
$$

$t\bar{t}$ **resonances**   For scenarios with mediator masses above the top-antitop threshold ($m_Y > 2m_t$), $t\bar{t}$ resonance searches from both ATLAS and CMS [221, 257, 258] can be used as probes of the model. We derive constraints on our model from the ATLAS 8 TeV $t\bar{t}$ resonance search [221] that relies on the reconstruction of the invariant mass of the top-quark pair to derive a 95% CL exclusion on the existence of a new scalar particle coupling to top quarks. The associated cross section limits range from 3.0 pb for a mass of 400 GeV to 0.03 pb for $m_Y = 2.5$ TeV, assuming that the narrow width
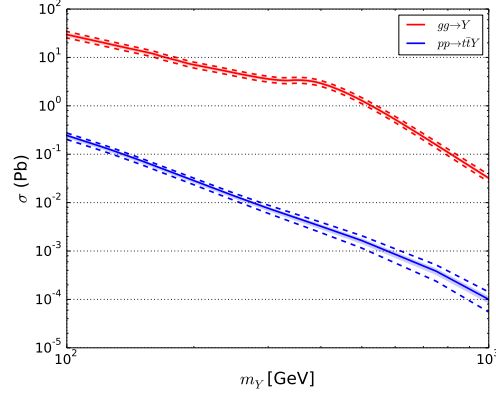
Figure 4.12: NNLO $gg \to Y_0$ and NLO $pp \to t\bar{t}Y_0$ production cross section taken from the HXSWG as a function of the Y mass. The color band shows QCD scale uncertainty, while dashed line represent the PDF+α_s uncertainty.

approximation is valid with a mediator width being of at most 3% of its mass and that there is no interference between the new physics and SM contributions to the $t\bar{t}$ signal.

Constraints are computed using the 8 TeV NNLO mediator production cross section from the Higgs Cross Section Working Group (HXSWG) (see Fig. 4.12) and the relevant top-antitop mediator branching ratio derived from the formulas presented in Eq. 4.6. The latter is in fact very close to one in the relevant region as the mediator decays into gluons and photons is loop-suppressed. The results are presented in the $(m_Y, \hat{g}_t)$ plane in Fig. 4.13. The left plot shows that scalar mediators with masses ranging from 400 GeV to 600 GeV could be excluded for $\hat{g}_t$ couplings in the $[1, 3]$ range, the exact value depending on m_Y and on the fact that the narrow-width approximation must be valid. When considering a pseudoscalar mediator instead (right plot of 4.13), we see that the excluded region for the coupling goes down to $[0.6, 1.6]$ because of the width limitation requirement and the higher production cross section. Results for a mixed case are not shown here as they can be guessed from the combination of the two plots. These two plots demonstrate the ability of the $t\bar{t}$ channel to probe a significant portion of the $m_Y > 2m_t$ region of the model parameter space.

Four-tops signals Scenarios featuring a mediator mass above twice the top-quark mass can be probed via a four-top signal, since the mediator can be produced in association with a pair of top quarks and further decay into a top-antitop system. Theoretically, the SM four-top cross section has been calculated with high precision [259], but the sensitivity of the 8 TeV LHC run was too low to measure the cross section. Instead,
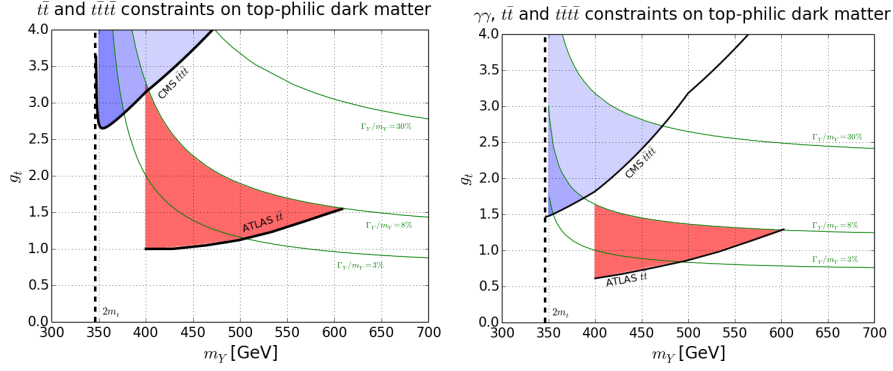
Figure 4.13: Resonance search constraints from the LHC results at a collision centre-of-mass energy of 8 TeV on the simplified top-philic model presented in terms of the mediator mass m_Y and the $\hat{g}_t$ coupling (left: scalar, right: pseudoscalar). The different coloured areas are excluded by the $t\bar{t}$ [221] (red) and $t\bar{t}t\bar{t}$ [256] (blue) searches. We include information on the mediator width to mass ratios (green curves). We assume a negligible branching ratio to the invisible sector.

an upper limit on the cross section at a centre-of-mass energy of 8 TeV has been derived [256, 260]. The four-top production rate is constrained to be below 32 fb [256], a value that has to be compared to the SM prediction of about 1.3 fb. Only models with new physics contributions well above the background (see *e.g.*Ref. [261]) can therefore be constrained by the four-top experimental results.

In our model, the new physics contributions to the four-top cross section can be approximated by the $t\bar{t}Y_0$ cross section, the branching ratio being $B(Y_0 \to t\bar{t}) \sim 1$. Using the NLO cross section (see Fig. 4.12), we derive limits that we represent in the $(m_Y, \hat{g}_t)$ plane in Fig. 4.13. For a scalar mediator a small region of the parameter space with $\hat{g}_t > 2.5$ and in which the mediator mass lies in the $[2m_t, \sim 450 \text{ GeV}]$ mass window turns out to be excluded. On the other hand for a pseudoscalar resonance, the region with $\hat{g}_t > 1.5$ in the mass range $[2m_t, \sim 500 \text{ GeV}]$ can be excluded. The weakness of the limit is related to the steeply decreasing cross section for $pp \to Y_0 t\bar{t}$ with the increase in m_Y.

The mediator width   In all the above studies, the mediator width has been assumed narrow. In the region where $m_Y > 2m_t$, the width of the mediator rises quickly with its mass, and the width over mass ratio rapidly exceeds the 3% value that has been imposed in the ATLAS $t\bar{t}$ resonance search [221] as can be seen in Fig. 4.13. The reinterpretation of the ATLAS results to a generic $t\bar{t}$ resonance model should

therefore be made carefully, as the limit cannot be necessarily applied to scenarios featuring significantly larger mediator widths. This is shown in Fig. 4.13 where we can also observe that most of the points that would have been excluded by the ATLAS search do not fulfil the requirement of a width below 3% of the mediator mass. In our excluded region of the parameter space, we allow the mediator width to reach 8% of its mass, by the virtue of the experimental resolution on the invariant mass of the $t\bar{t}$ system. This leads to the exclusion of scenarios with mediator masses up to 600 GeV.

The ATLAS resonance $t\bar{t}$ study claims that varying the width of the resonance from 10% to 40% results in a loss in sensitivity by a factor 2 for a 1 TeV resonance. An extension of the reinterpretation of the ATLAS limits on our simplified top-philic dark matter model to the case of larger resonance widths could then be performed by rescaling the limits by the appropriate correction factor. We have nonetheless found that no additional points are excluded even without rescaling the sensitivity of the search as the ATLAS analysis rapidly loses sensitivity for resonance masses above 600 GeV. Considering model points with a mediator width to mass ratio of at most about 8% therefore provides a realistic exclusion over the entire model parameter space.

Dijet and diphoton resonances   Dijet and diphoton resonance search results could (in principle) be used to constrain the simplified top-philic dark matter model. Due to double-loop suppressions, mediator-induced contributions to dijet and diphoton production are only relevant in the parameter space regions where $m_Y < 2m_X, 2m_t$ (*i.e.* where the mediator cannot decay into top quarks and/or dark matter particles). The partial mediator decay rate into gluons is then always dominant (as can be seen in Eq. 4.6) since

$$\frac{\Gamma(Y_0 \to \gamma\gamma)}{\Gamma(Y_0 \to gg)} \sim \frac{8}{9}\frac{\alpha_e^2}{\alpha_s^2} \approx 10^{-3} \ . \tag{4.8}$$

All LHC dijet resonance searches focus on the dijet high invariant-mass region, leading to no useful constraints on the top-philic dark matter model. The lowest mediator mass that is probed is ~ 500 GeV, with a visible cross section restricted to be smaller than 10 pb [254].

Although the branching ratio of the mediator into a photon pair is very small, the background associated with a diphoton signal is low so that one expects to be able to obtain stringent constraints on the model from the diphoton search results. We focus here on the CMS 8 TeV diphoton search [255] that investigates resonance masses ranging from 150 GeV to 850 GeV and derives limits on the corresponding cross section. For instance, the 95% CL upper bound on the mediator-induced diphoton production cross section $\sigma(pp \to Y_0 \to \gamma\gamma)$ is of 20 fb (4 fb) for a mediator mass of 150 GeV (300 GeV). Making use of the $pp \to Y_0$ cross section values shown in
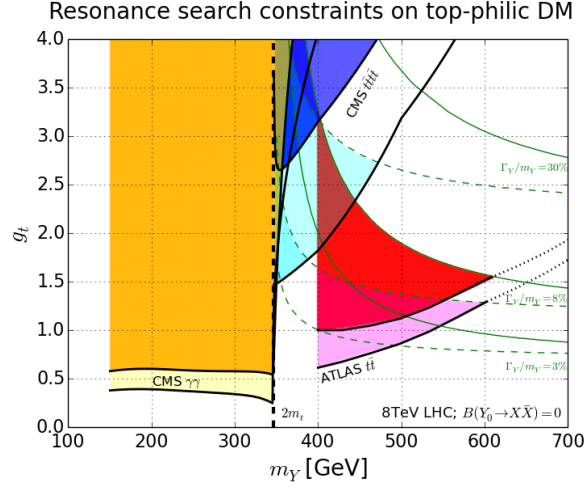
Figure 4.14: Resonance search constraints from the LHC results at a collision centre-of-mass energy of 8 TeV on the simplified top-philic dark matter model presented in terms of the mediator mass m_Y and the $\hat{g}_t$ coupling. The different coloured areas are excluded by the diphoton [255] (orange), $t\bar{t}$ [221] (red) and $t\bar{t}t\bar{t}$ [256] (blue) searches. Lighter colours (yellow, magenta, cyan) correspond to a pseudoscalar Y_0. We include information on the mediator width to mass ratios (green curves, solid: scalar, dashed: pseudoscalar). We assume a negligible branching ratio to the invisible sector.

Fig. 4.12 and the $Y_0 \rightarrow \gamma\gamma$ branching ratio computed from the formulas shown in Sec. 4.2.2, we present diphoton constraints on the model on top of the $t\bar{t}$ and four tops constraints in the $(m_Y, \hat{g}_t)$ plane in Fig. 4.14 for both spin-0 parity. These results assume that the dark matter particle is much heavier than the mediator that can thus not resonantly decay invisibly. The constraints are found to be stringent below the $2m_t$ threshold, where the $\hat{g}_t$ coupling cannot be larger than 0.6.

Concluding remarks on direct mediator searches Mediator resonance searches at 8 TeV show good prospects of constraining our simplified top-philic model in a complementary way, especially in the mediator mass range of 150–600 GeV by means of the top and diphoton searches. So far, the $t\bar{t}$ resonance searches are strictly applicable to a limited parameter space region of the simplified model, and considering larger widths in the interpretation of the future results would allow for a more straightforward reinterpretation of the limits to a wider range of parameters. Concerning the four-top analysis, it can presently only exclude a restricted part of the parameter space, but
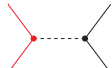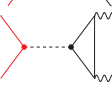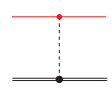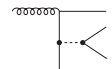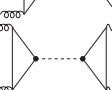
Cosmology	relic indirect	$m_X > m_t$	Planck, Fermi-LAT
		$m_X < m_t$	
Astrophysics		$m_X > m_Y$	
	direct	$m_X > 1\,\mathrm{GeV}$	LUX, CDMSLite
Colliders	no $\not{E}_T$	$m_Y > 2m_t$	$4t$
		$m_Y > 2m_t$	$t\bar{t}$
		$m_Y < 2m_X, 2m_t$	$\gamma\gamma$

Table 4.9: Signatures of our simplified top-philic dark matter model.

future measurements are expected to lead to more competitive bounds while diphoton imposes very stringent exclusion limits for lower Y_0 masses.

Combined results

Let's now have a look at how $t\bar{t}$, diphoton and four tops results can add constraints on our DM top philic model on top of the astrophysical and cosmological constraints coming from direct detection, relic density and indirect detection (see Tab. 4.9). Note that a comprehensive analysis have been performed including constraints for additional processes at the LHC including $t\bar{t}$+ MET constraints. However for the sake of brevity we stick here to the resonnance effect only. See [10] for more details. In the following, we explore the full four-dimensional model parameter space and present results in terms of two-dimensional projections.

We perform a four-dimensional sampling using the MULTINEST algorithm [262, 263]. The choice of prior ranges for the parameters is summarised in Tab. 4.10. We choose

MULTINEST parameter	Prior
$\log(m_X/\,\mathrm{GeV})$	$0 \to 3$
$\log(m_Y/\,\mathrm{GeV})$	$0 \to 3.7$
$\log(g_X)$	$-4 \to \log(\pi)$
$\log(\hat{g}_t)$	$-4 \to \log(\pi)$

Table 4.10: MULTINEST parameters and prior ranges for the four free parameters. All priors are uniform over the indicated range.

	Observable	Value/Constraint	Comment
Measurement	$\Omega_{\mathrm{DM}}h^2$	0.1198 ± 0.0015	Planck 2015 [264]
Limits	Γ_Y/m_Y	< 0.2	Narrow width approximation
	Γ_Y	$> 10^{-11}$ GeV	Ensures prompt decay at colliders
	σ_n^{SI}	$< \sigma_{\mathrm{LUX}}^{\mathrm{SI}}$ (90% CL)	LUX bound [265] ($m_X > 8$ GeV)
	σ_n^{SI}	$< \sigma_{\mathrm{CDMS}}^{\mathrm{SI}}$ (95% CL)	CDMSlite bound [266]
			($1\,\mathrm{GeV} < m_X < 8\,\mathrm{GeV}$)

Table 4.11: Summary of the observables and constraints used in this analysis and encoded into our MULTINEST routine. The relic density constraints assume a Gaussian likelihood function, while the direct detection limits use step likelihood functions smoothed with half a Gaussian.

to limit the coupling values to a maximum of π to ensure perturbativity. Tab. 4.11 summarises the constraints that we have imposed on the model parameter space.

Throughout our study, we assume that X is the dominant dark matter component, namely that it fully accommodates a relic density $\Omega_{\mathrm{DM}}h^2$ as measured by the Planck satellite [264]. Concerning the direct detection of dark matter, we consider the currently most stringent bounds on the spin-independent (SI) nucleon-DM cross section as measured by LUX for dark matter with $m_X > 8$ GeV [265] and by CDMSLite for $1\,\mathrm{GeV} < m_X < 8\,\mathrm{GeV}$ [266]. We also include indirect detection constraints that are imposed on the basis of the gamma-ray measurements achieved by the Fermi-LAT telescope [267,268]. For the purpose of the relic density and direct detection cross section calculations, we used both the MADDM [269, 270] and MICROMEGAS [271] numerical packages, although we only present the results obtained with MADDM.

We find that in the region where $g_X, \hat{g}_t \leq \pi$, the 8 TeV collider results on direct mediator production and decay into SM particles ($t\bar{t}, \gamma\gamma, t\bar{t}t\bar{t}$) provide relevant bounds.
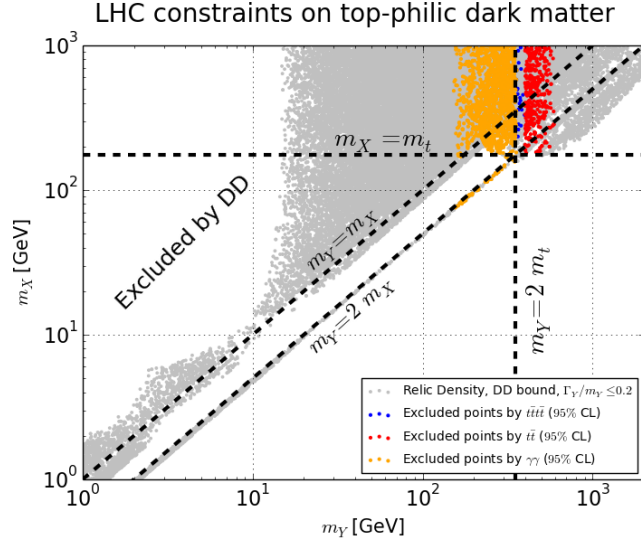
Figure 4.15: Results of our four-dimensional parameter scan projected onto the (m_Y, m_X) plane once constraints set from the LHC results are imposed for a scalar Y particle. The points excluded by the diphoton, the $t\bar{t}$ and the four-top considered searches all satisfy the relic density, narrow width and direct detection constraints.

Fig. 4.15 illustrates our results and shows the scenarios that are excluded by resonant top-pair searches as well as by the four-top analysis and diphoton constraints. All points in the plot accommodate the dark matter relic density and direct detection constraints, while the colours indicate points excluded by individual complementary collider bounds. The vast majority of excluded points lie in the region where $2m_X > m_Y$. This is the region where the mediator decay into a pair of dark matter particles is kinematically forbidden, ensuring large branching fractions for decays into SM particles. The $t\bar{t}$ results constrain the $400 < m_Y < 600$ GeV region. The four-top probe is able to exclude a narrow parameter space region close to $m_Y \sim 2m_t$, in agreement with the findings shown in Fig. 4.13 while the diphoton excludes lower Y_0 masses up to 150 GeV.

Relaxing the requirements on the relic density, the direct detection and the upper bound on the coupling strengths allows for another meaningful study of combined collider constraints. For this purpose we have performed a joint analysis of collider bounds on the top-philic simplified dark matter model in the scope of a four-dimensional parameter scan with a flat likelihood function over all dimensions. We

have performed the scan by restricting the couplings to be smaller than 2π, as well as by allowing the mediator widths to reach 50% of the mediator mass. Fig. 4.16 shows our results, where the panels show the points excluded by individual LHC Run I collider results.

To conclude, we saw that the 8 TeV $t\bar{t}$ resonance search provides constraints in the region of $m_Y \in [150, 600]$ GeV and $m_X \gtrsim 100$ GeV, and is able to rule out $\hat{g}_t$ couplings of $\mathcal{O}(1)$. The four top searches constrain roughly the same region of the (m_Y, m_X) parameter space as the $t\bar{t}$ searches. However, the characteristic size of the couplings that four top searches are able to constrain is significantly larger than the case of $t\bar{t}$.

4.5.2   A deeper analysis including interference effects at NLO

In this subsection we will use again the ATLAS $t\bar{t}$ resonant search at 8 Tev but now we will study the impact of the interference on such limits. We will go back to our simplified model of Eq. 4.2 and use our improved theoretical predictions to set constraints on our simplified model with an extra scalar or pseudoscalar particle coupling to the top quark. Our results can be reinterpreted in terms of 2HDM scenarios and be combined with other constraints.

Fig. 4.17 shows the width of a spin-0 resonance coupling to the top only as a function of its mass and the top Yukawa coupling for a scalar and pseudoscalar particle. The ATLAS 8 TeV $t\bar{t}$ resonance search limit is also shown on the plot, extracted by converting the 95% C.L. cross section to a value of the coupling using LO predictions. The region above the red line labelled "ATLAS 8 TeV" is excluded, if one assumes that the scalar particle only couples to the top quark. Our results show, as before, that scalar mediators with masses from 400 GeV to 550 GeV could be excluded for couplings $\hat{g}_t \gtrsim 1.5$ depending on the mass of the mediator. For a pseudoscalar, smaller values of the coupling can be excluded as the production cross-section is larger in this case. While the search extends to much larger masses of mediators we do not show any results above 550 GeV as within this model it is not feasible to obtain a limit satisfying the narrow width approximation. As shown in Fig. 4.17, the width over mass ratio rises quickly with $\hat{g}_t$ and m_Y. In order to apply the ATLAS results we allow widths below 8% of the mass (which is the experimental resolution of the invariant mass of the $t\bar{t}$ system), which allows masses up to 550 GeV to be tested.

Focussing on this region the width remains small for couplings $\hat{g}_t < 2$. Using our signal predictions at LO and NLO we extract the exclusion region in Fig. 4.18 for
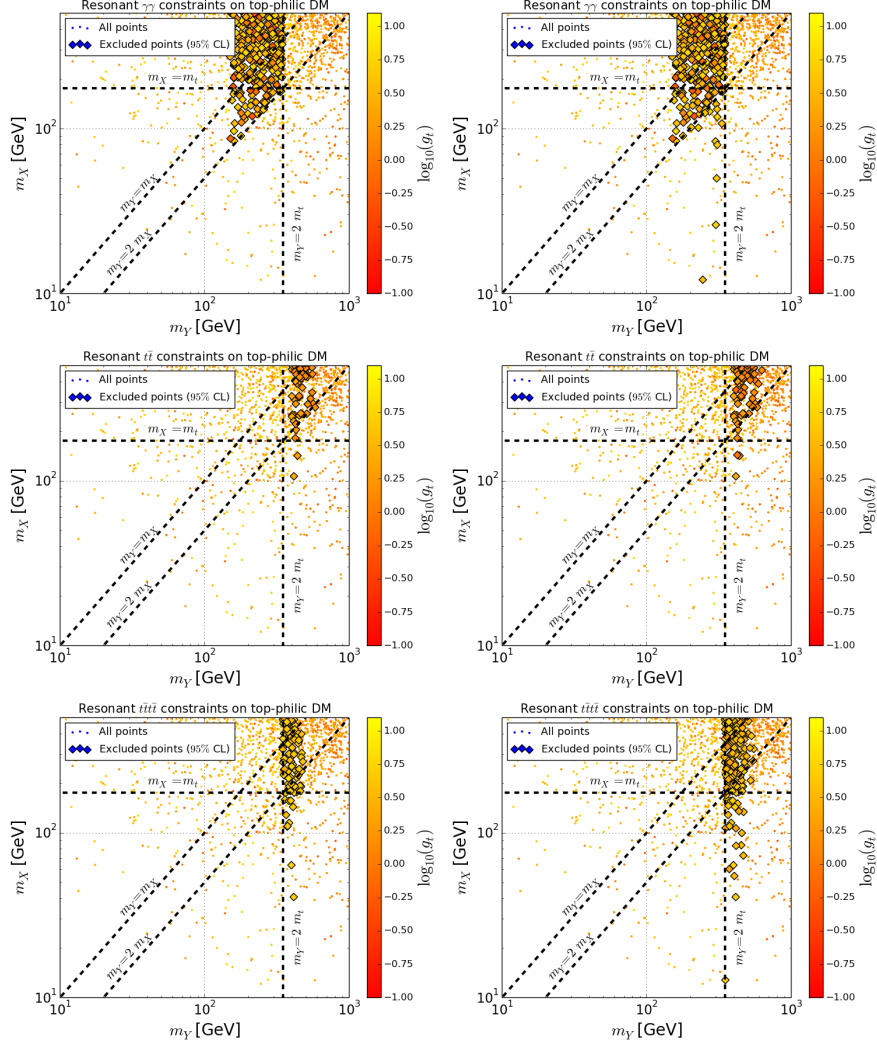
Figure 4.16: Constraints derived from the LHC Run I results on the simplified top-philic dark matter model. The panels show results of a four-dimensional parameter scan, uniform on the linear scale. The first row corresponds shows the points excluded (95% CL) by the resonant $\gamma\gamma$ constraints, the second row is for $t\bar{t}$ searches, while the last row shows the four top constraints. The left columns corresponds to a scalar mediator, while the right one is for a pseudoscalar mediator. The results assume couplings smaller than 2π and $\Gamma_Y/m_Y < 0.5$, with no constraints from astrophysics or cosmology being imposed.
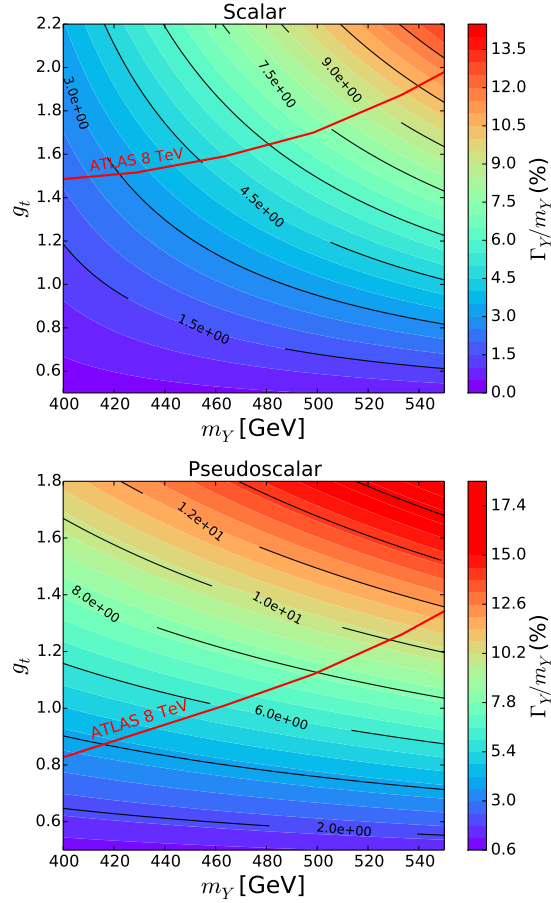
Figure 4.17: Width of a spin-0 resonance as a percentage of its mass as a function of the mass and coupling to the top. Top: scalar. Bottom: pseudoscalar. The region above the red curve labeled "ATLAS 8 TeV" is excluded when LO predictions for the signal are used.

a scalar and pseudoscalar resonance. As expected the exclusion region extends to smaller values of the coupling when we use the NLO predictions. We find that for the scalar mediator a larger region is excluded compared to the pseudoscalar one. The reason is the fact that the narrow width approximation is valid for larger values of the coupling for a scalar mediator compared to the pseudoscalar one. This allows us to apply the ATLAS results for a wider range of couplings for the scalar mediator.

Figure 4.18: Exclusion region obtained using the ATLAS 8 TeV $t\bar{t}$ resonance search results [221] for a scalar (top) and pseudoscalar (bottom) resonance coupling to the top only using LO (left) and NLO (right) predictions for the signal cross section. Grey points are discarded because of narrow width assumption, blue points have been tested but are not excluded while red points are.

We note here that the interference between signal and background is not taken into account by the ATLAS analysis. This implies that the search is based on the assumption that the signal will appear as a Breit-Wigner resonance over the SM background. In order to allow for the interference to be taken properly into account the experimental strategy would have to be modified, as the interference can lead to shapes which are very different from those expected for the signal only. This is particularly important when searches start focussing on resonances which are not extremely narrow. As we have already seen, the larger the width the bigger the impact of the interference.

It is clearly not possible to a posteriori account for the impact of any potential shape changes, i.e. deviations from a Breit-Wigner resonance shape, on the 95% C.L. exclusion cross-section obtained by ATLAS. Nevertheless we can estimate how including the interference at the total cross-section level can modify the limits set on the cou-
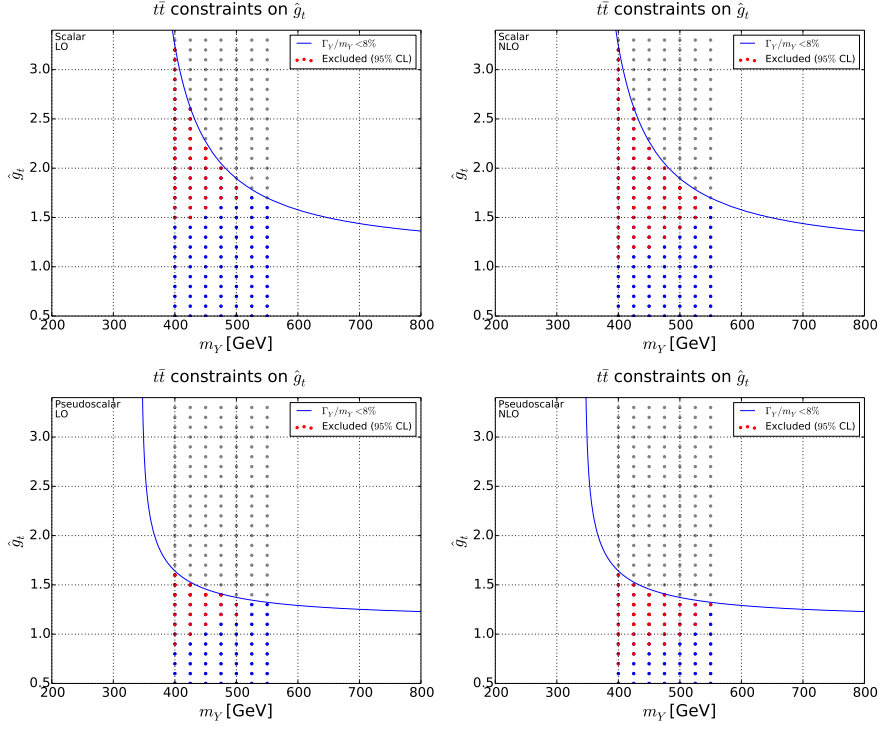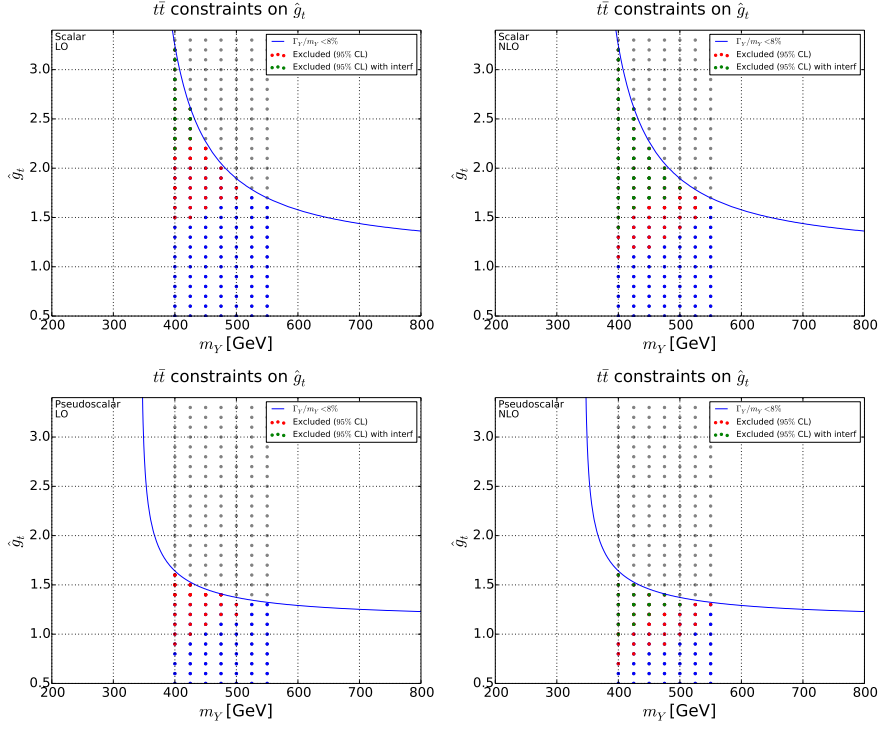
Figure 4.19: Exclusion region obtained using the ATLAS 8 TeV $t\bar{t}$ resonance search results [221] for a scalar (top) and pseudoscalar (bottom) resonance coupling to the top only using LO (left) and NLO (right) predictions for the BSM cross section. Red points are the same as in Fig. 4.18 and green points are points which are excluded even when the interference between the signal and background is taken into account.

pling in our simplified model, in the cases where the interference does not completely dominate the BSM contribution and therefore the shape of the deviation from the background.

In order to investigate this, we compute the interference for the parameter points of interest. The results for the exclusion regions are shown in Fig. 4.19, where the integrated interference rate is simply added to the signal. At LO in the scalar case we see that points with $\hat{g}_t > 2.1$ are excluded even when the interference is taken into account, while for the pseudoscalar no points are excluded which demonstrates the huge impact of the interference in these scenarios. This is particularly evident in the pseudoscalar case due to the small coupling restriction imposed by the 8% constraint

on the width. The absolute value of the interference can amount up to 50% of the signal in the scalar case and 65% in the pseudoscalar one.

At NLO also, for both scalar and pseudoscalar resonances, taking into account the interference[4] modifies the exclusion region by reducing the number of excluded points. Most of the affected parameter points have cross-sections which were excluded only when computed at NLO. For these points including the destructive interference reduces the cross section enough to fall below the 95% C.L. limit.

4.6   750 GeV diphoton excess

In this last section we discuss the possible implications of the diphoton excess reported at 750 GeV on top pair production. In the end this excess was simply a spurious signal, but it was nevertheless the occasion to stimulate new theoretical ideas. The signal in the diphoton spectrum [225, 226] was characterised, for ATLAS, by:

$$m_Y \sim 750\,\text{GeV}, \quad \Gamma_Y/m_Y < 6\% \quad \text{and} \quad \sigma_{\gamma\gamma} \sim 1 - 10\text{fb}. \tag{4.9}$$

By considering a 750 GeV spin-0 resonance we show the top pair invariant mass distribution in Fig. 4.20. The Yukawa couplings are allowed to vary and the widths are computed accordingly which demonstrates that the resonance becomes very broad for $\hat{g}_t > 1$ and even in that case deviations from the QCD background are at the percent level. Such a model does not give a sufficiently large diphoton signal. A simple computation shows that a simplified model with a scalar or pseudoscalar resonance coupling only to the top cannot satisfy the observed features of the excess, as to obtain a sufficiently large production cross section the coupling to the top and consequently the width is forced to be large and beyond perturbative values.

A possible way of enhancing the production cross section without increasing the width beyond the values observed at the LHC is to employ the dimension-5 operators of eq. 1.50. Using only an effective coupling to gluons is not sufficient. Indeed we find that in order to satisfy the signal strength properties of the diphoton excess one needs a large coupling to the top to generate the loop suppressed coupling of the scalar to photons. As the dominant decay mode is decay into top-quark pairs, this setup leads to large top-pair cross section values which have already been excluded by the resonant searches. To circumvent this problem we need to introduce direct couplings of the scalar to the photons as well as in Eq. 1.51.

To investigate the implications of the 750 GeV resonance on top pair production we employ the scalar couplings to tops, gluons and photons. The width of the scalar

---

[4]Again we use the LO value multiplied by $\sqrt{K_S K_B}$.
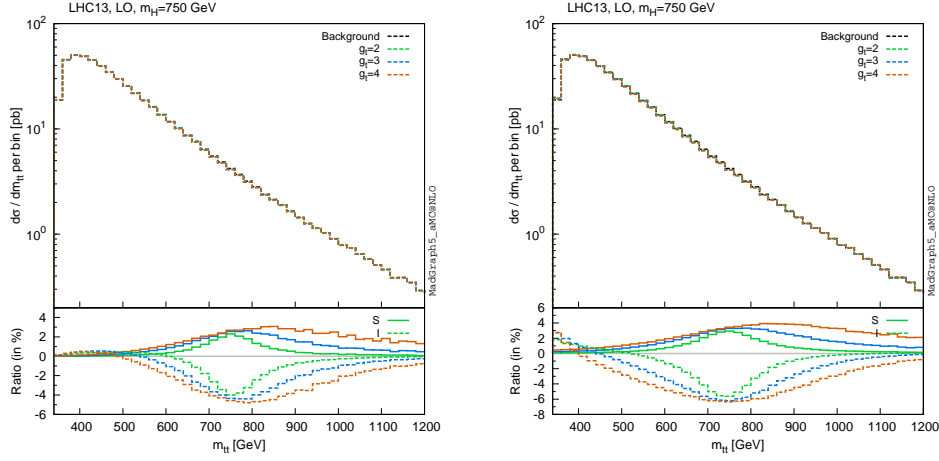
Figure 4.20: Top pair invariant mass distribution at the LHC at 13 TeV for a 750 GeV scalar coupling to the top with different Yukawa couplings. The width of the scalar is computed for each value of the Yukawa. Left: scalar. Right: pseudoscalar. The lower panels show the ratio of signal and interference over the QCD background.

	$\hat{g}_t$	c_g	c_γ	Γ_{tot}	$\sigma(pp \to Y \to \gamma\gamma)$	$\sigma(pp \to Y \to t\bar{t})$
Scalar	1	1.0	100	32.8	9.4 fb	0.2 pb
	1	1.5	55	31.7	6.7 fb	0.4 pb
	1	2.0	30	31.4	3.6 fb	0.7 pb
	1	2.5	20	31.4	2.5 fb	1.1 pb
Pseudoscalar	1	0.75	65	41.1	9.0 fb	0.2 pb
	1	1.0	45	40.3	7.8 fb	0.4 pb
	1	1.5	20	39.8	3.6 fb	0.9 pb
	1	1.75	10	39.7	1.2 fb	1.2 pb

Table 4.12: Example of benchmarks points in our simplified model satisfying the currently available information on the diphoton excess. The couplings of the scalar to tops, gluons and photons are given along with the total width (in GeV) and the narrow width diphoton and $t\bar{t}$ signal cross sections for a 750 GeV scalar or pseudoscalar resonance.

particle can then be computed from the partial widths to the tops, gluons and photons and has been given in Eq. 4.6.
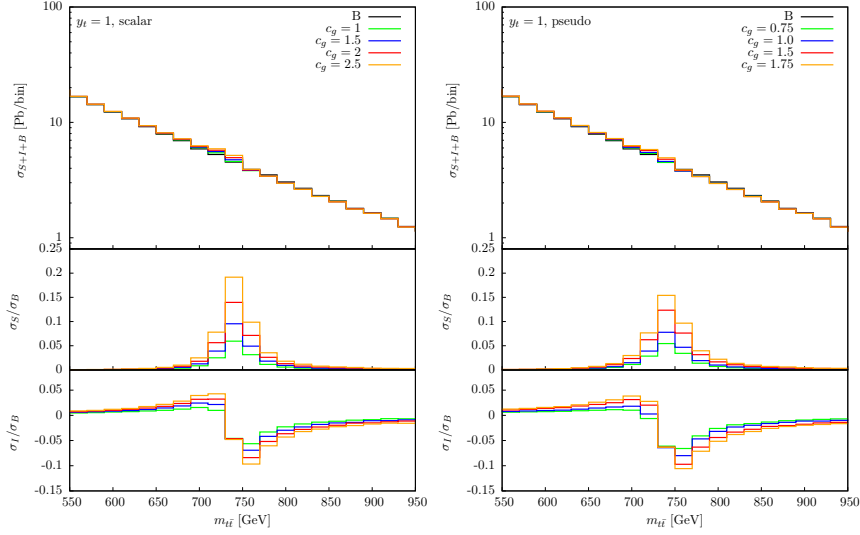
Figure 4.21: Top pair invariant mass distribution for the LHC at 13 TeV in the presence of a 750 GeV resonance coupling to gluons, photons and top quarks. The values of the couplings shown here satisfy the diphoton excess properties. The lower panels show the ratio of the signal and interference over the QCD background.

A selection of possible parameter setups which satisfy the diphoton observations of Eq. 4.9 is shown in Tab. 4.12 along with the scalar width, the diphoton and top–anti-top signal cross-sections computed in the narrow width approximation using NLO cross sections for the scalar production. We note that we have checked explicitly that the $t\bar{t}$ cross-section is smaller than what one would exclude at 750 GeV using the LHC resonant search results, despite the fact that the top branching ratio exceeds 95% for all scenarios listed here. For this selection of benchmark points, we present results for the signal and signal-background interference in top pair production in figure 4.21 for a scalar or pseudoscalar resonance of 750 GeV. In all cases the interference should be taken into account and has a significant impact on the line-shape of the resonance.

4.7 Conclusions

We have studied the interference between a new physics signal and the QCD background in the presence of additional scalars that decay into top quark pairs. The interference with the background needs to be taken into account to reliably predict the line-shape of the additional scalar. We have explored the impact of the interference

within a simplified model with a heavy scalar, pseudoscalar or mixed state as well as for a set of representative 2HDM scenarios. The interference leads to interesting peak-dip features in the invariant mass distribution of the top pair. While the observed features depend on the specific model parameters, we find that in general the impact of the interference becomes rapidly important once the width over mass ratio of the resonance rises above a few percent.

In addition to the $t\bar{t}$ process, the interference has been studied when the top pair is produced in association with a jet. We find that the size and shape of the interference compared to the background is not significantly modified compared to the $2 \rightarrow 2$ process but remains important in the determination of the shape of the invariant mass distribution. In order to improve the precision for the signal process we have computed it at NLO accuracy in QCD. We find large QCD corrections for all scenarios studied. While an exact NLO computation for the interference is beyond recent advances in loop technology, we approximate the interference at NLO using the geometric average of the signal and background K-factors, which provides an estimate of the higher order QCD effects. This procedure has also been validated by the $t\bar{t}$+jet calculation.

For a simplified model of an additional scalar coupling to the top only, we have studied the region of the parameter space of the model that can be excluded by the ATLAS top pair narrow-width resonance search. This simple scenario demonstrates the importance of taking into account both the NLO corrections and the interference with the QCD background when setting limits on BSM scenarios. While in our analysis only total rates have been used to set limits on the parameter space of the model, it is important to stress that the shapes of the distributions are significantly changed by the interference and the experimental analyses should be accordingly modified to account for this, in particular as they extend their search beyond the narrow width approximation.

Finally we have also discussed the implications of a hypothetical 750 GeV diphoton excess on top pair production. We have explored a scenario with a 750 GeV scalar boson coupling to gluons and photons through an effective coupling and in addition directly to top quarks. For parameters satisfying the characteristics of the excess we find that again the interference with the QCD background needs to be taken into account when searching for signs of the resonance in the top–anti-top channel.

Conclusion

In this thesis we studied and improved theoretical predictions for three very important channels in Higgs physics at the LHC: ZH produciton which is related to the well studied $l\bar{l}b\bar{b}, ll\tau^+\tau^-$ final state, HH production which, even if rates are very small, is linked to $\gamma\gamma b\bar{b}$, $b\bar{b}\tau^+\tau^-$ and $b\bar{b}W^+W^-$ final states and finally $H \rightarrow t\bar{t}$ production which is very important as it lies at the border of top and Higgs physics and could give interesting resonance patterns given that any heavy spin-0 particle would decay predominantly into top quarks.

We started by analysing the associated production of Higgs and Z boson via heavy-quark loops at the LHC in the Standard Model and beyond. We reviewed the main features of the Born $2 \rightarrow 2$ production and discussed the high-energy behaviour, angular distributions and Z boson polarisation. We also considered the effects of extra QCD radiation as described by the $2 \rightarrow 3$ loop matrix elements, and found that they dominate at high Higgs transverse momentum. We showed how merged samples of 0– and 1–jet multiplicities, matched to a parton shower can provide a reliable description of differential distributions in ZH production. In addition to the SM study, results in a generic 2HDM were presented for a set of representative and experimentally viable benchmarks for Zh^0, ZH^0 and ZA^0 production. We observed that various interesting features appear either due to the resonant enhancement of the cross-section or to interference patterns between resonant and non-resonant contributions. Merged results help improving predictions for this NNLO correction to the Drell-Yan ZH production process but full results at NLO would be required in order to take into account the virtual missing corrections and further reduce the dependence on the shower scale.

We then studied the production of Higgs boson pairs via gluon fusion at the LHC in the 2HDM. We presented predictions at NLO accuracy in QCD, matched to parton showers through the MC@NLO method. A dedicated reweighting technique was used to improve the NLO calculation upon the infinite top-mass limit. The inclusion of the

NLO corrections led to large K-factors of K (1.5-1.7) and significantly reduced theoretical uncertainties. We examined the seven 2HDM Higgs-pair combinations using a number of representative 2HDM scenarios. We showed how the model-specific features modify the Higgs-pair total rates and distribution shapes, leading to trademark signatures of an extended Higgs sector. Accent was put on the $h^0 h^0$ final state but similar results have been obtained for any other final state, except for $H^+ H^-$. In this case three different scales are involved in the box diagrams and hence are not computable with current loop technology. Pursuing effort in this direction is then required.

Finally we analysed the production of a top quark pair through a heavy scalar at the LHC. We reviewed the main features of the signal as well as the interference with the top–anti-top background at leading order in QCD. We then studied higher order QCD effects. While the background and the signal could be obtained at NNLO and NLO in QCD respectively, that was not the case for their interference, which is currently known only at LO. In order to improve the accuracy of the prediction for the interference term, we considered the effects of extra QCD radiation, i.e. the $2 \to 3$ (loop-induced) processes and obtained an estimate of the NLO corrections. As a result, we found that the contribution of the interference was important both at the total cross-section level and, most importantly, for the line-shape of the heavy scalar. In particular for resonances with widths larger than a couple of percent of the resonance mass, the interference term distorted the invariant mass distribution and generically led to a non-trivial peak-dip structure. We studied this process first in a simplified model involving an additional scalar or pseudoscalar resonance as well as in the 2HDM for a set of representative benchmarks. Then we turned to a top philic DM model where we combined constraints coming from collider with astrophysical and cosmological constraints. We presented the constraints on simplified models featuring an extra scalar as set by the LHC searches for top–anti-top resonances, and the implications of the 750 GeV diphoton excess reported by CMS and ATLAS in 2016 for the top pair production assuming a scalar or a pseudoscalar resonance. In order to improve exclusion regions further improvements in the interference computation at NLO are needed. Eventually such results would also confirm or reject our approximation in terms of K factors.

In these three processes we designed 2HDM benchmarks in order to exhibit particular and interesting features. Finding such benchmarks was not always an easy task, given the existence of the large amount of constraints coming from various sources: flavor physics, Tevatron, LHC, etc. The allowed parameters space shrinks more and more but 2HDM is not excluded yet and even if spectacular resonances are probably ruled-out, there remains space in the alignment region for $1 < \tan\beta < 10$.

Via the multiple uses and implementations of our reweighting techniques we set the path for future investigations. Going beyond this work and improving predictions for these processes will be based on the newly available two-loop results. A reweighting

strategy similar to the one we implemented has already been followed to get NLO-improved NNLO HEFT results before full NNLO results could be obtained in the future..

Bibliography

[1] Georges Aad et al., "Measurements of the Higgs boson production and decay rates and constraints on its couplings from a combined ATLAS and CMS analysis of the LHC pp collision data at $\sqrt{s} = 7$ and 8 TeV", *JHEP*, vol. 08, pp. 045, 2016.

[2] G.C. Branco, P.M. Ferreira, L. Lavoura, M.N. Rebelo, Marc Sher, et al., "Theory and phenomenology of two-Higgs-doublet models", *Phys.Rept.*, vol. 516, pp. 1–102, 2012.

[3] Mayumi Aoki, Renato Guedes, Shinya Kanemura, Stefano Moretti, Rui Santos, et al., "Light Charged Higgs bosons at the LHC in 2HDMs", *Phys.Rev.*, vol. D84, pp. 055028, 2011.

[4] Koji Tsumura, "Two Higgs doublet models at future colliders", in *Proceedings, 1st Toyama International Workshop on Higgs as a Probe of New Physics 2013 (HPNP2013): Toyama, Japan, February 13-16, 2013*, 2013.

[5] Robert V. Harlander, Stefan Liebler, and Tom Zirke, "Higgs Strahlung at the Large Hadron Collider in the 2-Higgs-Doublet Model", *JHEP*, vol. 1402, pp. 023, 2014.

[6] R. Harlander, M. Mühlleitner, J. Rathsman, M. Spira, and O. Stål, "Interim recommendations for the evaluation of Higgs production cross sections and branching ratios at the LHC in the Two-Higgs-Doublet Model", 2013.

[7] E. Bagnaschi, R. V. Harlander, S. Liebler, H. Mantler, P. Slavich, and A. Vicini, "Towards precise predictions for Higgs-boson production in the MSSM", *JHEP*, vol. 06, pp. 167, 2014.

[8] Benoit Hespel, David Lopez-Val, and Eleni Vryonidou, "Higgs pair production via gluon fusion in the Two-Higgs-Doublet Model", *JHEP*, vol. 09, pp. 124, 2014.

[9] B. Hespel, F. Maltoni, and E. Vryonidou, "Higgs and Z boson associated production via gluon fusion in the SM and the 2HDM", *JHEP*, vol. 06, pp. 065, 2015.

[10] Chiara Arina et al., "A comprehensive approach to dark matter studies: exploration of simplified top-philic models", *JHEP*, vol. 11, pp. 111, 2016.

[11] B. Hespel, F. Maltoni, and E. Vryonidou, "Signal background interference effects in heavy scalar production and decay to a top-anti-top pair", *JHEP*, vol. 10, pp. 016, 2016.

[12] D. de Florian et al., "Handbook of LHC Higgs Cross Sections: 4. Deciphering the Nature of the Higgs Sector", 2016.

[13] Michael E. Peskin and Daniel V. Schroeder, *An Introduction to quantum field theory*, Addison-Wesley, Reading, USA, 1995.

[14] C. Patrignani et al., "Review of Particle Physics", *Chin. Phys.*, vol. C40, no. 10, pp. 100001, 2016.

[15] Georges Aad et al., "Observation of a new particle in the search for the Standard Model Higgs boson with the ATLAS detector at the LHC", *Phys. Lett.*, vol. B716, pp. 1–29, 2012.

[16] A. D. Martin, W. J. Stirling, R. S. Thorne, and G. Watt, "Parton distributions for the LHC", *Eur. Phys. J.*, vol. C63, pp. 189–285, 2009.

[17] Charalampos Anastasiou, Claude Duhr, Falko Dulat, Elisabetta Furlan, Thomas Gehrmann, Franz Herzog, and Bernhard Mistlberger, "Higgs Boson GluonF-fusion Production Beyond Threshold in N^3LO QCD", *JHEP*, vol. 03, pp. 091, 2015.

[18] Paolo Bolzoni, Marco Zaro, Fabio Maltoni, and Sven-Olaf Moch, "Higgs production at NNLO in QCD: The VBF channel", *Nucl. Phys. Proc. Suppl.*, vol. 205-206, pp. 314–319, 2010.

[19] Giancarlo Ferrera, Massimiliano Grazzini, and Francesco Tramontano, "Associated ZH production at hadron colliders: the fully differential NNLO QCD calculation", *Phys. Lett.*, vol. B740, pp. 51–55, 2015.

[20] S. Dawson, C. Jackson, L. H. Orr, L. Reina, and D. Wackeroth, "Associated Higgs production with top quarks at the large hadron collider: NLO QCD corrections", *Phys. Rev.*, vol. D68, pp. 034022, 2003.

[21] S. Chatrchyan et al., "The CMS Experiment at the CERN LHC", *JINST*, vol. 3, pp. S08004, 2008.

[22] G. Aad et al., "The ATLAS Experiment at the CERN Large Hadron Collider", *JINST*, vol. 3, pp. S08003, 2008.

[23] Vardan Khachatryan et al., "Precise determination of the mass of the Higgs boson and tests of compatibility of its couplings with the standard model predictions using proton collisions at 7 and 8 TeV", *Eur. Phys. J.*, vol. C75, no. 5, pp. 212, 2015.

[24] Georges Aad et al., "Measurement of the Higgs boson mass from the $H \to \gamma\gamma$ and $H \to ZZ^* \to 4\ell$ channels with the ATLAS detector using 25 fb^{-1} of pp collision data", *Phys. Rev.*, vol. D90, no. 5, pp. 052004, 2014.

[25] Georges Aad et al., "Combined Measurement of the Higgs Boson Mass in pp Collisions at $\sqrt{s} = 7$ and 8 TeV with the ATLAS and CMS Experiments", *Phys. Rev. Lett.*, vol. 114, pp. 191803, 2015.

[26] Marcela S. Carena and Howard E. Haber, "Higgs boson theory and phenomenology", *Prog.Part.Nucl.Phys.*, vol. 50, pp. 63–152, 2003.

[27] John F. Gunion, Howard E. Haber, Gordon L. Kane, and Sally Dawson, "The Higgs Hunter's Guide", *Front.Phys.*, vol. 80, pp. 1–448, 2000.

[28] Berthold Stech, "The mass of the Higgs boson in the trinification subgroup of E6", *Phys.Rev.*, vol. D86, pp. 055003, 2012.

[29] Berthold Stech, "Phenomenology of $SU(3)_L \times SU(3)_R \times SU(3)_C$ and the Higgs Boson", *PoS*, vol. QFTHEP2013, pp. 084, 2014.

[30] David B. Kaplan, Howard Georgi, and Savas Dimopoulos, "Composite Higgs Scalars", *Phys.Lett.*, vol. B136, pp. 187, 1984.

[31] Kaustubh Agashe, Roberto Contino, and Alex Pomarol, "The Minimal composite Higgs model", *Nucl.Phys.*, vol. B719, pp. 165–187, 2005.

[32] Martin Schmaltz and David Tucker-Smith, "Little Higgs review", *Ann.Rev.Nucl.Part.Sci.*, vol. 55, pp. 229–270, 2005.

[33] Maxim Perelstein, "Little Higgs models and their phenomenology", *Prog.Part.Nucl.Phys.*, vol. 58, pp. 247–291, 2007.

[34] Ernest Ma, "Verifiable radiative seesaw mechanism of neutrino mass and dark matter", *Phys.Rev.*, vol. D73, pp. 077301, 2006.

[35] Indrani Chakraborty and Anirban Kundu, "Two-Higgs doublet models confront the naturalness problem", *Phys. Rev.*, vol. D90, no. 11, pp. 115017, 2014.

[36] James M. Cline, Kimmo Kainulainen, and Michael Trott, "Electroweak Baryogenesis in Two Higgs Doublet Models and B meson anomalies", *JHEP*, vol. 1111, pp. 089, 2011.

[37] G.C. Dorsch, S.J. Huber, and J.M. No, "A strong electroweak phase transition in the 2HDM after LHC8", *JHEP*, vol. 1310, pp. 029, 2013.

[38] Laura López Honorez and Carlos E. Yaguna, "The inert doublet model of dark matter revisited", *JHEP*, vol. 1009, pp. 046, 2010.

[39] Jinn-Ouk Gong, Hyun Min Lee, and Sin Kyu Kang, "Inflation and dark matter in two Higgs doublet models", *JHEP*, vol. 1204, pp. 128, 2012.

[40] Sheldon L. Glashow and Steven Weinberg, "Natural Conservation Laws for Neutral Currents", *Phys.Rev.*, vol. D15, pp. 1958, 1977.

[41] Howard E. Haber and Deva O'Neil, "Basis-independent methods for the two-Higgs-doublet model. II. The Significance of $\tan\beta$", *Phys.Rev.*, vol. D74, pp. 015018, 2006.

[42] J. M. Gerard and M. Herquet, "A Twisted custodial symmetry in the two-Higgs-doublet model", *Phys. Rev. Lett.*, vol. 98, pp. 251802, 2007.

[43] Simon de Visscher, Jean-Marc Gerard, Michel Herquet, Vincent Lemaitre, and Fabio Maltoni, "Unconventional phenomenology of a minimal two-Higgs-doublet model", *JHEP*, vol. 08, pp. 042, 2009.

[44] Christoph Englert, Frank Krauss, Michael Spannowsky, and Jennifer Thompson, "Di-Higgs phenomenology in $t\bar{t}hh$: The forgotten channel", *Phys. Lett.*, vol. B743, pp. 93–97, 2015.

[45] Abdelhak Djouadi, "The Anatomy of electro-weak symmetry breaking. I: The Higgs boson in the standard model", *Phys. Rept.*, vol. 457, pp. 1–216, 2008.

[46] Georges Aad et al., "Measurements of the Higgs boson production and decay rates and coupling strengths using pp collision data at $\sqrt{s} = 7$ and 8 TeV in the ATLAS experiment", *Eur. Phys. J.*, vol. C76, no. 1, pp. 6, 2016.

[47] Federico Demartin, Fabio Maltoni, Kentarou Mawatari, and Marco Zaro, "Higgs production in association with a single top quark at the LHC", *Eur. Phys. J.*, vol. C75, no. 6, pp. 267, 2015.

[48] J. Alwall, R. Frederix, S. Frixione, V. Hirschi, F. Maltoni, et al., "The automated computation of tree-level and next-to-leading order differential cross sections, and their matching to parton shower simulations", *JHEP*, vol. 1407, pp. 079, 2014.

[49] T. Gleisberg, Stefan. Hoeche, F. Krauss, M. Schonherr, S. Schumann, F. Siegert, and J. Winter, "Event generation with SHERPA 1.1", *JHEP*, vol. 02, pp. 007, 2009.

[50] Neil D. Christensen, Priscila de Aquino, Celine Degrande, Claude Duhr, Benjamin Fuks, Michel Herquet, Fabio Maltoni, and Steffen Schumann, "A Comprehensive approach to new physics simulations", *Eur. Phys. J.*, vol. C71, pp. 1541, 2011.

[51] Michelangelo L. Mangano, Mauro Moretti, Fulvio Piccinini, Roberto Pittau, and Antonio D. Polosa, "ALPGEN, a generator for hard multiparton processes in hadronic collisions", *JHEP*, vol. 07, pp. 001, 2003.

[52] Wolfgang Kilian, Thorsten Ohl, and Jurgen Reuter, "WHIZARD: Simulating Multi-Particle Processes at LHC and ILC", *Eur. Phys. J.*, vol. C71, pp. 1742, 2011.

[53] Valentin Hirschi and Olivier Mattelaer, "Automated event generation for loop-induced processes", *JHEP*, vol. 10, pp. 146, 2015.

[54] Olivier Mattelaer, "On the maximal use of Monte Carlo samples: re-weighting events at NLO accuracy", *Eur. Phys. J.*, vol. C76, no. 12, pp. 674, 2016.

[55] Adam Alloul, Neil D. Christensen, Celine Degrande, Claude Duhr, and Benjamin Fuks, "FeynRules 2.0 - A complete toolbox for tree-level phenomenology", *Comput.Phys.Commun.*, vol. 185, pp. 2250–2300, 2014.

[56] Wolfram Research, Inc., "Mathematica, Version 11.1", Champaign, IL, 2017.

[57] Torbjorn Sjostrand, Stephen Mrenna, and Peter Z. Skands, "A Brief Introduction to PYTHIA 8.1", *Comput.Phys.Commun.*, vol. 178, pp. 852–867, 2008.

[58] M. Bahr et al., "Herwig++ Physics and Manual", *Eur. Phys. J.*, vol. C58, pp. 639–707, 2008.

[59] Rikkert Frederix, Stefano Frixione, Valentin Hirschi, Fabio Maltoni, Roberto Pittau, et al., "Four-lepton production at hadron colliders: aMC@NLO predictions with theoretical uncertainties", *JHEP*, vol. 1202, pp. 099, 2012.

[60] Valentin Hirschi et al., "Automation of one-loop QCD corrections", *JHEP*, vol. 05, pp. 044, 2011.

[61] Giovanni Ossola, Costas G. Papadopoulos, and Roberto Pittau, "Reducing full one-loop amplitudes to scalar integrals at the integrand level", *Nucl.Phys.*, vol. B763, pp. 147–169, 2007.

[62] Giovanni Ossola, Costas G. Papadopoulos, and Roberto Pittau, "CutTools: A Program implementing the OPP reduction method to compute one-loop amplitudes", *JHEP*, vol. 0803, pp. 042, 2008.

[63] F. Maltoni, E. Vryonidou, and M. Zaro, "Top-quark mass effects in double and triple Higgs production in gluon-gluon fusion at NLO", *JHEP*, vol. 1411, pp. 079, 2014.

[64] Rikkert Frederix, Stefano Frixione, Eleni Vryonidou, and Marius Wiesemann, "Heavy-quark mass effects in Higgs plus jets production", *JHEP*, vol. 08, pp. 006, 2016.

[65] Celine Degrande, Claude Duhr, Benjamin Fuks, David Grellscheid, Olivier Mattelaer, et al., "UFO - The Universal FeynRules Output", *Comput.Phys.Commun.*, vol. 183, pp. 1201–1214, 2012.

[66] Priscila de Aquino, William Link, Fabio Maltoni, Olivier Mattelaer, and Tim Stelzer, "ALOHA: Automatic Libraries Of Helicity Amplitudes for Feynman Diagram Computations", *Comput.Phys.Commun.*, vol. 183, pp. 2254–2263, 2012.

[67] Sally Dawson, Elisabetta Furlan, and Ian Lewis, "Unravelling an extended quark sector through multiple Higgs production?", *Phys.Rev.*, vol. D87, pp. 014007, 2013.

[68] Matthew J. Dolan, Christoph Englert, and Michael Spannowsky, "Higgs self-coupling measurements at the LHC", *JHEP*, vol. 1210, pp. 112, 2012.

[69] T. Plehn, M. Spira, and P.M. Zerwas, "Pair production of neutral Higgs particles in gluon-gluon collisions", *Nucl.Phys.*, vol. B479, pp. 46–64, 1996.

[70] S. Dawson, S. Dittmaier, and M. Spira, "Neutral Higgs boson pair production at hadron colliders: QCD corrections", *Phys.Rev.*, vol. D58, pp. 115012, 1998.

[71] R. Frederix, S. Frixione, V. Hirschi, F. Maltoni, O. Mattelaer, P. Torrielli, E. Vryonidou, and M. Zaro, "Higgs pair production at the LHC with NLO and parton-shower effects", *Phys. Lett.*, vol. B732, pp. 142–149, 2014.

[72] S. Borowka, N. Greiner, G. Heinrich, S. P. Jones, M. Kerner, J. Schlenk, and T. Zirke, "Full top quark mass dependence in Higgs boson pair production at NLO", *JHEP*, vol. 10, pp. 107, 2016.

[73] Rikkert Frederix, Stefano Frixione, Fabio Maltoni, and Tim Stelzer, "Automation of next-to-leading order computations in QCD: the FKS subtraction", *JHEP*, vol. 10, pp. 003, 2009.

[74] S. Frixione, "A General approach to jet cross-sections in QCD", *Nucl.Phys.*, vol. B507, pp. 295–314, 1997.

[75] Stefano Frixione and Bryan R. Webber, "Matching NLO QCD computations and parton shower simulations", *JHEP*, vol. 06, pp. 029, 2002.

[76] Fabio Cascioli, Philipp Maierhofer, and Stefano Pozzorini, "Scattering Amplitudes with Open Loops", *Phys.Rev.Lett.*, vol. 108, pp. 111601, 2012.

[77] S. Catani, F. Krauss, R. Kuhn, and B.R. Webber, "QCD matrix elements + parton showers", *JHEP*, vol. 0111, pp. 063, 2001.

[78] F. Krauss, "Matrix elements and parton showers in hadronic interactions", *JHEP*, vol. 0208, pp. 015, 2002.

[79] Leif Lonnblad, "Correcting the color dipole cascade model with fixed order matrix elements", *JHEP*, vol. 0205, pp. 046, 2002.

[80] Keith Hamilton, Peter Richardson, and Jon Tully, "A Modified CKKW matrix element merging approach to angular-ordered parton showers", *JHEP*, vol. 0911, pp. 038, 2009.

[81] Michelangelo L. Mangano, Mauro Moretti, Fulvio Piccinini, and Michele Treccani, "Matching matrix elements and shower evolution for top-quark production in hadronic collisions", *JHEP*, vol. 0701, pp. 013, 2007.

[82] Rikkert Frederix and Stefano Frixione, "Merging meets matching in MC@NLO", *JHEP*, vol. 1212, pp. 061, 2012.

[83] Leif Lonnblad and Stefan Prestel, "Merging Multi-leg NLO Matrix Elements with Parton Showers", *JHEP*, vol. 1303, pp. 166, 2013.

[84] Johan Alwall, Simon de Visscher, and Fabio Maltoni, "QCD radiation in the production of heavy colored particles at the LHC", *JHEP*, vol. 0902, pp. 017, 2009.

[85] P. de Aquino, F. Maltoni, K. Mawatari, and B. Oexl, "Light Gravitino Production in Association with Gluinos at the LHC", *JHEP*, vol. 1210, pp. 008, 2012.

[86] Celine Degrande, "Automatic evaluation of UV and R2 terms for beyond the Standard Model Lagrangians: a proof-of-principle", *Comput. Phys. Commun.*, vol. 197, pp. 239–262, 2015.

[87] David Eriksson, Johan Rathsman, and Oscar Stål, "2HDMC: Two-Higgs-Doublet Model Calculator Physics and Manual", *Comput.Phys.Commun.*, vol. 181, pp. 189–205, 2010.

[88] Andrew G. Akeroyd, Abdesslam Arhrib, and El-Mokhtar Naimi, "Note on tree level unitarity in the general two Higgs doublet model", *Phys.Lett.*, vol. B490, pp. 119–124, 2000.

[89] I.F. Ginzburg and I.P. Ivanov, "Tree-level unitarity constraints in the most general 2HDM", *Phys.Rev.*, vol. D72, pp. 115010, 2005.

[90] John F. Gunion and Howard E. Haber, "The CP conserving two Higgs doublet model: The Approach to the decoupling limit", *Phys.Rev.*, vol. D67, pp. 075019, 2003.

[91] Chien-Yi Chen and S. Dawson, "Exploring Two Higgs Doublet Models Through Higgs Production", *Phys.Rev.*, vol. D87, no. 5, pp. 055016, 2013.

[92] Shuquan Nie and Marc Sher, "Vacuum stability bounds in the two Higgs doublet model", *Phys.Lett.*, vol. B449, pp. 89–92, 1999.

[93] M. Maniatis, A. von Manteuffel, O. Nachtmann, and F. Nagel, "Stability and symmetry breaking in the general two-Higgs-doublet model", *Eur.Phys.J.*, vol. C48, pp. 805–823, 2006.

[94] P.M. Ferreira and D.R.T. Jones, "Bounds on scalar masses in two Higgs doublet models", *JHEP*, vol. 0908, pp. 069, 2009.

[95] C.D. Froggatt, R.G. Moorhouse, and I.G. Knowles, "Leading radiative corrections in two scalar doublet models", *Phys.Rev.*, vol. D45, pp. 2471–2481, 1992.

[96] W. Grimus, L. Lavoura, O.M. Ogreid, and P. Osland, "The Oblique parameters in multi-Higgs-doublet models", *Nucl.Phys.*, vol. B801, pp. 81–96, 2008.

[97] Hong-Jian He, Nir Polonsky, and Shu-fang Su, "Extra families, Higgs spectrum and oblique corrections", *Phys.Rev.*, vol. D64, pp. 053004, 2001.

[98] M.J.G. Veltman, "Second Threshold in Weak Interactions", *Acta Phys.Polon.*, vol. B8, pp. 475, 1977.

[99] Michael E. Peskin and Tatsu Takeuchi, "A New constraint on a strongly interacting Higgs sector", *Phys.Rev.Lett.*, vol. 65, pp. 964–967, 1990.

[100] LEP Electroweak Working Group, "Precision Electroweak Measurements and Constraints on the Standard Model", 2010.

[101] M. Baak, M. Goebel, J. Haller, A. Hoecker, D. Ludwig, et al., "Updated Status of the Global Electroweak Fit and Constraints on New Physics", *Eur.Phys.J.*, vol. C72, pp. 2003, 2012.

[102] Serguei Chatrchyan et al., "Measurement of the properties of a Higgs boson in the four-lepton final state", *Phys. Rev.*, vol. D89, no. 9, pp. 092007, 2014.

[103] Georges Aad et al., "Measurements of Higgs boson production and couplings in the four-lepton channel in pp collisions at center-of-mass energies of 7 and 8 TeV with the ATLAS detector", *Phys. Rev.*, vol. D91, no. 1, pp. 012006, 2015.

[104] Vardan Khachatryan et al., "Search for a Higgs boson in the mass range from 145 to 1000 GeV decaying to a pair of W or Z bosons", *JHEP*, vol. 10, pp. 144, 2015.

[105] Georges Aad et al., "Determination of spin and parity of the Higgs boson in the $WW^* \rightarrow e\nu\mu\nu$ decay channel with the ATLAS detector", *Eur. Phys. J.*, vol. C75, no. 5, pp. 231, 2015.

[106] Vardan Khachatryan et al., "Search for two Higgs bosons in final states containing two photons and two bottom quarks in proton-proton collisions at 8 TeV", *Phys. Rev.*, vol. D94, no. 5, pp. 052012, 2016.

[107] Georges Aad et al., "Search for charged Higgs bosons decaying via $H^+ \rightarrow \tau\nu$ in top quark pair events using pp collision data at $\sqrt{s} = 7$ TeV with the ATLAS detector", *JHEP*, vol. 1206, pp. 039, 2012.

[108] G. Abbiendi et al., "Search for Charged Higgs bosons: Combined Results Using LEP Data", *Eur.Phys.J.*, vol. C73, pp. 2463, 2013.

[109] Bernard Aubert et al., "Measurement of the $B \rightarrow X_s\gamma$ branching fraction and photon energy spectrum using the recoil method", *Phys.Rev.*, vol. D77, pp. 051103, 2008.

[110] Mayumi Aoki, Shinya Kanemura, Koji Tsumura, and Kei Yagyu, "Models of Yukawa interaction in the two Higgs doublet model, and their collider phenomenology", *Phys.Rev.*, vol. D80, pp. 015017, 2009.

[111] Farvah Mahmoudi and Tobias Hurth, "Flavour data constraints on new physics and SuperIso", *PoS*, vol. ICHEP2012, pp. 324, 2013.

[112] Darwin Chang, We-Fu Chang, Chung-Hsien Chou, and Wai-Yee Keung, "Large two loop contributions to g-2 from a generic pseudoscalar boson", *Phys.Rev.*, vol. D63, pp. 091301, 2001.

[113] Kingman Cheung and Otto C.W. Kong, "Can the two Higgs doublet model survive the constraint from the muon anomalous magnetic moment as suggested?", *Phys.Rev.*, vol. D68, pp. 053003, 2003.

[114] Philip Bechtle, Oliver Brein, Sven Heinemeyer, Georg Weiglein, and Karina E. Williams, "HiggsBounds: Confronting Arbitrary Higgs Sectors with Exclusion Bounds from LEP and the Tevatron", *Comput.Phys.Commun.*, vol. 181, pp. 138–167, 2010.

[115] Philip Bechtle, Oliver Brein, Sven Heinemeyer, Georg Weiglein, and Karina E. Williams, "HiggsBounds 2.0.0: Confronting Neutral and Charged Higgs Sector Predictions with Exclusion Bounds from LEP and the Tevatron", *Comput.Phys.Commun.*, vol. 182, pp. 2605–2631, 2011.

[116] Philip Bechtle, Oliver Brein, Sven Heinemeyer, Oscar Stal, Tim Stefaniak, Georg Weiglein, and Karina Williams, "Recent Developments in HiggsBounds and a Preview of HiggsSignals", *PoS*, vol. CHARGED2012, pp. 024, 2012.

[117] Philip Bechtle, Sven Heinemeyer, Oscar Stål, Tim Stefaniak, and Georg Weiglein, "$HiggsSignals$: Confronting arbitrary Higgs sectors with measurements at the Tevatron and the LHC", *Eur.Phys.J.*, vol. C74, pp. 2711, 2014.

[118] Oscar Stål and Tim Stefaniak, "Constraining extended Higgs sectors with HiggsSignals", *PoS*, vol. EPS-HEP2013, pp. 314, 2013.

[119] F. Mahmoudi, "SuperIso: A Program for calculating the isospin asymmetry of $B \to K^*\gamma$ in the MSSM", *Comput.Phys.Commun.*, vol. 178, pp. 745–754, 2008.

[120] F. Mahmoudi, "SuperIso v2.3: A Program for calculating flavor physics observables in Supersymmetry", *Comput.Phys.Commun.*, vol. 180, pp. 1579–1613, 2009.

[121] Farvah Mahmoudi and Oscar Stal, "Flavor constraints on the two-Higgs-doublet model with general Yukawa couplings", *Phys. Rev.*, vol. D81, pp. 035016, 2010.

[122] Baradhwaj Coleppa, Felix Kling, and Shufang Su, "Constraining Type II 2HDM in Light of LHC Higgs Searches", *JHEP*, vol. 1401, pp. 161, 2014.

[123] Chien-Yi Chen, S. Dawson, and Marc Sher, "Heavy Higgs Searches and Constraints on Two Higgs Doublet Models", *Phys.Rev.*, vol. D88, pp. 015018, 2013.

[124] G. Belanger, B. Dumont, U. Ellwanger, J.F. Gunion, and S. Kraml, "Global fit to Higgs signal strengths and couplings and implications for extended Higgs sectors", *Phys.Rev.*, vol. D88, pp. 075008, 2013.

[125] Vernon Barger, Lisa L. Everett, Heather E. Logan, and Gabe Shaughnessy, "Scrutinizing the 125 GeV Higgs boson in two Higgs doublet models at the LHC, ILC, and Muon Collider", *Phys.Rev.*, vol. D88, no. 11, pp. 115003, 2013.

[126] Alejandro Celis, Victor Ilisie, and Antonio Pich, "Towards a general analysis of LHC data within two-Higgs-doublet models", *JHEP*, vol. 1312, pp. 095, 2013.

[127] John F. Gunion and Howard E. Haber, "Conditions for CP-violation in the general two-Higgs-doublet model", *Phys.Rev.*, vol. D72, pp. 095002, 2005.

[128] Lisa Randall, "Two Higgs Models for Large Tan Beta and Heavy Second Higgs", *JHEP*, vol. 0802, pp. 084, 2008.

[129] Marcela Carena, Ian Low, Nausheen R. Shah, and Carlos E.M. Wagner, "Impersonating the Standard Model Higgs Boson: Alignment without Decoupling", *JHEP*, vol. 1404, pp. 015, 2014.

[130] Antonio Delgado, Germano Nardini, and Mariano Quiros, "A Light Supersymmetric Higgs Sector Hidden by a Standard Model-like Higgs", *JHEP*, vol. 1307, pp. 054, 2013.

[131] "Combined CDF and D0 Search for Standard Model Higgs Boson Production with up to 10.0 fb^{-1} of Data", 2012.

[132] Georges Aad et al., "Search for the $b\bar{b}$ decay of the Standard Model Higgs boson in associated $(W/Z)H$ production with the ATLAS detector", *JHEP*, vol. 01, pp. 069, 2015.

[133] Serguei Chatrchyan et al., "Search for the standard model Higgs boson produced in association with a W or a Z boson and decaying to bottom quarks", *Phys.Rev.*, vol. D89, no. 1, pp. 012003, 2014.

[134] Georges Aad et al., "Search for a new resonance decaying to a W or Z boson and a Higgs boson in the $\ell\ell/\ell\nu/\nu\nu + b\bar{b}$ final states with the ATLAS detector", *Eur. Phys. J.*, vol. C75, no. 6, pp. 263, 2015.

[135] V. Khachatryan et al., "Combined search for anomalous pseudoscalar HVV couplings in VH(H $\rightarrow b\bar{b}$) production and H $\rightarrow$ VV decay", *Phys. Lett.*, vol. B759, pp. 672–696, 2016.

[136] Georges Aad et al., "Search for Invisible Decays of a Higgs Boson Produced in Association with a Z Boson in ATLAS", *Phys. Rev. Lett.*, vol. 112, pp. 201802, 2014.

[137] Vardan Khachatryan et al., "Searches for invisible decays of the Higgs boson in pp collisions at sqrt(s) = 7, 8, and 13 TeV", *JHEP*, vol. 02, pp. 135, 2017.

[138] R. Hamberg, W.L. van Neerven, and T. Matsuura, "A Complete calculation of the order α_s^2 correction to the Drell-Yan K factor", *Nucl.Phys.*, vol. B359, pp. 343–405, 1991.

[139] Oliver Brein, Abdelhak Djouadi, and Robert Harlander, "NNLO QCD corrections to the Higgs-strahlung processes at hadron colliders", *Phys.Lett.*, vol. B579, pp. 149–156, 2004.

[140] Oliver Brein, Robert Harlander, Marius Wiesemann, and Tom Zirke, "Top-Quark Mediated Effects in Hadronic Higgs-Strahlung", *Eur.Phys.J.*, vol. C72, pp. 1868, 2012.

[141] Oliver Brein, Robert V. Harlander, and Tom J.E. Zirke, "vh@nnlo - Higgs Strahlung at hadron colliders", *Comput.Phys.Commun.*, vol. 184, pp. 998–1003, 2013.

[142] M.L. Ciccolini, S. Dittmaier, and M. Kramer, "Electroweak radiative corrections to associated WH and ZH production at hadron colliders", *Phys.Rev.*, vol. D68, pp. 073003, 2003.

[143] Ansgar Denner, Stefan Dittmaier, Stefan Kallweit, and Alexander Mück, "HAWK 2.0: A Monte Carlo program for Higgs production in vector-boson fusion and Higgs strahlung at hadron colliders", *Comput. Phys. Commun.*, vol. 195, pp. 161–171, 2015.

[144] Simone Alioli, Paolo Nason, Carlo Oleari, and Emanuele Re, "A general framework for implementing NLO calculations in shower Monte Carlo programs: the POWHEG BOX", *JHEP*, vol. 1006, pp. 043, 2010.

[145] Duane A. Dicus and Chung Kao, "Higgs Boson - Z^0 Production From Gluon Fusion", *Phys.Rev.*, vol. D38, pp. 1008, 1988.

[146] Bernd A. Kniehl, "Associated Production of Higgs and Z Bosons From Gluon Fusion in Hadron Collisions", *Phys.Rev.*, vol. D42, pp. 2253–2258, 1990.

[147] Lukas Altenkamp, Stefan Dittmaier, Robert V. Harlander, Heidi Rzehak, and Tom J.E. Zirke, "Gluon-induced Higgs-strahlung at next-to-leading order QCD", *JHEP*, vol. 1302, pp. 078, 2013.

[148] Robert V. Harlander, Anna Kulesza, Vincent Theeuwes, and Tom Zirke, "Soft gluon resummation for gluon-induced Higgs Strahlung", *JHEP*, vol. 1411, pp. 082, 2014.

[149] Vardan Khachatryan et al., "Search for a pseudoscalar boson decaying into a Z boson and the 125 GeV Higgs boson in $l^+l^-b\bar{b}$ final states", *Phys. Lett.*, vol. B748, pp. 221–243, 2015.

[150] Vardan Khachatryan et al., "Search for neutral resonances decaying into a Z boson and a pair of b jets or τ leptons", *Phys. Lett.*, vol. B759, pp. 369–394, 2016.

[151] Vardan Khachatryan et al., "Searches for heavy Higgs bosons in two-Higgs-doublet models and for $t \rightarrow ch$ decay using multilepton and diphoton final states in pp collisions at 8 TeV", *Phys. Rev.*, vol. D90, pp. 112013, 2014.

[152] Christoph Englert, Matthew McCullough, and Michael Spannowsky, "Gluon-initiated associated production boosts Higgs physics", *Phys.Rev.*, vol. D89, no. 1, pp. 013013, 2014.

[153] Jonathan M. Butterworth, Adam R. Davison, Mathieu Rubin, and Gavin P. Salam, "Jet substructure as a new Higgs search channel at the LHC", *Phys.Rev.Lett.*, vol. 100, pp. 242001, 2008.

[154] Johan Alwall, Qiang Li, and Fabio Maltoni, "Matched predictions for Higgs production via heavy-quark loops in the SM and beyond", *Phys.Rev.*, vol. D85, pp. 014031, 2012.

[155] Qiang Li, Qi-Shu Yan, and Xiaoran Zhao, "Higgs Pair Production: Improved Description by Matrix Element Matching", *Phys.Rev.*, vol. D89, pp. 033015, 2014.

[156] Philipp Maierhofer and Andreas Papaefstathiou, "Higgs Boson pair production merged to one jet", *JHEP*, vol. 1403, pp. 126, 2014.

[157] Pankaj Agrawal and Ambresh Shivaji, "Gluon Fusion Contribution to VHj Production at Hadron Colliders", *Phys.Lett.*, vol. B741, pp. 111–116, 2014.

[158] Ansgar Denner, S. Dittmaier, M. Roth, and D. Wackeroth, "Predictions for all processes e+ e- 4 fermions + gamma", *Nucl.Phys.*, vol. B560, pp. 33–65, 1999.

[159] Ansgar Denner, S. Dittmaier, M. Roth, and L.H. Wieders, "Electroweak corrections to charged-current e+ e- 4 fermion processes: Technical details and further results", *Nucl.Phys.*, vol. B724, pp. 247–294, 2005.

[160] Charalampos Anastasiou, Stephan Buehler, Franz Herzog, and Achilleas Lazopoulos, "Total cross-section for Higgs boson hadroproduction with anomalous Standard Model interactions", *JHEP*, vol. 1112, pp. 058, 2011.

[161] F. Maltoni, K. Paul, T. Stelzer, and S. Willenbrock, "Associated production of Higgs and single top at hadron colliders", *Phys.Rev.*, vol. D64, pp. 094023, 2001.

[162] Sanjoy Biswas, Emidio Gabrielli, and Barbara Mele, "Single top and Higgs associated production as a probe of the Htt coupling sign at the LHC", *JHEP*, vol. 1301, pp. 088, 2013.

[163] Marco Farina, Christophe Grojean, Fabio Maltoni, Ennio Salvioni, and Andrea Thamm, "Lifting degeneracies in Higgs couplings using single top production in association with a Higgs boson", *JHEP*, vol. 1305, pp. 022, 2013.

[164] Fabio Maltoni, Kentarou Mawatari, and Marco Zaro, "Higgs characterisation via vector-boson fusion and associated production: NLO and parton-shower effects", *Eur.Phys.J.*, vol. C74, no. 1, pp. 2710, 2014.

[165] W.J. Stirling and E. Vryonidou, "Electroweak gauge boson polarisation at the LHC", *JHEP*, vol. 1207, pp. 124, 2012.

[166] H. Veltman, "The equivalence theorem", *Phys. Rev. D*, vol. 41, pp. 2294–2311, Apr 1990.

[167] Z. Bern, G. Diana, L.J. Dixon, F. Febres Cordero, D. Forde, et al., "Left-Handed W Bosons at the LHC", *Phys.Rev.*, vol. D84, pp. 034008, 2011.

[168] Torbjorn Sjostrand, Stefan Ask, Jesper R. Christiansen, Richard Corke, Nishita Desai, Philip Ilten, Stephen Mrenna, Stefan Prestel, Christine O. Rasmussen, and Peter Z. Skands, "An Introduction to PYTHIA 8.2", *Comput. Phys. Commun.*, vol. 191, pp. 159–177, 2015.

[169] Chung Kao, "Production of a pseudoscalar Higgs with a Z boson from gluon fusion", *Phys.Rev.*, vol. D46, pp. 4907–4913, 1992.

[170] Li Lin Yang, Chong Sheng Li, Jian Jun Liu, and Li Gang Jin, "Production of scalar Higgs bosons associated with Z0 boson at the CERN LHC in the MSSM", *J.Phys.*, vol. G30, pp. 1821–1835, 2004.

[171] Bernd A. Kniehl and Caesar P. Palisoc, "Associated production of Z and neutral Higgs bosons at the CERN Large Hadron Collider", *Phys.Rev.*, vol. D85, pp. 075027, 2012.

[172] G.C. Dorsch, S.J. Huber, K. Mimasu, and J.M. No, "Echoes of the Electroweak Phase Transition: Discovering a second Higgs doublet through $A_0 \rightarrow ZH_0$", *Phys.Rev.Lett.*, vol. 113, no. 21, pp. 211802, 2014.

[173] Chung Kao and Shankar Sachithanandam, "Detecting a Higgs pseudoscalar with a Z boson produced in bottom quark fusion", *Phys.Lett.*, vol. B620, pp. 80–87, 2005.

[174] Qiang Li, Chong Sheng Li, Jian Jun Liu, Li Gang Jin, and C.-P. Yuan, "Next-to-leading order QCD predictions for A0 Z0 associated production at the CERN large hadron collider", *Phys.Rev.*, vol. D72, pp. 034032, 2005.

[175] Robert Harlander, Michael Kramer, and Markus Schumacher, "Bottom-quark associated Higgs-boson production: reconciling the four- and five-flavour scheme approach", 2011.

[176] Julien Baglio, Otto Eberhardt, Ulrich Nierste, and Martin Wiebusch, "Benchmarks for Higgs Pair Production and Heavy Higgs boson Searches in the Two-Higgs-Doublet Model of Type II", *Phys. Rev.*, vol. D90, no. 1, pp. 015008, 2014.

[177] Georges Aad et al., "Search For Higgs Boson Pair Production in the $\gamma\gamma b\bar{b}$ Final State using pp Collision Data at $\sqrt{s} = 8$ TeV from the ATLAS Detector", *Phys. Rev. Lett.*, vol. 114, no. 8, pp. 081802, 2015.

[178] David López-Val, Tilman Plehn, and Michael Rauch, "Measuring Extended Higgs Sectors as a Consistent Free Couplings Model", *JHEP*, vol. 1310, pp. 134, 2013.

[179] A. Djouadi, W. Kilian, M. Muhlleitner, and P.M. Zerwas, "Production of neutral Higgs boson pairs at LHC", *Eur.Phys.J.*, vol. C10, pp. 45–49, 1999.

[180] Rick S. Gupta, Heidi Rzehak, and James D. Wells, "How well do we need to measure the Higgs boson mass and self-coupling?", *Phys.Rev.*, vol. D88, pp. 055024, 2013.

[181] Giuseppe Degrassi, Pier Paolo Giardino, Fabio Maltoni, and Davide Pagani, "Probing the Higgs self coupling via single Higgs production at the LHC", *JHEP*, vol. 12, pp. 080, 2016.

[182] Roberto Contino, Margherita Ghezzi, Mauro Moretti, Giuliano Panico, Fulvio Piccinini, et al., "Anomalous Couplings in Double Higgs Production", *JHEP*, vol. 1208, pp. 154, 2012.

[183] Graham D. Kribs and Adam Martin, "Enhanced di-Higgs Production through Light Colored Scalars", *Phys.Rev.*, vol. D86, pp. 095023, 2012.

[184] Matthew J. Dolan, Christoph Englert, and Michael Spannowsky, "New Physics in LHC Higgs boson pair production", *Phys.Rev.*, vol. D87, no. 5, pp. 055002, 2013.

[185] U. Baur, T. Plehn, and David L. Rainwater, "Examining the Higgs boson potential at lepton and hadron colliders: A Comparative analysis", *Phys.Rev.*, vol. D68, pp. 033001, 2003.

[186] U. Baur, T. Plehn, and David L. Rainwater, "Probing the Higgs selfcoupling at hadron colliders using rare decays", *Phys.Rev.*, vol. D69, pp. 053004, 2004.

[187] Tilman Plehn and Michael Rauch, "The quartic higgs coupling at hadron colliders", *Phys.Rev.*, vol. D72, pp. 053008, 2005.

[188] T. Binoth, S. Karg, N. Kauer, and R. Ruckl, "Multi-Higgs boson production in the Standard Model and beyond", *Phys.Rev.*, vol. D74, pp. 113008, 2006.

[189] Andreas Papaefstathiou, Li Lin Yang, and Jose Zurita, "Higgs boson pair production at the LHC in the $b\bar{b}W^+W^-$ channel", *Phys.Rev.*, vol. D87, pp. 011301, 2013.

[190] J. Baglio, A. Djouadi, R. Grober, M.M. Muhlleitner, J. Quevillon, et al., "The measurement of the Higgs self-coupling at the LHC: theoretical status", *JHEP*, vol. 1304, pp. 151, 2013.

[191] Florian Goertz, Andreas Papaefstathiou, Li Lin Yang, and Jose Zurita, "Higgs Boson self-coupling measurements using ratios of cross sections", *JHEP*, vol. 1306, pp. 016, 2013.

[192] Danilo Enoque Ferreira de Lima, Andreas Papaefstathiou, and Michael Spannowsky, "Standard model Higgs boson pair production in the ($b\bar{b}$)($b\bar{b}$) final state", *JHEP*, vol. 08, pp. 030, 2014.

[193] Vernon Barger, Lisa L. Everett, C.B. Jackson, and Gabe Shaughnessy, "Higgs-Pair Production and Measurement of the Triscalar Coupling at LHC(8,14)", *Phys.Lett.*, vol. B728, pp. 433–436, 2014.

[194] Howard E. Haber, Maria J. Herrero, Heather E. Logan, Siannah Penaranda, Stefano Rigolin, et al., "SUSY QCD corrections to the MSSM h0 $b\bar{b}$ vertex in the decoupling limit", *Phys.Rev.*, vol. D63, pp. 055004, 2001.

[195] P. M. Ferreira, John F. Gunion, Howard E. Haber, and Rui Santos, "Probing wrong-sign Yukawa couplings at the LHC and a future linear collider", *Phys. Rev.*, vol. D89, no. 11, pp. 115003, 2014.

[196] Beranger Dumont, John F. Gunion, Yun Jiang, and Sabine Kraml, "Constraints on and future prospects for Two-Higgs-Doublet Models in light of the LHC Higgs signal", *Phys. Rev.*, vol. D90, pp. 035021, 2014.

[197] A. Abbasabadi, W.W. Repko, Duane A. Dicus, and Roberto Vega, "Single and Double Higgs Production by Gauge Boson Fusion", *Phys.Lett.*, vol. B213, pp. 386, 1988.

[198] Wai-Yee Keung, "Double Higgs From $W - W$ Fusion", *Mod.Phys.Lett.*, vol. A2, pp. 765, 1987.

[199] Vernon D. Barger, Tao Han, and R.J.N. Phillips, "Double Higgs Boson Bremsstrahlung From W and Z Bosons at Supercolliders", *Phys.Rev.*, vol. D38, pp. 2766, 1988.

[200] Duane A. Dicus, Chung Kao, and Scott S.D. Willenbrock, "Higgs Boson Pair Production From Gluon Fusion", *Phys.Lett.*, vol. B203, pp. 457, 1988.

[201] Daniel de Florian and Javier Mazzitelli, "Two-loop virtual corrections to Higgs pair production", *Phys.Lett.*, vol. B724, pp. 306–309, 2013.

[202] Jonathan Grigo, Jens Hoff, Kirill Melnikov, and Matthias Steinhauser, "On the Higgs boson pair production at the LHC", *Nucl.Phys.*, vol. B875, pp. 1–17, 2013.

[203] Ding Yu Shao, Chong Sheng Li, Hai Tao Li, and Jian Wang, "Threshold resummation effects in Higgs boson pair production at the LHC", *JHEP*, vol. 1307, pp. 169, 2013.

[204] Thomas Hahn, "Generating Feynman diagrams and amplitudes with FeynArts 3", *Comput.Phys.Commun.*, vol. 140, pp. 418–431, 2001.

[205] Xin Li and M.B. Voloshin, "Remarks on double Higgs boson production by gluon fusion at threshold", *Phys.Rev.*, vol. D89, pp. 013012, 2014.

[206] Daniel de Florian and Javier Mazzitelli, "Higgs Boson Pair Production at Next-to-Next-to-Leading Order in QCD", *Phys. Rev. Lett. 111,*, vol. 201801, 2013.

[207] "*https://cp3.irmp.ucl.ac.be/projects/madgraph/wiki/HiggsPairProduction*".

[208] J. Ohnemus and J.F. Owens, "An Order α_s calculation of hadronic ZZ production", *Phys.Rev.*, vol. D43, pp. 3626–3639, 1991.

[209] J. Ohnemus, "An Order α_s calculation of hadronic $W^{\pm}Z$ production", *Phys.Rev.*, vol. D44, pp. 3477–3489, 1991.

[210] J. Ohnemus, "An Order α_s calculation of hadronic W^-W^+ production", *Phys.Rev.*, vol. D44, pp. 1403–1414, 1991.

[211] Ulrich Baur, Tilman Plehn, and David L. Rainwater, "Measuring the Higgs boson self coupling at the LHC and finite top mass matrix elements", *Phys.Rev.Lett.*, vol. 89, pp. 151801, 2002.

[212] M. Gillioz, R. Grober, C. Grojean, M. Muhlleitner, and E. Salvioni, "Higgs Low-Energy Theorem (and its corrections) in Composite Models", *JHEP*, vol. 1210, pp. 004, 2012.

[213] E. Bagnaschi, G. Degrassi, P. Slavich, and A. Vicini, "Higgs production via gluon fusion in the POWHEG approach in the SM and in the MSSM", *JHEP*, vol. 1202, pp. 088, 2012.

[214] G. Heinrich, S. P. Jones, M. Kerner, G. Luisoni, and E. Vryonidou, "NLO predictions for Higgs boson pair production with full top quark mass dependence matched to parton showers", 2017.

[215] J. A. Aguilar-Saavedra, "A Minimal set of top anomalous couplings", *Nucl. Phys.*, vol. B812, pp. 181–204, 2009.

[216] Cen Zhang and Scott Willenbrock, "Effective-Field-Theory Approach to Top-Quark Production and Decay", *Phys. Rev.*, vol. D83, pp. 034006, 2011.

[217] Celine Degrande, Jean-Marc Gerard, Christophe Grojean, Fabio Maltoni, and Geraldine Servant, "Non-resonant New Physics in Top Pair Production at Hadron Colliders", *JHEP*, vol. 1103, pp. 125, 2011.

[218] Vernon Barger, Tao Han, and Devin G. E. Walker, "Top Quark Pairs at High Invariant Mass: A Model-Independent Discriminator of New Physics at the LHC", *Phys. Rev. Lett.*, vol. 100, pp. 031801, 2008.

[219] Rikkert Frederix and Fabio Maltoni, "Top pair invariant mass distribution: A Window on new physics", *JHEP*, vol. 01, pp. 047, 2009.

[220] Serguei Chatrchyan et al., "Searches for new physics using the $t\bar{t}$ invariant mass distribution in pp collisions at $\sqrt{s}$=8 TeV", *Phys. Rev. Lett.*, vol. 111, no. 21, pp. 211804, 2013, [Erratum: Phys. Rev. Lett.112,no.11,119903(2014)].

[221] Georges Aad et al., "A search for $t\bar{t}$ resonances using lepton-plus-jets events in proton-proton collisions at $\sqrt{s} = 8$ TeV with the ATLAS detector", *JHEP*, vol. 08, pp. 148, 2015.

[222] K. J. F. Gaemers and F. Hoogeveen, "Higgs Production and Decay Into Heavy Flavors With the Gluon Fusion Mechanism", *Phys. Lett.*, vol. B146, pp. 347, 1984.

[223] D. Dicus, A. Stange, and S. Willenbrock, "Higgs decay to top quarks at hadron colliders", *Phys. Lett.*, vol. B333, pp. 126–131, 1994.

[224] Abdelhak Djouadi, John Ellis, and Jérémie Quevillon, "Interference Effects in the Decays of 750 GeV States into $\gamma\gamma$ and $t\bar{t}$", 2016.

[225] The ATLAS collaboration, "Search for resonances decaying to photon pairs in 3.2 fb^{-1} of pp collisions at $\sqrt{s}$ = 13 TeV with the ATLAS detector", 2015.

[226] CMS Collaboration, "Search for new physics in high mass diphoton events in proton-proton collisions at 13TeV", 2015.

[227] Michał Czakon, Paul Fiedler, and Alexander Mitov, "Total Top-Quark Pair-Production Cross Section at Hadron Colliders Through $O(\pm\frac{4}{S})$", *Phys. Rev. Lett.*, vol. 110, pp. 252004, 2013.

[228] Werner Bernreuther, Michael Fuecker, and Zong-Guo Si, "Weak interaction corrections to hadronic top quark pair production", *Phys. Rev.*, vol. D74, pp. 113005, 2006.

[229] Davide Pagani, Ioannis Tsinikos, and Marco Zaro, "The impact of the photon PDF and electroweak corrections on $t\bar{t}$ distributions", *Eur. Phys. J.*, vol. C76, no. 9, pp. 479, 2016.

[230] W. Bernreuther, P. Galler, C. Mellein, Z. G. Si, and P. Uwer, "Production of heavy Higgs bosons and decay into top quarks at the LHC", *Phys. Rev.*, vol. D93, no. 3, pp. 034032, 2016.

[231] Yeong Gyun Kim, Kang Young Lee, and Seodong Shin, "Singlet fermionic dark matter", *JHEP*, vol. 05, pp. 100, 2008.

[232] Seungwon Baek, P. Ko, and Wan-Il Park, "Search for the Higgs portal to a singlet fermionic dark matter at the LHC", *JHEP*, vol. 02, pp. 047, 2012.

[233] Laura Lopez-Honorez, Thomas Schwetz, and Jure Zupan, "Higgs portal, fermionic dark matter, and a Standard Model like Higgs at 125 GeV", *Phys. Lett.*, vol. B716, pp. 179–185, 2012.

[234] Seungwon Baek, P. Ko, and Wan-Il Park, "Invisible Higgs Decay Width vs. Dark Matter Direct Detection Cross Section in Higgs Portal Dark Matter Models", *Phys. Rev.*, vol. D90, no. 5, pp. 055014, 2014.

[235] Seungwon Baek, P. Ko, Myeonghun Park, Wan-Il Park, and Chaehyun Yu, "Beyond the Dark matter effective field theory and a simplified model approach at colliders", *Phys. Lett.*, vol. B756, pp. 289–294, 2016.

[236] P. Ko and Hiroshi Yokoya, "Search for Higgs portal DM at the ILC", *JHEP*, vol. 08, pp. 109, 2016.

[237] Christoph Englert, Matthew McCullough, and Michael Spannowsky, "S-Channel Dark Matter Simplified Models and Unitarity", *Phys. Dark Univ.*, vol. 14, pp. 48–56, 2016.

[238] Daniele Barducci, Aoife Bharucha, Nishita Desai, Michele Frigerio, Benjamin Fuks, Andreas Goudelis, Suchita Kulkarni, Giacomo Polesello, and Dipan Sengupta, "Monojet searches for momentum-dependent dark matter interactions", *JHEP*, vol. 01, pp. 078, 2017.

[239] Mihailo Backovic, Michael Kramer, Fabio Maltoni, Antony Martini, Kentarou Mawatari, and Mathieu Pellen, "Higher-order QCD predictions for dark matter production at the LHC in simplified models with s-channel mediators", *Eur. Phys. J.*, vol. C75, no. 10, pp. 482, 2015.

[240] Olivier Mattelaer and Eleni Vryonidou, "Dark matter production through loop-induced processes at the LHC: the s-channel mediator case", *Eur. Phys. J.*, vol. C75, no. 9, pp. 436, 2015.

[241] Sunghoon Jung, Jeonghyeon Song, and Yeo Woong Yoon, "Dip or nothingness of a Higgs resonance from the interference with a complex phase", *Phys. Rev.*, vol. D92, no. 5, pp. 055009, 2015.

[242] L. A. Harland-Lang, A. D. Martin, P. Motylinski, and R. S. Thorne, "Parton distributions in the LHC era: MMHT 2014 PDFs", *Eur. Phys. J.*, vol. C75, no. 5, pp. 204, 2015.

[243] M. Spira, A. Djouadi, D. Graudenz, and P. M. Zerwas, "Higgs boson production at the LHC", *Nucl. Phys.*, vol. B453, pp. 17–82, 1995.

[244] Robert Harlander and Philipp Kant, "Higgs production and decay: Analytic results at next-to-leading order QCD", *JHEP*, vol. 12, pp. 015, 2005.

[245] A. Djouadi, M. Spira, and P. M. Zerwas, "QCD corrections to hadronic Higgs decays", *Z. Phys.*, vol. C70, pp. 427–434, 1996.

[246] Robert V. Harlander, Stefan Liebler, and Hendrik Mantler, "SusHi: A program for the calculation of Higgs production in gluon fusion and bottom-quark annihilation in the Standard Model and the MSSM", *Comput. Phys. Commun.*, vol. 184, pp. 1605–1617, 2013.

[247] Hendrik Mantler and Marius Wiesemann, "Hadronic Higgs production through NLO + PS in the SM, the 2HDM and the MSSM", *Eur. Phys. J.*, vol. C75, no. 6, pp. 257, 2015.

[248] Gianfranco Bertone, Dan Hooper, and Joseph Silk, "Particle dark matter: Evidence, candidates and constraints", *Phys. Rept.*, vol. 405, pp. 279–390, 2005.

[249] Gianfranco Bertone, *Particle dark matter: observations, models and searches*, Cambridge Univ. Press, Cambridge, 2010.

[250] Manuel Drees and Gilles Gerbier, "Mini-Review of Dark Matter: 2012", 2012.

[251] Douglas Clowe, Marusa Bradac, Anthony H. Gonzalez, Maxim Markevitch, Scott W. Randall, Christine Jones, and Dennis Zaritsky, "A direct empirical proof of the existence of dark matter", *Astrophys. J.*, vol. 648, pp. L109–L113, 2006.

[252] Daniele Alves, "Simplified Models for LHC New Physics Searches", *J. Phys.*, vol. G39, pp. 105005, 2012.

[253] J R Andersen et al., "Handbook of LHC Higgs Cross Sections: 3. Higgs Properties", 2013.

[254] Vardan Khachatryan et al., "Search for narrow resonances in dijet final states at $\sqrt{(s)} = 8$ TeV with the novel CMS technique of data scouting", *Phys. Rev. Lett.*, vol. 117, no. 3, pp. 031802, 2016.

[255] Vardan Khachatryan et al., "Search for diphoton resonances in the mass range from 150 to 850 GeV in pp collisions at $\sqrt{s} = 8$ TeV", *Phys. Lett.*, vol. B750, pp. 494–519, 2015.

[256] Vardan Khachatryan et al., "Search for Standard Model Production of Four Top Quarks in the Lepton + Jets Channel in pp Collisions at $\sqrt{s} = 8$ TeV", *JHEP*, vol. 11, pp. 154, 2014.

[257] Vardan Khachatryan et al., "Search for resonant $t\bar{t}$ production in proton-proton collisions at $\sqrt{s} = 8$ TeV", *Phys. Rev.*, vol. D93, no. 1, pp. 012001, 2016.

[258] Albert M Sirunyan et al., "Search for $t\bar{t}$ resonances in highly boosted lepton+jets and fully hadronic final states in proton-proton collisions at $\sqrt{s} = 13$ TeV", *JHEP*, vol. 07, pp. 001, 2017.

[259] G. Bevilacqua and M. Worek, "Constraining BSM Physics at the LHC: Four top final states with NLO accuracy in perturbative QCD", *JHEP*, vol. 07, pp. 111, 2012.

[260] Serguei Chatrchyan et al., "Search for new physics in events with same-sign dileptons and jets in pp collisions at $\sqrt{s} = 8$ TeV", *JHEP*, vol. 01, pp. 163, 2014, [Erratum: JHEP01,014(2015)].

[261] Lana Beck, Freya Blekman, Didar Dobur, Benjamin Fuks, James Keaveney, and Kentarou Mawatari, "Probing top-philic sgluons with LHC Run I data", *Phys. Lett.*, vol. B746, pp. 48–52, 2015.

[262] Farhan Feroz and M.P. Hobson, "Multimodal nested sampling: an efficient and robust alternative to MCMC methods for astronomical data analysis", *Mon.Not.Roy.Astron.Soc.*, vol. 384, pp. 449, 2008.

[263] F. Feroz, M.P. Hobson, and M. Bridges, "MultiNest: an efficient and robust Bayesian inference tool for cosmology and particle physics", *Mon.Not.Roy.Astron.Soc.*, vol. 398, pp. 1601–1614, 2009.

[264] P. A. R. Ade et al., "Planck 2015 results. XIII. Cosmological parameters", *Astron. Astrophys.*, vol. 594, pp. A13, 2016.

[265] D.S. Akerib et al., "First results from the LUX dark matter experiment at the Sanford Underground Research Facility", *Phys.Rev.Lett.*, vol. 112, pp. 091303, 2014.

[266] R. Agnese et al., "New Results from the Search for Low-Mass Weakly Interacting Massive Particles with the CDMS Low Ionization Threshold Experiment", *Phys. Rev. Lett.*, vol. 116, no. 7, pp. 071301, 2016.

[267] M. Ackermann et al., "Searching for Dark Matter Annihilation from Milky Way Dwarf Spheroidal Galaxies with Six Years of Fermi Large Area Telescope Data", *Phys. Rev. Lett.*, vol. 115, no. 23, pp. 231301, 2015.

[268] M. Ackermann et al., "Updated search for spectral lines from Galactic dark matter interactions with pass 8 data from the Fermi Large Area Telescope", *Phys. Rev.*, vol. D91, no. 12, pp. 122002, 2015.

[269] Mihailo Backovic, Kyoungchul Kong, and Mathew McCaskey, "MadDM v.1.0: Computation of Dark Matter Relic Abundance Using MadGraph5", *Physics of the Dark Universe*, vol. 5-6, pp. 18–28, 2014.

[270] Mihailo Backovic, Antony Martini, Olivier Mattelaer, Kyoungchul Kong, and Gopolang Mohlabeng, "Direct Detection of Dark Matter with MadDM v.2.0", *Phys. Dark Univ.*, vol. 9-10, pp. 37–50, 2015.

[271] G. Bélanger, F. Boudjema, A. Pukhov, and A. Semenov, "micrOMEGAs4.1: two dark matter candidates", *Comput.Phys.Commun.*, vol. 192, pp. 322–329, 2015.